The Role of Convective-Scale Processes in Tropical Cyclone Development

by

James J. Hack and Wayne H. Schubert

Department of Atmospheric Science
Colorado State University
Fort Collins, Colorado

Colorado State University

Department of Atmospheric Science

THE ROLE OF CONVECTIVE-SCALE PROCESSES
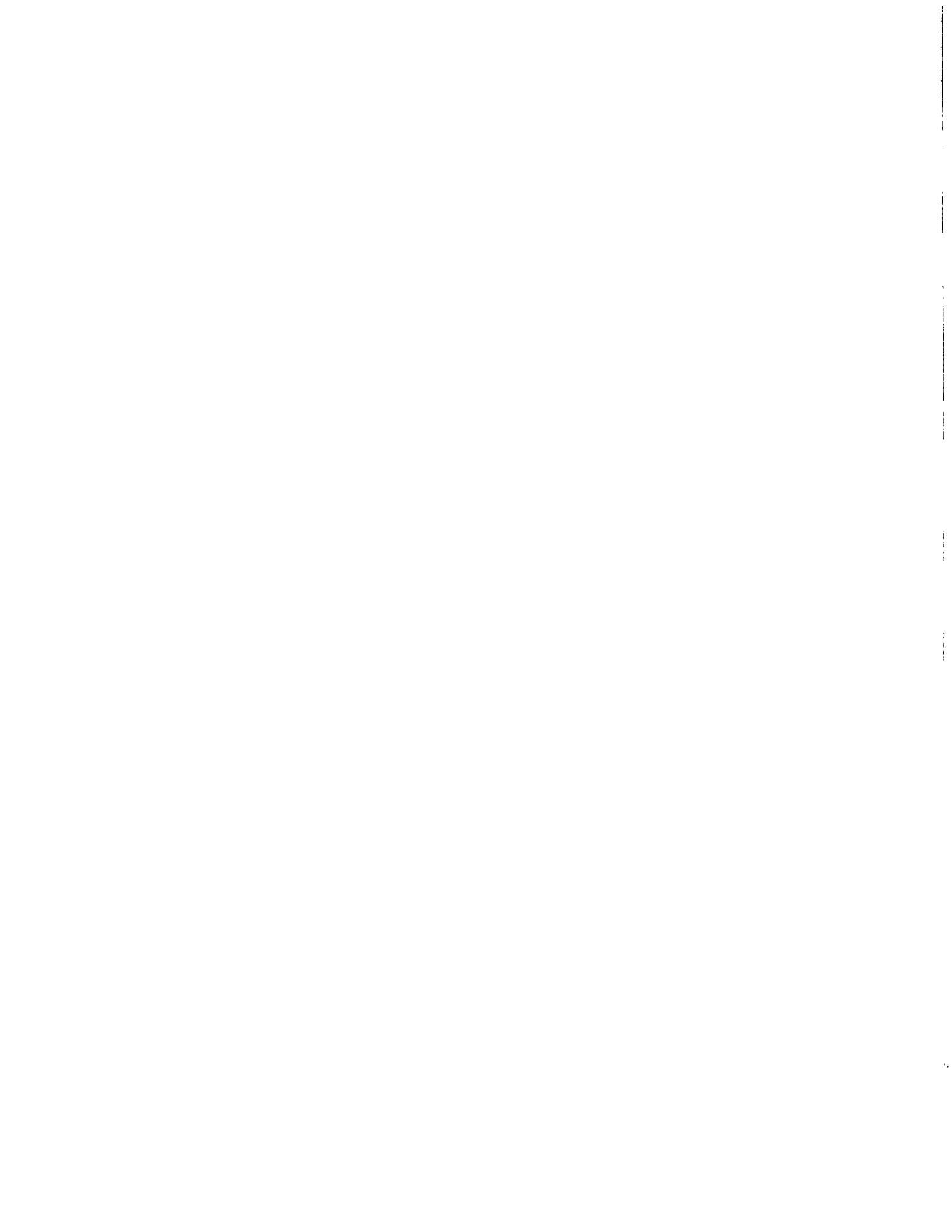
IN TROPICAL CYCLONE DEVELOPMENT

by

James J. Hack

Wayne H. Schubert

Department of Atmospheric Science
Colorado State University
Fort Collins, Colorado

December, 1980

ABSTRACT

An eighteen level axisymmetric primitive equation tropical cyclone model which incorporates the Arakawa-Schubert (1974) spectral cumulus parameterization is presented. The quasi-equilibrium hypothesis, which involves the solution of an integral equation for the cloud base mass flux distribution, is successfully formulated as an optimization problem to guarantee a nonnegative solution. A linear analysis suggests that in the tropics a large fraction of the available potential energy generated by the release of latent heat is partitioned to gravity-inertia wave motion and hence is radiated away to the far field. Therefore, an approximate pure gravity wave radiation boundary condition is derived which minimizes the reflection of gravity-inertia waves by the lateral boundary of the model.

The sensitivity of axisymmetric model storm development to the exact form of the lateral boundary condition, initial moisture distribution, and latent heat release mechanism is tested. It is demonstrated that the development of a hurricane-like circulation can be simulated without parameterized convection as suggested by Rosenthal (1978). Several other sensitivity experiments are conducted to address the roles of radiation and cumulus momentum transport in tropical cyclone development. The numerical results lead to the conclusion that neither of these processes should be neglected in attempts to numerically simulate the life cycle of the tropical cyclone since they appear to contribute significantly to the organization and scale of tropical disturbances.

ACKNOWLEDGEMENTS

TABLE OF CONTENTS

1.0 INTRODUCTION

The genesis and intensification of the tropical cyclone must certainly rank among the most spectacular of atmospheric phenomena. Observational studies have long since established that the energy to drive these storms is obtained from the release of latent heat in deep cumulus convection (e.g. Riehl and Malkus, 1961; Yanai, 1961a, b). Unfortunately, however, the details of the interactions between the cumulus and large-scale which give rise to the formation of a tropical storm are much less well understood.

Early linear stability analyses of the growth of small amplitude perturbations in a conditionally unstable environment were unable to explain the observed size and growth rates of the tropical cyclone (e.g. Haque, 1952; Syōno, 1953; Lilly, 1960). Thus, Charney and Eliassen (1964) and Ooyama (1964) proposed a mathematical theory in which the cloud field is organized so as to give rise to a heat source, which causes amplification of the large-scale disturbance, which in turn amplifies the cloud field. This cooperative interaction between the cloud field and large-scale circulation is more commonly referred to as Conditional Instability of the Second Kind (CISK).

Since the dynamical processes of the tropical cyclone generally occur on two widely different space and time scales (large-scale and cumulus-scale) both Charney and Eliassen and Ooyama treated the convective-scale implicitly, or by what is now called cumulus parameterization. Their approach stimulated many efforts to numerically simulate the life cycle of the tropical cyclone with more complicated nonlinear models (e.g. Ooyama, 1969a, b; Sundqvist, 1970a, b; Yamasaki, 1968a, b; Rosenthal, 1970; Anthes, 1972). The cumulus parameterization

methods employed in these models were highly empirical, neglecting many of the physical processes involved in the mutual interaction of the convective-scale and large-scale. Although these schemes have performed rather well, it is generally agreed that their relatively crude character limits their ability to contribute to a greater understanding of the processes which lead to tropical cyclone formation.

A theoretically complete and much more satisfying approach to cumulus parameterization has been proposed by Arakawa and Schubert (1974). Their theory describes the mutual interaction between an ensemble of cumulus clouds and the large-scale environment. The cloud field (or cloud ensemble) is represented by a spectrum of idealized model clouds ('sub-ensembles') each of which has its own mass, heat and moisture budget. The vertical transports accomplished by this spectrum of model clouds are actually the convective-scale eddy fluxes which appear, for example, in the horizontally averaged budget equations for dry static energy s, and water substance q (e.g. Yanai et al., 1973). Thus, knowledge of these eddy fluxes reduces to the determination of the cloud base mass flux for each member of the spectrum of model clouds. In order to predict the convective-scale eddy fluxes, Arakawa and Schubert propose the concept of quasi-equilibrium which assumes that the cloud base mass flux distribution can be related to time changes in the large-scale thermodynamic fields. Since this theory is the most physical and mathematically elegant approach proposed to date we believe it has the most potential for providing additional insight into the interactions between the cumulus-scale and large-scale which lead to tropical cyclone development. Surprisingly, with the exception of one investigation

(Wada, 1979), the theory has yet to be used in the numerical simulation of a tropical cyclone.

In this thesis, we briefly review the axisymmetric primitive equation tropical cyclone model first presented by Hack and Schubert (1976). The two unique aspects of the model are the convective parameterization, which follows the theory presented by Arakawa and Schubert (1974), and the formulation of the lateral boundary condition, which can be described as an approximate pure gravity wave radiation condition.

From a computational point of view, the most difficult aspect of the Arakawa-Schubert cumulus parameterization is the solution of the integral equation for the cloud base mass flux distribution. The various techniques suggested for solving this equation are all deficient since they do not guarantee a nonnegative mass flux distribution which is a necessary constraint if the solution is to be considered physically reasonable. By relaxing the quasi-equilibrium assumption, however, it is possible to formulate an optimization problem which constrains the cloud base mass flux to be nonnegative. This procedure, which is referred to as the optimal adjustment method, is discussed in chapter 2.

The particular formulation of the lateral boundary condition is motivated by the recent linear studies of geostrophic adjustment by Schubert et al. (1980) and Silva Dias and Schubert (1979) which suggest that in low latitudes most of the available potential energy generated by the release of latent heat is partitioned to gravity-wave motion and is therefore radiated away to the far field. A similar argument

is extended to a fully stratified model atmosphere (chapter 3) which gives rise to the lateral boundary condition employed in the model.

For nearly two decades the numerical simulation of the development of a hurricane circulation with the explicit release of latent heat was regarded as unachievable since early attempts to do so ended in apparent failure (Kasahara, 1961, 1962; Syōno, 1962). Recently, however, Rosenthal (1978) has successfully simulated the development of a tropical cyclone in which convective elements are explicitly resolved, demonstrating that the failure of these early investigations was probably not related to the explicit release of latent heat in a conditionally unstable atmosphere, but rather to a deficient model design. In chapter 5 we show that the tropical cyclone model used in this study is also capable of producing a hurricane circulation using only the explicit release of latent heat, although the desirability of such an approach is questionable.

Recent diagnostic studies of tropical weather systems have identified net longwave radiational cooling and cumulus-scale transports of horizontal momentum as two processes which appear to contribute significantly to the large-scale dynamic and thermodynamic budgets (e.g. Yanai et al., 1976; Reed and Johnson, 1974; Shapiro, 1978, Stevens, 1979). Previous numerical simulations of the tropical cyclone have generally neglected each of these convectively modulated processes. In chapter 6 we consider the sensitivity of model storm development to the incorporation of each process as well as to the combination. Other experiments which examine the sensitivity of model storm development to the initial moisture field and the lateral boundary condition are also conducted (see chapter 5). The response of the model is used to

assess the significance of each of these effects on tropical cyclone development.

2.0 MODEL DESCRIPTION

2.1 Large-Scale Governing Equations

We begin by noting that the large-scale governing equations are formulated for an f-plane using axisymmetric cylindrical coordinates in the horizontal, and the σ-coordinate in the vertical. Following Arakawa and Lamb (1977) we define σ as

$$\sigma \equiv \frac{p - p_T}{p_S - p_T} \equiv \frac{p - p_T}{\pi} , \qquad (2.1)$$

where the top boundary pressure p_T is a specified constant, and the surface pressure p_S (or equivalently π) is a function of the horizontal coordinate and time. The upper and lower boundaries are respectively given by $\sigma = 0$ and $\sigma = 1$. In the special case where $p_T = 0$, (2.1) reduces to the definition originally proposed by Phillips (1957).

The governing equations, which consist of the horizontal momentum equations, the hydrostatic equation, the mass continuity equation, the thermodynamic equation, the ideal gas law, and the water vapor mass continuity equation can be written

$$\frac{du}{dt} - \left(f + \frac{v}{r}\right) v + \frac{\partial \phi}{\partial r} + \sigma\alpha \frac{\partial \pi}{\partial r} = S_u , \qquad (2.2)$$

$$\frac{dv}{dt} + \left(f + \frac{v}{r}\right) u = S_v , \qquad (2.3)$$

$$\frac{\partial \phi}{\partial \sigma} = - \pi\alpha , \qquad (2.4)$$

$$\frac{d\pi}{dt} + \pi \left(\frac{\partial ru}{r \partial r} + \frac{\partial \dot{\sigma}}{\partial \sigma}\right) = 0 , \qquad (2.5)$$

$$\frac{dT}{dt} - \frac{\kappa T}{p} \frac{dp}{dt} = \frac{L}{c_p} (C - E) + S_T , \qquad (2.6)$$

$$p\alpha = RT \, , \tag{2.7}$$

$$\frac{dq}{dt} = -(C - E) + S_q \, , \tag{2.8}$$

where the individual time derivative of an arbitrary scalar quantity ψ is given by

$$\frac{d\psi}{dt} = \frac{\partial\psi}{\partial t} + u \frac{\partial\psi}{\partial r} + \dot{\sigma} \frac{\partial\psi}{\partial\sigma} \, , \tag{2.9}$$

and the symbols are defined as follows:

r   - radius

t   - time

u   - radial wind component

v   - tangential wind component

$\dot{\sigma}$ - vertical σ velocity, $d\sigma/dt$

p   - pressure

α - specific volume

T   - temperature

ϕ - geopotential

q   - water vapor mixing ratio

C   - rate of large-scale condensation per unit mass of dry air

E   - rate of large-scale evaporation per unit mass of dry air

S_u -

S_v -

S_T -   } convective scale source/sink terms

S_q -

f   - constant Coriolis parameter

R   - gas constant for air

c_p - specific heat capacity for air

κ - R/c_p

L - latent heat of evaporation

The formulation of the convective-scale source/sink terms is discussed in sections 2.2 and 2.3, while the formulation of the large-scale condensation (C) and evaporation (E) is presented in section 2.4. In the absence of these terms, (2.2)-(2.7) govern adiabatic inviscid flow.

As upper and lower boundary conditions we require that air particles do not cross the $\sigma = 0$ and $\sigma = 1$ coordinate surfaces, i.e.

$$\dot{\sigma} = 0 \quad \text{at} \quad \sigma = 0, 1 \; . \tag{2.10}$$

Integrating (2.5) over the entire vertical column using the boundary conditions (2.10) gives

$$\frac{\partial \pi}{\partial t} = - \frac{\partial}{r\partial r} \int_0^1 \pi r u d\sigma \; . \tag{2.11}$$

If we now integrate (2.5) from the top of the vertical column to σ using the upper boundary condition, we obtain yet another form of the continuity equation

$$\pi \dot{\sigma} = - \left[\sigma \frac{\partial \pi}{\partial t} + \frac{\partial}{r\partial r} \int_0^\sigma \pi r u d\sigma' \right] \; . \tag{2.12}$$

Thus, knowledge of the radial wind component u allows computation of $\frac{\partial \pi}{\partial t}$ by means of (2.11), and $\pi\dot{\sigma}$ may then be diagnosed at any σ level using (2.12).

Defining the potential temperature

$$\theta \equiv T \left(\frac{p_0}{p}\right)^\kappa \tag{2.13}$$

and using the definition of the vertical coordinate (2.1), allows us to rewrite the thermodynamic equation (2.6) as

$$\frac{\partial T}{\partial t} + u \frac{\partial T}{\partial r} + \dot{\sigma} \left(\frac{p}{P_o} \right)^K \frac{\partial \theta}{\partial \sigma} - \frac{\sigma \alpha}{c_p} \frac{d\pi}{dt} = \frac{L}{c_p} (C-E) + S_T \ . \qquad (2.14)$$

The system of equations is now complete consisting of ten equations (2.11, 2.2, 2.3, 2.14, 2.8, 2.1, 2.12, 2.7, 2.4 and 2.13) in the ten unknown variables π, u, v, T, q, p, $\dot{\sigma}$, α, ϕ, and θ, all of which are functions of the three independent variables (r,σ,t) with the exception of π which is a function of (r,t) only. Five of these variables are predicted (π, u, v, T and q) while the others are diagnosed.

For purposes of numerical integration it is more convenient to consider the five prognostic equations in flux form rather than in the advective form in which they have been introduced. Using the form of the continuity equation given by (2.5) and the definition of the total derivative (2.9), we obtain the flux form of the individual time derivative of an arbitrary scalar quantity ψ as

$$\pi \frac{d\psi}{dt} = \frac{\partial}{\partial t} (\pi \psi) + \frac{\partial}{r \partial r} (\pi r u \psi) + \frac{\partial}{\partial \sigma} (\pi \dot{\sigma} \psi) \ . \qquad (2.15)$$

Accordingly, the prognostic equations can be rewritten, and the complete system of equations can be arranged for numerical integration in the following order.

$$\frac{\partial}{\partial t} (\pi r) = - \frac{\partial}{\partial r} \int_0^1 \pi r u d\sigma \ , \qquad (2.16)$$

$$\pi r \dot{\sigma} = - \left| \sigma \frac{\partial}{\partial t} (\pi r) + \frac{\partial}{\partial r} \int_0^\sigma \pi r u d\sigma' \right| \ , \qquad (2.17)$$

$$p = p_T + \pi \sigma \ , \qquad (2.18)$$

$$\alpha = \frac{RT}{p} \ , \qquad (2.19)$$

$$\frac{\partial \phi}{\partial \sigma} = - \pi \alpha \quad , \tag{2.20}$$

$$\frac{\partial}{\partial t} (\pi r u) = - \frac{\partial}{\partial r} (\pi r u u) - \frac{\partial}{\partial \sigma} (\pi r \dot{\sigma} u) + (f + \frac{v}{r}) \pi r v$$
$$- r(\pi \frac{\partial \phi}{\partial r} + \sigma \pi \alpha \frac{\partial \pi}{\partial r}) + \pi r S_u \quad , \tag{2.21}$$

$$\frac{\partial}{\partial t} (\pi r v) = - \frac{\partial}{\partial r} (\pi r u v) - \frac{\partial}{\partial \sigma} (\pi r \dot{\sigma} v) - (f + \frac{v}{r}) \pi r u + \pi r S_v \quad , \tag{2.22}$$

$$\theta = T \left(\frac{p_o}{p}\right)^K \quad , \tag{2.23}$$

$$\frac{\partial}{\partial t} (\pi r T) = - \frac{\partial}{\partial r} (\pi r u T) - \left(\frac{p}{p_o}\right)^K \frac{\partial}{\partial \sigma} (\pi r \dot{\sigma} \theta)$$
$$+ \frac{\pi r \sigma \alpha}{c_p} \left[\frac{\partial}{\partial t} + u \frac{\partial}{\partial r}\right] \pi + \pi r \frac{L}{c_p} (C - E) + \pi r S_T \quad , \tag{2.24}$$

$$\frac{\partial}{\partial t} (\pi r q) = - \frac{\partial}{\partial r} (\pi r u q) - \frac{\partial}{\partial \sigma} (\pi r \dot{\sigma} q) + \pi r (-C + E) + \pi r S_q \quad . \tag{2.25}$$

Initial conditions are required on the five prognostic variables π, u, v, T and q. The initialization procedure as well as the initial conditions are discussed in chapter 4. The procedure followed in a single prognostic cycle is as follows.

1) Calculate the tendency of π from (2.16).

2) Using the tendency of π just calculated, calculate $\pi r \dot{\sigma}$ from (2.17).

3) Using (2.18) and (2.19), calculate the geopotential ϕ from (2.20).

4) Calculate the tendencies of u and v from (2.21) and (2.22).

5) Using (2.23) calculate the tendency of T from (2.24).

6) Calculate the tendency of q from (2.25).

7) Return to the first step.

The discrete model consists of 18 levels in the vertical direction ($p_T = 100$ mb) and 64 grid points in the horizontal direction ($\Delta r = 15$ km). Horizontal and vertical finite differencing of (2.16)-(2.25) follow the schemes proposed by Arakawa (1972) and Arakawa, Mintz et al. (1974) for the UCLA GCM. The vertical differencing is identical to the 1972 UCLA scheme while the horizontal differencing is somewhat different due to the use of cylindrical coordinates and considerably simpler due to our assumption of axisymmetry. A discussion of the finite differencing of the large-scale governing equations (2.16)-(2.25) is included in Appendix A.

2.2 Parameterization of Cumulus Convection

The importance of cumulus convection to the genesis, intensification and maintenance of the tropical cyclone has long been established by observational studies (e.g. Riehl and Malkus, 1961; Yanai, 1961a, b). However, early stability analyses (Haque, 1952; Syono, 1953; Lilly, 1960), which treat the dynamics of the cyclone in most respects like a cloud, were unable to account for the observed size and growth rates of tropical cyclones. This apparent failure of theory led Charney and Eliasser (1964) and Ooyama (1964) to introduce the concept of Conditional Instability of the Second Kind (CISK) which embodies a cooperative interaction between the cumulus-scale and large-scale. In a broad sense, CISK describes a situation in which the large-scale circulation is responsible for organizing and maintaining cumulus convection by providing the necessary transport of water vapor, while the cumulus-scale drives the large-scale circulation through the

release of latent heat in deep convective elements. Both Charney and Eliassen and Ooyama dealt with the large-scale explicitly, but treated the convective scale implicitly, i.e. the cumulus activity was specified to be a function of the large-scale fields, or was treated by what is now commonly referred to as cumulus parameterization.

Although Charney and Eliassen's and Ooyama's work dealt only with the initial growth of a tropical depression, their approach stimulated efforts to numerically simulate the life cycle of tropical cyclones with more complicated non-linear models. The convective parameterizations employed in these tropical cyclone models were highly empirical, neglecting many of the physical processes involved in the mutual interaction of cloud and environment. These included schemes in which the convective-scale heating rates were dependent upon the large-scale convergence of water vapor in the atmospheric boundary layer (Ooyama, 1969a, b; Ogura, 1964), and the net large-scale convergence of water vapor throughout the depth of the troposphere (Kuo, 1965). Such schemes have performed surprisingly well in numerical integrations (e.g. Yamasaki, 1968a, b; Ooyama, 1969a, b; Rosenthal, 1970; Sundqvist, 1970a, b) in which the models have produced many of the important features observed in tropical cyclones. It is generally agreed, however, that these relatively crude techniques are limited in their ability to contribute to a greater understanding of the interaction between cumulus clouds and the cyclone-scale flow in tropical storms, especially during the developing (or nondeveloping) stages. Unfortunately, suitable alternatives were lacking for many years, primarily because of a lack of knowledge regarding the interaction of clouds with the larger scale.

The problem of establishing the physical nature of the interaction of organized cumulus convection with the large-scale fields is fundamental to tropical meteorology. A clear understanding of this interaction is in all likelihood essential to an understanding of why the tropical cyclone is such a rare event. In recent years, many diagnostic (and some prognostic) studies have been made which have led to an improvement in our knowledge of cumulus convection, and consequently to an improvement in cumulus parameterization theory. Simple one dimensional cloud models have proven to be useful in diagnosing the interaction of precipitating cumulus ensembles with the larger-scale motions (e.g. Yanai et al., 1973; Ogura and Cho, 1973; Gray, 1973; Nitta, 1977, 1978; Yanai et al., 1976; Johnson, 1976, 1977). The use of such idealized models of convection has enabled observationalists for the first time to extract convective-scale properties directly from the large-scale observations. The simpler problem of non-precipitating trade wind cumulus convection has also been studied (e.g. Augstein et al., 1973; Holland and Rasmussen, 1973; Betts, 1975; Nitta, 1975) and has contributed to a better understanding of the way in which the convective-scale fluxes contribute to the growth and maintenance the trade inversion. These and other studies have helped to establish a general consensus on how cumulus clouds modify the large-scale thermodynamic fields.

Ooyama (1971) recognized the need to improve cumulus parameterization theory, and was the first to propose a theory taking into account the coexistence of a spectrum of clouds. The clouds were represented by independent entraining buoyant elements dispatched from the mixed

layer. The theory was not closed, however, since the determination of the 'dispatcher function' was left to future consideration. Even so, several numerical experiments have been conducted with the theory (using empirically derived forms of the dispatcher function) yielding reasonable results (Ooyama, 1973; Rosenthal, 1973).

Arakawa and Schubert (1974) have proposed a closed cumulus parameterization theory which describes the interaction of a spectrally divided cumulus cloud ensemble with the large-scale environment. With the exception of one investigation (Wada, 1979) this theory has yet to be used in the numerical simulation of a tropical cylcone. Since the theory is the most complete theory proposed to date, we will make use of it in this study with the hope that it may help provide additional insight into the interactions between the cumulus-scale and large-scale which lead to tropical cyclone development. In this section we discuss the formulation of the Arakawa-Schubert cumulus parameterization theory. Several simplifications have been made to the theory for computational reasons and will be noted in the discussion.

The mutual interaction between the cloud ensemble and the large-scale environment is conceptually illustrated in Fig. 2.1 where the equations of the theory have been grouped into three categories: feedback, static control, and dynamic control (Schubert, 1974). The equations which constitute the feedback part of the loop describe how the cumulus-scale transport terms and source/sink terms modify the large-scale thermodynamic fields, while the equations comprising the static and dynamic control parts of the interaction loop describe

FEEDBACK

cumulus terms in prognostic equations for $\bar{s}(p)$, $\bar{q}(p)$

LARGE — SCALE ENVIRONMENT

$\bar{s}(p)$ $\bar{q}(p)$

s_M q_M

CUMULUS CLOUD ENSEMBLE

$\eta\ (p,\hat{p})$
$s_c(p,\hat{p})$
$q_c(p,\hat{p})$
$\ell\ (p,\hat{p})$
$\hat{p}_D(p)$ or $p_D(\hat{p})$

$m_B(\hat{p})$

STATIC CONTROL

sub-ensemble budgets, saturation relation, vanishing buoyancy at detrainment level.

DYNAMIC CONTROL

integral equation for $m_B(\hat{p})$.
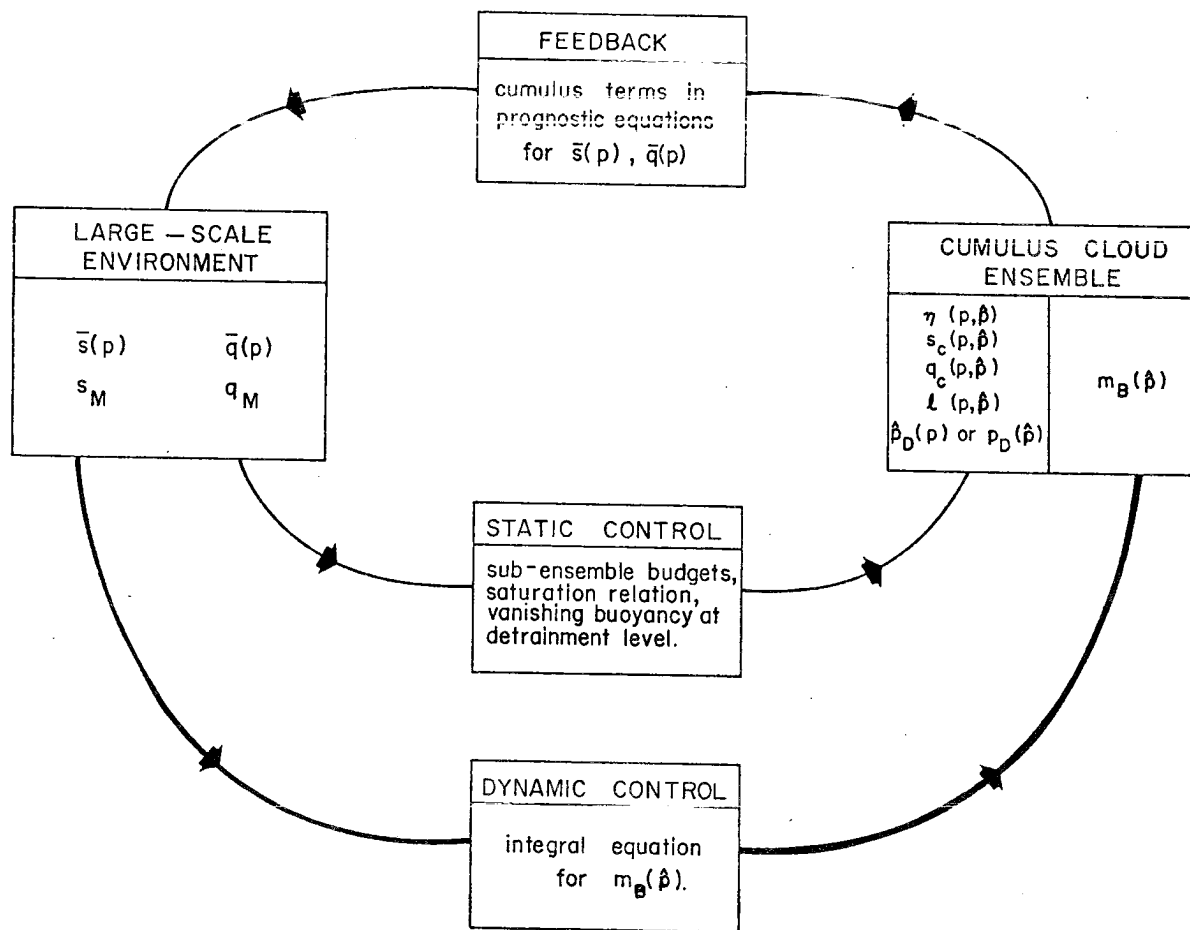
Figure 2.1   Schematic representation of cloud-environment interaction (after Schubert, 1974).

how the properties of the cloud ensemble are controlled by the large-scale fields. We continue our discussion of the parameterization theory within this framework.

2.2.1 Feedback

The complete theory divides the large-scale environment into a subcloud mixed layer of variable depth and the region of cumulus convection above the mixed layer, separated by an infinitesimally thin transition layer (see Fig. 2.2). In the subcloud mixed layer the dry static energy $(s \equiv c_p T + \phi)$, water vapor mixing ratio q, and therefore the moist static energy h, are constant with height and are denoted by the symbols s_M, q_M, and h_M. The top of the subcloud mixed layer p_B is generally somewhat below cloud base p_C. Below p_B, convective-scale transports are accomplished by the turbulence of the mixed layer, where the turbulence is confined below p_B by the stable and infinitesimally thin transition layer. Across the transition layer there can be discontinuities in the dry static energy and moisture, as well as discontinuities in the convective-scale fluxes. Above p_B the convective-scale transports are accomplished by the cloud ensemble. Let us write the heat and moisture budget equations for this region in terms of dry static energy s and water vapor mixing ratio q (c*. Yanai et al., 1973). These are

$$\frac{\partial \bar{s}}{\partial t} = -\overline{V} \cdot \nabla \bar{s} - \bar{\omega} \frac{\partial \bar{s}}{\partial p} - \frac{\partial}{\partial p} (\overline{\omega' s_\ell'}) + L\bar{R} + Q_R \qquad (2.26)$$

and

Figure 2.2 Typical ITCZ profiles of $\bar{s}$, $\bar{h}$, and $\bar{h}^*$. Above p_B these profiles are those of Yanai et al. (1973). The sc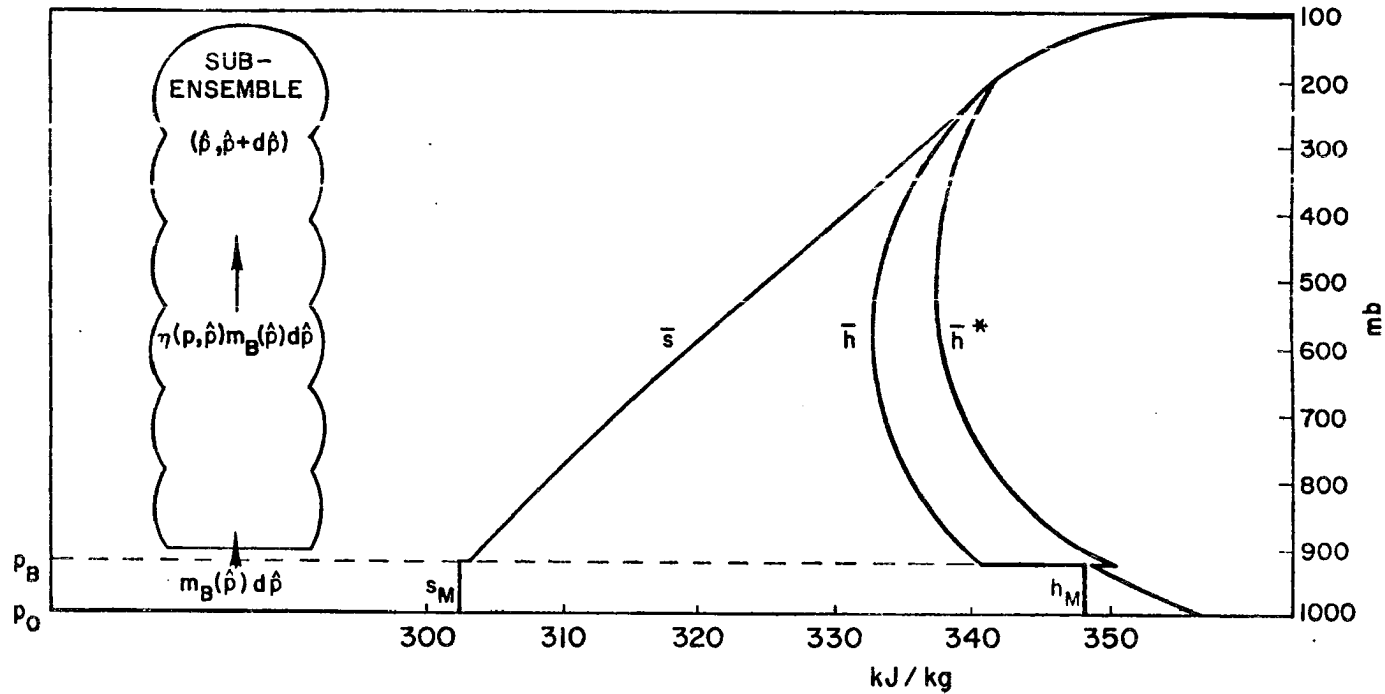hematic sub-ensemble has cloud base p_C slightly above p_B. The mass flux at level p is $\eta(p,\hat{p})m_B(\hat{p})d\hat{p}$, while the mass flux at p_B is $m_B(\hat{p})d\hat{p}$.

$$\frac{\partial \bar{q}}{\partial t} = -\overline{W} \cdot \nabla \bar{q} - \bar{\omega} \frac{\partial \bar{q}}{\partial p} - \frac{\partial}{\partial p} [\overline{\omega'(q'+\ell')}] - R \ . \qquad (2.27)$$

The barred quantities represent horizontal averages over an area large enough to contain an ensemble of clouds, but small enough so as only to cover a fraction of a large-scale disturbance. The primed quantities represent deviations from the horizontal averages and are interpreted as convective-scale properties, while the quantity R is the convective-scale liquid water sink (i.e. the water removed by convection in the form of precipitation). The liquid water static energy $s_\ell \equiv s - L\ell$ is the static energy analogue of the liquid water potential temperature introduced by Betts (1975).

In addition to the vertical transport of heat and moisture, we allow the cumulus ensemble to vertically transport (i.e. redistribute) horizontal momentum. A budget equation, which is similar to those for heat and moisture, can be derived for the horizontal momentum W and is written

$$\frac{\partial \overline{W}}{\partial t} = -\overline{W} \cdot \nabla \overline{W} - \bar{\omega} \frac{\partial \overline{W}}{\partial p} - f \, lkx \ \overline{W} - \nabla \bar{\phi} - \frac{\partial}{\partial p} (\overline{\omega' W'}) \ . \qquad (2.28)$$

Following Schubert (1974) we express the convective-scale fluxes of dry static energy, water vapor, liquid water, and horizontal momentum as

$$\frac{1}{g} (-\overline{\omega' s'}) \equiv F_s(p) =$$

$$-\int_{p_B-p_T}^{p_B-p} \eta(p,\hat{p}) \ [s_c(p,\hat{p}) - \bar{s}(p)] \ m_B(\hat{p}) \ d\hat{p} \qquad p \leq p_B , \qquad (2.29)$$

$$\frac{1}{g}\,(\overline{-\omega'c'}) \equiv F_q(p) =$$

$$-\int_{p_B-p_T}^{p_B-p} n(p,\hat{p})\,[q_c(p,\hat{p})-\overline{q}(p)]\,m_B(\hat{p})\,d\hat{p} \qquad p \le p_B\ , \qquad (2.30)$$

$$\frac{1}{g}\,(\overline{-\omega'\ell'}) \equiv F_\ell(p) =$$

$$-\int_{p_B-p_T}^{p_B-p} n(p,\hat{p})\,\ell(p,\hat{p})\,m_B(\hat{p})\,d\hat{p} \qquad p \le p_B\ , \qquad (2.31)$$

$$\frac{1}{g}\,(\overline{-\omega'\,\overrightarrow{V}'}) \equiv F_V(p) =$$

$$-\int_{p_B-p_T}^{p_B-p} n(p,\hat{p})\,[\overrightarrow{V}_c(p,\hat{p})-\overline{\overrightarrow{V}}(p)]\,m_B(\hat{p})\,d\hat{p} \qquad p \le p_B.\,(2.32)$$

We see from (2.29)-(2.32) that the cumulus cloud ensemble has been spectrally divided into 'sub-ensembles' each of which is characterized by its pressure depth $\hat{p} \equiv p_B-p_D$, where p_D is the detrainment pressure level. Our use of $\hat{p}$ as the spectral parameter differs from the original formulation in which the sub-ensembles were characterized by the fractional entrainment rate λ. This alteration is motivated by computational convenience and will be discussed further when we consider the dynamic control part of the theory. Thus, the dry static energy, water vapor, liquid water and horizontal vector momentum inside sub-ensemble $\hat{p}$ at level p are respectively denoted by $s_c(p,\hat{p})$, $q_c(p,\hat{p})$, $\ell(p,\hat{p})$ and $\overrightarrow{V}_c(p,\hat{p})$. The vertical mass flux at level p due to sub-ensemble $\hat{p}$ is $n(p,\hat{p})m_B(\hat{p})d\hat{p}$ where $n(p,\hat{p})$ is the normalized mass flux

which has unit value at the top of the sub-cloud mixed layer p_B. A simple physical interpretation of (2.29)-(2.32) is that for each sub-ensemble $\hat{b}$, the net upward flux at level p of a particular quantity (such as s or W) is given by the difference between the upward flux of that quantity inside the sub-ensemble (denoted by subscript c) and the downward flux of the environmental value (denoted by a bar). This downward mass flux in the environment is merely the compensating subsidence produced by the sub-ensemble. Since the environment does not contain liquid water there is no downward flux of liquid water due to environmental subsidence, and the convective-scale liquid water flux takes a simpler form. The total ensemble flux at level p of any quantity (such as F_s or F_W) is then given by an integral over all sub-ensembles which penetrate level p.

By combining the three basic fluxes F_s, F_q, and F_ℓ we can rewrite (2.26) and (2.27) as

$$\frac{\partial \bar{s}}{\partial t} = \frac{\partial \bar{s}}{\partial t}\bigg|_{L.S.} + g\frac{\partial}{\partial p} F_{s-L\ell} + LR \tag{2.33}$$

and

$$\frac{\partial \bar{q}}{\partial t} = \frac{\partial \bar{q}}{\partial t}\bigg|_{L.S.} + g\frac{\partial}{\partial p} F_{q+\ell} - R \tag{2.34}$$

where

$$F_{s-L\ell} \equiv F_s - LF_\ell \quad , \tag{2.35}$$

$$F_{q+\ell} \equiv F_q + F_\ell \quad , \tag{2.36}$$

and the larger scale contributions to the time derivatives on the left
hand side of (2.26) and (2.27) have been grouped into one term denoted
with the subscript L.S. Similarly, (2.28) can also be rewritten

$$\frac{\partial \overline{W}}{\partial t} = \frac{\partial W}{\partial t}\bigg|_{L.S.} + g\frac{\partial}{\partial p} F_W \ . \tag{2.37}$$

The convective liquid water sink R is defined by

$$R(p) \equiv -g \int_{p_B-p_T}^{p_B-p} \eta(p,\hat{p})\ c_0(\hat{p})\ell(p,\hat{p})m_B(\hat{p})\ d\hat{p} \ . \tag{2.38}$$

The expression for R states that the quantity of water removed from
the atmosphere at level p by sub-ensemble $\hat{p}$ is simply proportional to
the sub-ensemble liquid water content at that level. Physically this
means that a certain fraction of the liquid water content (or cloud
droplets) of each sub-ensemble is converted to raindroplets (as
specified by the coefficient $c_0(\hat{p})$) which are immediately removed
from the system (i.e. they are assumed to reach the ground without
evaporating). As originally formulated, Arakawa and Schubert chose
a constant autoconversion coefficient c_0 of $2.0 \times 10^{-3}m^{-1}$ so that the
calculated values of the cloud liquid water content would approximately
agree with observed values. However, Silva Dias and Schubert (1977)
used the results of a theoretical parametric model of cumulus convection
(Lopez, 1973) to demonstrate that a constant value of c_0 probably
underestimated the precipitation associated with deep clouds while
overestimating the precipitation associated with shallow clouds. In
a one dimensional ('semi-prognostic') model which incorporated the

Arakawa-Schubert parameterization scheme, they went on to show that the choice of a variable autoconversion coefficient (which produced more reasonable precipitation rates) had little effect on the cloud population produced by the model, although it did slightly decrease the magnitude of the temperature and moisture tendencies associated with the parameterized convection. Thus, we have chosen to use an autoconversion coefficient c_0 which is dependent upon $\hat{p}$ (see Fig. 2.3) such that the deep clouds are more efficient at producing precipitation while the shallow clouds are less efficient.

Since $R(p)$ then represents the total ensemble sink of liquid water at level p, we obtain the total ensemble precipitation rate (P) by integrating $R(p)$ over the depth of the model atmosphere,

$$P = \frac{1}{g} \int_{p_T}^{p_B} R(p)dp \ . \tag{2.39}$$

Below p_B the convective-scale fluxes of s, q and W are linear in pressure with the values $(F_s)_S$, $(F_q)_S$ and $(F_W)_S$ at the surface, and the convective-scale flux of ℓ is zero everywhere. In the complete theory, the surface fluxes and convective-scale fluxes of heat and moisture at p_{B-} determine the time variation of the depth of the subcloud mixed layer. However, the present version of the tropical cyclone model does not include a mixed layer of variable depth, but rather a 'mixed layer' whose top is defined by a fixed sigma coordinate surface. Thus, for computational reasons, we find it necessary to modify the way in which the cumulus ensemble interacts with the mixed layer. This modification involves allowing the cumulus convection to directly influence the energy budget of the mixed layer, rather than
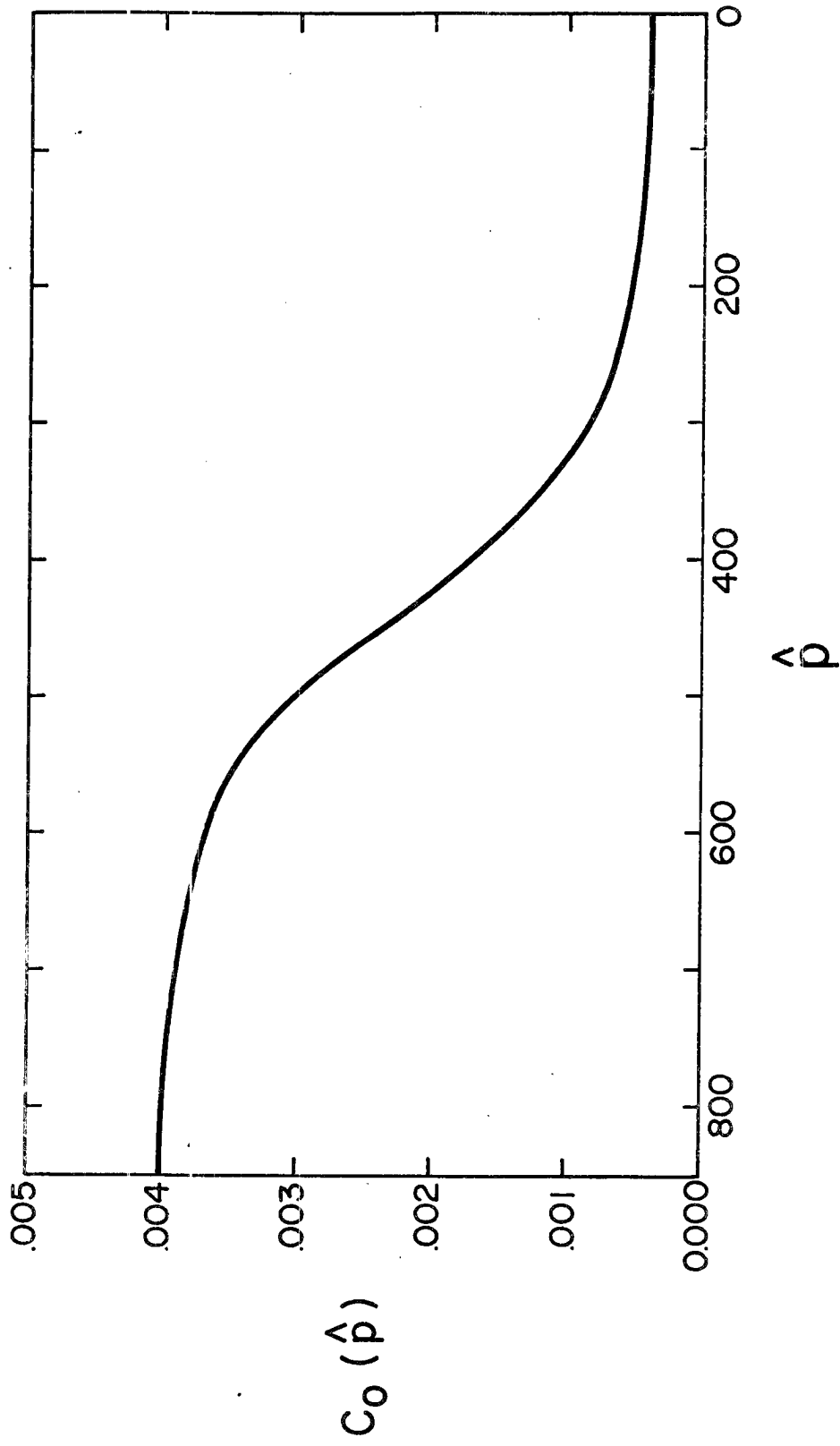
Figure 2.3   The autoconversion coefficient $c_o(\hat{p})$.

determining the depth of the mixed layer as in the more general theory. The budget equations for the dry static energy, moisture and momentum of the mixed layer (s_M, q_M and W_M respectively) are given by

$$\frac{\partial s_M}{\partial t} = - W_M \cdot \nabla s_M + \frac{g}{p_S - p_B} [(F_s)_S - (F_s)_B] + (Q_2)_M , \qquad (2.40)$$

$$\frac{\partial q_M}{\partial t} = - W_M \cdot \nabla q_M + \frac{g}{p_S - p_B} [(F_q)_S - (F_q)_B] , \qquad (2.41)$$

and

$$\frac{\partial W_M}{\partial t} = - W_M \cdot \nabla W_M + \frac{g}{p_S - p_B} [(F_W)_S - (F_W)_B] \qquad (2.42)$$

where

$$\left. \begin{array}{l} (F_s)_B = \Delta s M_B \\ (F_q)_B = \Delta q M_B \\ (F_W)_B = \Delta W M_B \end{array} \right\} . \qquad (2.43)$$

In (2.43) the symbol delta represents the jump of the particular property across the top of the sub-cloud mixed layer p_B (e.g. $\Delta s \equiv \bar{s}(p_{B-}) - \bar{s}_M$). The quantity M_B is the total cloud base mass flux associated with the cumulus ensemble, i.e.

$$M_B = -\int_{p_B - p_T}^{0} m_B(\hat{p}) \, d\hat{p} . \qquad (2.44)$$

We note that in the above formulation, the convective-scale fluxes of s and q are continuous across the top of the subcloud mixed layer even though the large-scale values are not. One additional approximation we make is that the cloud base p_C and the top of the model mixed layer p_B are one and the same.

The cumulus ensemble transport terms, $F_{s-L\ell}$, $F_{q+\ell}$, F_V, M_B, and the cumulus ensemble source/sink term R constitute the feedback part of the interaction loop shown in Fig. 2.1. From (2.29), (2.30), (2.31), (2.32), (2.38) and (2.44) we see that the determination of these quantities is equivalent to the determination of $\eta(p,\hat{p})$, $s_c(p,\hat{p})$, $q_c(p,\hat{p})$, $\ell(p,\hat{p})$, $W_c(p,\hat{p})$ and $m_B(\hat{p})$. All except $m_B(\hat{p})$ are determined in the static control part of the interaction loop while $m_B(\hat{p})$ is determined by the dynamic control. Once these quantities are known, it is possible to predict the time variation of the temperature and moisture field both above and below p_B.

2.2.2 Static control

The sub-ensemble normalized mass flux, moist static energy and total water content are determined from their respective budget equations. These are given by

$$\frac{\partial \eta(p,\hat{p})}{\partial p} = -\lambda(\hat{p})\eta(p,\hat{p}) , \qquad (2.45)$$

$$\frac{\partial}{\partial p} [\eta(p,\hat{p})h_c(p,\hat{p})] = -\lambda(\hat{p})\eta(p,\hat{p})\bar{h}(p) , \qquad (2.46)$$

and

$$\frac{\partial}{\partial p} \{\eta(p,\hat{p})[q_c(p,\hat{p})+\ell(p,\hat{p})]\} = \eta(p,\hat{p})c_0(\hat{p})\ell(p,\hat{p})-\lambda(\hat{p})\eta(p,\hat{p})\bar{q}(p) , \qquad (2.47)$$

where the fractional entrainment rate $\lambda(\hat{p})$ has the units Pa^{-1}. The air inside the sub-ensembles (or clouds) is assumed to be saturated at a temperature only slightly different than the environment, an assumption which gives rise to the saturation relation

$$q_c(p,\hat{p}) = \bar{q}*(p) + \frac{\gamma(p)}{1+\gamma(p)} \frac{1}{L} [h_c(p,\hat{p})- \bar{h}*(p)] , \qquad (2.48)$$

where $\bar{q}^*(p)$ is the saturation value of q at level p, $\bar{h}^*(p)$ is the saturated moist static energy at level p and $\gamma(p) \equiv \frac{L}{c_p} \left[\frac{\partial q^*}{\partial T} \right]_p$ (cf. Arakawa, 1969). In order to determine the individual sub-ensemble budgets, knowledge of the fractional entrainment rate $\lambda(\hat{p})$ is required. This entrainment rate is given by the vanishing bouyancy condition

$$s_{v_c}(p,\hat{p}) = \bar{s}_v(p) ,$$ (2.49)

or using the definition of the virtual dry static energy[1]

$$s_{v_c}(p,\hat{p}) = \bar{s}(p) + c_p \bar{T}(p) \, \delta[q_c(p,\hat{p}) - \bar{q}(p)] ,$$ (2.50)

where $\delta = 0.608$.

The sub-ensemble horizontal momentum $W_c(p,\hat{p})$ must be determined as a function of the large-scale dynamic and thermodynamic fields. This is a more difficult problem, since $W_c(p,\hat{p})$ is not a conserved quantity as are some thermodynamic properties. Convective-scale pressure gradients, as well as stresses produced by the large shears present between the updraft and environment motions, are likely to produce some modification to the 'in cloud' horizontal momentum. However, here we follow the simple alternative (e.g. Ooyama, 1971; Arakawa, Mintz et al., 1974; Schneider and Lindzen, 1976) of assuming that W_c is conservative. This leads to the sub-ensemble budget equation for momentum

$$\frac{\partial}{\partial p} [\eta(p,\hat{p}) \, W_c(p,\hat{p})] = -\lambda(\hat{p})\eta(p,\hat{p}) \, \overline{W}(p) .$$ (2.51)

Thus, the static control part of the interaction loop consists of the six equations (2.45)-(2.48), (2.50), and (2.51) in the six unknown

---

[1] The effects of liquid water have been neglected.

variables $\eta(p,\hat{p})$, $s_c(p,\hat{p})$, $q_c(p,\hat{p})$, $\ell(p,\hat{p})$, $\lambda(\hat{p})$, and $\mathbb{W}_c(p,\hat{p})$. Since (2.45)-(2.47) and (2.51) are differential equations which are solved upward from p_B, they require the appropriate boundary conditions which are $\eta(p_B,\hat{p}) = 1$, $h_c(p_B,\hat{p}) = h_M$, $q_c(p_B,\hat{p}) = q_M$, $\ell(p_B,\hat{p}) = 0$ and $\mathbb{W}_c(p_B,\hat{p}) = \mathbb{W}_M$.

2.2.3 Dynamic control and the optimal adjustment method

The last remaining problem is the determination of the mass flux distribution function $m_B(\hat{p})$ since once it is known, the time variation of the temperature, moisture and momentum fields can be predicted from (2.33), (2.34), (2.37) and (2.40)-(2.42). In order to determine $m_B(\hat{p})$, Arakawa and Schubert first introduce the cloud work function

$$A(\hat{p}) = \int_{p_D(\hat{p})}^{p_B} \eta(p,\hat{p}) \ [s_{v_c}(p,\hat{p}) - \bar{s}_v(p)] \ \frac{dp}{p} , \qquad (2.52)$$

an integral measure of the bouyancy force associated with sub-ensemble $\hat{p}$, with the weighting function $\eta(p,\hat{p})$. Physically, $A(\hat{p}) > 0$ can be thought of as a generalized criterion for moist convective instability, while $A(\hat{p}) \leq 0$ is indicative of a neutral or stable situation. It is also a measure of the efficiency of kinetic energy generation by buoyancy forces for sub-ensemble $\hat{p}$. Since the variables in the integrand of (2.52) are either prognostic variables, or are related diagnostically to prognostic variables, the time rate of change of $A(\hat{p})$ can be written in terms of the time derivatives of s_M, q_M, $\bar{s}(p)$, and $\bar{q}(p)$ (we here-after refer to barred and mixed layer quantities as 'large-scale' quantities). These time derivatives are in turn related to two types of terms: convective-scale terms which are proportional to the cloud base mass flux distribution $m_B(\hat{p})$, and the large-scale terms which

include horizontal and vertical advection, radiation, and surface eddy fluxes (see equations (2.26), (2.27) and (2.40)-(2.41)). Thus, the time rate of change of $A(\hat{p})$ can be expressed as the sum of convectively induced changes and large-scale changes (in which we have included surface eddy fluxes), or

$$\frac{\partial A(\hat{p})}{\partial t} = \left.\frac{\partial A(\hat{p})}{\partial t}\right|_{C.S.} + \left.\frac{\partial A(\hat{p})}{\partial t}\right|_{L.S.} . \tag{2.53}$$

Since the convective-scale terms depend linearly on $m_B(\hat{p})$ and all sub-ensembles participate in determining $\left.\frac{\partial A(\hat{p})}{\partial t}\right|_{C.S.}$, we can write

$$\frac{\partial A(\hat{p})}{\partial t} = -\int_{p_B-p_T}^{0} K(\hat{p},\hat{p}\prime)\, m_B(\hat{p}\prime)\, d\hat{p}\prime + F_{L.S.}(\hat{p}) , \tag{2.54}$$

where the kernel $K(\hat{p},\hat{p}\prime)$ and the forcing $F_{L.S.}(\hat{p})$ are known. The kernel represents either a destruction or generation of $A(\hat{p})$ by sub-ensemble $\hat{p}\prime$ if sub-ensemble $\hat{p}\prime$ has unit cloud base mass flux.

Arakawa and Schubert proposed a closure hypothesis, referred to as quasi-equilibrium, which requires balance between the large-scale generation of $A(\hat{p})$ and the convective-scale destruction of $A(\hat{p})$ for all sub-ensembles. Mathematically this closure hypothesis takes the form

$$-\int_{p_B-p_T}^{0} K(\hat{p},\hat{p}\prime)\, m_B(\hat{p}\prime)\, d\hat{p}\prime + F_{L.S.}(\hat{p}) = 0 . \tag{2.55}$$

It is appropriate at this point to consider the use of $\hat{p}$ (pressure depth) as the spectral parameter, rather than λ (fractional entrainment rate) as in the original theory. Because we will be incorporating the parameterization scheme in a vertically discrete model atmosphere,

the use of λ as the spectral parameter must be reconsidered since in order to follow sub-ensemble λ in time, the detrainment pressure level $p_D(\lambda)$ (and hence the detrainment sigma level $\sigma_D(\lambda)$) would become a function of time. Since the vertical coordinate is fixed for all time at a finite number of points, λ could be retained only with interpolation of the cloud work function in λ-space which would introduce significant errors in the application of the theory. Thus we have chosen $\hat{p}$, the cloud depth pressure as the spectral parameter since the calculation of $\frac{\partial A(\hat{p})}{\partial t}$ poses much less of a computational problem.

We now note that this change in the spectral parameter somewhat alters quasi-equilibrium as originally formulated, since $\frac{\partial A(\hat{p})}{\partial t} \neq \frac{\partial A(\lambda)}{\partial t}$. The exact relationship between the two forms can be written

$$\frac{\partial A(\hat{p})}{\partial t} = \left[\frac{\partial A(\hat{p})}{\partial t}\right]_\lambda + \left[\frac{\partial A(\hat{p})}{\partial \lambda}\right]_t \left[\frac{\partial \lambda(\hat{p})}{\partial t}\right] . \tag{2.56}$$

The use of $\hat{p}$ as the spectral parameter gives rise to a second term which was not present in the original theory. This involves the time rate of change of the fractional entrainment rate of sub-ensemble $\hat{p}$, since λ is now an independent variable. The selection of the spectral parameter is one of the arbitrary aspects of the cloud model, and it is not clear that the choice of λ has any more physical significance than the choice of $\hat{p}$; i.e. the choice of $\hat{p}$ as the spectral parameter may be just as reasonable as the choice of λ. As one example, Lord (1978) has recently assembled observational evidence which shows the cloud work function to be a quasi-universal function of detrainment level p_D[1]. Since this is yet an unresolved aspect of the cloud model,

---

[1] In the absence of surface pressure variations, our spectral parameter of sub-ensemble pressure depth reduces to sub-ensemble detrainment pressure level as suggested by Lord (1978).

and since from a computational point of view we are forced to use a spectral parameter other than fractional entrainment rate, we proceed with our use of $\hat{p}$ noting the modification this makes to the original formulation of quasi-equilibrium.

Requiring balance between the large-scale generation and convective-scale destruction of $A(\hat{p})$ means that our equation for $m_B(\hat{p})$ takes the form of a Fredholm integral equation of the first kind. The various schemes suggested for solving this type of equation do not guarantee a non-negative mass flux distribution which is a necessary constraint if the solution is to be regarded as physically reasonable. In order to avoid the difficulties associated with obtaining negative cloud base mass fluxes in the solution, we have chosen to restate the quasi-equilibrium hypothesis as an optimization problem (Hack and Schubert, 1976) which can be written in the following form. Let $\hat{P}$ represent the subset of the $\hat{p}$ domain for which $F_{L.S.}(\hat{p}) > 0$. We wish then to

$$\text{minimize} \left\{ \int_{\hat{P}} c(\hat{p}) \frac{\partial A(\hat{p})}{\partial t} \, d\hat{p} \right\} ,$$

subject to

$$\frac{\partial A(\hat{p})}{\partial t} = \int_{\hat{P}} K(\hat{p},\hat{p}')m_B(\hat{p}')d\hat{p}' + F_{L.S.}(\hat{p}) ,$$

$$m_B(\hat{p}) \geq 0 ,$$

$$\frac{\partial A(\hat{p})}{\partial t} \leq 0 . \tag{2.57}$$

Formulating the problem in this way requires quasi-equilibrium to be satisfied as closely as possible while constraining the cloud base mass flux distribution to be non-negative. This particular formulation

of the problem is referred to as the 'overadjustment case' by Silva

Dias and Schubert (1977) who have investigated other formulations of

the optimation problem (underadjustment and free variable cases). In

(2.57) both $\frac{\partial A(\hat{p})}{\partial t}$ and $m_B(\hat{p})$ are regarded as unknowns while $c(\hat{p})$,

$K(\hat{p},\hat{p}')$ and $F_{L.S.}(\hat{p})$ are regarded as knowns. The weighting function

$c(\hat{p})$ is defined to be negative in order to maintain a mathematically

well posec minimization problem. The discrete form of (2.57) turns

out to be a linear programming problem which is readily solved using

the simplex method (Dantzig, 1963; Luenberger, 1973) and is discussed

in the following paragraphs as the optimal adjustment method.

As we saw in section 2.2.1, the processes which contribute to

changes in the large-scale temperature, moisture, and momentum fields

can be divided into two parts: large-scale terms, consisting of large-

scale horizontal and vertical advection, large-scale pressure gradient

and Coriolis accelerations, radiation and surface eddy fluxes; and

convective-scale terms, consisting of convective-scale flux divergence

and source/sink terms (see equations (2.26), (2.27), (2.28), (2.40)-

(2.42)). In the tropical cyclone model, the large-scale terms and

convective-scale terms are computed separately using different time

steps. Typically these time steps are 20 seconds for the large-scale

terms and 300 seconds for the convective-scale terms. Thus, it is

convenient from a computational point of view to formulate the cumulus

parameterization in terms of an adjustment process. Although we have

used the word 'adjustment' our procedure should not be confused with

the moist convective adjustment methods used in many numerical models.

The adjustment process we will discuss is purely a consequence of the

time discretization associated with the numerical model.

Let us define the atmosphere to be stable to sub-ensemble $\hat{p}$ if the cloud work function $A(\hat{p})$ is smaller than some critical value $A_c(\hat{p})$. Thus, the atmosphere is considered to be respectively neutral or unstable to each sub-ensemble depending on whether $A(\hat{p})$ equals or exceeds this critical value. If the large-scale terms push the atmosphere into an unstable state, it is the job of the dynamic control (2.57) to determine a mass flux distribution which will adjust the atmosphere back at least to (but at the same time as close as possible to) the neutral state for each $\hat{p}$ subject to the constraint that each sub-ensemble mass flux be non-negative (see Fig. 2.4). This is the discrete analogue of (2.57) which we will discuss in mathematical form in the remainder of this section.

Suppose we have n cloud types (where a 'cloud-type' is the discrete analogue of 'sub-ensemble'). Let m_{B_i} be the cloud base mass flux of the ith cloud type and b_i be the amount that the ith cloud work function exceeds the neutral (or critical) value $(b_i > 0)$. If cloud type j contributes an amount K_{ij} per unit mass flux to the reduction of b_i (where K_{ij} is the discrete analogue of the kernel $K(\hat{p},\hat{p}')$), we can write

$$K_{11}m_{B_1} + K_{12}m_{B_2} + \ldots + K_{1n}m_{B_n} \geq b_1$$

$$K_{21}m_{B_1} + K_{22}m_{B_2} + \ldots + K_{2n}m_{B_n} \geq b_2$$

$$\vdots \qquad \vdots \qquad \qquad \vdots \qquad \vdots$$

$$K_{n1}m_{B_1} + K_{n2}m_{B_2} + \ldots + K_{nn}m_{B_n} \geq b_n \, ,$$

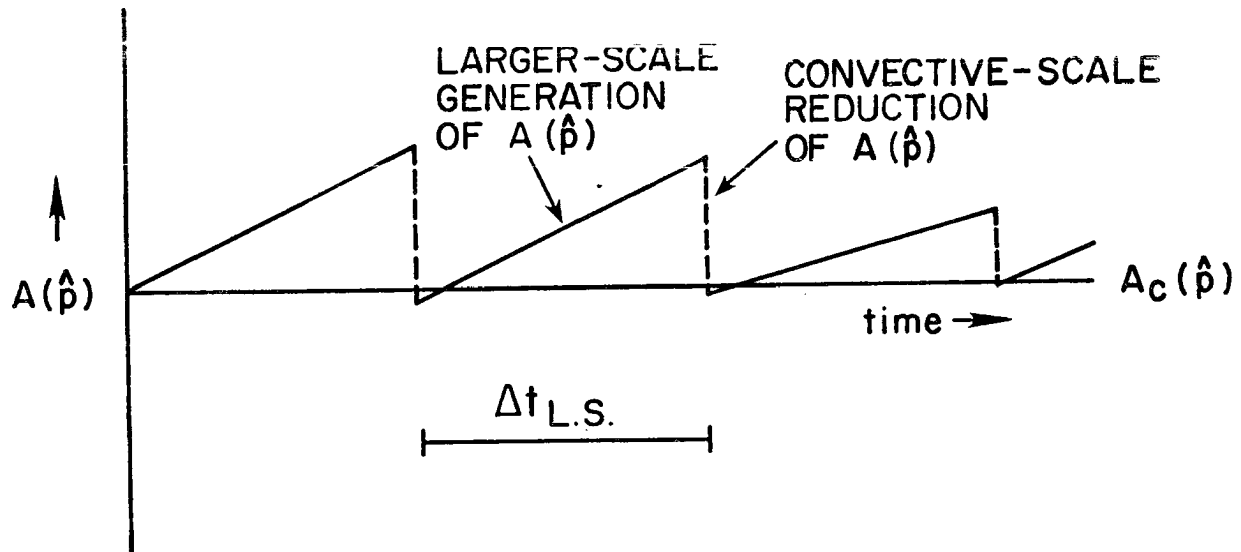$$m_{B_1} \geq 0, \quad m_{B_2} \geq 0 \quad \ldots \quad m_{B_n} \geq 0 \, . \tag{2.58}$$

Figure 2.4   Schematic representation of the optimal adjustment method.

Equation (2.58) states that an adjustment greater than or equal to b must occur for each i and that each sub-ensemble (cloud type) mass flux must be non-negative.

Each inequality in (2.58) can be converted to an equality by introducing a 'surplus variable' x. For inequality i, the surplus variable x_i represents the surplus adjustment done to work function i. Thus, inequality i takes the form

$$K_{i1}m_{B_1} + K_{i2}m_{B_2} + \ldots + K_{in}m_{B_n} - x_i = b_i \, . \qquad (2.59)$$

The objective is to minimize some measure of the surplus adjustment. Assuming that this measure is linear and gross in character we can write

$$\text{minimize} \left\{ \sum_{i=1}^{n} c_i x_i \right\}$$

subject to

$$K_{11}m_{B_1} + K_{12}m_{B_2} + \ldots + K_{1n}m_{B_n} - x_1 = b_1$$

$$K_{21}m_{B_1} + K_{22}m_{B_2} + \ldots + K_{2n}m_{B_n} - x_2 = b_2$$

$$\vdots \qquad \vdots \qquad \qquad \vdots \qquad \qquad \vdots$$

$$K_{n1}m_{B_1} + K_{n2}m_{B_2} + \ldots + K_{nn}m_{B_n} - x_n = b_n \, ,$$

and

$$m_{B_1} \geq 0 \, , \quad m_{B_2} \geq 0 \quad \ldots \quad m_{B_n} \geq 0 \, ,$$

$$x_1 \geq 0 \, , \quad x_2 \geq 0 \quad \ldots \quad x_n \geq 0 \, ; \qquad (2.60)$$

where c_i are the weights. In more compact vector notation we can write

$$\text{minimize } \vec{c} \cdot \vec{x} ,$$

subject to

$$\mathbb{K} \, \vec{m}_B - \vec{x} = \vec{b} ,$$

$$\vec{m}_B \geq 0 ,$$

$$\vec{x} \geq 0 . \qquad\qquad (2.61)$$

Thus we have one minimization objective, n adjustment constraints and 2n non-negativity constraints. Solution of the problem yields the n unknown sub-ensemble mass fluxes, the n unknown surplus adjustments, and the value of our objective function, $\sum\limits_{i=1}^{n} c_i x_i$, which is a gross measure of the surplus adjustment. The optimization problem as formulated is easily solved using the simplex method of linear programming. From a computational point of view however this 'overadjustment' formulation is not the most convenient way to go since the simplex procedure requires a basic feasible solution with which to start. A simple reinterpretation of the optimization problem allows the formulation of the 'underadjustment case' which can be written (cf. Silva Dias and Schubert, 1977)

$$\text{minimize } \vec{c} \cdot \vec{x} ,$$

subject to

$$- \mathbb{K} \, \vec{m}_B + \vec{x} = -\vec{b} ,$$

$$\vec{m}_B \geq 0 ,$$

$$\vec{x} \geq 0 . \qquad\qquad (2.62)$$

In this case, the initial basic feasible solution required by the simplex procedure is given by the 'slack variables' $\vec{x}$.

Silva Dias and Schubert (1977) have studied the sensitivity of the linear programming problem to the selection of the weighting function

$\vec{c}$ and have determined that the most physically reasonable results are obtained when using $c_i = b_i^{-1}$ (i.e. making the weighting function inversely proportional to the desired adjustment). This is the procedure we follow in this study.

2.3 Representation of Other Convective-Scale Processes and Radiation

2.3.1 Surface energy exchanges

As knowledge of the planetary boundary layer has improved, so have boundary layer parameterization methods. A large number of these methods now exist in the published literature, many of which treat boundary layer processes in detail employing sophisticated techniques to estimate surface energy interactions. Although some recent modeling efforts have begun to make use of some of these approaches (e.g. Kurihara and Tuleya, 1974; Rosenthal, 1978), the crude assumptions we have made in section 2.2 regarding the behavior of our model 'mixed layer' would not seem to justify the immediate use of these schemes. Consequently, all surface energy exchanges are simply parameterized by the bulk aerodynamic method.

The flux of dry static energy (equivalently sensible heat) from the sea surface is given by

$$(F_s)_S = c_p \rho_S c_D |W_S| [T_{SEA} - T_S] , \tag{2.63}$$

the flux of total water (water vapor) by

$$(F_q)_S = \rho_S c_D |W_S| [q^*(T_{SEA}, P_S) - q_S] , \tag{2.64}$$

and the surface stress by

$$(F_W)_S = -\rho_S c_D |W_S| W_S , \tag{2.65}$$

where there is no distinction between the exchange coefficients for heat, moisture, or momentum. We have chosen

$$c_D = 0.0015,$$ (2.66)

a value which is most consistent with those estimated from observations (see Businger and Sequin, 1977).

2.3.2 Horizontal and vertical diffusion processes

In addition to the parameterized vertical transports of heat, moisture and momentum discussed in section 2.2, we also include non-linear horizontal and vertical eddy diffusion processes. These can be written as

$$D_u = \frac{1}{\pi r} \left[\frac{\partial}{\partial r} \left(\pi K_H r \frac{\partial u}{\partial r} \right) - \frac{\pi K_H u}{r} \right] + \frac{g}{\pi} \frac{\partial}{\partial \sigma} \tau_u ,$$ (2.67)

$$D_v = \frac{1}{\pi r} \left[\frac{\partial}{\partial r} \left(\pi K_H r \frac{\partial u}{\partial r} \right) - \frac{\pi K_H v}{r} \right] + \frac{g}{\pi} \frac{\partial}{\partial \sigma} \tau_v ,$$ (2.68)

$$D_T = \frac{1}{\pi r} \frac{\partial}{\partial r} \left(\pi K_H r \frac{\partial T}{\partial r} \right) ,$$ (2.69)

and

$$D_q = \frac{1}{\pi r} \frac{\partial}{\partial r} \left(\pi K_H r \frac{\partial q}{\partial r} \right) .$$ (2.70)

The lateral eddy mixing coefficient is written as the sum of a linear and nonlinear term

$$K_H = K_{H_o} + \ell_H^2 |D| ,$$ (2.71)

where the second term comes from the nonlinear viscosity scheme proposed by Smagorinsky (1963). The quantity $|D|$ is the magnitude of the total deformation field defined as

$$|D| \equiv r \left[\left(\frac{\partial}{\partial r} \left(\frac{u}{r} \right) \right)^2 + \left(\frac{\partial}{\partial r} \left(\frac{v}{r} \right) \right)^2 \right]^{\frac{1}{2}} ,$$ (2.72)

and the characteristic horizontal length scale ℓ_H is given by

$$\ell_H = k_0 \Delta r \; . \tag{2.73}$$

A value of 0.2 is used for the parameter k_0. This value has been used in previous modeling studies of the tropical cyclone giving maximum values of the nonlinear term on the order of $2 \times 10^4 \; m^2/s$ in the eyewall of the model storm (Kurihara, 1975; Rosenthal, 1978).

The turbulent fluxes of momentum (or internal stresses) attributable to convective-scale eddies (other than those due to parameterized moist convection) are given by

$$\tau_k = - \frac{K_v g \rho^2}{\pi} \frac{\partial u}{\partial \sigma} \tag{2.74}$$

and

$$\tau_v = - \frac{K_v g \rho 2}{\pi} \frac{\partial v}{\partial \sigma} \; , \tag{2.75}$$

where ρ is the density and K_v is the vertical eddy mixing coefficient defined as

$$K_v = K_{v_0} + \ell_v^2 \frac{g \rho}{\pi} \left| \frac{\partial W}{\partial \sigma} \right| \; . \tag{2.76}$$

A constant vertical mixing length of 30 m is chosen for ℓ_v which corresponds to the 'neutral mixing length' used in Kurihara and Tuleya (1974).

In order to gain some insight into what constitute acceptable values of the constant eddy mixing coefficients K_{H_0} and K_{V_0}, we proceed with the following analysis. We start with the horizontal diffusion problem by considering a linearized tangential momentum equation of the form

$$\frac{\partial v}{\partial t} = K_{H_0} \left[\nabla^2 - \frac{1}{r^2} \right] v = K_{H_0} \left[\frac{\partial}{r \partial r} \left(r \frac{\partial v}{\partial r} \right) - \frac{v}{r^2} \right] \ . \qquad (2.77)$$

Defining the order m Hankel transform pair as

$$\left. \begin{array}{l} \psi(r,t) = \displaystyle\int_0^\infty \hat{\psi}(k,t) \ J_m(kr) \ kdk \\[2ex] \hat{\psi}(k,t) = \displaystyle\int_0^\infty \psi(r,t) \ J_m(kr) \ rdr \end{array} \right\} \ , \qquad (2.78)$$

the first order transform of (2.77) can be written as

$$\frac{\partial \hat{v}}{\partial t} = K_{H_0} \int_0^\infty \left[\frac{\partial}{r \partial r} \left(r \frac{\partial v}{\partial r} \right) - \frac{v}{r^2} \right] J_1(kr) \ rdr \ . \qquad (2.79)$$

Integrating (2.79) by parts gives

$$\frac{\partial \hat{v}}{\partial t} = K_{H_0} \int_0^\infty v \left[\frac{\partial}{r \partial r} \left(r \frac{\partial J_1(kr)}{\partial r} \right) - \frac{1}{r^2} J_1(kr) \right] rdr \ , \qquad (2.80)$$

which can be simplified to

$$\frac{\partial \hat{v}}{\partial t} = - K_{H_0} \int_0^\infty vk^2 J_1(kr) \ rdr = - K_{H_0} k^2 \hat{v} \ . \qquad (2.81)$$

The solution to the transformed governing equation is

$$\hat{v}(k,t) = \hat{v}(k,0) \ e^{-K_{H_0} k^2 t} \ , \qquad (2.82)$$

from which we obtain the solution to our original equation (2.77) as

$$v(r,t) = \int_0^\infty \hat{v}(k,0) \ e^{-K_{H_0} k^2 t} \ J_1(kr) \ kdk \ . \qquad (2.83)$$

In order to see more clearly what effect the choice of K_{H_0} has on the solution, we evaluate (2.83) for an initial tangential wind of the form
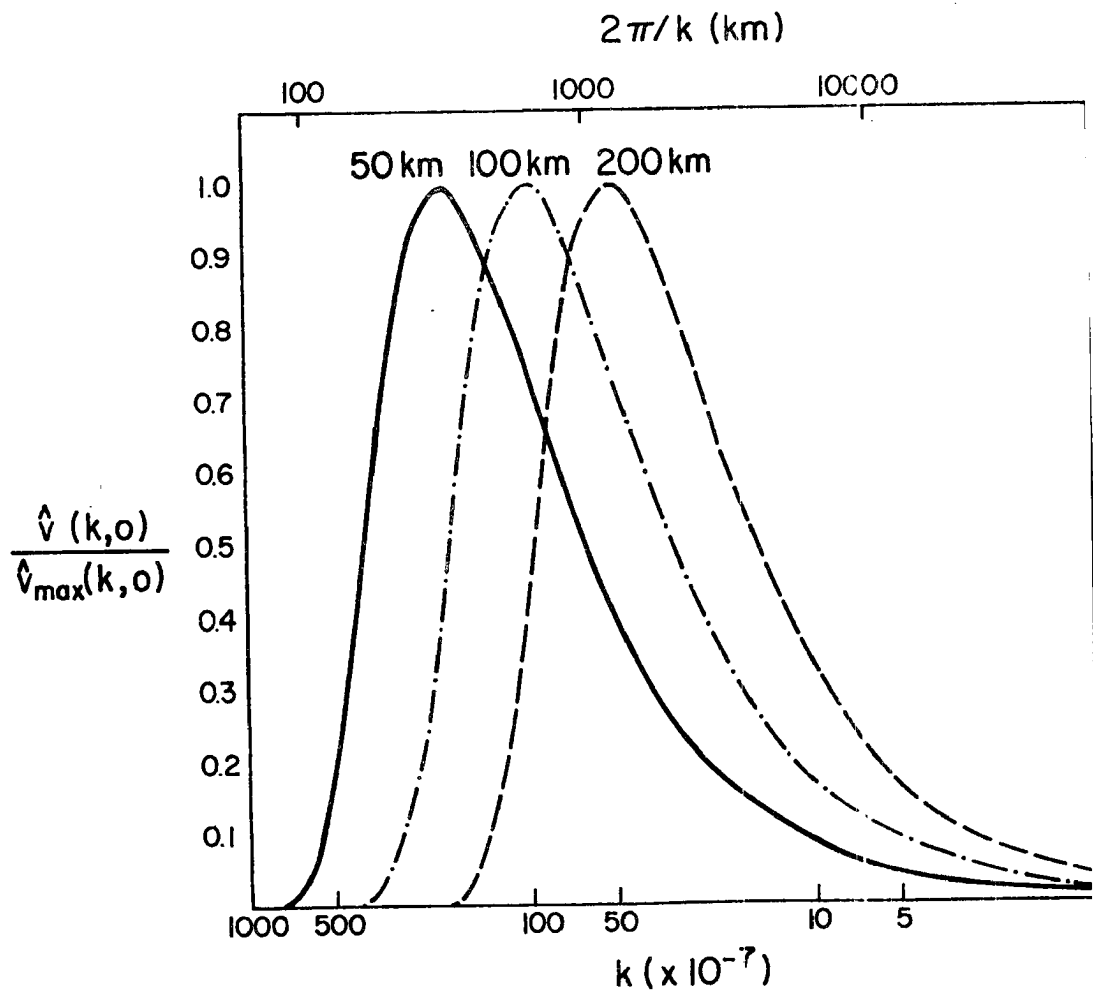
Figure 2.5 The normalized Hankel transform of the initial wind
field given by (2.84).

$$v(r,0) = \frac{r}{r_0} e^{\frac{1}{2}(1-r^2/r_0^2)} \quad . \tag{2.84}$$

The Hankel transformed initial condition is

$$\hat{v}(k,0) = \frac{e^{\frac{1}{2}}}{a} \int_0^\infty r\, e^{-r^2/2r_0^2}\, J_1(kr)r\, dr \quad , \tag{2.85}$$

which can also be written (see Erdelyi et al., 1954, Volume 2, pg. 29)

$$\hat{v}(k,0) = r_0^3 k\, e^{\frac{1}{2}(1-k^2 r_0^2)} \quad . \tag{2.86}$$

This transform is plotted for selected values of r_0 (50, 100, and 200 km) in Fig. 2.5. This figure (which shows $\hat{v}(k,0)$ normalized by its maximum value as a function of k) suggests considerably faster decay for the smaller of the three vortices since a much larger portion of its amplitude spectrum is concentrated in high wavenumbers. Substituting (2.86) into (2.83) we obtain the time dependent solution for initial condition (2.84) as

$$v(r,t) = \left(1 + \frac{2K_{H_0} t}{r_0^2}\right)^{-2} \frac{r}{r_0} e^{\left[\frac{1}{2}\left[1-r^2/r_0^2\left(1 + \frac{2K_{H_0} t}{r_0^2}\right)^{-1}\right]\right]} \quad . \tag{2.87}$$

The solution is plotted as a function of r/r_0 for selected values of t (where t is expressed in terms of r_0 and K_{H_0}) in Fig. 2.6.

It is often more useful to study the time dependent nature of some property of the solution such as kinetic energy. Defining the total kinetic energy of the system to be $KE \equiv \int_0^\infty v^2 r\, dr$, we use (2.87) to obtain the normalized kinetic energy as a function of time
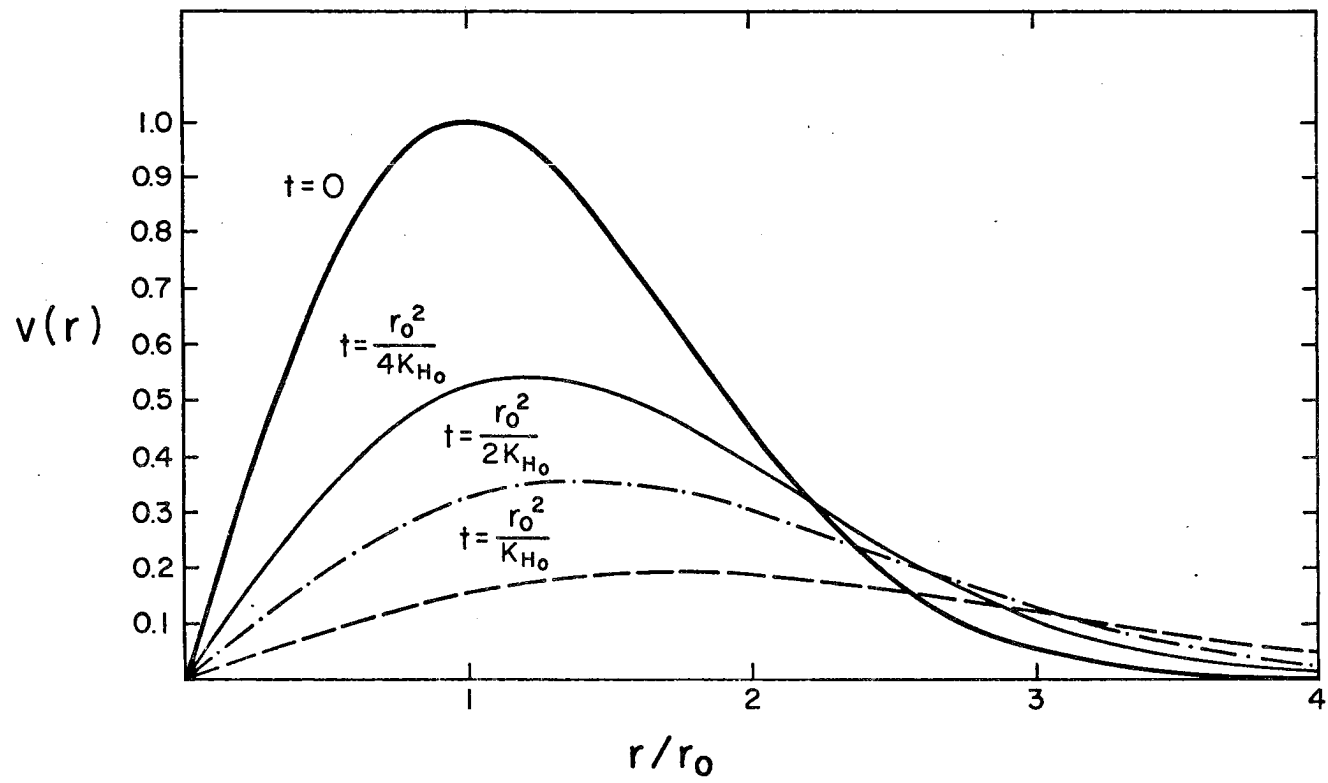
Figure 2.6 Time dependent behavior of the initial wind field given by (2.84).

$$\frac{KE}{(KE)_0} = \left[1 + \frac{2K_{H_0} t}{r_0^2} \right]^{-2} \quad , \tag{2.88}$$

where $(KE)_0$ is the initial total kinetic energy associated with (2.84). This normalzed kinetic energy is plotted as a function of dimension-

less time $\left[\frac{2K_{H_0} t}{r_0^2} \right]$ in Fig. 2.7. Let us contrast the dissipation of

kinetic energy with the decay of the maximum tangential wind. The radius of the maximum tangential wind can be expressed by

$$\left[\frac{r}{r_0} \right]_{v=v_{max}} = \left[1 + \frac{2K_{H_0} t}{r_0^2} \right] \quad . \tag{2.89}$$

Substituting this relation into (2.87) leads to an expression for the maximum tangential wind as a function of time

$$v_{max} = \left[1 + \frac{2K_{H_0} t}{r_0^2} \right]^{-3/2} \quad , \tag{2.90}$$

which is plotted in Fig. 2.8. Comparison of (2.88) and (2.90) shows that the kinetic energy of the system is at all times decaying at a faster rate.

Thus, we consider the time it takes to halve the initial vortex kinetic energy as a function of K_{H_0}. (The maximum tangential wind for this time is given by $v_{max} = 0.595$.) Since previous axisymmetric tropical cyclone (cloud cluster) models have used values of K_{H_0} which range from 10^3 m^2/s (e.g. Ooyama, 1969a) to 10^5 m^2/s (e.g. Fingerhut, 1978), we have constructed Table 2.1 which shows the time (in days) it takes to halve the initial total kinetic energy for $r_0 = 50$, 100, and
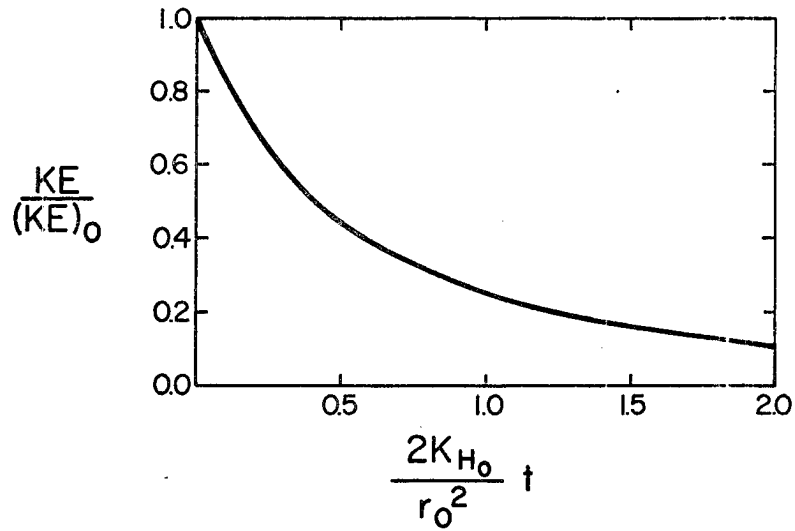
Figure 2.7 Time dependent behavior of the normalized
total kinetic energy associated with the
initial wind field given by (2.84).
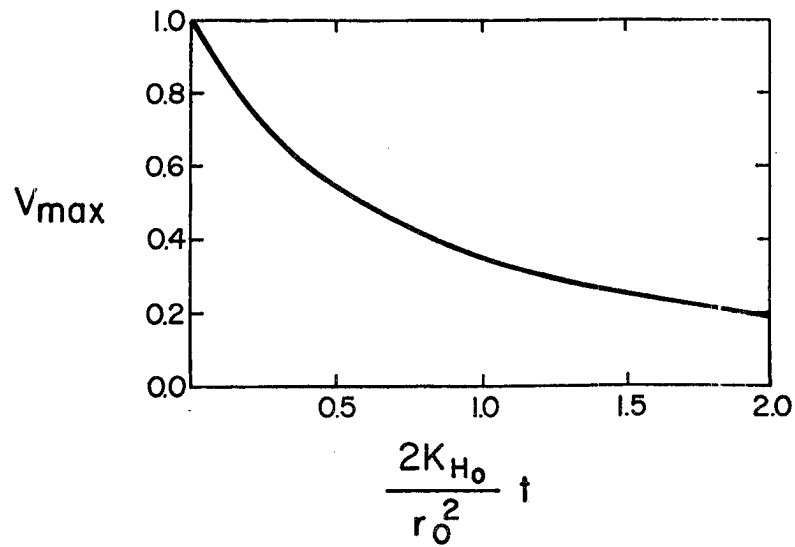
Figure 2.8 Time dependent behavior of the maximum wind
associated with the vortex initially given
by (2.84).

K_{H_0} (m^2/s)	r_0(km)		
	50	100	200
10^3	5.993	23.971	95.883
10^4	0.599	2.397	9.588
10^5	0.060	0.240	0.959

Table 2.1 The time (in days) required to halve
the initial total kinetic energy of
the vortex given by (2.84) for
r_0 = 50, 100 and 200 km.

200 km, and $K_{H_0} = 10^3$, 10^4, and 10^5 m^2/s. Values of the constant horizontal eddy mixing coefficient in excess of 10^4 m^2/s seem to give unacceptably high decay rates. Consequently, we have chosen $K_{H_0} = 5.0 \times 10^3$ m^2/s for the numerical results presented in this study (cf. Rosenthal, 1978).

Finally, we address the problem of selecting a reasonable value of K_{V_0} by considering the linear equation

$$\frac{\partial v}{\partial t} = \left(\frac{g\rho}{\pi}\right)^2 K_{V_0} \frac{\partial^2 v}{\partial \sigma^2} = \mu^2 \frac{\partial^2 v}{\partial \sigma^2} \quad , \tag{2.91}$$

where ρ = constant has been assumed for the purpose of this analysis. Assuming a solution of the form $v(\sigma,t) = V\, e^{-\lambda^2 t}\, \Psi(\sigma)$ we obtain

$$\frac{\partial^2 \Psi}{\partial \sigma^2} + \frac{\lambda^2}{\mu^2} \Psi = 0 \quad , \tag{2.92}$$

the solution of which may be written

$$\Psi(\sigma) = A\cos\left(\frac{\lambda}{\mu}\sigma\right) + B\sin\left(\frac{\lambda}{\mu}\sigma\right) \quad . \tag{2.93}$$

Since we wish only to investigate the role of internal stresses, we apply no stress boundary conditions $\frac{\partial \Psi}{\partial \sigma} = 0$ at $\sigma = 0,1$ to (2.93) which yields an expression for the eigenfunctions $\Psi_n(\sigma)$

where
$$\Psi_n(\sigma) = A_n \cos\left(\frac{\lambda_n}{\mu}\sigma\right) \quad , \\ \lambda_n = n\pi\mu \quad . \tag{2.94}$$

The coefficient A_n is chosen to be

$$A_n = \begin{cases} 1 & n = 0 \\ \sqrt{2} & n \neq 0 \end{cases} \tag{2.95}$$

in order to guarantee the orthonormality of the eigenfunctions Ψ_n .
Thus the complete solution can be written

$$v(\sigma,t) = \sum_n V_n \, e^{-(n\pi\mu)^2 t} \, \Psi_n(\sigma) \qquad (2.96)$$

where

$$V_n = \int_0^1 v(\sigma,0) \, \Psi_n(\sigma) \, d\sigma . \qquad (2.97)$$

As an example, we consider the following initial condition

$$v(\sigma,0) = \begin{cases} \left[\dfrac{\sigma-\sigma_2}{\sigma_1-\sigma_2} - 1 \right]^2 \left[2\,\dfrac{\sigma-\sigma_2}{\sigma_1-\sigma_2} + 1 \right] & \sigma_1 \le \sigma \le \sigma_2 \\[3em] \left[\dfrac{\sigma-\sigma_2}{\sigma_3-\sigma_2} - 1 \right]^2 \left[2\,\dfrac{\sigma-\sigma_2}{\sigma_1-\sigma_2} + 1 \right] & \sigma_2 \le \sigma \le \sigma_3 \end{cases} \qquad (2.98)$$

where $\sigma_1 = 0$ and $\sigma_3 = 1$. From (2.97) we have

$$V_n = A_n \left\{ \int_0^{\sigma_2^-} \left(\dfrac{\sigma-\sigma_2}{-\sigma_2} - 1 \right)^2 \left[2\,\dfrac{\sigma-\sigma_2}{-\sigma_2} + 1 \right] \cos(n\pi\sigma) \, d\sigma \right.$$

$$\left. - \int_0^{\sigma_2^+} \left(\dfrac{\sigma-\sigma_2}{1-\sigma_2} - 1 \right)^2 \left[2\,\dfrac{\sigma-\sigma_2}{1-\sigma_2} + 1 \right] \cos(n\pi\sigma) \, d\sigma \right\} , \qquad (2.99)$$

which when integrated by parts gives

$$\left. \begin{aligned} V_0 &= \tfrac{1}{2} \\[2em] V_n &= -\dfrac{c_1\sqrt{2}}{(n\pi)^4} \left[(-1)^n + 1 - 2\cos(n\pi/2) \right] \end{aligned} \right\} , \qquad (2.100)$$

where $c_1 = 96$ and we have chosen $\sigma_2 = \tfrac{1}{2}$. Substituting this result
into (2.96) gives the solution

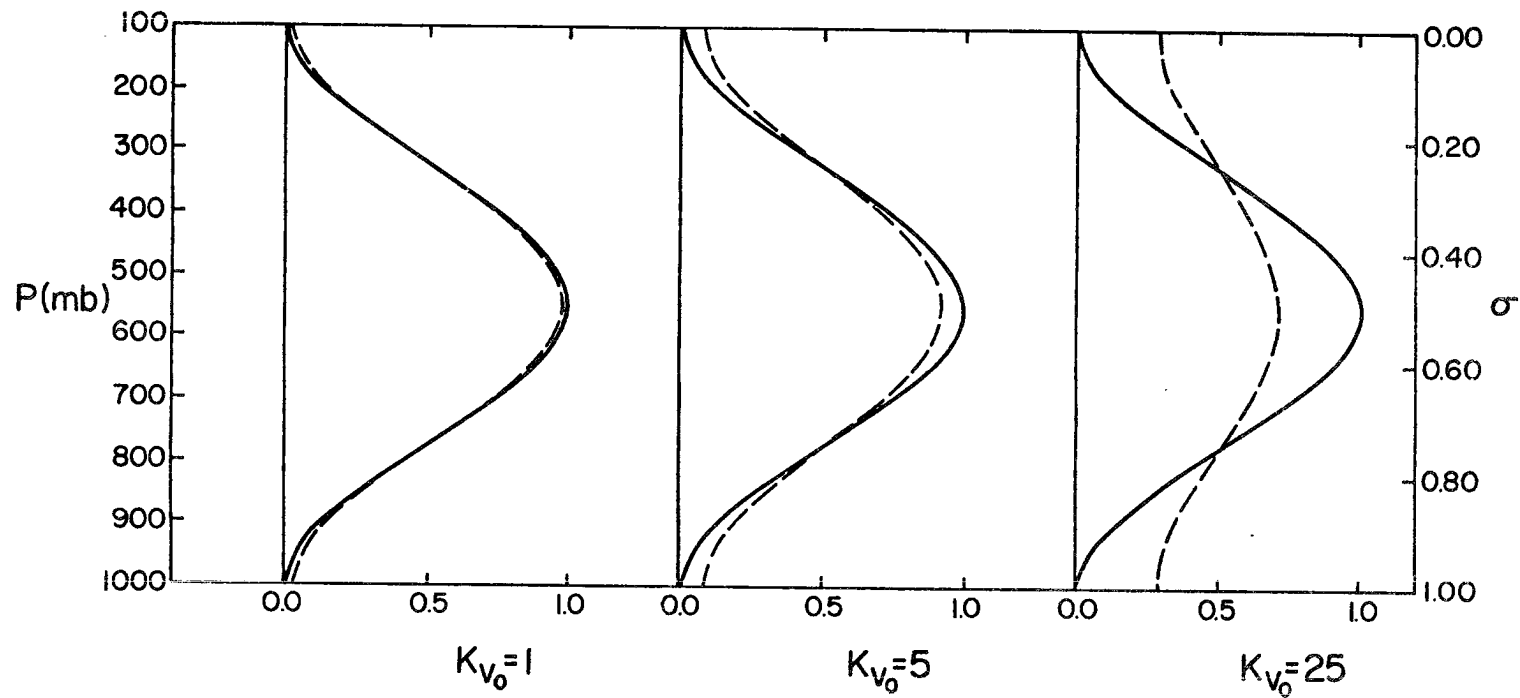Figure 2.9 The vertical structure of the wind field at t=0 and t=24 hours for values of the constant vertical eddy mixing coefficient of 1, 5 and 25 m^2/s.

$$v(\sigma,t) = \frac{1}{2} - \sum_{n=1}^{\infty} \frac{2c_1}{(n\pi)^4} [(-1)^n + 1 - 2\cos(n\pi/2)] \, e^{-(n\pi\mu)^2 t} \cos(n\pi\sigma).$$

$$(2.101)$$

The solution at $t = 0$ and $t = 1$ day is shown for three different values of μ^2 (which are interpreted in terms of K_{v_o} assuming $\rho = 0.92$ kg m^{-3} and a surface pressure p_S of 1000 mb) in Fig. 2.9. The use of $K_{v_o} = 25$ m^2/s as in Anthes (1977) appears from this analysis to produce an unacceptably large modification of the initial profile after one day. Although $K_{v_o} = 5$ is more reasonable, we choose $K_{v_o} = 1$ for the numerical simulations conducted in this study since the vertical diffusion is meant to represent turbulent momentum transport attributable to processes other than parameterized convection. In a linear sense, we assume this is a small effect.

2.3.3 Dry convection

If the potential temperature is ever found to decrease with height, we assume that convective-scale dry convection will occur and that a dry adiabatic lapse rate will result. This dry adiabatic adjustment (or dry convective adjustment) is accomplished with a procedure developed by J. W. Kim and A. Arakawa for the UCLA GCM, and is described in Appendix C.

2.3.4 Longwave and shortwave radiative processes

The effects of longwave and shortwave radiation are included by a simple radiative parameterization scheme in which the term Q_R is determined as the weighted average of a perturbed and unperturbed net radiative heating rate. Four radiative heating profiles are contained in a lookup table in the model, consisting of a longwave and shortwave profile for both the convectively disturbed and convectively
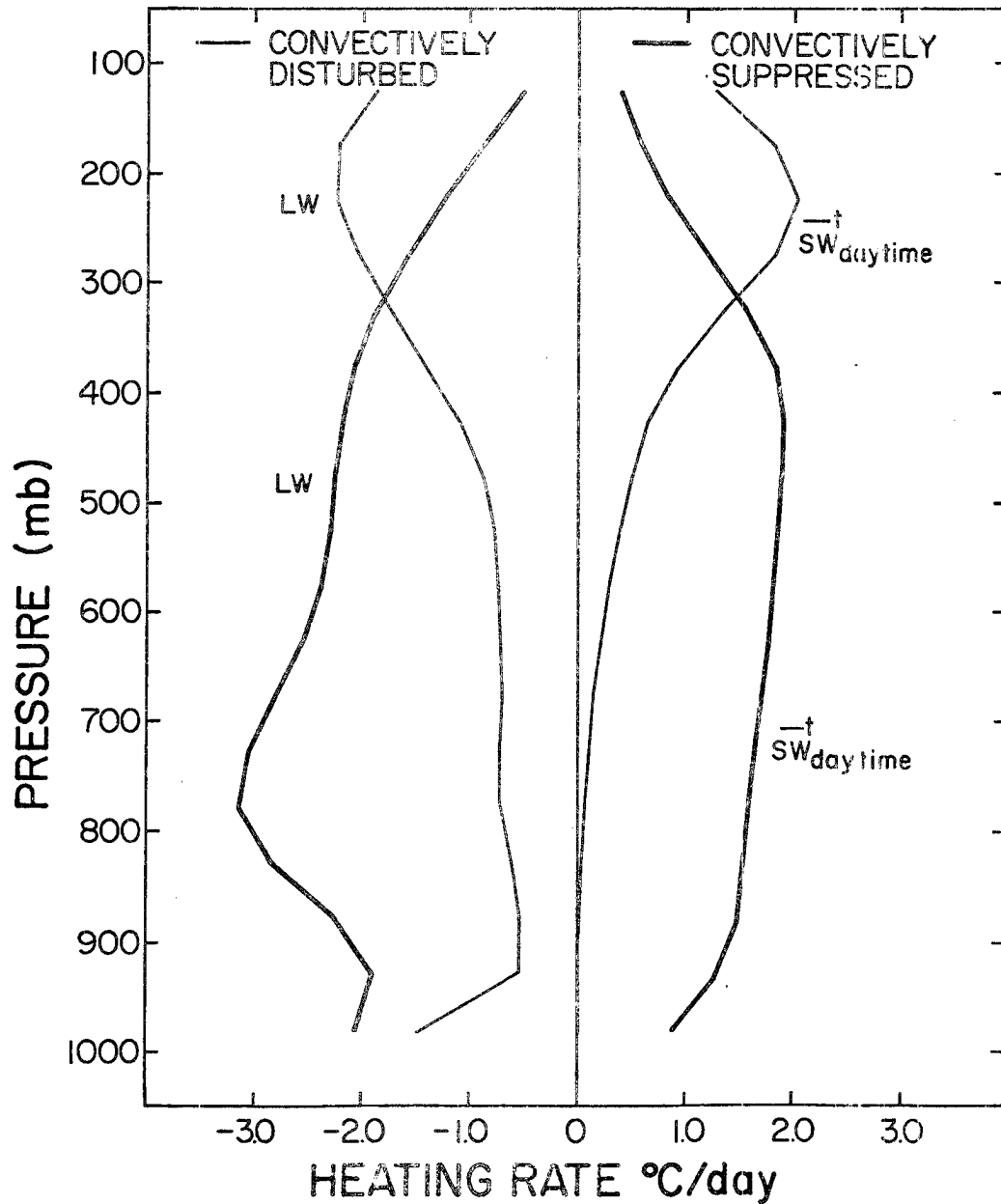
Figure 2.10 The longwave and shortwave radiative heating rates for the convectively disturbed and convectively suppressed cases (after Cox and Griffith, 1979). The shortwave component represents an average shortwave heating rate for the 12 daylight hours.

suppressed cases discussed by Cox and Griffith (1979). These profiles are shown in Fig. 2.10. The net radiative heating rates (for both the disturbed and suppressed case) are obtained as the sum of their respective longwave and shortwave components

$$Q = Q_{SW} + Q_{LW} \tag{2.102}$$

where the shortwave component is given by

$$Q_{SW}(t) = \max \begin{cases} 0 \\ \frac{\pi}{2} \overline{Q}_{SW} \cos \left[2\pi \left(\frac{t-12}{24} \right) \right] \end{cases} \tag{2.103}$$

and $\overline{Q}_{SW}$ is the shortwave component averaged over the twelve daylight hours (see Fig. 2.10). The total radiative heating rate Q_R/c_p is obtained as a weighted average of the two profiles (disturbed and suppressed) determined above according to the relation

$$Q_R = (1-a) \, Q_{suppressed} + a \, Q_{disturbed} \, . \tag{2.104}$$

The weighting parameter is given by

$$a = \max \begin{cases} 0 \\ \min \begin{cases} 1 \\ 1 - \dfrac{\overline{RH}_{max} - \overline{RH}}{\overline{RH}_{max} - \overline{RH}_{min}} \end{cases} \end{cases} \tag{2.105}$$

where $\overline{RH}$ is an average relative humidity in the upper troposphere. Presently, we obtain $\overline{RH}$ from the upper four layers ($\sim 200\,mb$) of the model and use values of $\overline{RH}_{max} = 0.85$ and $\overline{RH}_{min} = 0.45$.

2.3.5 Summary of the convective-scale source terms and radiation

Let us now summarize the convective-scale source terms which appear in the large-scale governing equations. They consist of the

many processes which have been described in sections 2.2 and 2.3 and can be written as

$$S_u = \frac{g}{\pi} \frac{\partial F_u}{\partial \sigma} + \frac{1}{\pi r} \left\{ \frac{\partial}{\partial r} \left(\pi K_H r \frac{\partial u}{\partial r} \right) - \frac{\pi K_H u}{r} \right\} + \frac{g}{\pi} \frac{\partial}{\partial \sigma} \left(K_V \frac{g\rho^2}{\pi} \frac{\partial v}{\partial \sigma} \right), \quad (2.106)$$

$$S_v = \frac{g}{\pi} \frac{\partial F_v}{\partial \sigma} + \frac{1}{\pi r} \left\{ \frac{\partial}{\partial r} \left(\pi K_H r \frac{\partial v}{\partial r} \right) - \frac{\pi K_H v}{r} \right\} + \frac{g}{\pi} \frac{\partial}{\partial \sigma} \left(K_V \frac{g\rho^2}{\pi} \frac{\partial v}{\partial \sigma} \right), \quad (2.107)$$

$$S_T = \frac{1}{c_p} \left\{ \frac{g}{\pi} \frac{\partial}{\partial \sigma} F_{s-L\ell} + LR \right\} + \frac{1}{\pi r} \frac{\partial}{\partial r} \left[\pi K_H r \frac{\partial T}{\partial r} \right] + Q_R \quad , \quad (2.108)$$

$$S_q = \frac{g}{\pi} \frac{\partial}{\partial \sigma} F_{q+\ell} - R + \frac{1}{\pi r} \frac{\partial}{\partial r} \left[\pi K_H r \frac{\partial q}{\partial r} \right] \quad , \quad (2.109)$$

2.4 Large-Scale Condensation

The convective scale condensation, evaporation and precipitation caused by the parameterized cumulus convection discussed in section 2.2 can occur when the atmosphere is not saturated in a large-scale sense. In addition, large-scale condensation, evaporation and precipitation can occur when the air becomes saturated and remains saturated in a large-scale sense.

Neglecting for the moment convective-scale contributions to the heat and moisture budgets allows the thermodynamic equation (2.6) and water vapor mass continuity equation (2.8) to be written as

$$\frac{dT}{dt} - \frac{\alpha}{c_p} \frac{dp}{dt} = \frac{L}{c_p} (C-E) \quad (2.110)$$

and

$$\frac{dq}{dt} = -(C-E) \quad , \quad (2.111)$$

where C and E are respectively the rates of large-scale condensation and evaporation per unit mass of dry air. If the air is saturated and remains saturated, E vanishes and C is related to the individual time change of the saturation mixing ratio such that

$$C = \frac{dq^*}{dt} \quad . \tag{2.112}$$

Thus, if in the course of integration the air becomes super-saturated on the scale of the grid, large-scale condensation and release of latent heat is assumed to occur. The excess water removed from a supersaturated layer is allowed to precipitate into the next lower layer and to evaporate completely. This process may bring that layer to supersaturation, in which case the excess is removed and precipitated to the next lower layer. When the bottom layer of the model is reached, an excess is assumed to fall to the earth's surface as large-scale precipitation.

The procedure described above is identical to that developed by A. Arakawa and J. W. Kim for the UCLA GCM. However, the computational procedure employed in the model is somewhat different and is described in Appendix C.

3.0 THE LATERAL BOUNDARY CONDITION

Numerical simulations of tropical cyclones are invariably attempted using models of limited horizontal extent, making the task of formulating an appropriate set of lateral boundary conditions unavoidable. The model used in the present study and discussed in chapter 2 is no exception. The presence of a lateral boundary to the computational domains of these models is an artificial construct mandated only by the limitations of the computer. Thus it is important that one seek a condition which minimizes the impact of this artificial boundary on the dynamical behavior of the phenomena being simulated inside it.

In a tropical cyclone, the large amount of latent heat released in deep convection continually disrupts any approximate balance of the mass and wind fields. The way in which the atmosphere responds to this heating (through the process of geostrophic or gradient adjustment) provides a basis for attaching great importance to the formulation of lateral boundary conditions in tropical cyclone models. Most of the available potential energy generated by latent heat release (especially on small horizontal spatial scales) is partitioned to gravity-inertia wave motion. Examples of this energy partition for axisymmetric flow on an f-plane can be found in section 3.3 of this thesis, and in Schubert et al. (1980), while examples on the equatorial β-plane can be found in Silva Dias and Schubert (1979). This has led us to the view that tropical cyclones may be highly radiating systems. Consequently, if the process of geostrophic or gradient adjustment is to be properly represented, it is essential that the lateral boundary condition be able to transmit the gravity-inertia wave energy generated by the release of latent heat in the interior of the model.

54

There are two broad classes of tropical cyclone models: balanced models and primitive equation models. In a balanced model (e.g. Ogura, 1964; Kuo, 1965; Ooyama, 1969a, b; Sundqvist, 1970a, b) the flow is assumed to be axisymmetric and in gradient wind balance. Since gravity-inertia waves are then filtered, the transient aspects of the geostrophic adjustment[1] process are not simulated. Primitive equation models, however, may be axisymmetric (e.g. Yamasaki, 1968a, b; Rosenthal, 1970, 1971, 1978; Kurihara, 1975) or asymmetric (e.g. Anthes et al., 1971a, b; Anthes, 1972; Harrison, 1973; Kurihara and Tuleya, 1974; Mather, 1974; Madala and Piacsek, 1975; Jones, 1977; Kurihara et al., 1979) and in either case the geostrophic adjustment process becomes one of the important physical processes which must be accurately simulated. Because of their filtered nature, the formulation of lateral boundary conditions in balanced models is not so difficult. Discussions of this problem can be found in Ooyama (1969a) and Sundqvist (1970a). The problem of formulating lateral boundary conditions for primitive equation models is not so well understood. We will confine our discussion of this problem to the formulation of a lateral boundary condition for axisymmetric primitive equation models.

A survey of the literature on primitive equation tropical cyclone models indicates that the lateral boundary conditions on the normal wind component which have been used involve either the condition of zero divergence (Rosenthal, 1970; Anthes, 1971, 1977; Anthes et al., 1971a, b; Jones, 1977) or the condition of zero radial wind (Yamasaki, 1968a, b; Kurihara and Tuleya, 1974; Kurihara, 1975; Rosenthal, 1978).

---

[1] We shall henceforth use the term 'geostrophic adjustment' in the broad sense of adjustment to either geostrophic or gradient balance.

Rosenthal (1971) has examined the sensitivity of an axisymmetric primitive equation tropical cyclone model to these two boundary conditions as functions of the computational domain size. The criterion used to assess the behavior of the boundary conditions was the magnitude of the maximum surface wind attained during the course of the numerical integration (and to a lesser extent, the time required to reach this mature state). Results of the numerical integrations indicated that the maximum surface winds attained in those experiments incorporating the condition of zero divergence were relatively insensitive to the size of the computational domain. Surface winds in excess of 40 m/s were always achieved. In contrast, when using the condition of zero radial wind, the model produced weaker surface winds which were highly sensitive to the size of the computational domain such that there was a linear increase of the maximum surface wind with domain size (~16 m/s per 1000 km). After extrapolating these results to domain sizes in excess of 2000 km, Rosenthal concludes that by enlarging the computational domain to somewhere between 2000 and 3000 km, differences in the numerical result attributable to differences in boundary conditions can be minimized. We believe that this is not the only viable interpretation of these results. Another interpretation is that in a gross sense (since the transient behavior of the simulated storm is not considered) those experiments incorporating the condition of zero radial wind begin to behave more like those incorporating the condition of zero divergence as the computational domain is increased in size. The broader issue of whether either boundary condition behaves realistically is not addressed.

Thus, we have chosen to approach the problem of lateral boundary conditions from a different, essentially linear, point of view, with the goal of minimizing the reflection of gravity-inertia waves, and consequently the distortion of the geostrophic adjustment process. We shall show that such false reflections can be controlled by the use of a gravity wave radiation condition, if the condition is applied separately to each vertical mode. The application of an interface boundary condition to selected vertical modes has been discussed for limited area nested forecast models by Elvius (1977).

Since the primitive equation tropical cyclone model discussed in chapter 2 is based on the sigma coordinate (as are many others), we derive in section 3.1 a linearized system of equations formulated in this coordinate. The linearized system can be split into two problems: the vertical structure problem and the horizontal structure problem. In section 3.2 we solve the vertical structure problem obtaining the eigenvalues and associated vertical structure functions for both an atmosphere characterized by a constant static stability and a mean tropical static stability. Using these results we explore in section 3.3 the energy partition between geostrophic flow and gravity-inertia waves for an unbalanced initial condition in the mass field. The conclusion that most of the initial available potential energy is partitioned to gravity-inertia wave motion motivates a search for a radiation condition which has low reflectivity (section 3.4). Since the boundary condition found in section 3.4 is only an approximate condition, its usefulness is explored numerically (section 3.5) by comparing it with several other conditions, including those recently proposed for use in convection models by Orlanski (1976), Klemp and Wilhelmson (1978), Clark (1979) and Lilly (1980).

3.1 Linearization of the Large-Scale Governing Equations

For the purpose of our analysis it is more convenient to consider the linear version of (2.2)-(2.7). Neglecting the convective-scale source/sink terms, and large-scale condensation and evaporation terms, and linearizing about a basic state which is at rest, we obtain

$$\frac{\partial u}{\partial t} - fv + \frac{\partial}{\partial r} (\phi + \sigma \bar{\alpha} \pi) = 0 \ , \tag{3.1}$$

$$\frac{\partial v}{\partial t} + fu = 0 \ , \tag{3.2}$$

$$\frac{\partial \pi}{\partial t} + \bar{\pi} \left[\frac{\partial ru}{r \partial r} + \frac{\partial \dot{\sigma}}{\partial \sigma} \right] = 0 \ , \tag{3.3}$$

$$\frac{\partial}{\partial t} \left\{ \frac{\partial \phi}{\partial \sigma} + \left(1 - \frac{\sigma \bar{\pi}}{\gamma \bar{p}} \right) \bar{\alpha} \pi \right\} + S\dot{\sigma} = 0 \ , \tag{3.4}$$

where $\gamma = c_p/c_v$ and the basic state static stability has been defined

as $\quad S \equiv \frac{R\bar{\pi}}{\bar{p}} \left(\frac{\bar{\pi} \, \bar{\alpha}}{c_p} - \frac{d\bar{T}}{d\sigma} \right)$.

Following the approach of Robert et al. (1972), Daley (1979), Temperton and Williamson (1979) and Kasahara and Puri (1980) we define two new dependent variables Φ and ω by

$$\Phi = \phi + \sigma \bar{\alpha} \pi \ , \tag{3.5a}$$

$$\omega = \bar{\pi} \dot{\sigma} + \sigma \frac{\partial \pi}{\partial t} \ . \tag{3.5b}$$

The use of (3.5) allows (3.1)-(3.4) to be written

$$\frac{\partial u}{\partial t} - fv + \frac{\partial \Phi}{\partial r} = 0 \ , \tag{3.6}$$

$$\frac{\partial v}{\partial t} + fu = 0 \ , \tag{3.7}$$

$$\overline{\pi} \frac{\partial ru}{r \partial r} + \frac{\partial \omega}{\partial \sigma} = 0 \, , \tag{3.8}$$

$$\overline{\pi} \frac{\partial}{\partial t} \left(\frac{\partial \Phi}{\partial \sigma} \right) + S\omega = 0 \, , \tag{3.9}$$

The boundary conditions (2.8) become

$$\omega = 0 \quad \text{at} \quad \sigma = 0 \quad \text{and} \quad \frac{\partial \Phi}{\partial t} - \overline{\alpha}\omega = 0 \quad \text{at} \quad \sigma = 1 \, . \tag{3.10}$$

Equations (3.8) and (3.9) can be combined to eliminate ω so that we obtain

$$\frac{\partial}{\partial t} \left[\frac{\partial}{\partial \sigma} \left(\frac{1}{S} \frac{\partial \Phi}{\partial \sigma} \right) \right] - \frac{\partial ru}{r \partial r} = 0 \, . \tag{3.11}$$

Thus, the governing system of linear equations consists of (3.6), (3.7) and (3.11) in the unknowns u, v and Φ . We will now assume that the σ dependence of u, v and Φ is separable from the (r,t) dependence, i.e.

$$\begin{Bmatrix} u(r,\sigma,t) \\ v(r,\sigma,t) \\ \Phi(r,\sigma,t) \end{Bmatrix} = \begin{Bmatrix} \hat{u}(r,t) \\ \hat{v}(r,t) \\ \hat{\Phi}(r,t) \end{Bmatrix} \Psi(\sigma) \, . \tag{3.12}$$

Substitution into (3.6), (3.7) and (3.11) yields

$$\frac{\partial \hat{u}}{\partial t} - f\hat{v} + \frac{\partial \hat{\Phi}}{\partial r} = 0 \, , \tag{3.13}$$

$$\frac{\partial \hat{v}}{\partial t} + f\hat{u} = 0 \, , \tag{3.14}$$

$$\frac{\partial \hat{\Phi}}{\partial t} + gh \frac{\partial r\hat{u}}{r \partial r} = 0 \, , \tag{3.15}$$

$$\frac{d}{d\sigma} \left(\frac{1}{S} \frac{d\Psi}{d\sigma} \right) + \frac{1}{gh} \Psi = 0 \, , \tag{3.16}$$

where gh is the separation constant. The boundary conditions for (3.16) can be obtained from (3.10) and are

$$\frac{d\Psi}{d\sigma} = 0 \quad \text{at} \quad \sigma = 0 \quad \text{and} \quad \frac{d\Psi}{d\sigma} + \frac{S}{\pi \alpha} \Psi = 0 \quad \text{at} \quad \sigma = 1 \ . \qquad (3.17)$$

Equation (3.16) is the vertical structure equation for our problem and, along with boundary conditions (3.17), gives rise to a countably infinite set of eigenvalues gh_n, and a corresponding set of vertical structure functions (eigenfunctions) $\Psi_n(\sigma)$. Since (3.16) and (3.17) constitute a Sturm-Liouville problem, the vertical structure functions $\Psi_n(\sigma)$ form a complete and orthogonal set on the interval $[0,1]$. They may also be normalized so that

$$\int_0^1 \Psi_m(\sigma) \ \Psi_n(\sigma) \ d\sigma = \begin{cases} 1 & m = n \\ 0 & m \neq n \end{cases} . \qquad (3.18)$$

Accordingly any function of (r,σ,t) can be represented by the series

$$F(r,\sigma,t) = \sum_n \hat{F}_n(r,t) \ \Psi_n(\sigma) \ , \qquad (3.19)$$

where $\hat{F}_n(r,t)$ is obtained from

$$\hat{F}_n(r,t) = \int_0^1 F(r,\sigma,t) \ \Psi_n(\sigma) \ d\sigma \ . \qquad (3.20)$$

We shall present some solutions of (3.16) and (3.17) in section 3.2.

The linear system (3.13)-(3.15) constitutes the horizontal struc-ture problem and is more commonly referred to as the divergent baro-tropic system of equations, or the shallow water equations. In their simplest context (3.13)-(3.15) govern small amplitude perturbations in a rotating, homogeneous, incompressible, inviscid and hydrostatic fluid with a mean free surface height h. We note that the phase speed of a pure gravity wave in such a fluid is given by $(gh)^{\frac{1}{2}}$. For the more general stratified problem (3.13)-(3.15) govern the horizontal be-havior of each of the vertical modes arising from the solution of
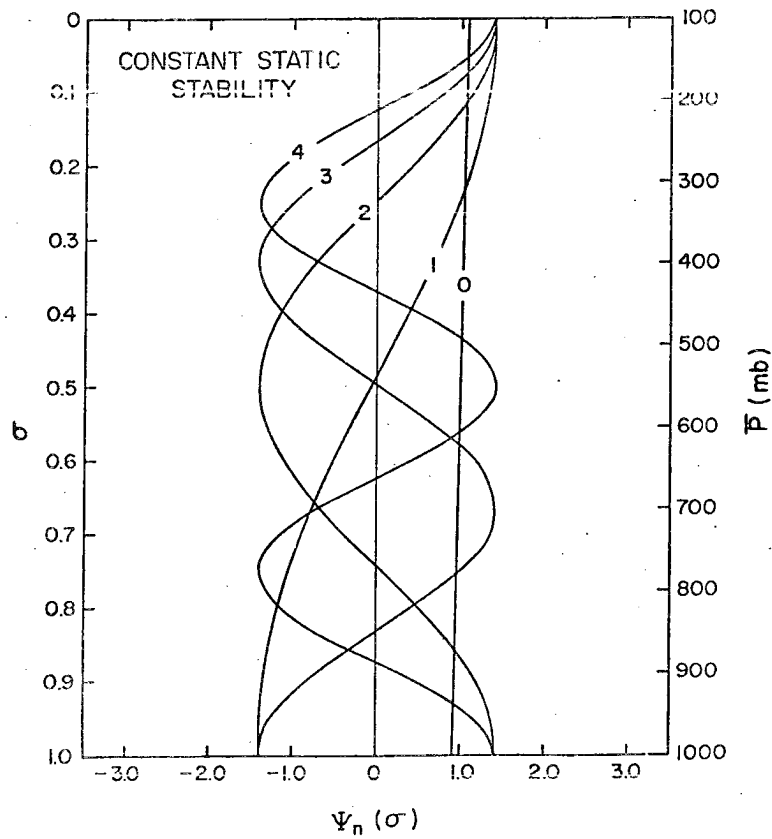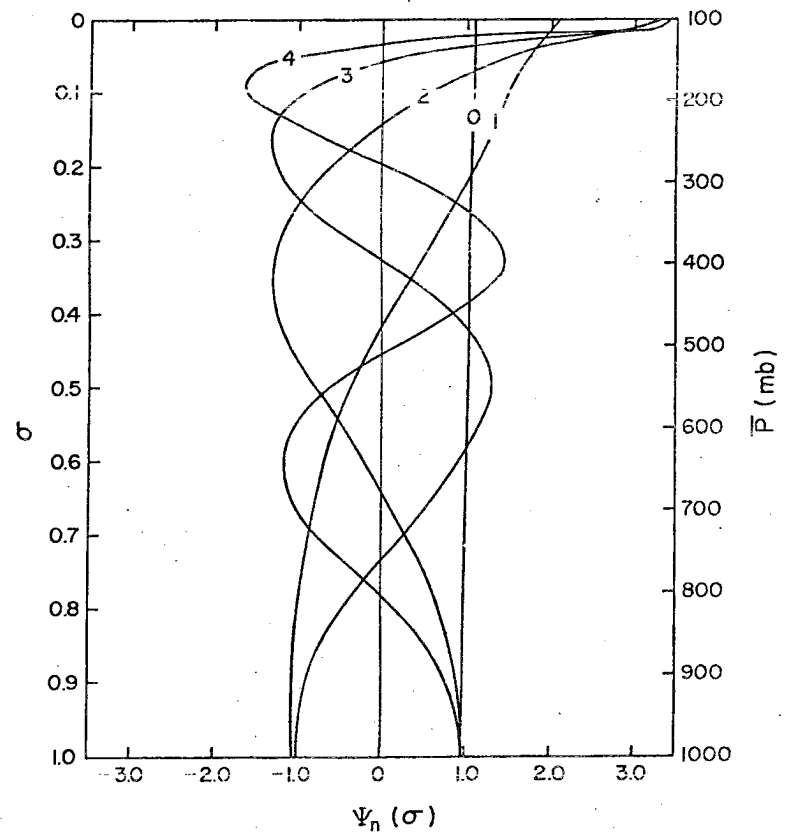
Figure 3.1   (a) Eigenfunctions $\Psi_n(\sigma)$ for constant static stability; (b) eigenfunctions $\Psi_n(\sigma)$ for the static stability profile of Fig. 3.3.

(3.16) and (3.17). Consequently, the eigenvalue $(gh_r)^{1/2}$, where h_n is known as the equivalent depth, is interpreted as the pure gravity wave phase velocity of the associated vertical mode $\Psi_n(\sigma)$. In section 3.4 we shall use (3.13)-(3.14) to determine an approximate outgoing wave condition and to examine the reflectivity of boundary conditions in general.

3.2 Analysis of the Vertical Structure Problem

The solution of the vertical structure problem requires the specification of the basic state static stability. The simplest case that can be considered is one in which the static stability is a constant. For such a situation the normalized eigenfunctions of (3.16) and (3.17) are given by

$$\Psi_n(\sigma) = \left[\frac{2}{1 + (2\lambda_n)^{-1} \sin 2\lambda_n} \right]^{1/2} \cos \lambda_n \sigma \ , \qquad (3.21)$$

where $\lambda_n \equiv \left(\dfrac{S}{gh_n} \right)^{1/2}$ is determined from the eigenvalue relation

$$\lambda_n \tan \lambda_n = \frac{S}{\overline{\pi} \, \overline{\alpha} \, (1)} \qquad n = 0,1,2,\ldots \ . \qquad (3.22)$$

A good approximation to (3.22) is

$$\left. \begin{aligned} (gh_0)^{1/2} &\approx \left[\overline{\pi} \, \overline{\alpha} \, (1) \right]^{1/2} \\[2mm] (gh_n)^{1/2} &\approx \frac{S^{1/2}}{n\pi} \quad \text{for} \quad n = 1,2,3,\ldots \end{aligned} \right\} \qquad . \qquad (3.23)$$

We see from this approximation that except for the external mode $(n = 0)$, the eigenvalues $(gh_n)^{1/2}$ are proportional to $1/n$. The first eighteen exact and approximate eigenvalues, determined from (3.22) and (3.23) respectively, are listed in Table 3.1. These results are based on $\overline{\pi} = 90$ kPa, $\alpha(1) = 0.861$ $m^3 kg^{-1}$, and $S^{1/2} = 162.77$ m s^{-1}. The first five
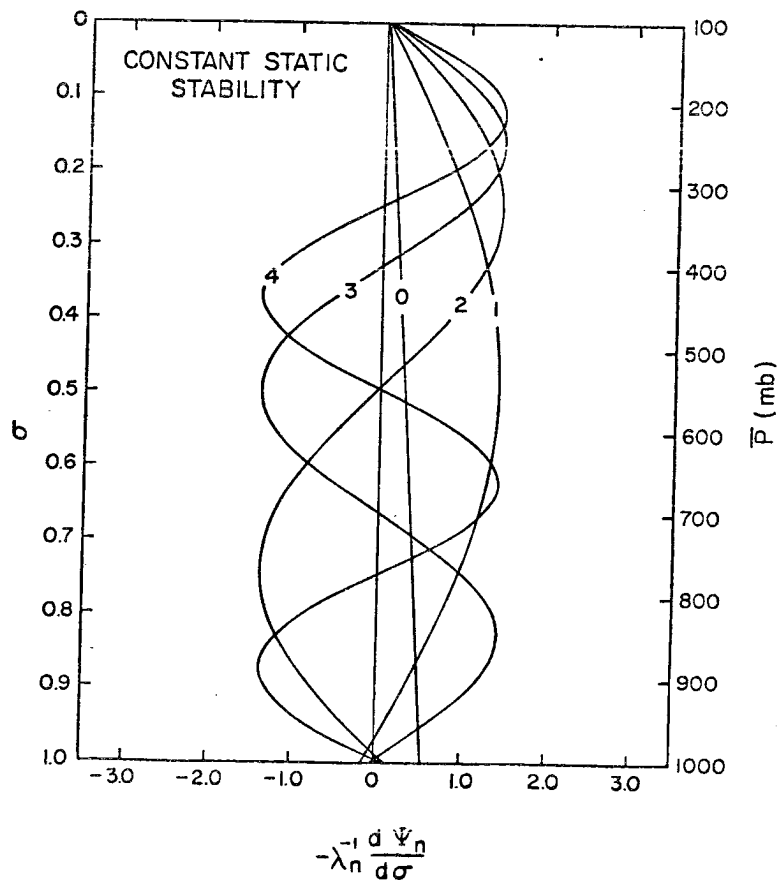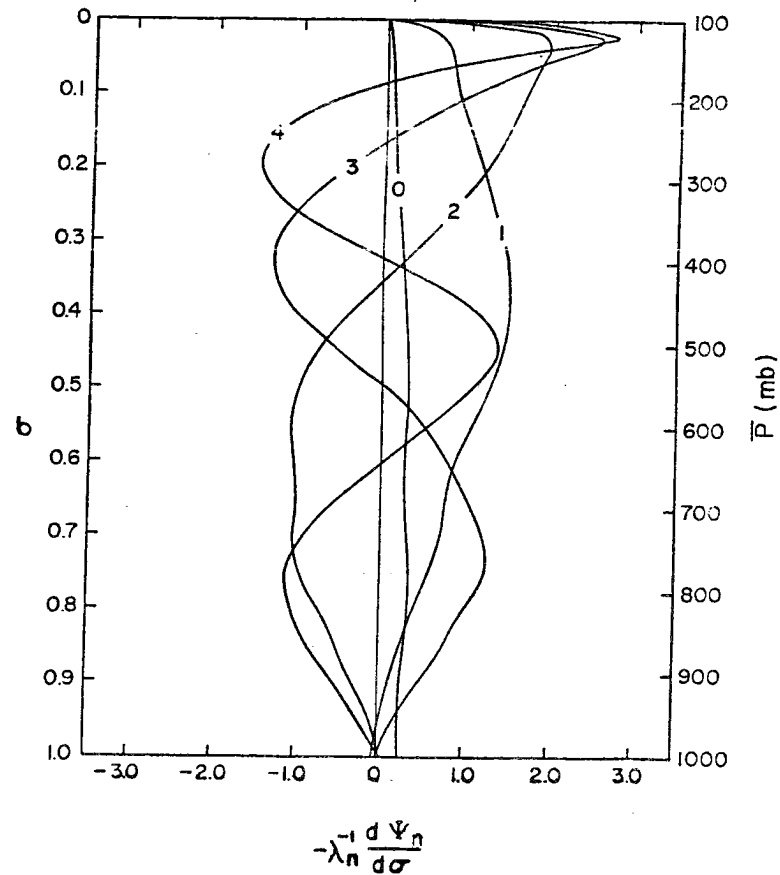
Figure 3.2 Vertical profiles of $-\lambda_n^{-1} \dfrac{d\psi_n}{d\sigma}$ for (a) constant static stability and (b) the static stability of Fig. 3.3.

eigenfunctions determined from (3.21) and (3.22) are shown in Fig. 3.1a. These eigenfunctions portray the vertical structure of the dependent variables u, v and Φ. The variable ω has a vertical structure proportional to $-\lambda_n^{-1} \frac{d\Psi}{d\sigma}$, which is plotted for the first five modes in Fig. 3.2a.

In the tropical atmosphere the basic state static stability varies considerably. This is illustrated in Fig. 3.3 where the vertical profile of $S^{\frac{1}{2}}$ was calculated from the mean tropical clear area temperature profile of Gray et al. (1975). The constant value of $S^{\frac{1}{2}}$ used in the earlier calculations is indicated by the vertical dashed line. The vertical structure problem (3.16) and (3.17) can be solved numerically for this more realistic $S^{\frac{1}{2}}$ profile. The eigenvalues which are obtained are shown in the last column of Table 3.1, and eigenfunctions Ψ_n and $-\lambda_n^{-1} \frac{d\Psi_n}{d\sigma}$ are shown in Figs. 3.1b and 3.2b respectively. We see that the effect of the variable static stability is primarily to increase the propagation speeds of the higher order vertical modes. This is probably a consequence of the large values of $S^{\frac{1}{2}}$ in the upper troposphere. We also note that the vertical structure functions are strongly modified in this region of high static stability, such that the vertical wavelengths are shortened and the amplitudes are increased.

3.3 Importance of the Lateral Boundary Condition

Before considering several lateral boundary conditions in the next section, we attempt to establish the importance of carefully formulated lateral boundary conditions in tropical cyclone models. The argument presented in this section is that when latent heat generates available potential energy on horizontal scales typical of a tropical cyclone

Vertical Mode n	Constant Static Stability		Static Stability of Fig. 3.3
	Equ. (3.22) (exact)	Equ. (3.23) (approximate)	
0	294.15	278.39	287.55
1	50.14	51.81	51.61
2	25.69	25.91	26.81
3	17.21	17.27	19.40
4	12.93	12.95	14.81
5	10.35	10.36	11.80
6	8.63	8.64	9.77
7	7.40	7.40	8.39
8	6.47	6.48	7.42
9	5.75	5.76	6.64
10	5.18	5.18	6.02
11	4.71	4.71	5.49
12	4.32	4.32	5.04
13	3.99	3.99	4.65
14	3.70	3.70	4.31
15	3.45	3.45	4.02
16	3.24	3.24	3.76
17	3.05	3.05	3.53

Table 3.1. The first eighteen exact and approximate eigenvlaues $(gh_n)^{1/2}$, determined from (3.22) and (3.23) for the constant static stability case, and numerically for the static stability profile of Fig. 3.3. Units are m s^{-1}.
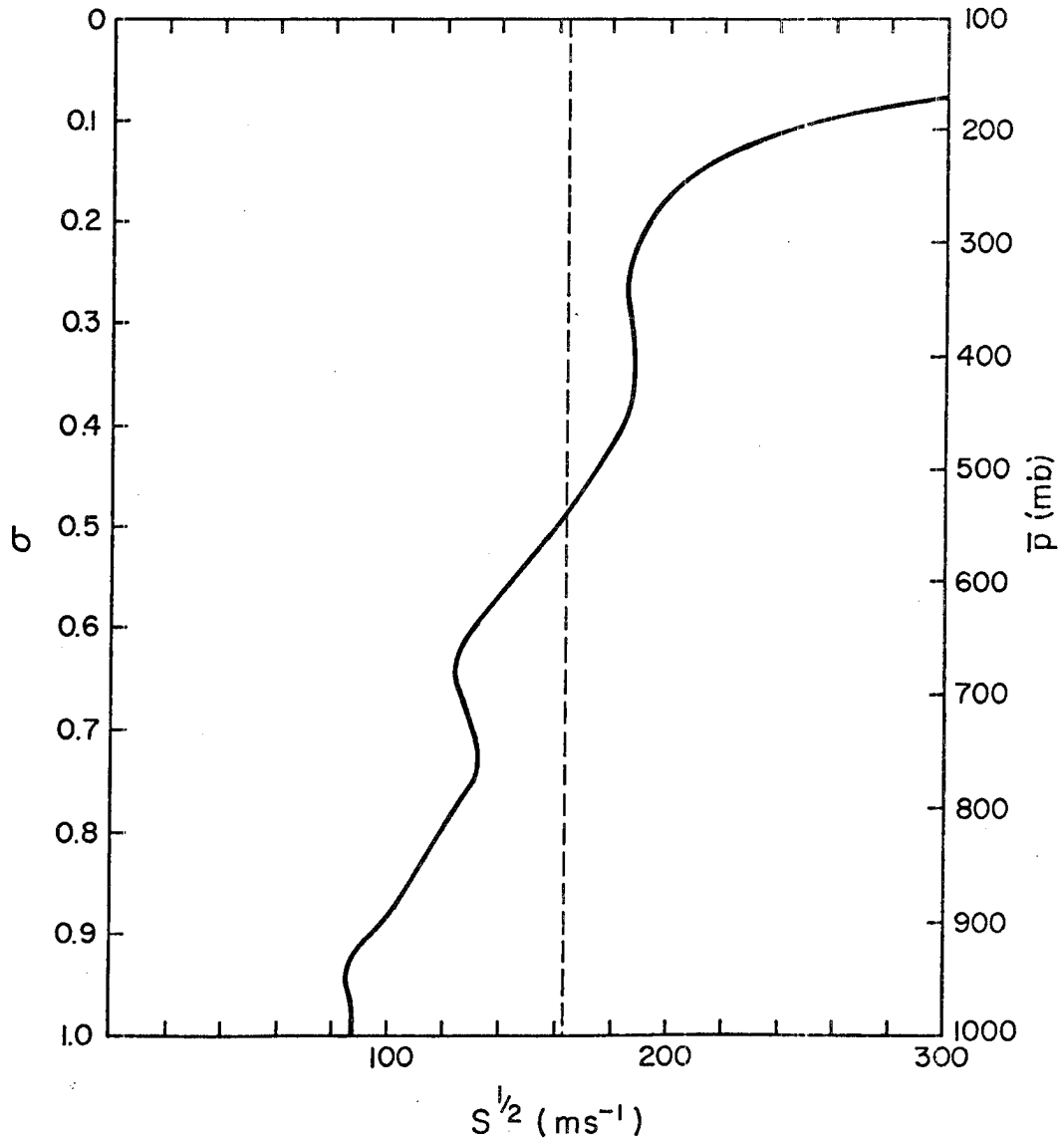
Figure 3.3 Square root of the basic state static stability computed from the mean tropical clear area temperature profile of Gray et al. (1975).

in low latitudes, only a small fraction of the energy ends up in balanced flow. The major portion of this energy is partitioned to outward propagating gravity-inertia waves. This lopsided energy partition can be illustrated with a simple example.

For vertical mode n we can show from (3.14) and (3.15) that the potential vorticity $\dfrac{\partial r \hat{v}_n}{r \partial r} - \dfrac{f}{gh_n} \hat{\Phi}_n$ is locally invariant. Thus, the initial and final potential vorticity fields are related by

$$\frac{dr\hat{v}_n(r,\infty)}{rdr} - \frac{f}{gh_n} \hat{\Phi}_n(r,\infty) = \frac{dr\hat{v}_n(r,0)}{rdr} - \frac{f}{gh_n} \hat{\Phi}_n(r,0) \ . \quad (3.24)$$

If we assume that the final tangential flow is geostrophic, that the initial vorticity vanishes and that the initial geopotential is given by

$$\hat{\Phi}_n(r,0) = \begin{cases} -gh_n & r < a \\ \\ 0 & r > a \ , \end{cases} \quad (3.25)$$

then (3.24) reduces to

$$\frac{d^2\hat{\Phi}_n(r,\infty)}{dr^2} + \frac{d\hat{\Phi}_n(r,\infty)}{rdr} - \frac{f^2}{gh_n} \hat{\Phi}_n(r,\infty) = \begin{cases} f^2 & r < a \\ \\ 0 & r > a \ . \end{cases} \quad (3.26)$$

The solution of (3.26) which remains bounded at the origin and at infinity and which possesses continuous $\hat{\Phi}_n(r,\infty)$ and $\hat{v}_n(r,\infty)$ at $r = a$ is

$$\hat{\Phi}_n(r,\infty) = \begin{cases} -fa(gh_n)^{\frac{1}{2}} \left\{ \dfrac{(gh_n)^{\frac{1}{2}}}{fa} - K_1 \left[\dfrac{f}{(gh_n)^{\frac{1}{2}}} a \right] I_0 \left[\dfrac{f}{(gh_n)^{\frac{1}{2}}} r \right] \right\} & r < a \\ \\ -fa(gh_n)^{\frac{1}{2}} I_1 \left[\dfrac{f}{(gh_n)^{\frac{1}{2}}} a \right] K_0 \left[\dfrac{f}{(gh_n)^{\frac{1}{2}}} r \right] & r > a , \end{cases}$$

$$(3.27)$$

where I_m and K_m are the order m modified Bessel functions.

The sum of the kinetic energy and the available potential energy associated with the final geostrophic flow, $K_\infty + P_\infty$, can be obtained by multiplying (3.24) by $\hat{\phi}_n(r,\infty)$ and integrating over area. The result is

$$K_\infty + P_\infty \equiv \int_0^\infty \tfrac{1}{2} \left[\hat{v}_n^2(r,\infty) + \frac{1}{gh_n} \hat{\phi}_n^2(r,\infty) \right] r\,dr$$

(3.28)

$$= \frac{1}{2gh_n} \int_0^\infty \hat{\phi}_n(r,\infty)\, \hat{\phi}_n(r,0)\, r\,dr \quad .$$

Substituting (3.25) and (3.27) into (3.28) and normalizing by the initial available potential energy P_0 we obtain

$$\frac{K_\infty + P_\infty}{P_0} = 1 - 2K_1 \left[\frac{f}{(gh_n)^{1/2}} a \right] I_1 \left[\frac{f}{(gh_n)^{1/2}} a \right] \quad .$$

(3.29)

The fraction of the initial energy which ends up in geostrophic flow, $\dfrac{K_\infty + P_\infty}{P_0}$, yields a single curve if we plot it as a function of the dimensionless horizontal scale $\dfrac{f}{(gh_n)^{1/2}} a$. However, for convenient physical interpretation, we have plotted in Fig. 3.4 the energy partition $\dfrac{K_\infty + P_\infty}{P_0}$ as a function of the dimensional horizontal scale a, at 20°N, for the first five values of $(gh_n)^{1/2}$ given in the last column of Table 3.1. For a given horizontal scale a, the difference between $\dfrac{K_\infty + P_\infty}{P_0}$ and unity represents the fraction of the initial energy partitioned to outward propagating gravity-inertia waves. We see that for horizontal scales ≤ 300 km, the majority of the initial energy is partitioned to gravity-inertia wave motion. In light of the large amounts of latent heat released in tropical storms it would be reasonable to conclude that the gravity-inertia wave energy leaving the vicinity of a tropical cyclone must be substantial, especially for the low order vertical modes. Although the energy partition curves shown
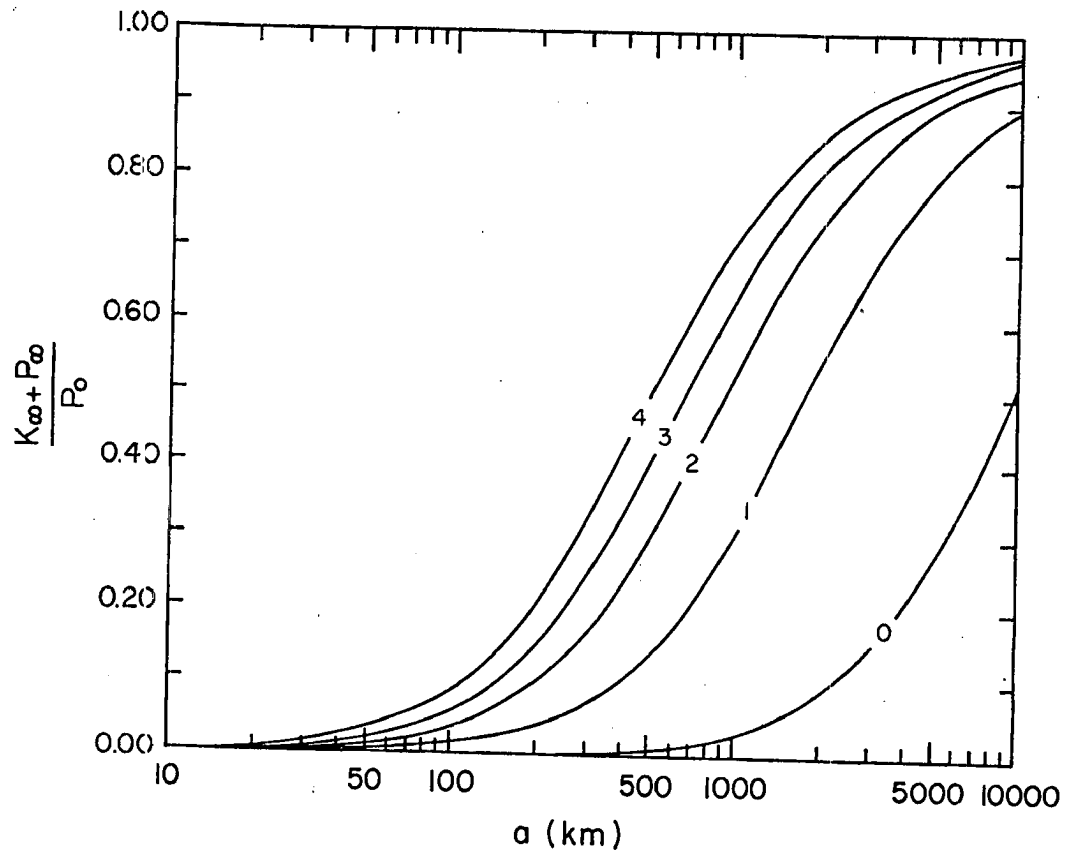
Figure 3.4   The fraction of the initial energy which is parti-
tioned to geostrophic flow as a function of the
horizontal scale of the initial geopotential dis-
turbance.   The curves have been computed using
(3.29) with the first five values of $(gh_n)^{1/2}$ given
in the last column of Table 3.1 and with an f
corresponding to a latitude of 20°N.

in Fig. 3.4 depend on the form of the initial condition chosen, these curves are typical of other examples we have investigated (Schubert et al., 1980). They show the very low efficiency of geostrophic energy generation by tropical cyclone scale heating in low latitudes and lead naturally to the view that, in terms of gravity-inertia wave energy, tropical cyclones should be regarded as highly radiating systems.

There are of course real physical situations in which gravity-inertia waves might be reflected back toward their source. However, the imposition of a lateral boundary to the computational domain of a numerical model should not result in the reflection of incident waves. Improper reflection of gravity-inertia waves in a model which carries water vapor as a dependent variable can become intolerable since the vertical motion field associated with these reflected waves (see Figure 3.2b) can interact nonlinearly with the moisture field to produce an erroneous pattern of latent heat release. Consequently, a poorly formulated lateral boundary condition may indirectly contribute to significant alterations of the numerical solution, especially with regard to the transient behavior of the simulated disturbance.

3.4 Analysis of the Horizontal Structure Problem

3.4.1 An 'exact' outgoing wave condition

A fairly thorough study of open boundary conditions for dispersive waves has been conducted by Bennett (1976). We apply his approach to our problem by considering the horizontal structure equations (3.13)-(3.15) for the vertical mode n. Defining $\tilde{F}(r,s)$ as the Laplace transform of $\hat{F}(r,t)$ and assuming no initial disturbance for $r \geq a$, we transform (3.13)-(3.15) and eliminate $\tilde{\phi}_n(r,s)$ and $\tilde{v}_n(r,s)$ to obtain

$$r^2 \frac{d^2 \tilde{u}_n}{dr^2} + r \frac{d\tilde{u}_n}{dr} - \left[\left(\frac{s^2 + f^2}{gh_n} \right) r^2 + 1 \right] \tilde{u}_n = 0 \quad \text{for} \quad r \geq a . \quad (3.30)$$

The solution of (3.30) which remains bounded as $r \to \infty$ is given by

$$\tilde{u}_n(r,s) = A(s) \, K_1 \left[\left(\frac{s^2 + f^2}{gh_n} \right)^{1/2} r \right] \quad \text{for} \quad r \geq a . \quad (3.31)$$

It can be shown that the transformed radial wind component $\tilde{u}_n(r,s)$ also satisfies

$$\tilde{u}_n \frac{d}{dr} \left\{ r^{1/2} \, K_1 \left[\left(\frac{s^2 + f^2}{gh_n} \right)^{1/2} r \right] \right\} - \frac{dr^{1/2} \, \tilde{u}_n}{dr} \, K_1 \left[\left(\frac{s^2 + f^2}{gh_n} \right)^{1/2} r \right] = 0 \quad \text{for} \quad r \geq a . \quad (3.32)$$

An exact outgoing wave condition can be obtained by inverting (3.32). Unfortunately this procedure yields an expression which is quite complicated and of questionable practical value. This is more readily illustrated if we utilize the large argument asymptotic form of the modified Bessel function K_1 to simplify (3.32) to

$$s\tilde{u}_n + (gh_n)^{1/2} \frac{dr^{1/2} \, \tilde{u}_n}{r^{1/2} dr} = (gh_n)^{1/2} \left[\frac{(s^2 + f^2)^{1/2} - s}{(s^2 + f^2)^{1/2}} \right] \frac{dr^{1/2} \, \tilde{u}_n}{r^{1/2} dr} \quad \text{for} \quad r \geq a , \quad (3.33)$$

which when inverted gives

$$\frac{\partial \hat{u}_n(r,t)}{\partial t} + (gh_n)^{1/2} \frac{\partial r^{1/2} \hat{u}_n(r,t)}{r^{1/2} \, \partial r} = f(gh_n)^{1/2} \int_0^t J_1[f(t-t')] \frac{\partial r^{1/2} \hat{u}_n(r,t')}{r^{1/2} \, \partial r} \, dt'$$

$$\text{for} \quad r \geq a . \quad (3.34)$$

Relationships of this kind require that we store and repeatedly sum (with different weights) boundary values of $\hat{u}_n$ and its horizontal derivative. The storage requirements alone are effectively equivalent to allowing the computational domain to expand in time. Since this is what we are attempting to avoid, the idea of using an exact outgoing wave condition will be abandoned for practical reasons.

3.4.2 Reflectivity analysis

We are now faced with the problem of finding an approximate boundary condition which will keep the distortion of the adjustment process within some tolerable limit. This can be accomplished by analytically studying the reflectivities of boundary conditions in general. We begin by noting that the system (3.13)-(3.15) has solutions of the form

$$
\begin{bmatrix} \hat{u}_n(r,t) \\ \hat{v}_n(r,t) \\ \hat{\Phi}_n(r,t) \end{bmatrix} \propto \begin{bmatrix} 1 \\ -\dfrac{if}{\nu_n} \\ -\dfrac{igh_n k}{\nu_n} \end{bmatrix} \left\{ \begin{bmatrix} H_1^{(1)}(kr) \\ H_1^{(1)}(kr) \\ H_0^{(1)}(kr) \end{bmatrix} + R \begin{bmatrix} H_1^{(2)}(kr) \\ H_1^{(2)}(kr) \\ H_0^{(2)}(kr) \end{bmatrix} \right\} e^{-i\nu_n t},
$$

(3.35)

where the frequency ν_n is given by $\nu_n = (f^2 + gh_n k^2)^{\frac{1}{2}}$, k is the horizontal wavenumber, R is a complex constant, and $H_m^{(1)}(kr)$ and $H_m^{(2)}(kr)$ are the order m Hankel functions of the first and second kind. The use of asymptotic expansions valid for large kr allows (3.35) to be written

$$
\begin{bmatrix} \hat{u}_n(r,t) \\ \hat{v}_n(r,t) \\ \hat{\Phi}_n(r,t) \end{bmatrix} \sim \left(\frac{2}{\pi kr}\right)^{\frac{1}{2}} e^{-\frac{3\pi i}{4}} \begin{bmatrix} 1 \\ -\dfrac{if}{\nu_n} \\ \dfrac{gh_n k}{\nu_n} \end{bmatrix} \left\{ e^{i(kr-\nu_n t)} - iR e^{-i(kr+\nu_n t)} \right\}.
$$

(3.36)

The first term in both (3.35) and (3.36) corresponds to an outward propagating wave while the second term corresponds to an inward propagating wave. Thus, at large radius a (e.g. the radius of the model boundary), the asymptotic form of the outward propagating wave satisfies the radiation condition

$$\frac{\partial \hat{u}_n}{\partial t} + \frac{\nu_n}{k} \frac{\partial r^{\frac{1}{2}} \hat{u}_n}{r^{\frac{1}{2}} \partial r} = 0 \quad \text{at} \quad r = a \;. \tag{I}$$

If a disturbance in the form of a wave packet centered on wavenumber k approaches the boundary, the use of boundary condition I should result in low reflectivity as long as $ka \gg 1$. The primary disadvantage of I is that it is difficult to apply in physical space because knowledge of $\frac{\nu_n}{k}$ is required. However, since $\frac{\nu_n}{k} \to (gh_n)^{\frac{1}{2}}$ as $k \to \infty$, we might approximate I by

$$\frac{\partial \hat{u}_n}{\partial t} + (gh_n)^{\frac{1}{2}} \frac{\partial r^{\frac{1}{2}} \hat{u}_n}{r^{\frac{1}{2}} \partial r} = 0 \quad \text{at} \quad r = a \;, \tag{II}$$

which is much easier to apply in physical space because $(gh_n)^{\frac{1}{2}}$ is known from the solution of the vertical structure problem. This approximation is equivalent to neglecting the Coriolis parameter and confining our study to non-dispersive or pure gravity wave motion. For such a physical situation II can be obtained directly from (3.34) by setting $f = 0$. One additional approximation can be made to II, and that is to neglect the effects of cylindrical geometry, which gives

$$\frac{\partial \hat{u}_n}{\partial t} + (gh_n)^{\frac{1}{2}} \frac{\partial \hat{u}_n}{\partial r} = 0 \quad \text{at} \quad r = a \;. \tag{III}$$

Let us also consider the two most widely used boundary conditions in tropical cyclone models which are the condition of zero divergence,

$$\frac{\partial r \hat{u}_n}{r \partial r} = 0 \quad \text{at} \quad r = a \;, \tag{IV}$$

and the condition of zero radial wind,

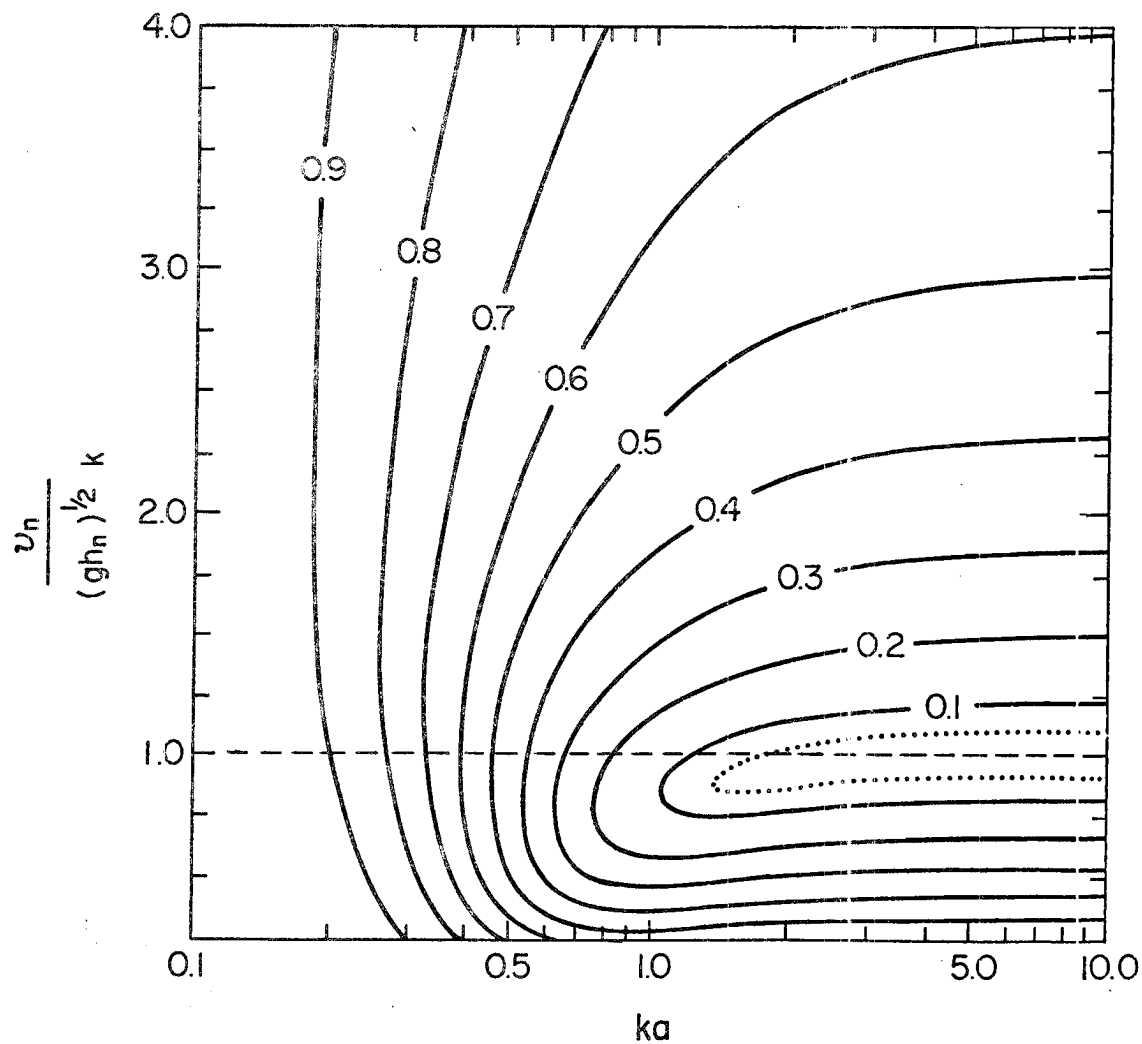$$\hat{u}_n = 0 \quad \text{at} \quad r = a \;. \tag{V}$$

Figure 3.5 Isolines of $|R|$ as a function of ka and $\dfrac{\nu_n}{(gh_n)^{\frac{1}{2}}k}$ for boundary condition II. The reflectivity of boundary condition I is a function of ka only and can be obtained by moving along the $\dfrac{\nu_n}{(gh_n)^{\frac{1}{2}}k} = 1$ line in this figure.

The reflectivity of each of the conditions I-V can be found by substituting (3.35) and solving for $|R|$. The mathematical expressions are given in Table 3.2. Since conditions IV and V have unit reflectivity and the reflectivity of III is larger than II (Schubert et al., 1980), we confine the remainder of this discussion to a comparison of I and II. As can be seen from Table 3.2 the reflectivity of boundary condition I is a function of ka only, while the reflectivity of boundary condition II is a function of both ka and $\frac{\nu_n}{(gh_n)^{1/2}k}$. In Fig. 3.5 we have drawn isolines of $|R|$ in the $\left(ka, \frac{\nu_n}{(gh_n)^{1/2}k}\right)$ plane for boundary condition II. From Fig. 3.5 one can also obtain the reflectivity of I since it is identical to the reflectivity of II along the line $\frac{\nu_n}{(gh_n)^{1/2}k} = 1$. As long as $(gh_n)^{1/2}$ is within about 10% of $\frac{\nu_n}{k}$ and $ka \geq 1.5$, the reflectivity can be held under 5%. It should be noted, however, that there is more or less an optimal domain size beyond which little improvement in the reflectivities can be expected. To illustrate this more clearly we have plotted the reflectivities of boundary condition II for selected dimensionless wavenumbers $\frac{(gh_n)^{1/2}}{f} k$ as functions of dimensionless domain size $\frac{fa}{(gh_n)^{1/2}}$ in Fig. 3.6. In this diagram we see that by choosing the domain size properly, the reflectivity for any wavenumber (or family of wavenumbers) can be minimized. As an example, in order to minimize the reflectivities for wavenumbers $\frac{(gh_n)^{1/2}}{f} k \geq 10$, the domain size need be no larger than $\frac{fa}{(gh_n)^{1/2}} \approx 0.6$. It is interesting to note that an optimal domain size corresponds
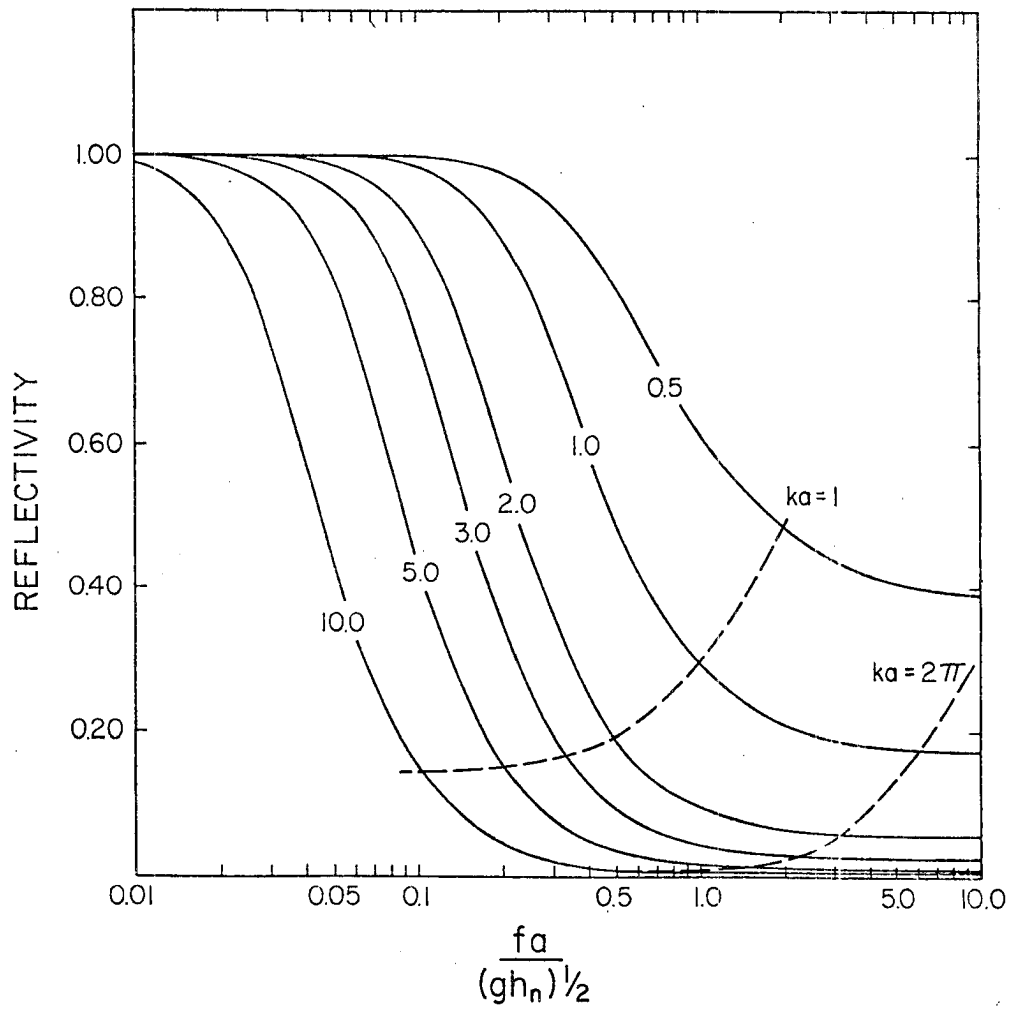
Figure 3.6 Reflectivities of selected dimensionless wave-numbers $\dfrac{(gh_n)^{\frac{1}{2}}}{f} k$ as a function of dimensionless domain size $\dfrac{fa}{(gh_n)^{\frac{1}{2}}}$ for BCII.

Boundary Condition	Reflectivity
(I) $\dfrac{\partial \hat{u}_n}{\partial t} + \dfrac{\nu_n}{k}\dfrac{\partial r^{1/2}\hat{u}_n}{r^{1/2}\partial r} = 0$	$\|R\| = \dfrac{\left\| H_0^{(1)}(ka) - \left[\dfrac{1}{2ka} + i\right]H_1^{(1)}(ka)\right\|}{\left\| H_0^{(2)}(ka) - \left[\dfrac{1}{2ka} + i\right]H_1^{(2)}(ka)\right\|}$
(II) $\dfrac{\partial \hat{u}_n}{\partial t} + (gh_n)^{1/2}\dfrac{\partial r^{1/2}\hat{u}_n}{r^{1/2}\partial r} = 0$	$\|R\| = \dfrac{\left\| H_0^{(1)}(ka) - \left[\dfrac{1}{2ka} + \dfrac{i\nu_n}{(gh_n)^{1/2}k}\right]H_1^{(1)}(ka)\right\|}{\left\| H_0^{(2)}(ka) - \left[\dfrac{1}{2ka} + \dfrac{i\nu_n}{(gh_n)^{1/2}k}\right]H_1^{(2)}(ka)\right\|}$
(III) $\dfrac{\partial \hat{u}_n}{\partial t} + (gh_n)^{1/2}\dfrac{\partial \hat{u}_n}{\partial r} = 0$	$\|R\| = \dfrac{\left\| H_0^{(1)}(ka) - \left[\dfrac{1}{ka} + \dfrac{i\nu_n}{(gh_n)^{1/2}k}\right]H_1^{(1)}(ka)\right\|}{\left\| H_0^{(2)}(ka) - \left[\dfrac{1}{ka} + \dfrac{i\nu_n}{(gh_n)^{1/2}k}\right]H_1^{(2)}(ka)\right\|}$
(IV) $\dfrac{\partial r\hat{u}_n}{r\partial r} = 0$	$\|R\| = 1$
(V) $\hat{u}_n = 0$	$\|R\| = 1$

Table 3.2 Reflectivities for the various boundary conditions.

to the approximate wavelength $\dfrac{2\pi f}{k(gh_n)^{\frac{1}{2}}}$ of the wavenumber for which

the reflectivities are to be minimized.

In order to understand the implications of the reflectivity rela-

tions for a particular model situation it is more convenient to display

the results in dimensional form. The reflectivities of the eighteen

vertical modes which have the eigenvalues listed in the last column

of Table 3.1 are illustrated in Fig. 3.7 for boundary condition II.

These reflectivities are calculated for a domain size of 960 km, and

for an f corresponding to a latitude of 20°N. We see that, for a

given wavenumber k, a larger fraction of the incident wave is reflected

as the vertical mode is increased. This result is due to the fact that

the higher order modes propagate at a slower rate and hence have longer

periods. Thus, the Coriolis force plays a larger role in the dynamics

of these waves, but is neglected in the boundary condition since ν_n/k

has been approximated by its pure gravity wave value $(gh_n)^{\frac{1}{2}}$. Accord-

ingly, boundary condition II is mode dependent, while boundary condi-

tion I is mode independent, its reflection curve being indistinguish-

able from the $n = 0$ curve in Fig. 3.7. Even though boundary condition

II does have higher reflectivities than I, for low order vertical

modes and horizontal wavelengths smaller than the size of the computa-

tional domain, the approximation made in boundary condition II does

not introduce serious reflection problems.

3.5 Numerical Examples

3.5.1 Single vertical mode

In this subsection we shall compare the results of numerical

integrations of (3.13)-(3.15) using boundary conditions I, IV and V.
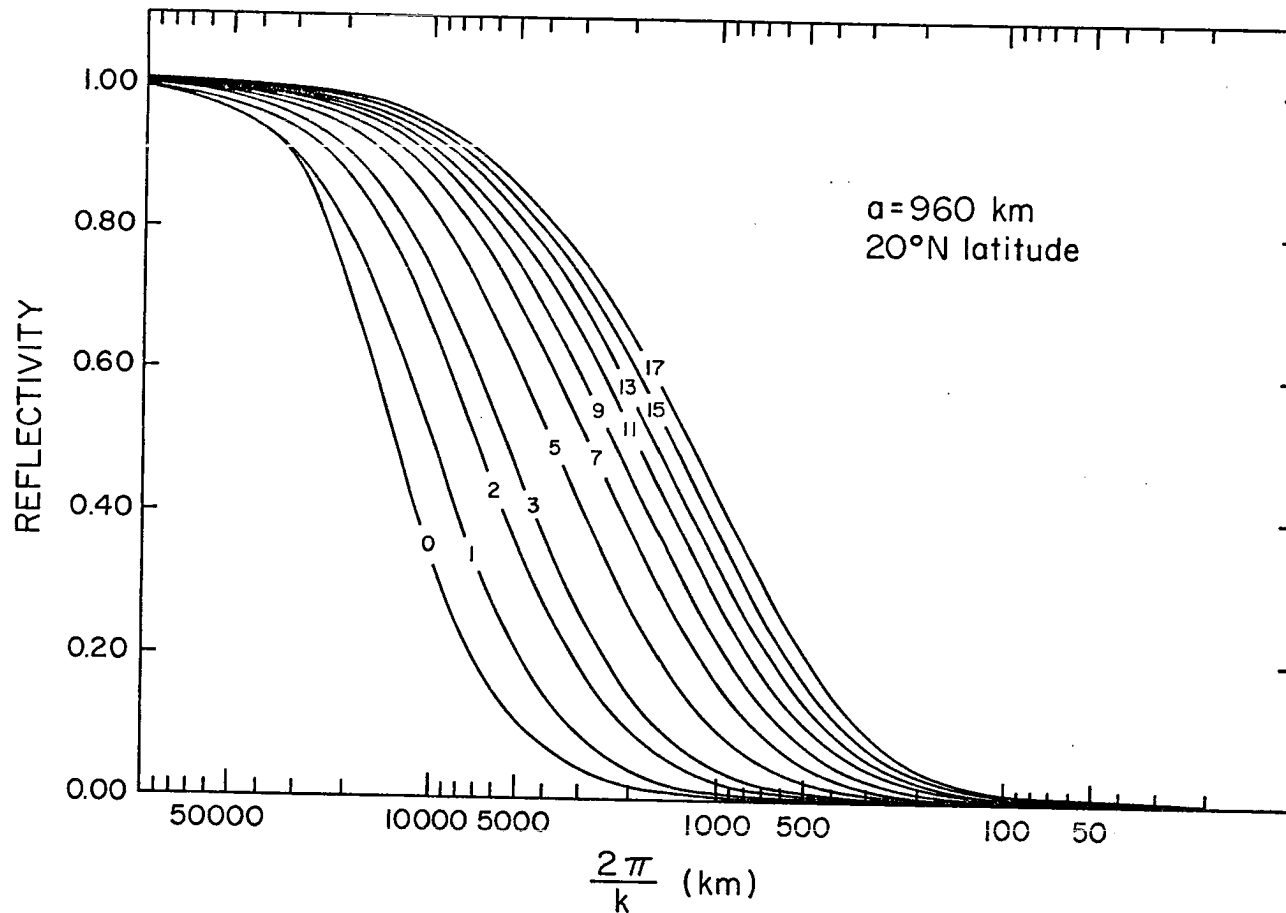
Figure 3.7   The reflectivities of boundary condition II for the eighteen vertical modes which have the eigenvalues listed in the last column of Table 3.1. These reflectivities have been calculated for a domain size of 960 km and for an f corresponding to a latitude of 20°N. The reflectivity of boundary condition I is essentially the same as the n = 0 curve.

In addition we shall show results obtained using the numerical extrapolation technique of Orlanski (1976). In Orlanski's method the condition

$$\frac{\partial \hat{u}}{\partial t} + c \frac{\partial \hat{u}}{\partial r} = 0 \qquad \text{(VIa)}$$

is used to predict $\hat{u}$ at the model boundary after

$$c = - \frac{\frac{\partial \hat{u}}{\partial t}}{\frac{\partial \hat{u}}{\partial r}} \qquad \text{(VIb)}$$

has been used to diagnose c at the previous time step just inside the model boundary. The estimate of c is not allowed to become negative nor to exceed the radial grid interval divided by the time step. For further details the reader is referred to Orlanski's (1976) paper.

In order to conduct the following single mode tests we have made use of a numerical model for which the horizontal space differencing method corresponds to scheme B (staggered grid) of Arakawa and Lamb (1977). (The finite difference analogues are given in Appendix D.) The time differencing is accomplished with a leap frog scheme coupled with an Asselin (1972) time filter (see Appendix A.2, Time differencing). The model consists of 43 grid points spaced 0.0125 dimensionless units apart (i.e. $\Delta r = 0.0125 \ (gh_n)^{\frac{1}{2}}/f$).

In the experiments illustrated here, the fluid is initially at rest but has a free surface perturbation

$$\hat{\Phi}(r,o) \propto \left\{ \frac{r^2}{2r_0^2} \left[1 + \frac{4 - r^2/r_0^2}{4 + \frac{f^2 r_0^2}{gh}} \right] - 1 \right\} e^{-r^2/2r_0^2} , \qquad (3.37)$$

where r_0 is a measure of the perturbation half width which has been specified to be $r_0 = 0.1$ $(gh)^{\frac{1}{2}}/f$. This initial value problem was first studied by Obukhov (1949). For the linear problem, the final geo-strophically adjusted state can be obtained analytically by solving the potential vorticity equation (Schubert et al., 1980, section 6), providing an independent check on the performance of the model.

The results of five experiments will now be shown, the first being the control, or 'infinite domain', experiment and the remaining four using boundary conditions II, IV, V and VI. In the 'infinite domain' experiment the computational domain was expanded to eliminate all pos-sible boundary effects on the solution in the interior 43 grid points of the model. The results of the five numerical tests are shown in Figs. 3.8 and 3.9. Fig. 3.8 is common to all those given in Fig. 3.9, and shows the early propagation of the wave which is excited in the u field (the divergent component of the wind). Up to time $ft = 0.25$, the numerical solutions are essentially the same for all five experi-ments. After this time, however, the solutions diverge due to the differences in the lateral boundary conditions, as can be seen in Fig. 3.9. Fig. 3.9a shows the results of the control experiment and can be regarded as the ideal result since there are no boundary effects. At the final time level shown ($ft = 0.85$), the computational domain is essentially in geostrophic balance. In the interior $\dfrac{fr}{(gh)^{\frac{1}{2}}} \leq 0.5$, the solution is well within 1% of the analytically calculated final adjusted state. The remaining figures show the numerical solutions for those experiments incorporating boundary condition II (Fig. 3.9b), boundary condition VI (Fig. 3.9c), boundary condition IV (Fig. 3.9d) and boundary condition V (Fig. 3.9e). Clearly, boundary conditions
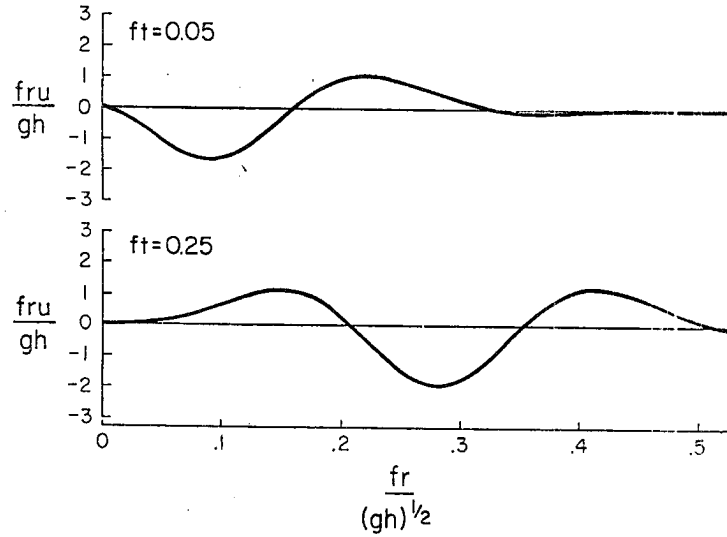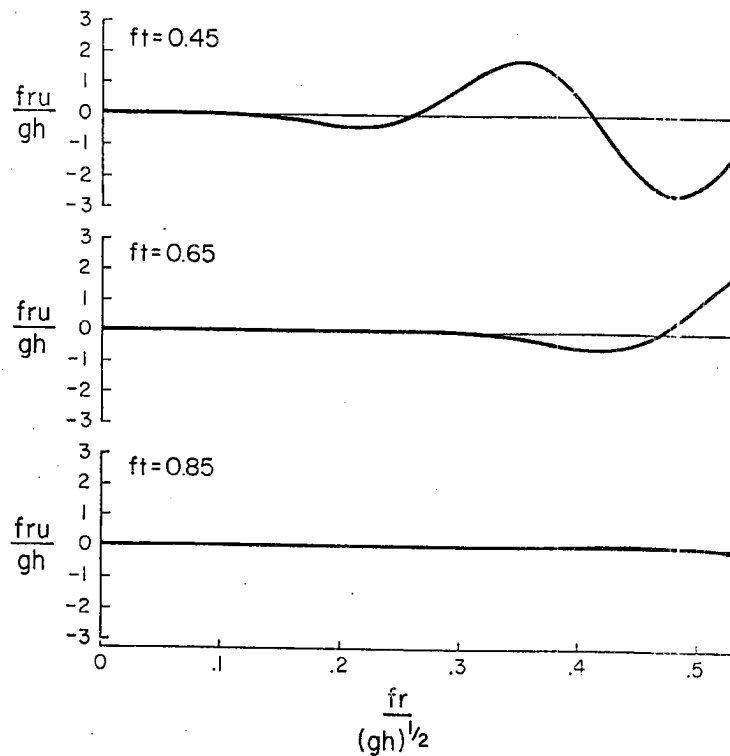
Figure 3.8 The $\frac{fru}{gh}$ field at ft = 0.05 and 0.25 for all single vertical mode initial value experiments. See text for further discussion.

(a)

Figure 3.9 The $\frac{fru}{gh}$ field at ft = 0.45, 0.65 and 0.85 for single vertical mode initial value experiments employing (a) 'infinite domain'.
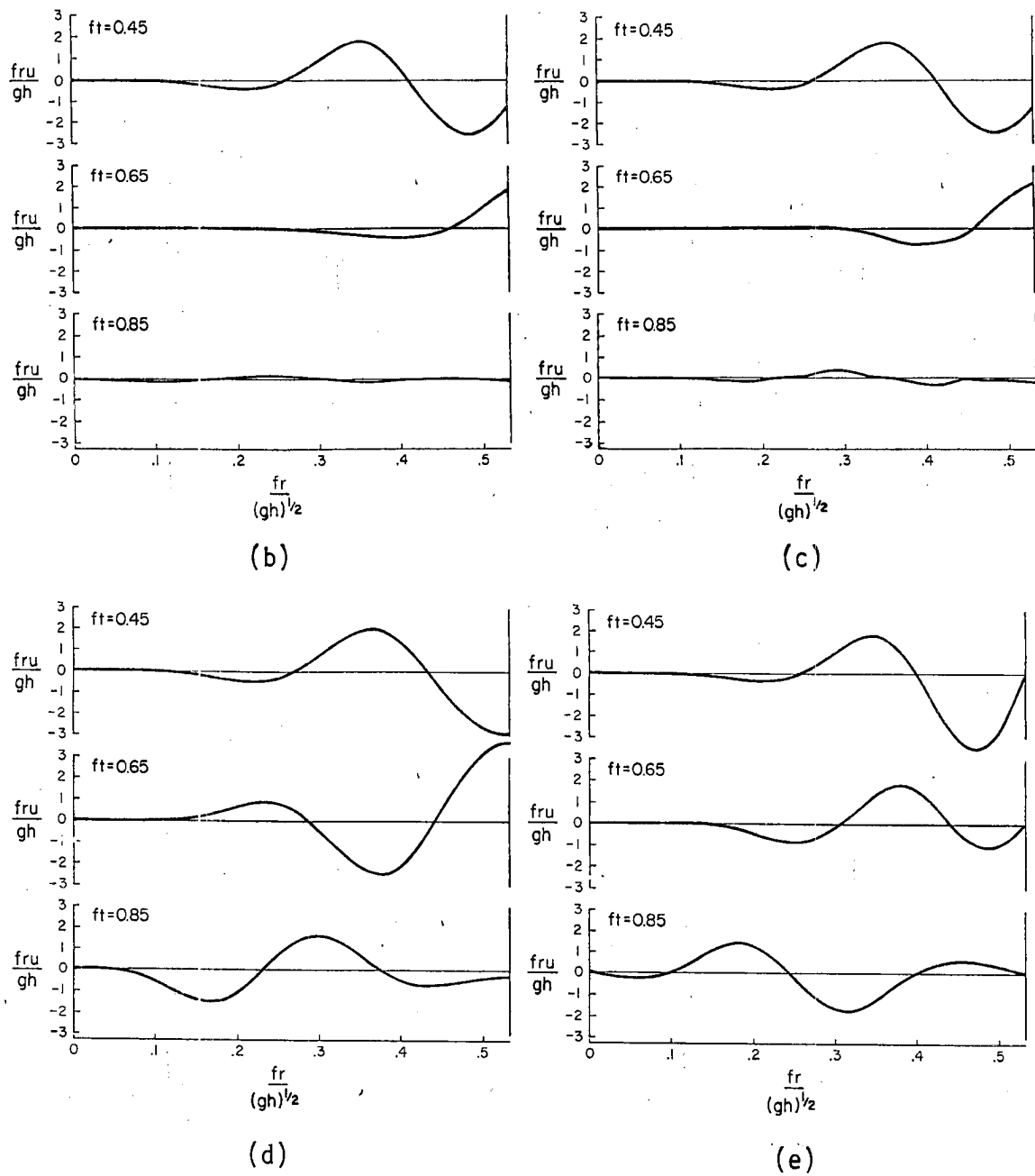
Figure 3.9   The $\frac{fru}{gh}$ field at ft = 0.45, 0.65 and 0.85 for single vertical mode initial value experiments employing (b) boundary condition II, (c) boundary condition VI, (d) boundary condition IV and (e) boundary condition V.

II and VI give results closest to the control, with boundary condition II producing the least reflection.

3.5.2 Fully stratified case

The results of section 3.5.1 are now extended to the more general case of a fully stratified model atmosphere. In this section we compare the behavior of boundary conditions II, IV, V and VI in the stratified numerical model and consider one additional boundary condition for which the relation

$$\frac{\partial u}{\partial t} + c \frac{\partial u}{\partial r} = 0 \tag{VII}$$

is applied at the lateral boundary grid points where the phase velocity c is a constant chosen to be representative of the first internal mode of the model (Klemp and Wilhelmson, 1978).

The numerical experiments are conducted with a dry, adiabatic, inviscid version of the tropical cyclone model described in section 2.1 (where the finite difference equations can be found in Appendix A). The horizontal and vertical resolution (and domain) is the same as described in section 2.1.

Boundary conditions IV, V, VI and VII are all applied level by level. Boundary condition II, however, is applied to each vertical mode. Thus, in order to apply boundary condition II it is necessary to project the boundary values of the dependent variables onto the vertical structure functions and thus obtain the amplitude of each vertical mode. In practice, we obtain these vertical structure functions via a method which will more accurately represent the effects of the vertical differencing scheme we have employed. This approach can be summarized as follows. Noting that boundary condition II is
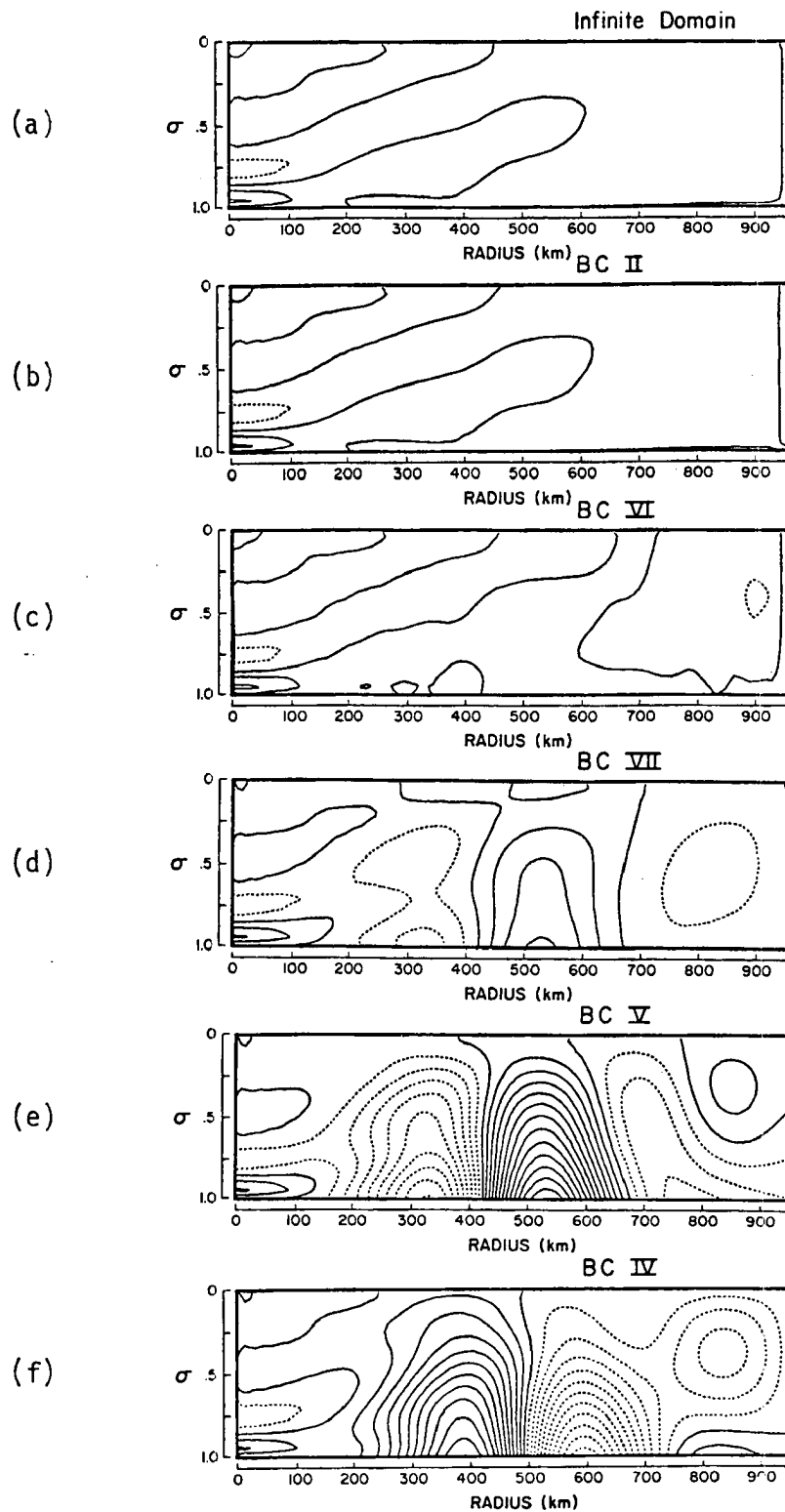
Figure 3.10 The vertical motion field ω at t=6 hrs for the fully
stratified initial value experiments employing (a)
'infinite domain', (b) boundary condition II, (c)
boundary condition VI, (d) boundary condition VII,
(e) boundary condition V and (f) boundary condition IV.
The contour interval is 2.5 mb/day with dashed lines
indicating sinking motion.

asymptotically valid as $k \to \infty$, and that in this case f can be eliminated, we can linearize (2.2)-(2.7), assume a solution of the form

$$
\begin{Bmatrix} u(r,\sigma,t) \\ T(r,\sigma,t) \\ \pi(r, t) \end{Bmatrix} = \begin{Bmatrix} \hat{u}(\sigma)[H_1^{(1)}(kr) + R\, H_1^{(2)}(kr)] \\ \hat{T}(\sigma)[H_0^{(1)}(kr) + R\, H_0^{(2)}(kr)] \\ \hat{\pi}\,[H_0^{(1)}(kr) + R\, H_0^{(2)}(kr)] \end{Bmatrix} e^{-i\nu t} , \qquad (3.38)
$$

and obtain

$$
i\,\frac{\nu}{k}\,\hat{u} + \int_\sigma^1 \overline{\pi}\,\overline{\alpha}\left(\frac{\hat{T}}{\overline{T}} + \frac{p_T}{\overline{P}}\,\frac{\hat{\pi}}{\overline{\pi}}\right) d\sigma' + \sigma\overline{\alpha}\hat{\pi} = 0 , \qquad (3.39)
$$

$$
i\,\frac{\nu}{k}\,\hat{T} - \frac{d\overline{T}}{d\sigma}\,\sigma \int_0^1 \hat{u}\,d\sigma + \left(\frac{d\overline{T}}{d\sigma} - \frac{\overline{\pi}\,\overline{\alpha}}{c_p}\right) \int_0^\sigma \hat{u}\,d\sigma' = 0 , \qquad (3.40)
$$

$$
i\,\frac{\nu}{k}\,\hat{\pi} - \overline{\pi} \int_0^1 \hat{u}\,d\sigma = 0 . \qquad (3.41)
$$

In practice we follow the above procedure with the governing equations in differential-difference form (radius and time being continuous, sigma discrete). Then the above integrals become sums and we can regard the resulting problem as an algebraic eigenvalue problem, with $\frac{\nu}{k}$ as the eigenvalue. This procedure is summarized for our axisymmetric model in Appendix E. For a vertically discrete model atmosphere with N velocity levels (3.39)-(3.41) yields a system of either 2N or 2N+1 vertically discrete equations depending on whether the temperature levels are staggered. For Lorenz (1960) type vertical differencing schemes (non-staggered temperature as in the present study) there are 2N+1 vertically discrete equations. This allows the mass field one additional degree of freedom which is not under the control of the geostrophic adjustment process. Although the results presented
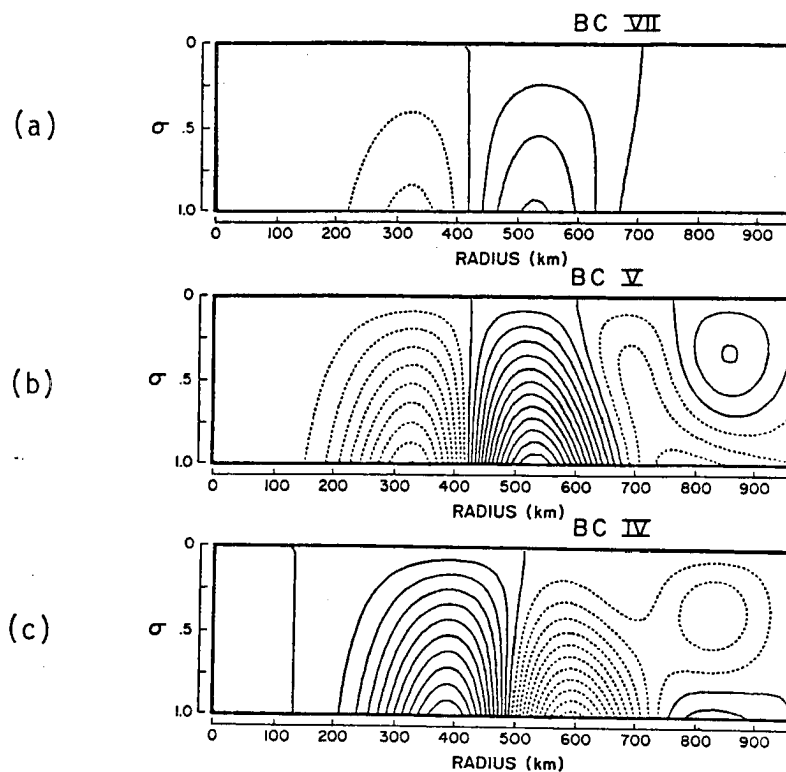
BC VII

(a)

BC V

(b)

BC IV

(c)

Figure 3.11   The reflected vertical motion field at t=6 hrs for
the fully stratified initial value experiments
employing (a) boundary condition VII, (b) boundary
condition V and (c) boundary condition IV.   The
contour interval is 2.5 mb/day with dashed lines
indicating sinking motion.

here are from a model with Lorenz type vertical differencing, the extra degree of freedom in the mass field does not seem to be any problem. The set of eigenvectors obtained from the discrete versions of (3.39)-(3.41) is not orthogonal, but this poses no difficulty with respect to the projection process since it is easy to calculate from the transpose of the matrix a set of eigenvectors which are orthogonal to the original set (e.g. Twomey, 1977, Chapter 4).

For a numerical experiment we again consider an initial value problem in which a Gaussian perturbation is introduced in the π or surface pressure field. Thus, the initial π field is of the form

$$\pi(r,0) = \bar{\pi} - Ae^{-(r/r_0)^2}, \qquad (3.42)$$

where $r_0 = 150$ km, $A = 1$ mb and $\bar{\pi}$ is a specified constant. The initial temperature field is independent of radius along constant σ surfaces and the initial motion field is identically zero.

A control experiment is first conducted for which the lateral boundary is moved to 3840 km in order to exclude boundary effects on the numerical solution in the interior 960 km. The vertical motion field at $t = 6$ hrs is displayed for all the experiments in Fig. 3.10. Fig. 3.10a, which corresponds to the control or infinite domain experiment, is the desired result, and indicates that only relatively small amplitude (high vertical wave number) motions remain in the computational domain at this time. Boundary conditions II and VI (Figs. 3.10b and 3.10c) appear to give results closest to the control experiments with boundary conditions IV and V (Figs. 3.10e and 3.10d) deviating significantly from the control. Fig. 3.11 illustrates the reflected vertical motion field for boundary conditions VII, V and IV
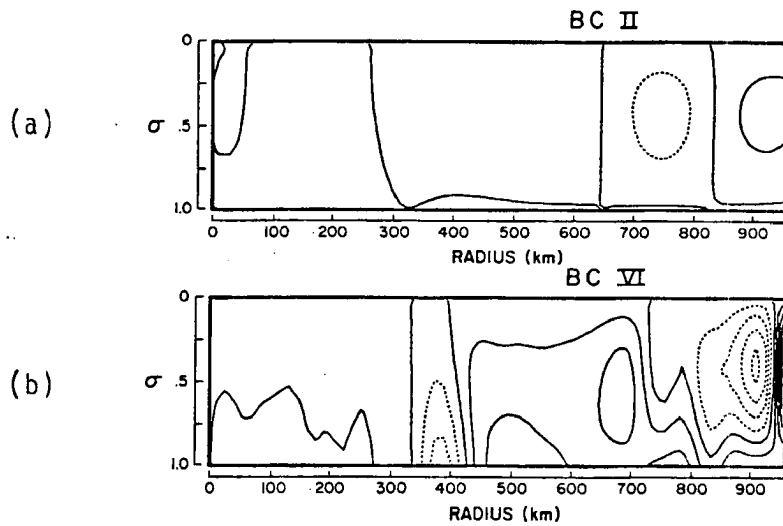
BC II

(a)

BC VI

(b)

Figure 3.12   The reflected vertical motion field at t=6 hrs for
the fully stratified initial value experiments
employing (a) boundary condition II and (b) boundary
condition VI. The contour interval is 0.25 mb/day
with dashed lines indicating sinking motion.

where the contour intervals are 2.5 mb/day. Since the reflections for boundary conditions II and VI are much smaller, they are given separately in Fig. 3.12 where the contour interval is reduced by a factor of ten to 0.25 mb/day. For the cases of zero radial wind (Fig. 3.11b) and zero divergence (Fig. 3.11c) we see that the external mode and first internal mode have reached the boundary and have been reflected[1]. Boundary condition VII gives much better results than either of these since the amplitude of the external mode is significantly reduced, and very little of the first internal mode is reflected. These results should be expected since the constant phase speed has been chosen to be representative of the first internal mode. The theoretical reflectivity for boundary condition VII can be calculated for each vertical mode and reveals that the choice of a single phase speed results in large reflectivities for all vertical modes except for those modes which propagate at a rate which is close to the chosen c. This result appears to be independent of the choice of c, suggesting a fundamental weakness in choosing a constant phase speed to represent all waves.

The reflected vertical motion fields shown in Fig. 3.12 indicate that boundary condition VI gives stronger reflection than does boundary condition II. In addition, a considerable amount of computational noise is introduced into the reflected wave by boundary condition VI. This is more easily seen in Fig. 3.13 for which the reflected vertical motion field at $t = 6$ hrs along the $\sigma = 0.778$ surface has been plotted for both boundary conditions II and VI. An interesting and perhaps serious difference is illustrated in Fig. 3.14, which shows the domain

_____

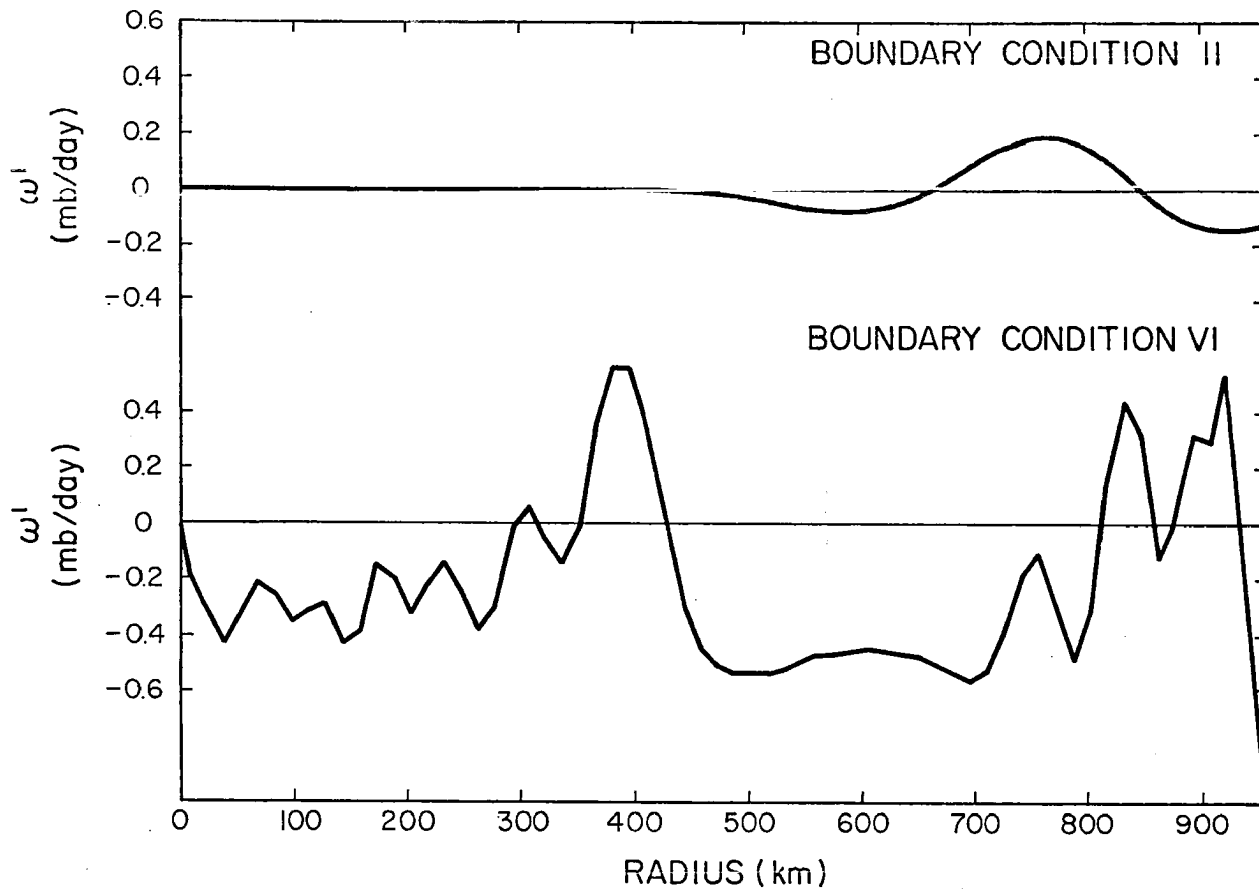[1]In fact, the external mode has been reflected three times, while the first internal mode has experienced only one reflection.

Figure 3.13 The reflected vertical motion field at t=6 hrs along the σ = 0.778 surface for fully stratified initial value experiments employing boundary condition II and VI.

averaged surface pressure as a function of time. We see that the use
of boundary condition VI results in a fictitious 'mass sink' for the
computational domain, a mass trend which could adversely impact long
term numerical integrations.

3.6 Summary of the Lateral Boundary Condition Analysis

In summary then, we believe that our analysis has demonstrated the
importance of properly formulating the lateral boundary condition in
tropical cyclone models, such that it does not reflect outward propa-
gating gravity-inertia waves. We have shown that it is possible to
derive approximate outgoing wave conditions (boundary conditions I-III)
for the fully stratified axisymmetric case. We have examined theoret-
ically the reflectivities of these three approximate conditions as
well as two other lateral boundary conditions in common use, the con-
ditions of zero divergence and zero radial wind (boundary conditions
IV and V). The results of this analysis show that boundary condition
I has the lowest reflectivity, although boundary condition II, which
is much easier to implement, is nearly as good for the lower order
vertical modes. It is also clear from our analysis that the condition
of zero divergence is not in the true sense an 'open' lateral boundary
condition since it results in unit reflection of gravity-inertia waves.
In this regard, it is as poor a boundary condition as the condition
of zero radial wind, which also gives unit reflection.

The behavior of two other lateral boundary conditions has been
examined numerically. These are the method proposed by Orlanski (1976)
(boundary condition VI) and the method proposed by Klemp and Wilhelmson
(1978) (boundary condition VII). The basic problem with the latter
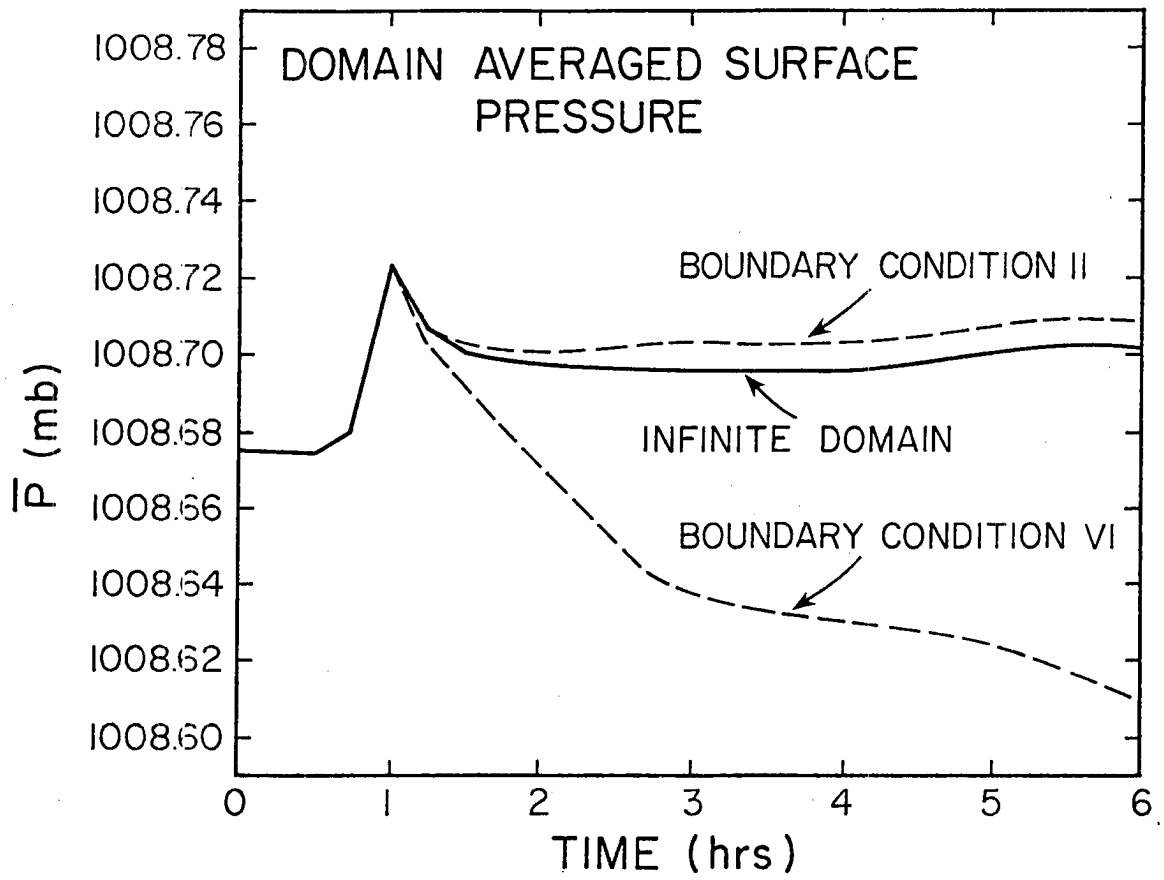approach in tropical cylcone models is the choice of a single phase

Figure 3.14   The domain averaged surface pressure field as a func-
tion of time for the fully stratified initial value
experiments employing the infinite domain, boundary
condition II and boundary condition VI.

speed to represent all waves. Only those waves moving at or very near this phase speed will be treated properly, and since there is such a wide range of propagation speeds in a stratified model, it is difficult to 'tune' the choice of this constant phase velocity. However, in the situation where an external mode does not occur, or where the amplitude spectrum of the vertical modes in the model has a narrow distribution, boundary condition VII may give fairly good results.

Although there is some reflection (5-15%) associated with boundary condition VI, it produces results which appear to closely approximate those of the control experiment. We believe, however, that there are several difficulties associated with boundary condition VI. Since this method is applied level by level it may have difficulty when two or more vertical modes (moving at different phase velocities) reach the boundary simultaneously. This vertically independent specification of the lateral boundary condition in a hydrostatic model is questionable from a theoretical viewpoint since the results of sections 3.2 and 3.4 would suggest that the boundary condition should be applied to each vertical mode. For the examples we have examined, the numerical estimates of the phase velocity c tend to vary considerably, which introduces noise into the computational domain. In addition we have experienced fictitious mass trends when using boundary condition VI.

Consequently, we have chosen to use lateral boundary condition II in the axisymmetric tropical cyclone model discussed in chapter 2. Although this boundary condition has been shown to give reasonably good results in the fully stratified case, it is by no means perfect. It includes both the asymptotic approximation for Hankel functions and the pure gravity wave approximation for the gravity-inertia wave

frequency. Better results could undoubtedly be obtained by using boundary condition I, but this involves a spectral representation in the horizontal as well as the vertical. Although present tropical cyclone models are all based on grid point methods, it would appear that models with spectral representations in both the horizontal and vertical would have distinct advantages.

4.0 SPECIFICATION OF INITIAL CONDITIONS

4.1 Initialization Procedure

To begin integration of the model, initial conditions on the prognostic variables π, u, v, T and q must be specified. We shall assume that initially there is no transverse circulation, i.e., u = 0 everywhere, that the π, v and ϕ fields are in gradient wind balance. Since the π, v, T and ϕ fields are initially related by hydrostatic and gradient wind balance, specification of the initital v field allcws computation of the initial π and T fields. Applying gradient wind balance at the sea surface we obtain

$$\left(f + \frac{v_S}{r} \right) v_S = RT_S \frac{\partial \ell n p_S}{\partial r} \quad \text{at } \sigma = 1 \ , \tag{4.1}$$

where $\frac{\partial \phi}{\partial r}$ disappears since ϕ is zero in the model everywhere along the $\sigma = 1$ surface. Knowing v_S and T_S everywhere, (4.1) allows computaticn of p_S, and hence π, provided an outer boundary condition on p_S has been specified.

The gradient wind equation at an interior point takes the form

$$\left(f + \frac{v}{r} \right) v = \frac{\partial \phi}{\partial r} + \sigma \alpha \frac{\partial \pi}{\partial r} \ . \tag{4.2}$$

Differentiating (4.2) with respect to sigma and using the hydrostatic equation, we obtain the thermal wind relation in the σ-coordinate

$$\sigma \frac{\partial \pi}{\partial r} \frac{\partial \alpha}{\partial \sigma} - \pi \frac{\partial \alpha}{\partial r} = \frac{\partial}{\partial \sigma} \left[\left(f + \frac{v}{r} \right) v \right] \ . \tag{4.3}$$

Since π and v are known, (4.3) can be regarded as a first order partial differential equation in α. Knowledge of α at the sea surface and at the outer boundary allows us to solve for α at all interior points, after which T can be determined from the ideal gas law. The
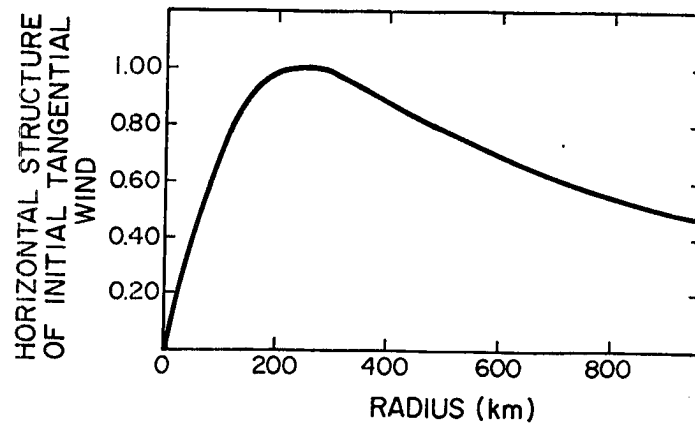
Figure 4.1 Horizontal structure of the initial
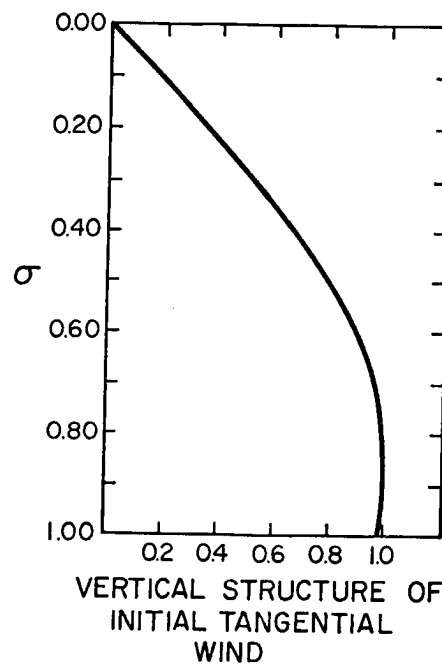tangential wind.

Figure 4.2 Vertical structure of the initial
tangential wind.

exact form of the initial tangential wind distribution is discussed in the next section, as is the initial condition on water vapor.

4.2 Initial Conditions on Wind, Temperature and Moisture

The initialization procedure described in section 4.1 requires the specification of an initial tangential wind as well as an initial outer boundary temperature profile and surface pressure p_s. The initial tangential wind is specified to be the product of a horizontal struc-ture term and a vertical structure term

$$v(r,\pi,0) = \hat{v}\left[\frac{2(r/\hat{r})}{1+(r/\hat{r})^2}\right]\left[\frac{3(\sigma/\hat{\sigma})}{2+(\sigma/\hat{\sigma})^3}\right], \qquad (4.4)$$

where $\hat{v}$ is the maximum amplitude. The horizontal structure is identi-cal to that used by Ooyama (1969a), and is shown in Fig. 4.1 for $\hat{r} = 240$ km. The vertical structure is shown in Fig. 4.2 for $\hat{\sigma} = 0.861$. Using a value of 7 m/s for $\hat{v}$ gives the initial tangential wind field shown in Fig. 4.3. This initial condition on wind is used for all of the numerical integrations conducted in this study.

The initial temperature profile at the model boundary (which is also used for all of the numerical integrations presented) corresponds to the mean tropical clear profile of Gray et al. (1975) (see Fig. 4.4). Using this temperature profile, and a value of 1008.7 mb for p_s at the model boundary, gives the initial temperature deviation field shown in Fig. 4.5, and the initial surface pressure distribution plotted in Fig. 4.6.

Two different initial moisture fields are used in this study, the first of which specifies the water vapor mixing ratio to be independent of radius, with the vertical dependence corresponding to the mean tropical 'cluster environment' profile of Gray et al. (1975). This
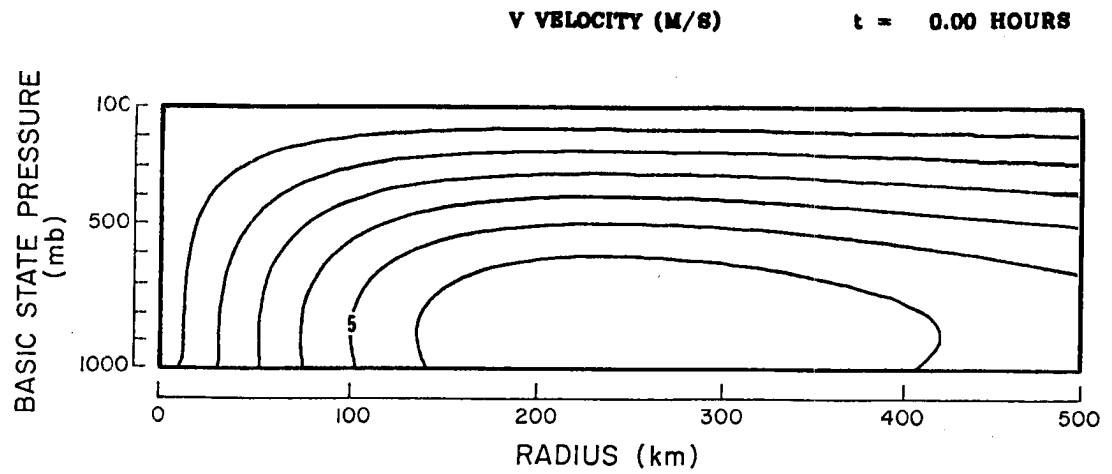
Figure 4.3 The initial tangential wind field. The contour interval is 1 m/s (the 5 m/s isoline is labelled for reference).
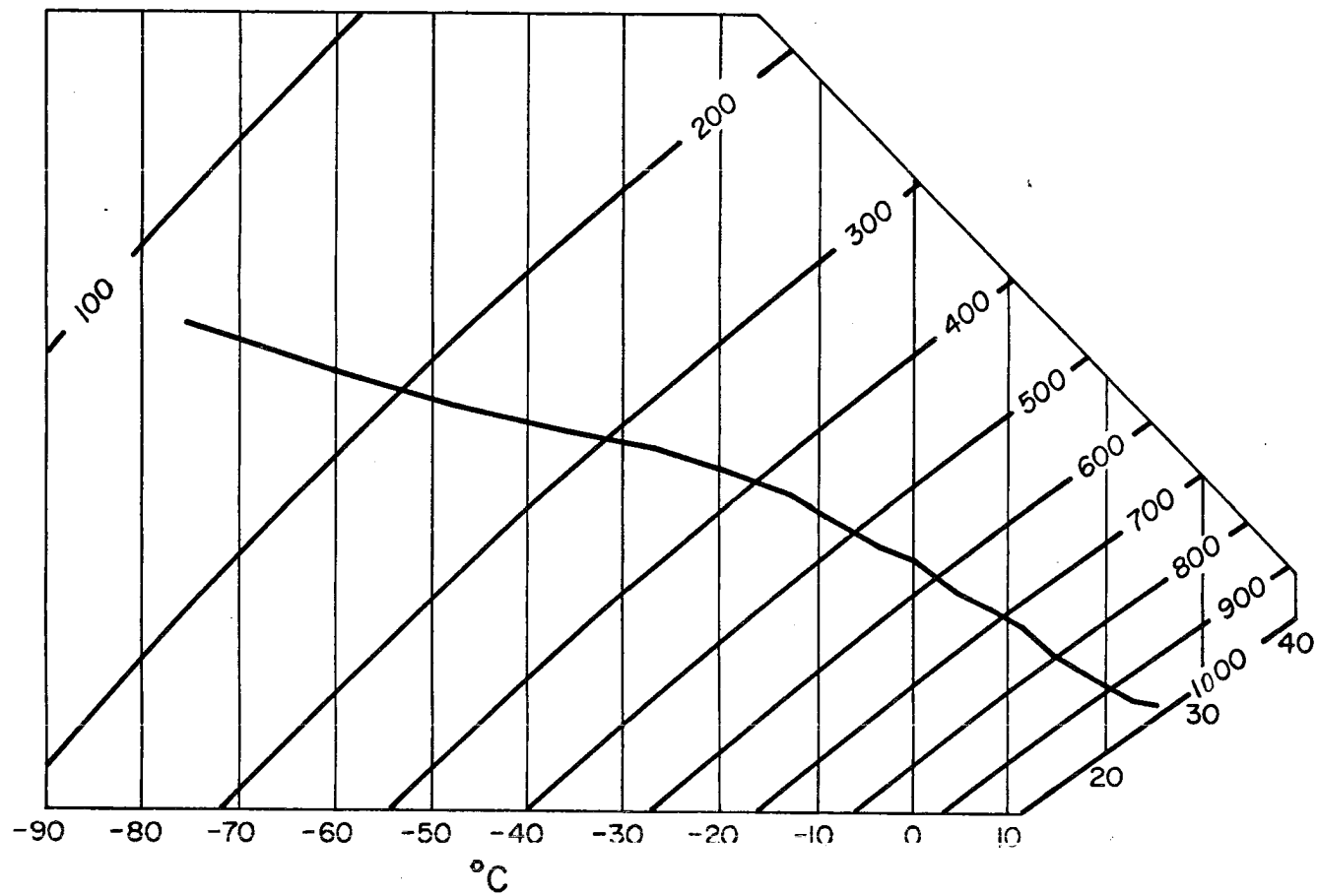
Figure 4.4   The initial outer boundary temperature profile
(after Gray et al., 1975).
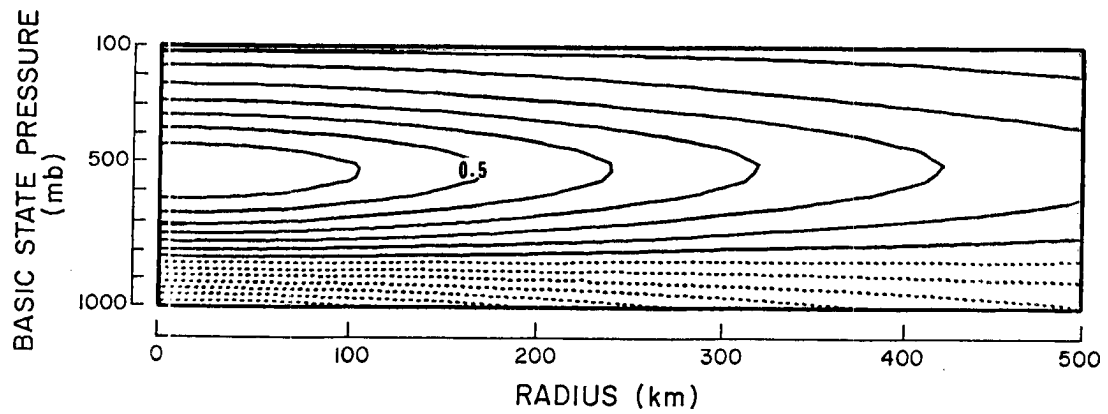
TEMPERATURE PERTURBATION (K)   t =   0.00 HOURS

Figure 4.5   The initial temperature deviation field. The
contour interval is 0.1°C (the 0.5°C isoline is
labelled for reference).
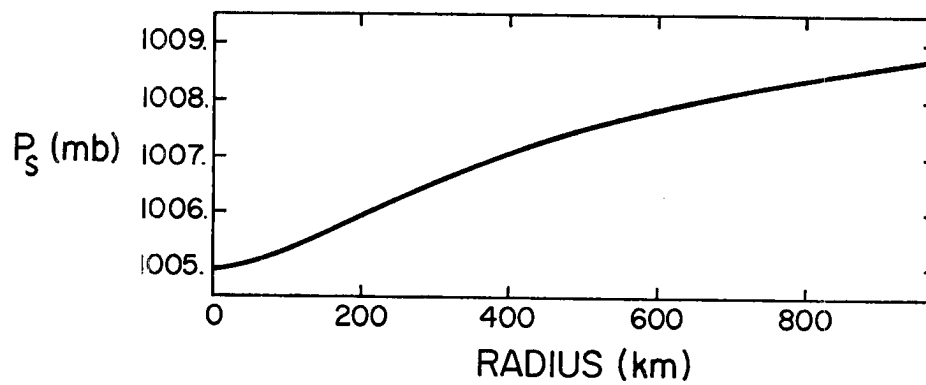
Figure 4.6   The initial surface pressure distribution.

RELATIVE HUMIDITY   **t = 0.00 HOURS**
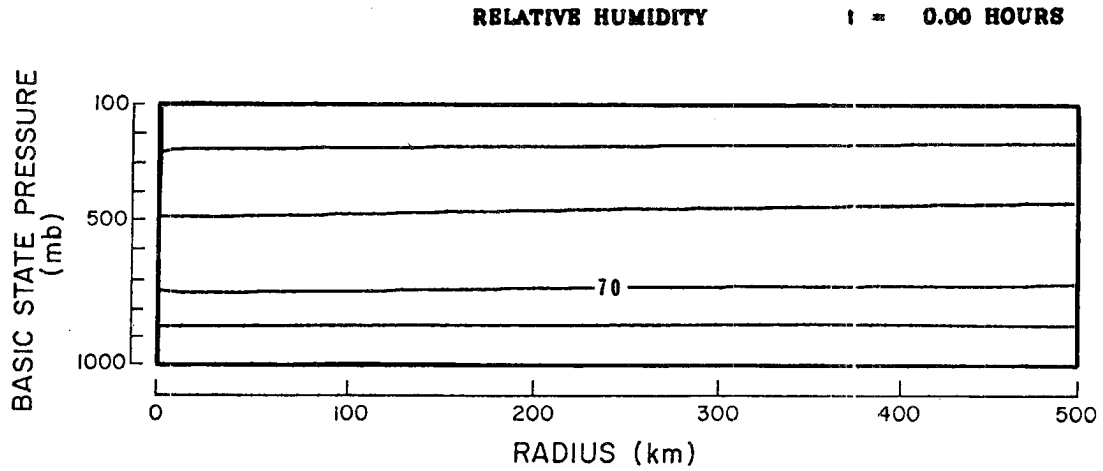
Figure 4.7   The initial relative humidity field for the moisture field which is a function of σ only, and corresponds to the mean tropical 'cluster environment' profile of Gray et al. (1975). The contour interval is 10%.

RELATIVE HUMIDITY   **t = 0.00 HOURS**
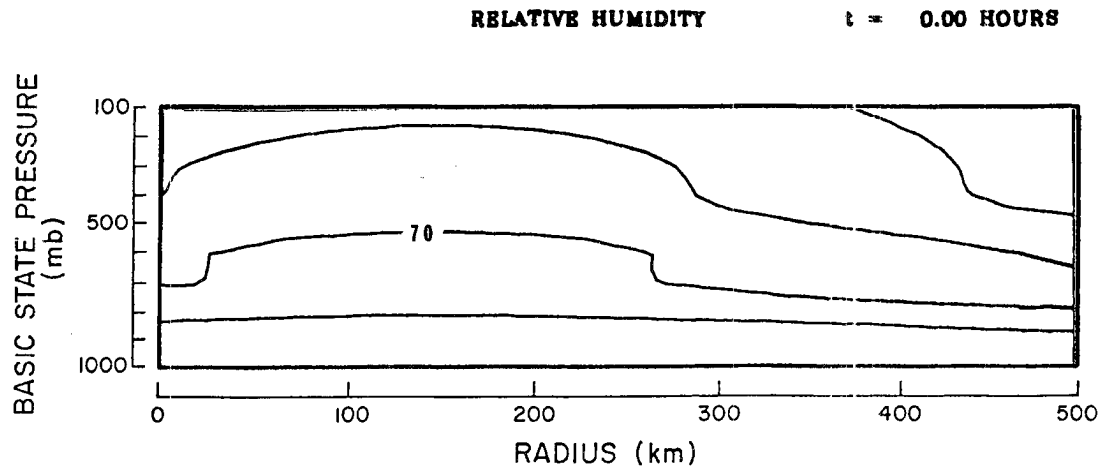

Figure 4.8   The initial relative humidity field for the moisture distribution which is a function of both r and σ. The relative humidities in the interior correspond more closely to the mean tropical 'cluster region' humidities of Gray et al. (1975). The contour interval is 10%.

leads to the initial relative humidity field shown in Fig. 4.7. The second initial moisture distribution is specified to be both a function of r and of σ such that the initial relative humidity is more realistic. At the outer boundary, the vertical distribution of relative humidity corresponds to the mean tropical 'clear region' relative humidity profile given by Gray et al. (1975) while the interior regions correspond more closely to the mean tropical 'cluster region' relative humidities (see Fig. 4.8).

4.3 Selection of the Critical Cloud Work Function

The computational procedure for determining the cloud base mass flux distribution in the Arakawa-Schubert cumulus parameterization theory which is outlined in section 2.2.3 (the optimal adjustment method) involves an adjustment process. For computational simplicity, this adjustment to the time dependent cloud work function is formulated with respect to a 'critical cloud work function' $A_c(\hat{p})$ such that the cumulus ensemble is always attempting to insure that $A(\hat{p},t) < A_c(\hat{p})$. This approach may not be so unreasonable since Lord (1978) has obtained similar (non-zero) values of the cloud work function $(A(p_D))$ for a variety of synoptic conditions. In any event, we believe that the results should not be highly sensitive to the critical cloud work function since, once $A(\hat{p})$ exceeds $A_c(\hat{p})$, the cumulus ensemble in effect responds to $\left.\frac{\partial A(\hat{p})}{\partial t}\right|_{L.S.}$. Therefore, a careful selection of $A_c(\hat{p})$ (so as not to substantially exceed the cloud work function of the initial condition) should minimize the impact of using a critical cloud work function.

The cloud work function was calculated for the initial distribution of temperature and moisture at the boundary of the model. The

$$A_c(\hat{p}) \ (J/kg)$$
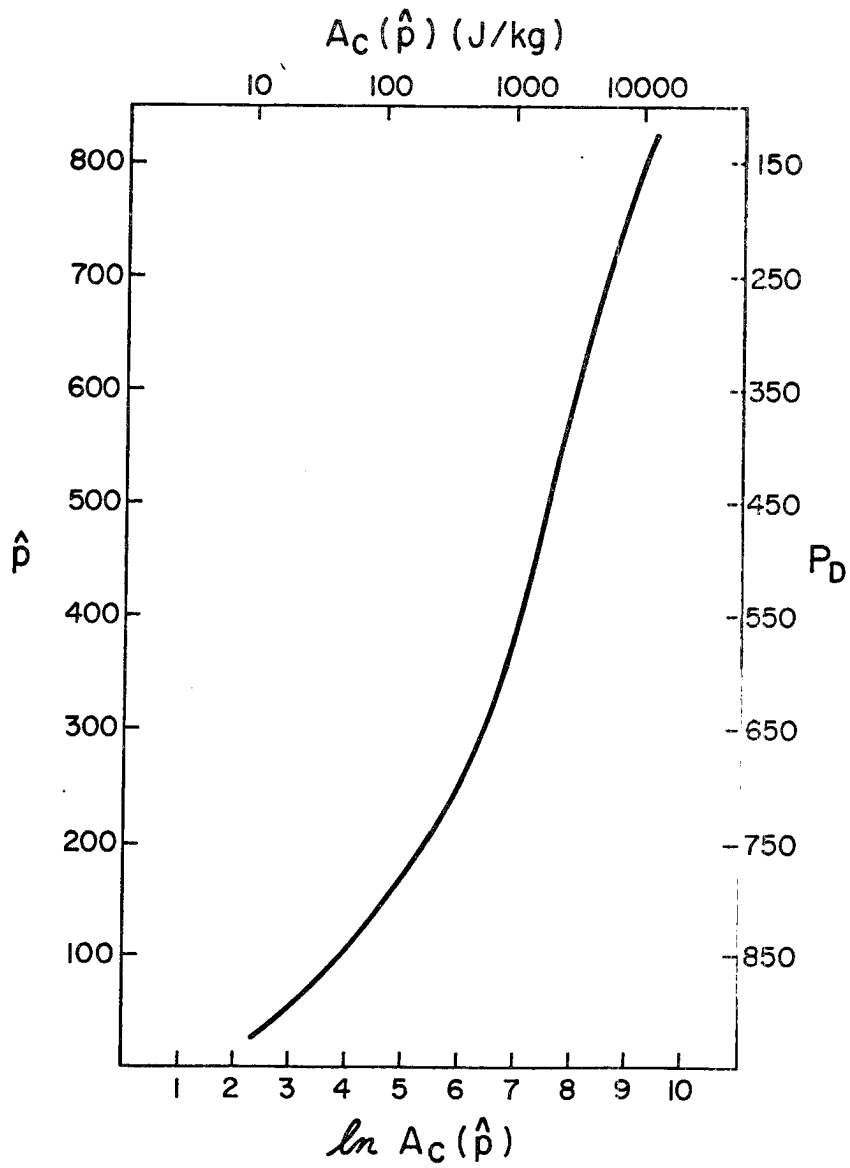
Figure 4.9 The critical cloud work function $A_c(\hat{p})$.
For a constant surface pressure of 1000 mb,
this can be interpreted in terms of detrain-
ment pressure p_D as labelled on the right hand
side of the diagram.

critical cloud work function $A_c(\hat{p})$ was then determined such that $A_c(\hat{p}) > A(\hat{p})$ for all $\hat{p}$ at the model boundary (see Fig. 4.9). This choice of $A_c(\hat{p})$ proves to be sufficiently large so that convection does not spontaneously begin anywhere in the model during the initial few time steps.

5.0 EXAMPLES OF THE SENSITIVITY OF MODEL STORM DEVELOPMENT TO THE INITIAL CONDITION, THE LATENT HEAT RELEASE MECHANISM, AND THE LATERAL BOUNDARY CONDITION

In the next two chapters we will discuss some of the numerical results we have obtained using the tropical cyclone model described in chapter 2. Eleven different experiments designed to test the sensitivity of the model are examined. These experiments are listed in the cross reference Table 5.1. In this chapter, we consider the sensitivity of model storm development to the initial condition on the moisture field (IC1 and IC2), to the explicit release of latent heat, and to three of the lateral boundary conditions discussed in chapter 3 (BCII, BCIV, and BCV). The remaining numerical experiments, which deal with the sensitivity of tropical cyclone development to the incorporation of longwave radiation and cumulus momentum transport, are considered in chapter 6. All numerical experiments are conducted at a latitude of 20°N using a sea surface temperature of 301°K (27.85°C).

5.1 Sensitivity to the Initial Distribution of Moisture

The effect of the initial distribution of water vapor on the numerically simulated development of a tropical cyclone was first addressed by Rosenthal (1970). In his tropical cyclone model, as in ours, the initial condition on wind is one of gradient wind balance, and no initial radial circulation. Consequently, an organizational period is required for such a circulation to develop. Rosenthal's numerical results indicated that a marked decrease in this organizational period could be achieved by increasing the initial relative humidity. We also have examined the sensitivity of our model storm development to the initial moisture distribution and have obtained qualitatively similar results which are discussed below.

	EXPLICIT RELEASE OF LATENT HEAT	PARAMETERIZED HEAT RELEASE				
		No Radiation No Momentum Transport	Radiation No Momentum Transport	No Radiation Momentum Transport	Radiation Momentum Transport	
IC1	AA9	AB1	—	—	—	BCII
	AA4	AB4	AD1	AE1	AF1	BCII
IC2	AA5	AB5	—	—	—	BCIV
	AA6	AB6	—	—	—	BCV
	Discussed in Chapter 5	Discussed in Chapter 6				

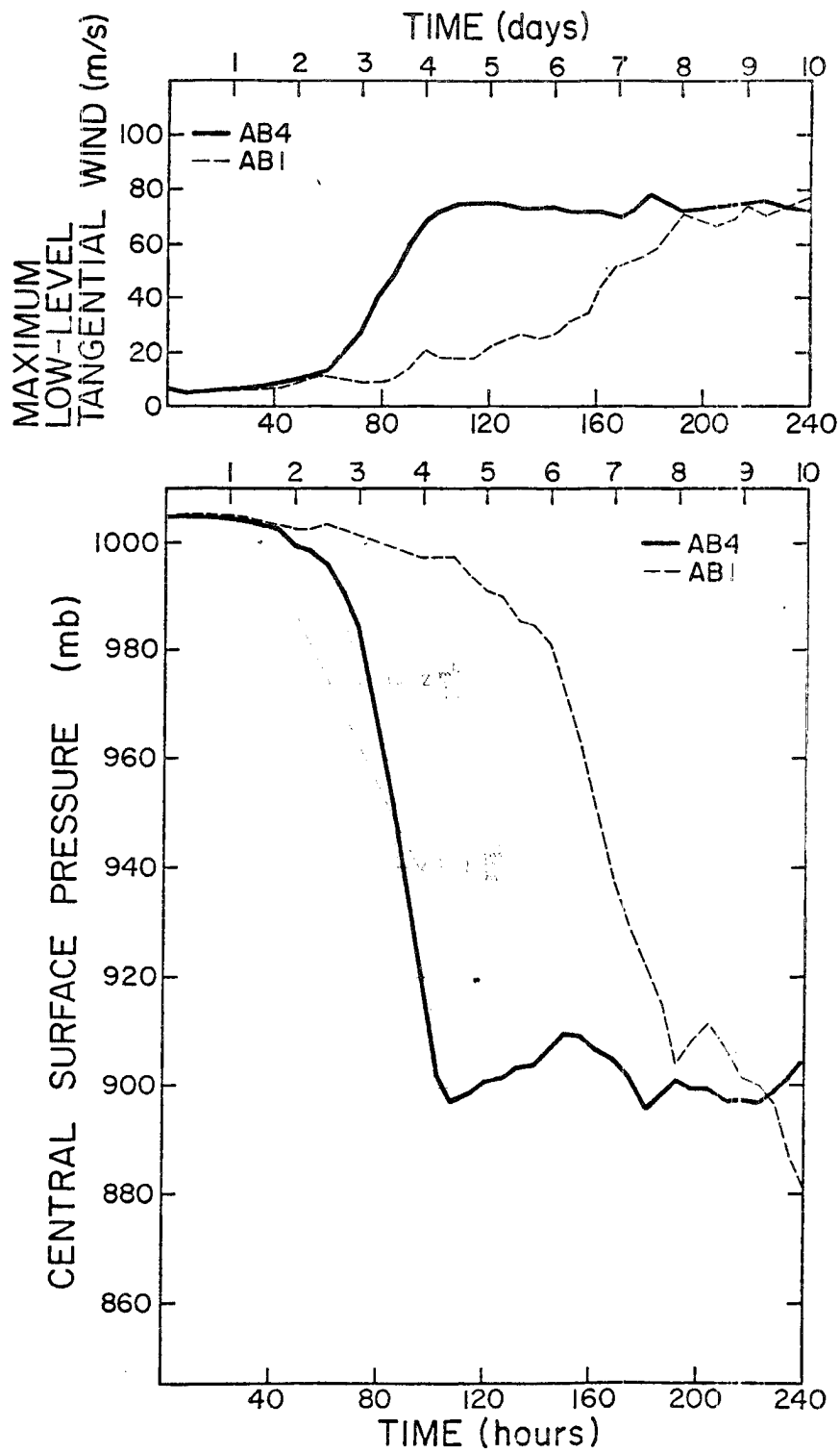Table 5.1   Cross reference table for the numerical experiments presented in chapters 5 and 6.

Figure 5.1   The time evolution of the maximum low level
(z ∿ 225 m) tangential wind and central sur-
face pressure for experiments AB1 and AB4.

As was shown in chapter 4, two initial conditions on the moisture field were considered in this study. The first, which we shall refer to as IC1, specifies the initial water vapor mixing ratio q to be a function of σ only, while the second (IC2) specifies the initial water vapor mixing ratio to be a function of both r and σ. Two numerical integrations were conducted using the Arakawa-Schubert cumulus parameterization and the two initial moisture distributions. Experiment AB1 uses the initial water vapor distribution given by IC1, while experiment A34 uses the initial water vapor distribution given by IC2. The development of the model storms are summarized in Fig. 5.1 which shows the time evolution of the maximum low level (z ~ 225 m) tangential wind and central surface pressure. A significant difference in the development times of the model storms is seen such that the use of IC1 results in considerably slower development. In terms of the time required to achieve hurricane force winds (33 m s^{-1}), experiment AB4 (IC2) takes 76 hours while experiment AB1 (IC1) requires an additional 80 hours.

The way in which each of the model storms develop is also strikingly different. Figs. 5.2 and 5.3 show the time behavior of the radius of maximum wind and the interior and exterior extent of the gale (22 m s^{-1}) and hurricane (33 m s^{-1}) force winds for experiments AB1 and AB4 respectively. In experiment AB4, a well defined radius of maximum wind moves slowly inward during the developing stages of the vortex to a radius of about 50 km once the storm is fully mature. On the other hand, experiment AB1 establishes a very broad tangential circulation with a large radius of maximum wind shortly into the
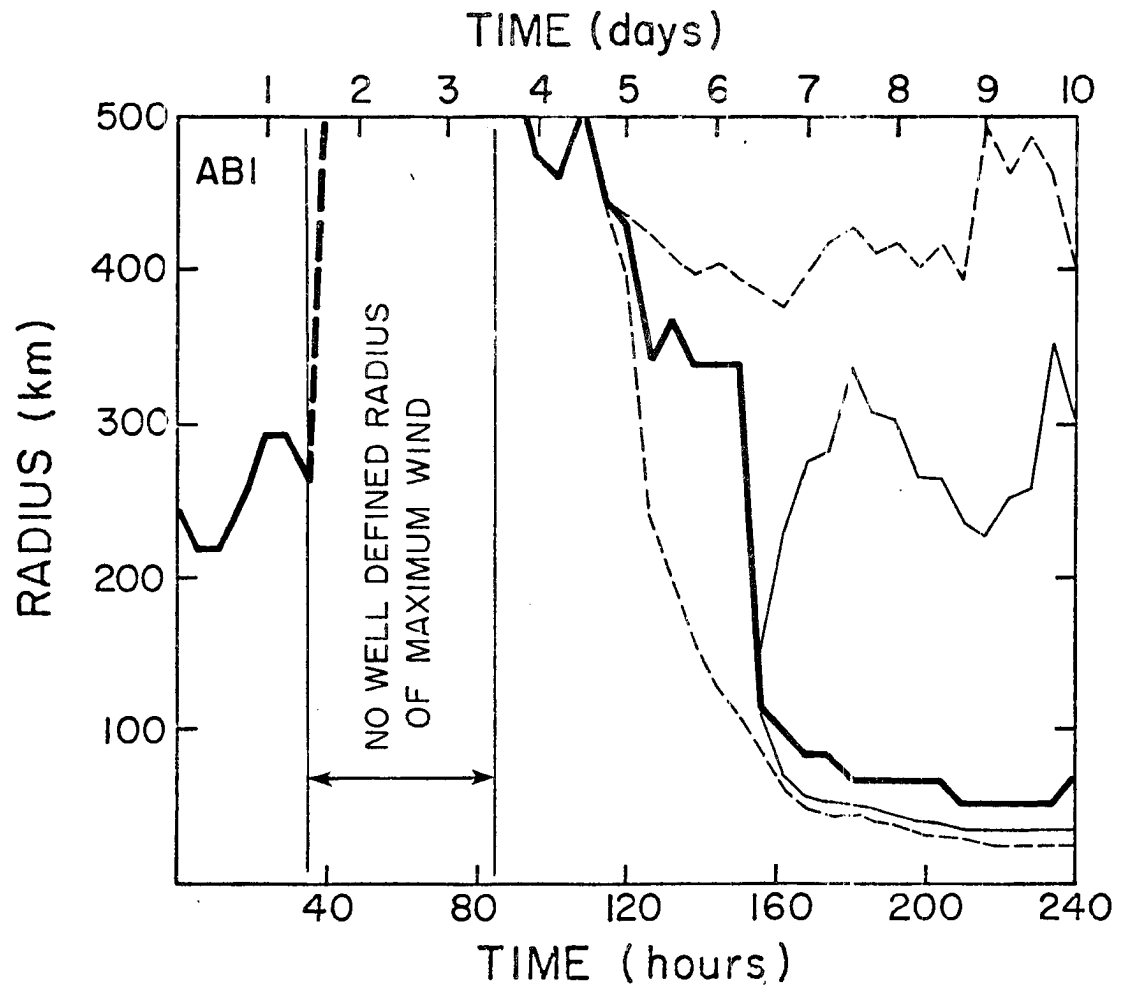
Figure 5.2   The time evolution of the radius of maximum
             winds (heavy solid line), and the horizontal
             extent of the gale (light dashed line) and
             hurricane (light solid line) force winds for
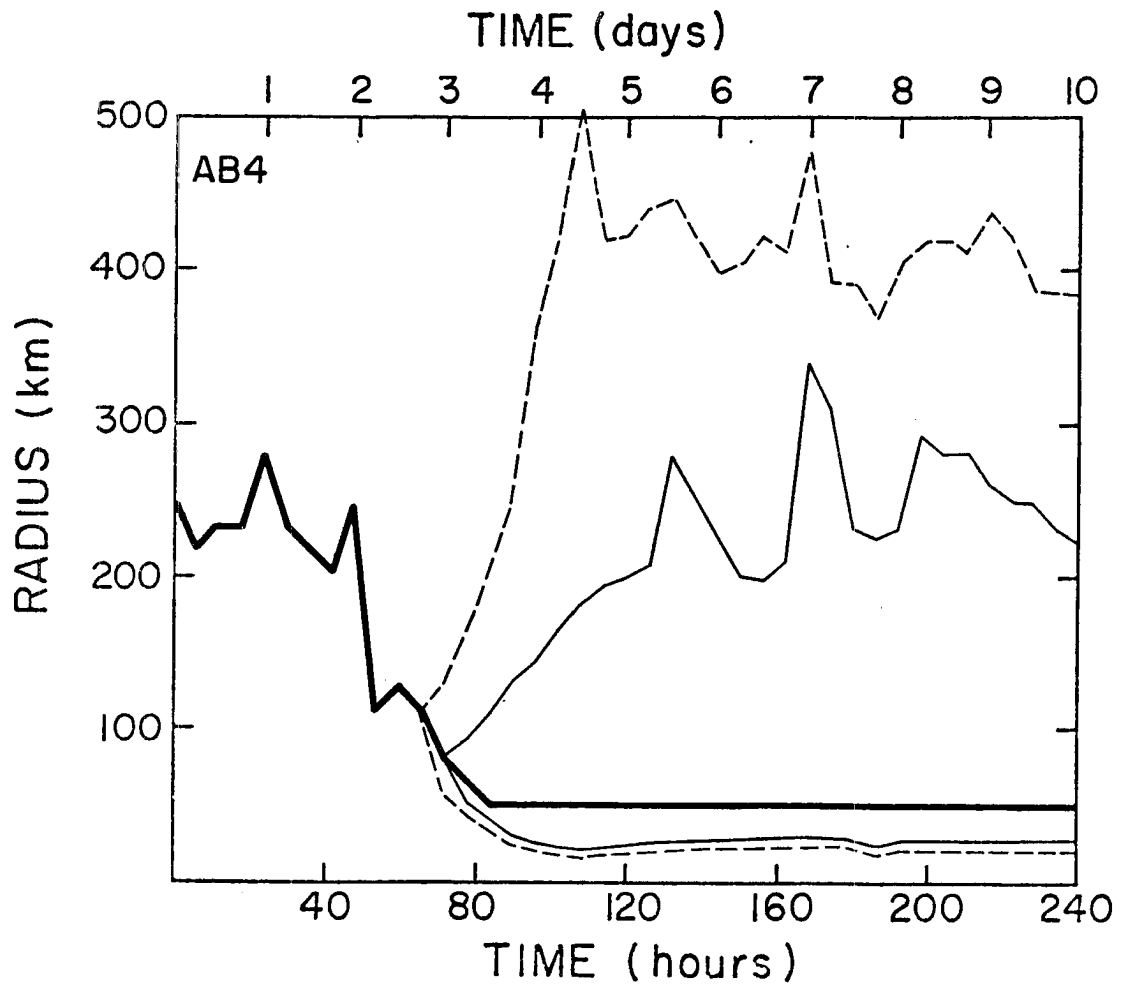   experiment AB1.

Figure 5.3 Same as Figure 5.2 but for experiment AB4.

numerical integration (36-48 hrs). This broad circulation pattern then moves very slowly inward over a period of about 6 days until a vortex which is similar in scale and intensity to AB4 is attained.

The unusual nature of the development of AB1 appears to be related to the horizontal distribution of the parameterized convection which in the early part of the numerical integration differs quite noticeably from experiment AB4. The time evolution of the cloud base mass flux distribution (Figs. 5.4 and 5.5) shows a weak uniform horizontal distribution of cumulus convection for AB1, while AB4 exhibits stronger cloud base mass fluxes which are confined to a narrower region inside 250 km. Thus, AB1 does not appear to have a preferred region for deep cumulus convection as does AB4. We believe that this difference can easily be explained to be a consequence of the initial water vapor distribution and the initial condition of gradient wind balance.

The cumulus ensemble predicted by the dynamic control is in response to a 'large-scale' forcing (which includes surface eddy fluxes). Because of the initial condition of gradient wind balance, the large-scale forcing of cumulus convection initially consists of surface eddy fluxes of heat and moisture coupled with weak low level convergence. Under such circumstances, deep cumulus convection can only be expected to take place if the large-scale environment is relatively moist. We note, however, that for the initial moisture distribution IC1, the interior regions of the initial disturbance are less moist in a relative sense than are the outer regions, and are consequently less favorable to deep convection. This is attributable to the warm core nature of the initial vortex.

EXPERIMENT AB1   CLOUD BASE MASS FLUX(KG/M**2/HR)   T =   6.00 HOURS

EXPERIMENT AB1   CLOUD BASE MASS FLUX(KG/M**2/HR)   T =   12.00 HOURS

EXPERIMENT AB1   CLOUD BASE MASS FLUX(KG/M**2/HR)   T =   18.00 HOURS

EXPERIMENT AB1   CLOUD BASE MASS FLUX(KG/M**2/HR)   T =   24.00 HOURS
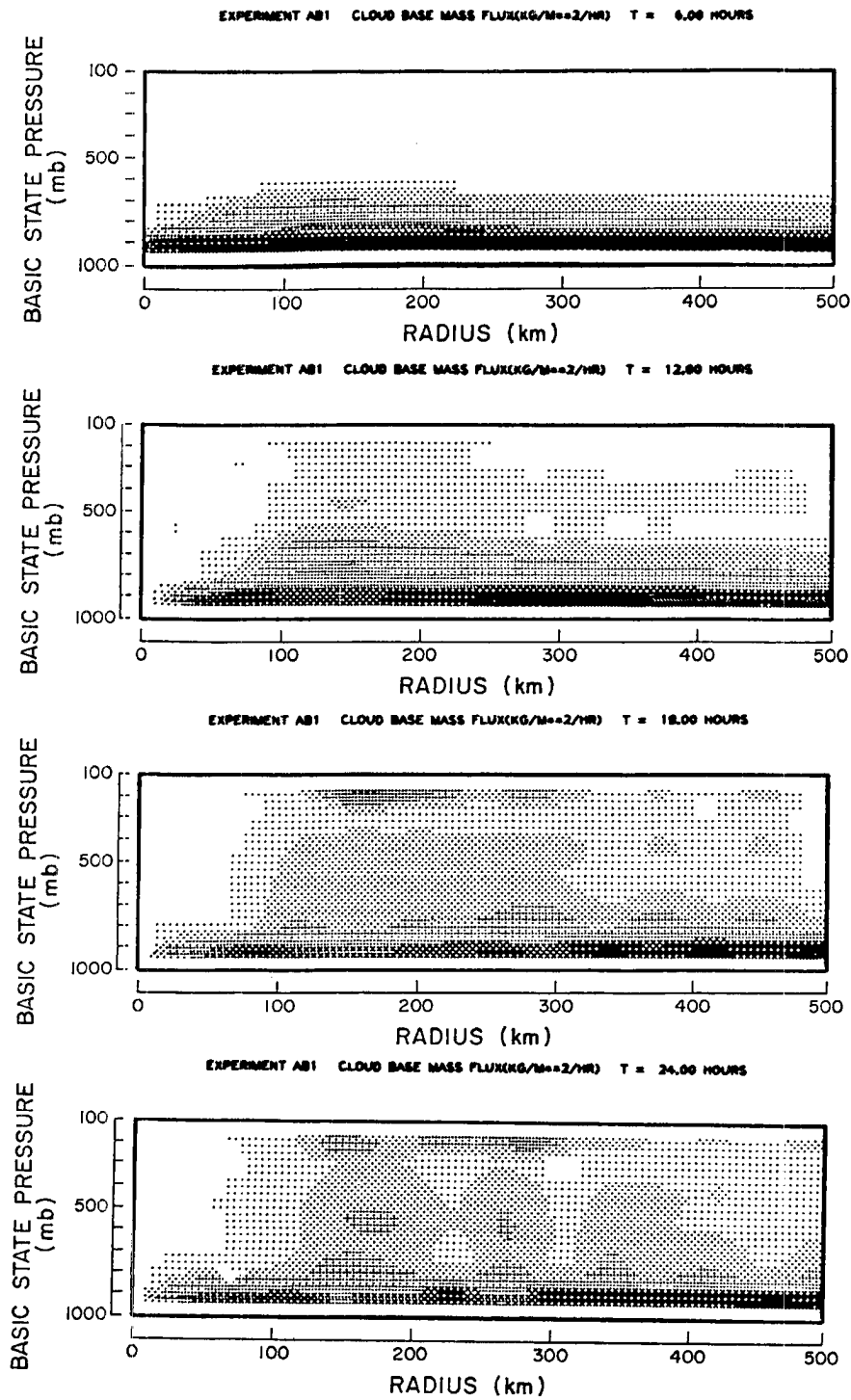
Figure 5.4   Cloud base mass flux distribution for experiment
AB1.   The intensity of the shading at any level
p is proportional to the cloud base mass flux
of the sub-ensemble detraining at that level.

EXPERIMENT AB4   CLOUD BASE MASS FLUX(KG/M==2/HR)   T =   6.00 HOURS

EXPERIMENT AB4   CLOUD BASE MASS FLUX(KG/M==2/HR)   T =   12.00 HOURS

EXPERIMENT AB4   CLOUD BASE MASS FLUX(KG/M==2/HR)   T =   18.00 HOURS

EXPERIMENT AB4   CLOUD BASE MASS FLUX(KG/M==2/HR)   T =   24.00 HOURS

Figure 5.5   Same as Figure 5.4 but for experiment AB4.

Fig. 5.6 shows the initial vertical profiles of moist static

energy h and saturated moist static energy h* at 30 km and 900 km for

both IC1 and IC2. It is clear that for IC1 the 900 km profile is more

unstable to moist convection than is the profile at 30 km. Thus, in

the absence of an organized large-scale circulation, it should not be

surprising that the cumulus convection predicted by the Arakawa-Schubert

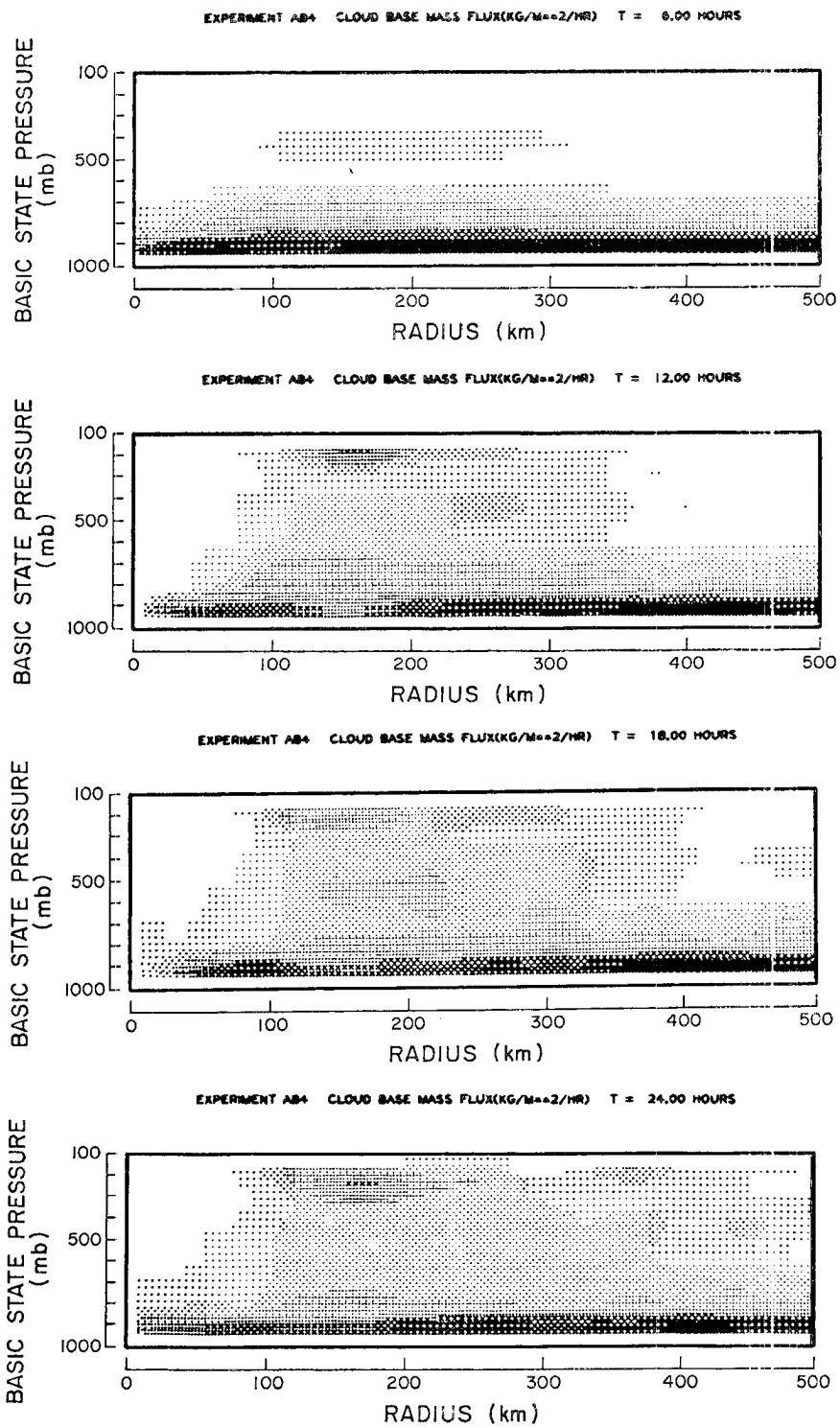scheme is so disorganized for experiment AB1.

The use of the more realistic initial moisture distribution IC2

provides a more favorable environment for deep cumulus convection in

the interior regions (see Fig. 5.5). We wish to emphasize, however,

that the increase in the water vapor mixing ratio in this region is

quite modest, with the largest increase less than 0.9 gm/kg (see Fig.

5.7). The most important aspect of IC2 appears to be the very dry

middle and upper level moisture distribution at large radius. This

tends to suppress or delay the onset of deep convection in the outer

regions until a large-scale radial circulation can be established. A

period of slow intensification occurs for about 60 hrs followed by

rapid deepening. The rate at which the model vortex deepens is similar

to results obtained with other axisymmetric models (e.g. Kurihara, 1975)

although the mature steady state storm which is produced by 96 hours is

somewhat deeper.

For purposes of comparison, we show the tangential wind, tempera-

ture perturbation, relative humidity, vertical motion and cloud base

mass flux fields at 120 hours in Fig. 5.8 and 5.9 for experiments AB1

and AB4 respectively. Fig. 5.8 shows a very broad and weakly organized

tangential circulation centered at large radius with a maximum in the
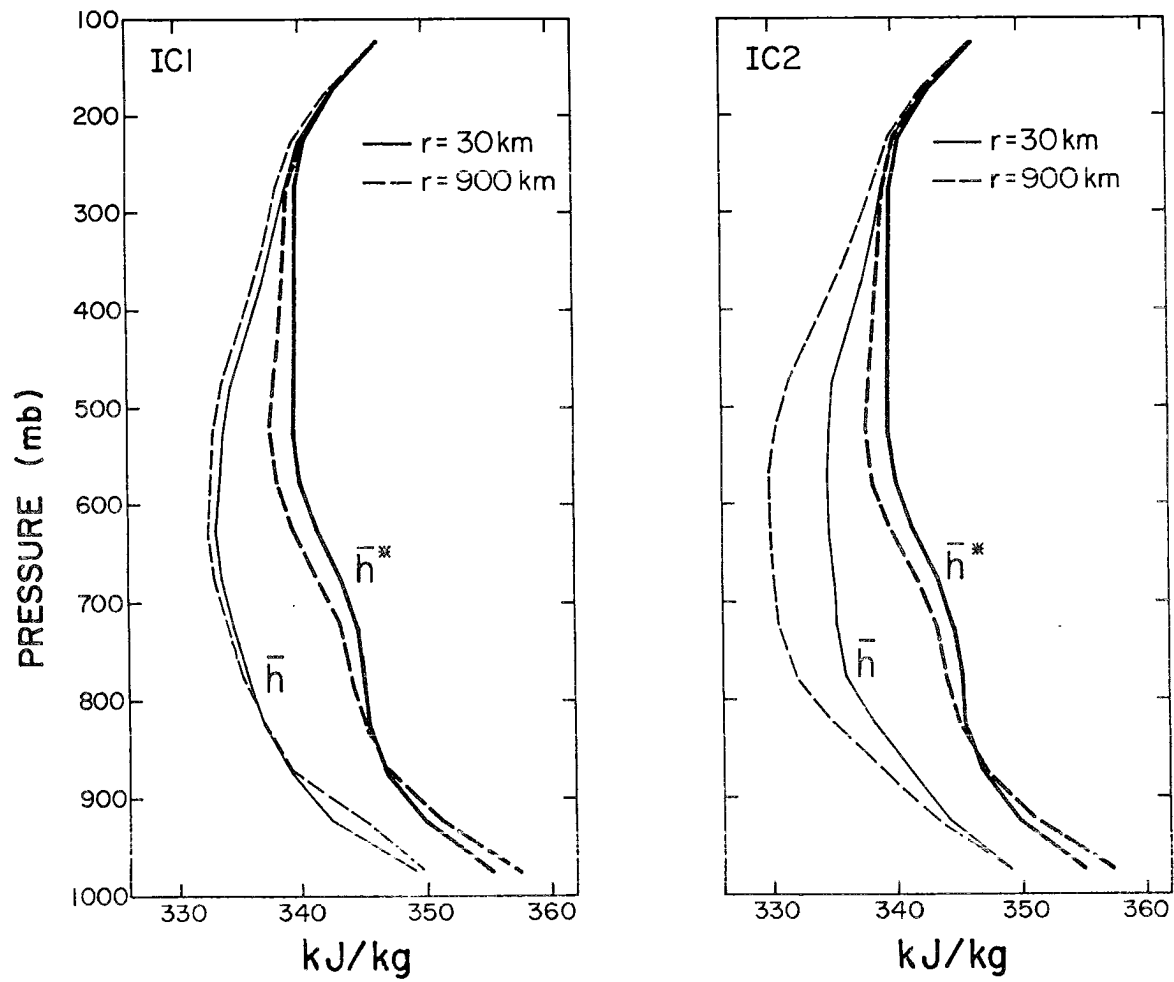
Figure 5.6 The initial profiles of moist static energy h and saturated moist static energy h* at 30 km and 900 km for initial moisture distributions IC1 and IC2.
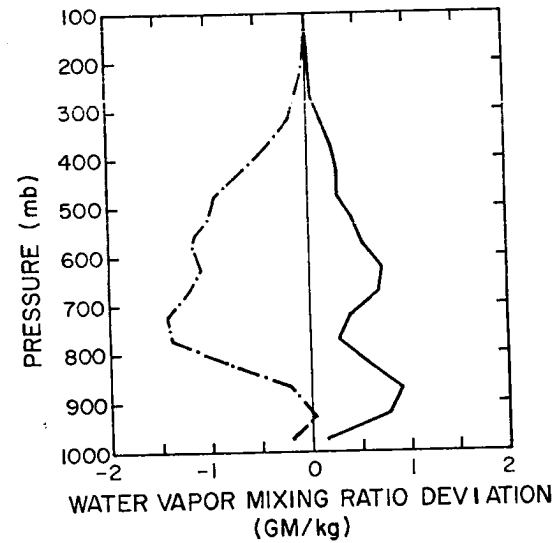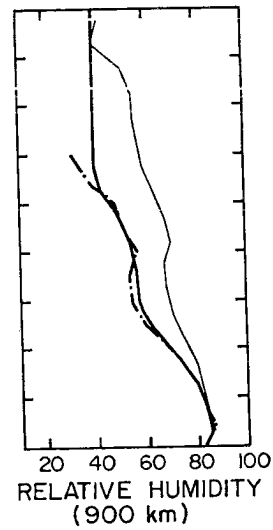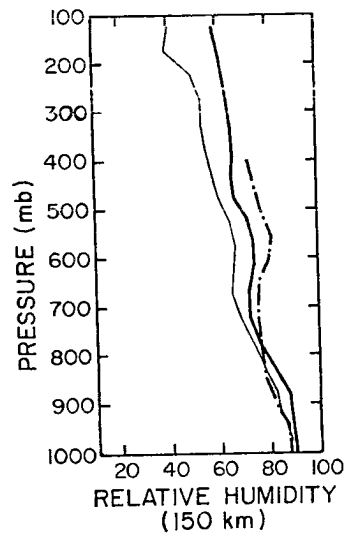
Figure 5.7. (a) The initial relative humidities at 150 and 900 km for IC1 (light solid), IC2 (dark solid), and the Gray et al., (1975) mean tropical 'clear' and 'cluster' observations.

(b) The deviation of the IC2 water vapor mixing ratio profile from the IC1 profile at 150 km (solid) and 900 km.
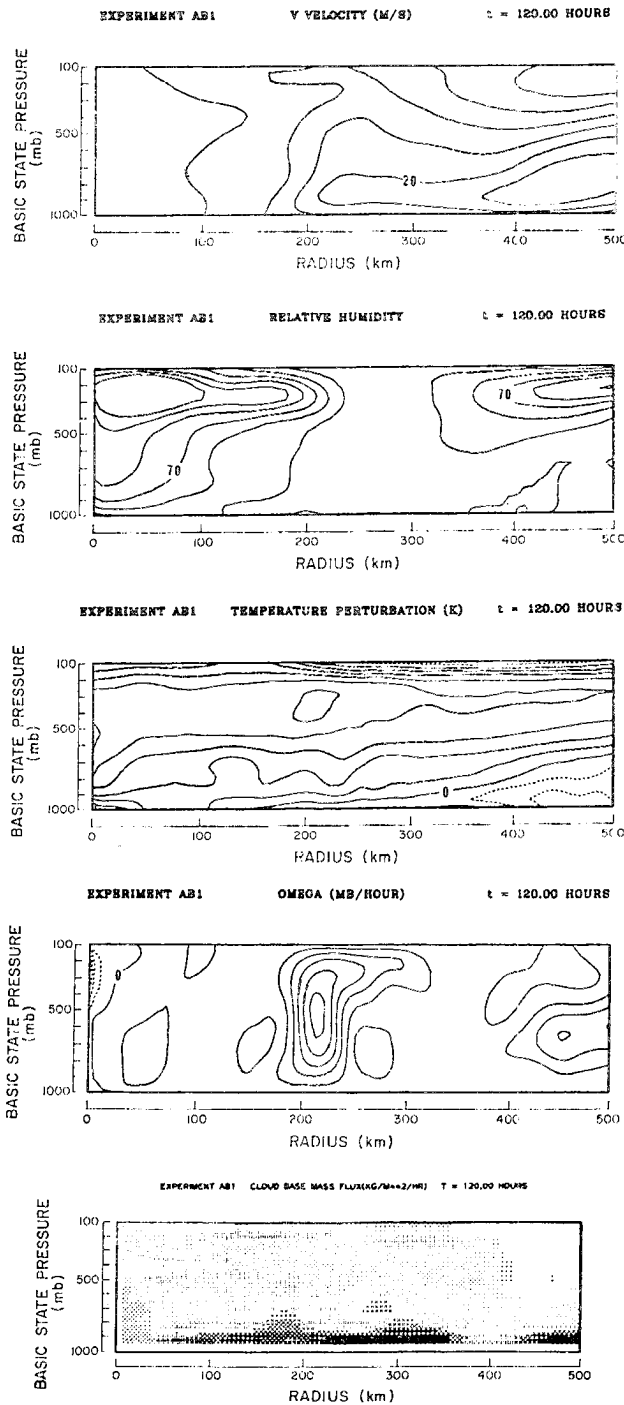
Figure 5.8 The tangential wind (5 m/s), relative humidity (10%), temperature deviation (1°C), vertical motion (25 mb/hr), and cloud base mass flux distribution fields at 120 hours for experiment AB1. The quantities in parentheses denote the respective contour interval.

EXPERIMENT AB4   V VELOCITY (M/S)   t = 120.00 HOURS

EXPERIMENT AB4   RELATIVE HUMIDITY   t = 120.00 HOURS

EXPERIMENT AB4   TEMPERATURE PERTURBATION (K)   t = 120.00 HOURS

EXPERIMENT AB4   OMEGA (MB/HOUR)   t = 120.00 HOURS

EXPERIMENT AB4   CLOUD BASE MASS FLUX(KG/M**2/HR)   T = 120.00 HOURS

Figure 5.9   Same as Figure 5.8 but for experiment AB4.

vertical motion field located at approximately 220 km. The cloud base

mass flux distribution continues to show a fairly disorganized pattern

of convection as in the early stages of the numerical integration (Fig.

5.4). In sharp contrast Fig. 5.9 shows a well organized upper level

warm core tangential circulation with maximum winds in excess of 70 m/s

at 80 km just above the mixed layer. The vertical motion field peaks

at -250 mb/hr just inside this maximum in the tangential circulation.

Also note the highly organized bimodal character of the cloud base

mass flux distribution inside 300 km. The absence of parameterized

convection inside 60 km is due to the transition from parameterized

heat release to resolvable heat release in the eyewall region at this

stage of development.

5.2 Numerical Simulations With the Explicit Release of Latent Heat

The earliest attempts to numerically simulate the life cycle of
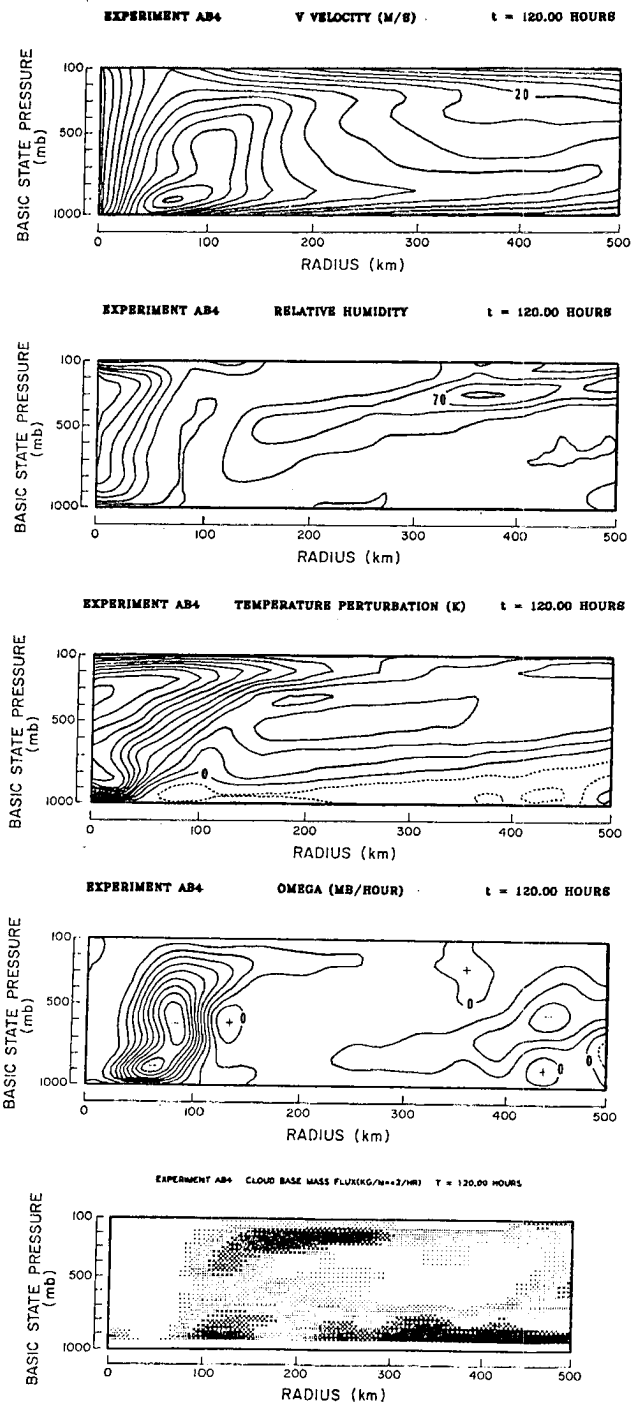
the tropical cyclone included only the explicit release of latent heat

(e.g. Kasahara, 1961, 1962; Syōno, 1962). These numerical integrations

were carried out to only a few hours during which small-scale (grid-

scale) features in the vertical motion field grew rapidly to the point

where they appeared to dominate the large-scale fields. Linear sta-

bility analyses of the growth of small amplitude disturbances in a

conditionally unstable environment had previously predicted the smallest

scale (or cloud scale) motions to have the largest growth rates (Haque,

1952; Syōno, 1953; Lilly, 1960). Consequently, the above numerical

solutions were interpreted as a confirmation of the linear studies.

This apparent failure to simulate the growth of a cyclone-scale circu-

lation by explicitly resolving the convective release of latent heat
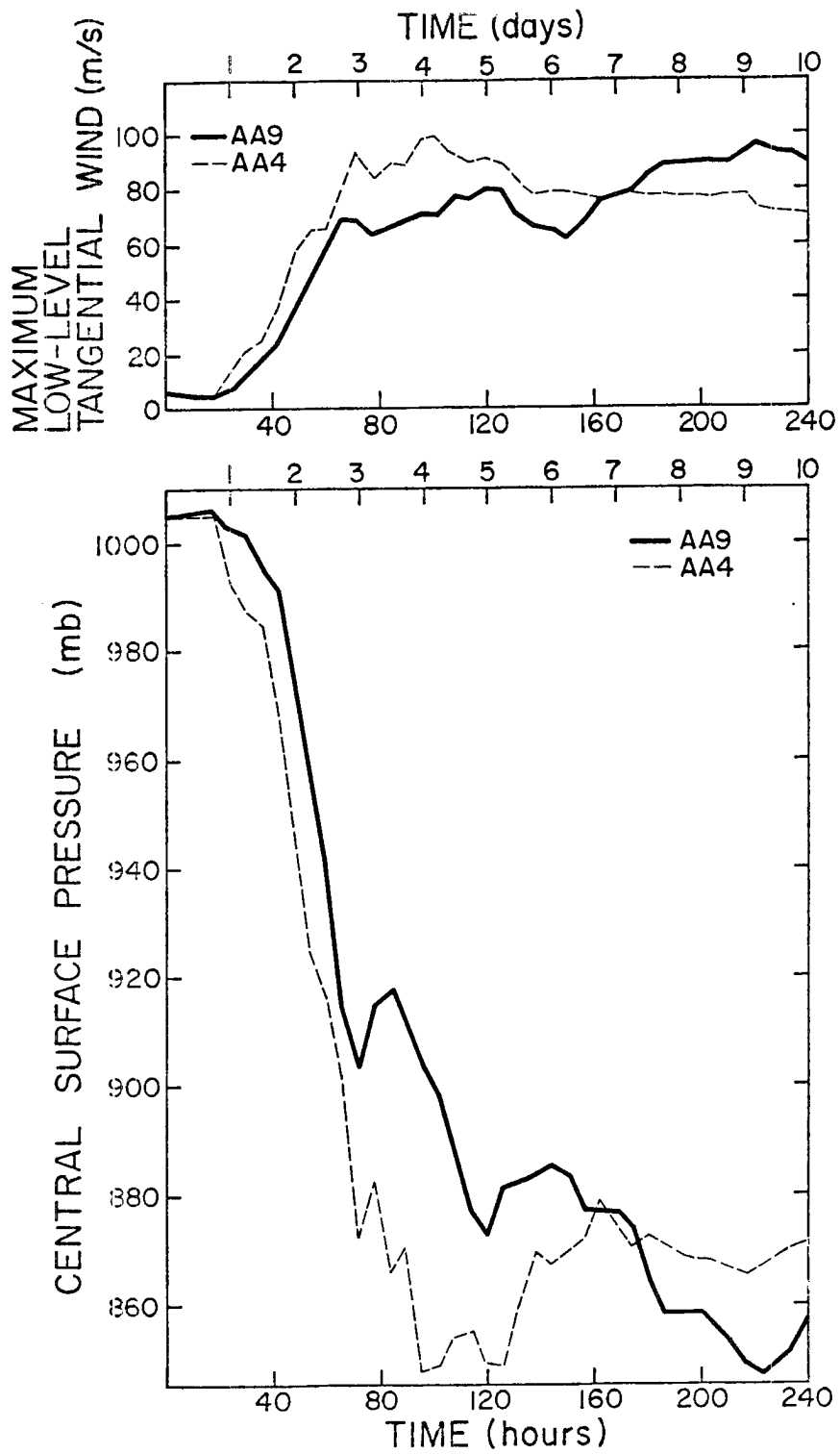
Figure 5.10   Same as Figure 5.1 but for experiments AA9 and AA4.

led to the development of cumulus parameterization techniques, which although crude, were nevertheless employed with great success. Recently however, investigations by Yamasaki (1977) and Rosenthal (1978) have raised questions regarding the need and desirability to parameterize cumulus convection in tropical cyclone models.

Yamasaki (1977) has used a non-hydrostatic axisymmetric model in which cumulus convection is explicitly resolved on a telescoping horizontal grid (400 m interior resolution) to produce a tropical cyclone like circulation. But also interesting is the study conducted by Rosenthal (1978) in which he successfully simulates the development of a tropical cyclone using a hydrostatic axisymmetric model in which latent heat release occurs totally in 'convective elements' that are explicitly resolved on a 20 km grid. What makes this work so remarkable is that it essentially follows the same approach attempted without success by Kasahara (1961, 1962) and Syōno (1962), which leads to the conclusion that these early failures were most likely attributable to deficient model design.

The model described by Rosenthal (1978) carries liquid water as a dependent variable, and consequently employs a more sophisticated resolvable heat release process. Thus, in order to determine whether his numerical results might be dependent on this process, we proceeded to conduct several numerical experiments in which parameterized convection was excluded, leaving the treatment of the release of latent heat to the large-scale condensation process. The results of two of these numerical integrations are shown in Figs. 5.10 and 5.11. Experiment AA9 uses the initial moisture distribution given by IC1 while
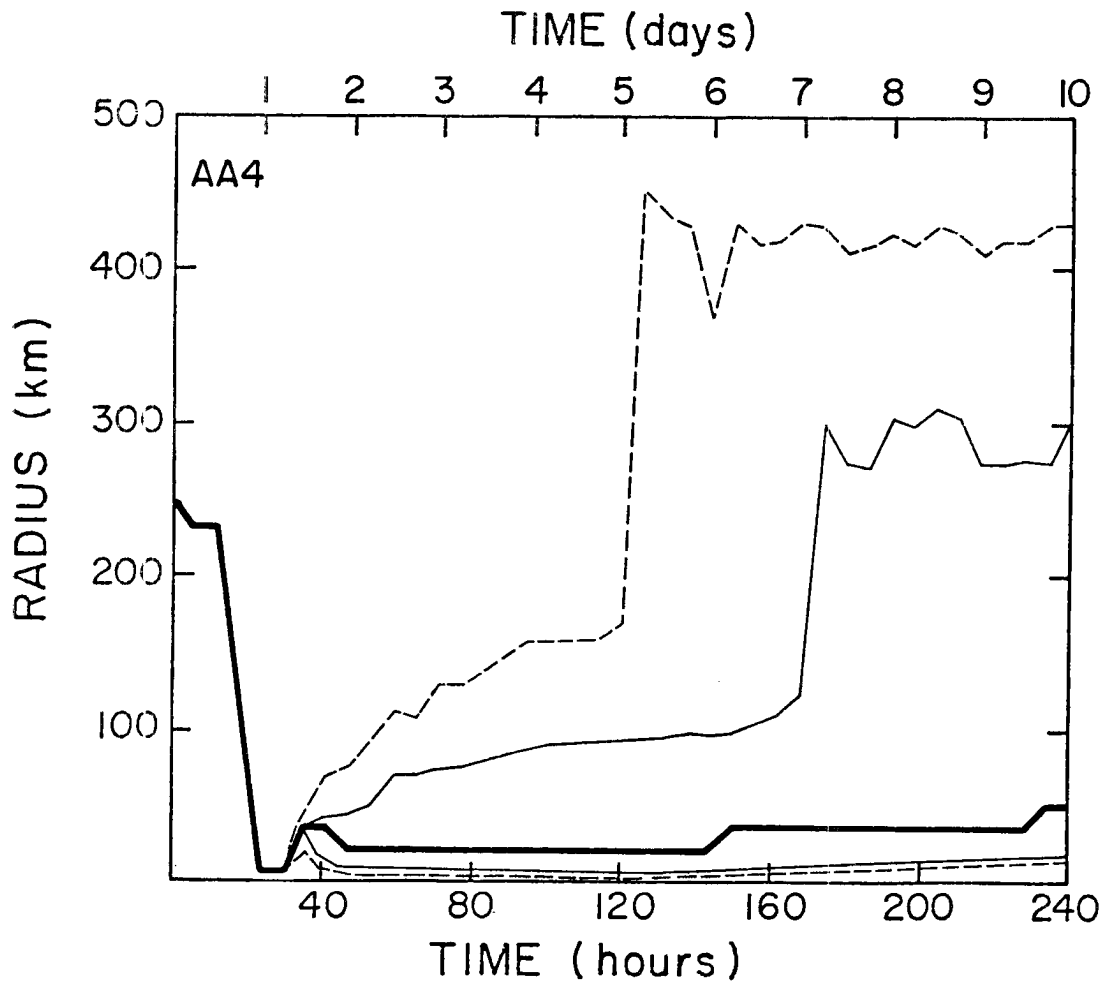
Figure 5.11   Same as Figure 5.2 but for experiment AA4.

experiment AA4 uses the initial moisture distribution given by IC2.
In both cases we see very early, rapid and deep development of a
hurricane-like circulation. In contrast to the parameterized heat
release counterparts AB1 and AB4, only a weak sensitivity to the
initial moisture distribution can be seen. Hurricane force winds are
achieved only about 6 hours sooner for experiment AA4, and in both
cases these winds occur within two days of the initial condition.
The gross structure of experiment AA4 is depicted in Fig. 5.11
(experiment AA9 is similar), which shows a very rapid collapse
of the radius of maximum winds to radii of 7.5-37.5 km followed by
the onset of gale and hurricane force winds.

The horizontal extent of the gale and hurricane force winds is
fairly confined until hour 120 at which point the gale force winds
jump out to a radius of 450 km. A similar jump in the exterior hur-
ricane force winds occurs at about 170 hours. The large horizontal
extent of the gale and hurricane force winds may be a consequence of
both the assumption of axisymmetry, and an inadequate frictional
coupling between the mixed layer and the region above. We do not
believe it to be the result of the particular method of heat release.
Since the motions are assumed to be axisymmetric, air particles spiral
directly toward the center of the vortex from larger radius, allowing
surface friction little time to act as a sink for angular momentum.
If the frictional coupling between the mixed layer and the region
above is too weak, the gale and hurricane force circulations which are
established tend to be quite broad in horizontal extent. The expan-
sion of the tangential circulation is most pronounced in the case
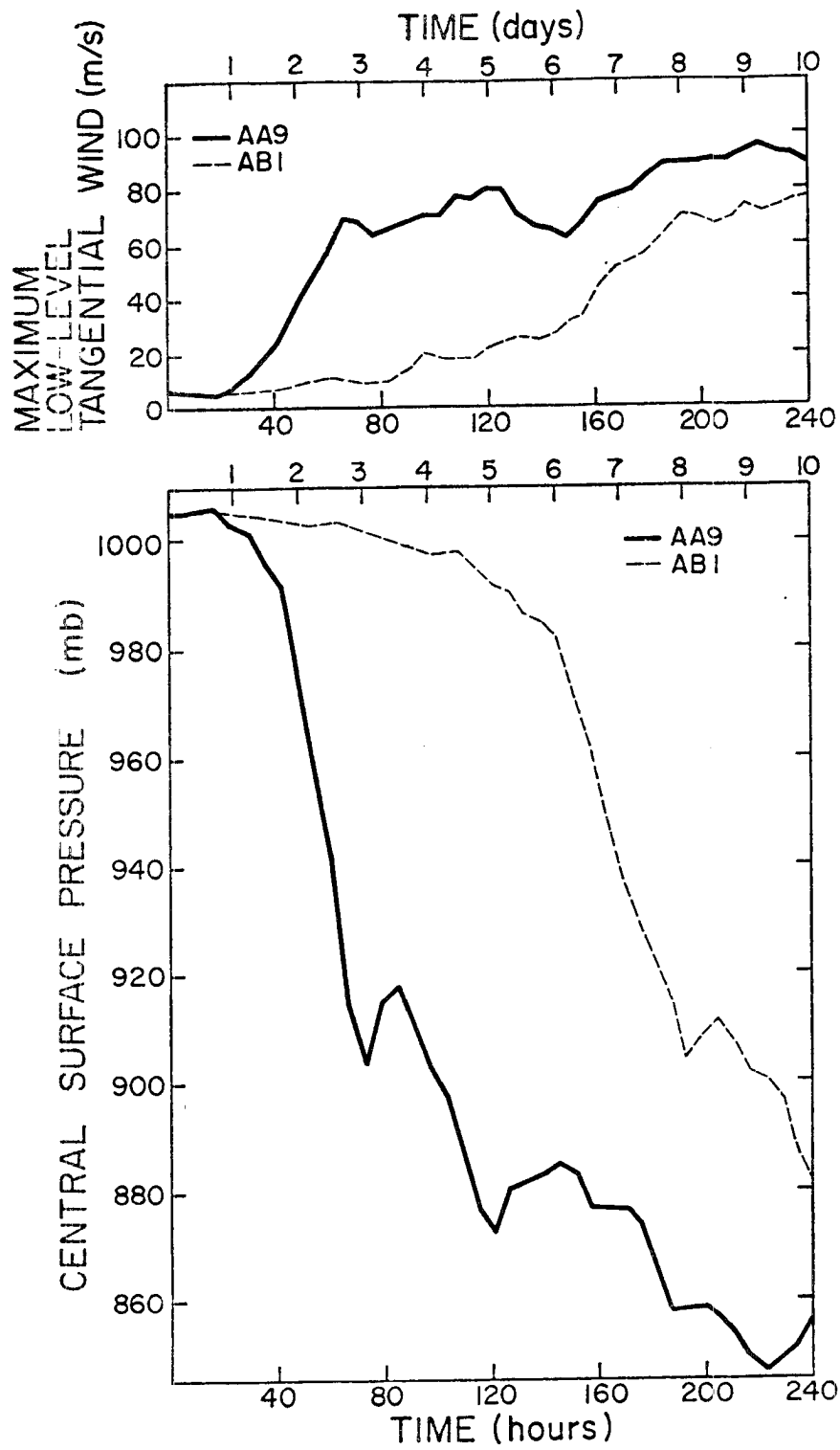
Figure 5.12   Same as Figure 5.1 but for experiments
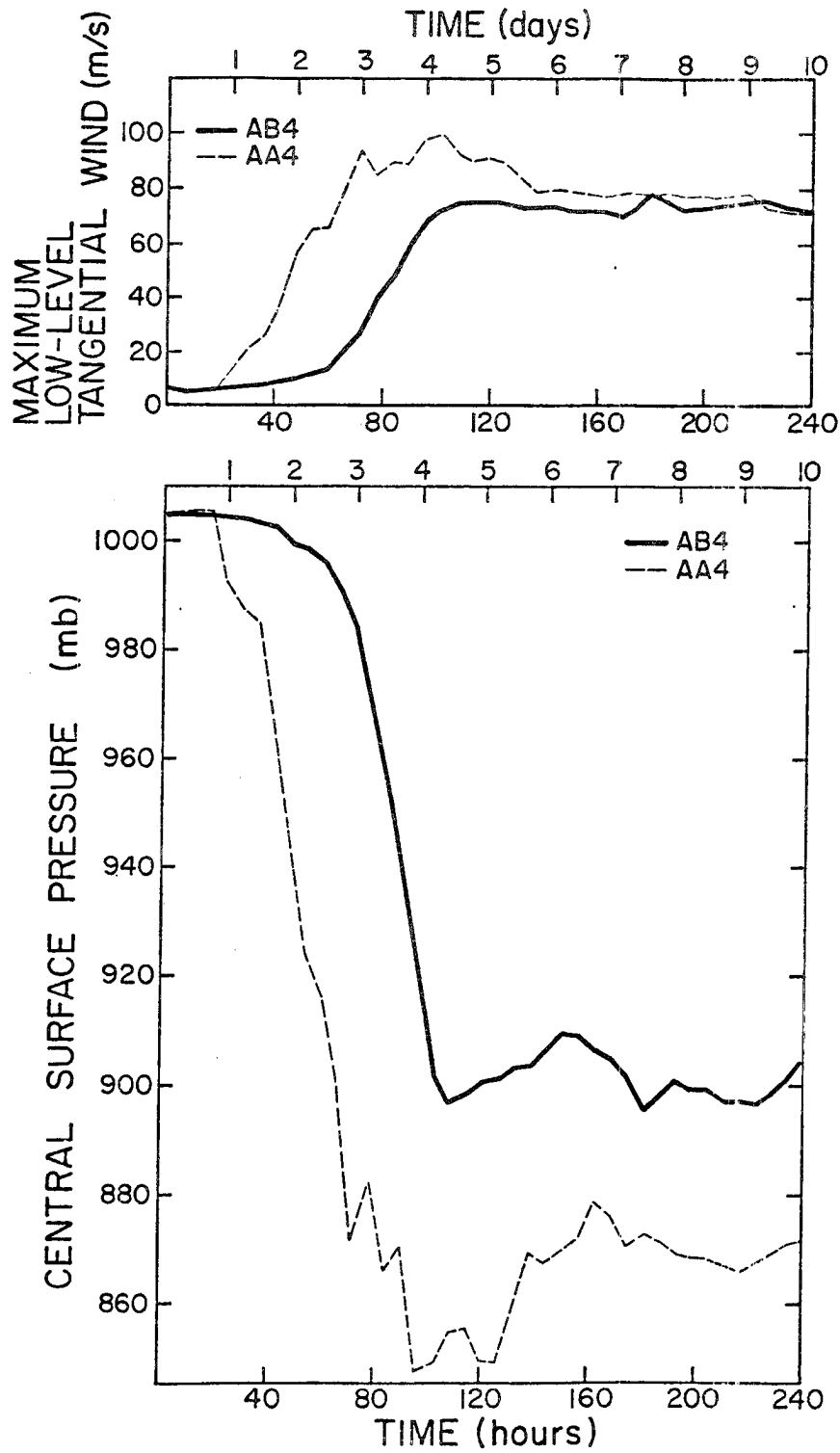AA9 and AB1.

Figure 5.13 Same as Figure 5.1 but for experiments AA4 and AB4.

of the resolvable heat release experiments due to the nature of the development of the vortex, which is rapid and initially confined to a very small region in the interior. As time goes on, however, the horizontal scale and intensity of the radial circulation grows, intensifying the tangential circulation which ultimately gives the appearance of a sudden jump in the horizontal extent of the gale and hurricane force winds. Although such a sudden jump is not as obvious in the cases of parameterized heat release AB1 and AB4, we note that the scale of all these vortices is quite similar once they reach a mature stage. The incorporation of radiative processes and cumulus momentum transport (which provides a stronger frictional coupling between the mixed layer and the region above) can help to reduce the size of the tangential circulation as we shall see later.

In Figs. 5.12 and 5.13 we compare the resolvable and parameterized heat release experiments for each of the initial moisture distributions. Shown is the time evolution of the maximum low level tangential wind and central surface pressure. Although the intensification rates are similar for all model storms, the time required to reach this intensifying stage and the strength and structure of the mature storm differ significantly between the parameterized heat release experiments and the explicit heat release experiments (see Fig. 5.14).

It would be incorrect to attempt to draw general conclusions regarding the issue of the need to parameterize cumulus convection in a model such as ours. There are substantial differences, however, between the parameterized and explicit heat release experiments we have conducted. Perhaps the most significant conclusion that can be drawn from our simulations with the explicit release of latent heat

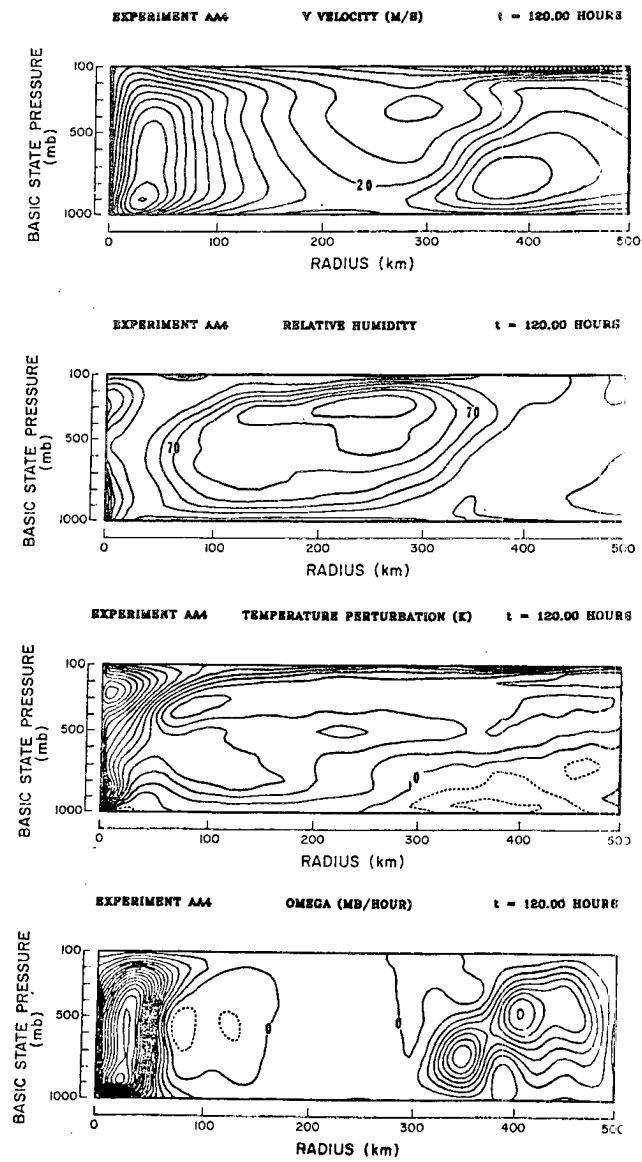Figure 5.14   The tangential wind (5 m/s), relative humidity
(10%), temperature perturbation (1°C) and
vertical motion (25 mb/hr) fields at 120 hours
for experiment AA4.   The quantities in paren-
theses denote the respective contour interval.
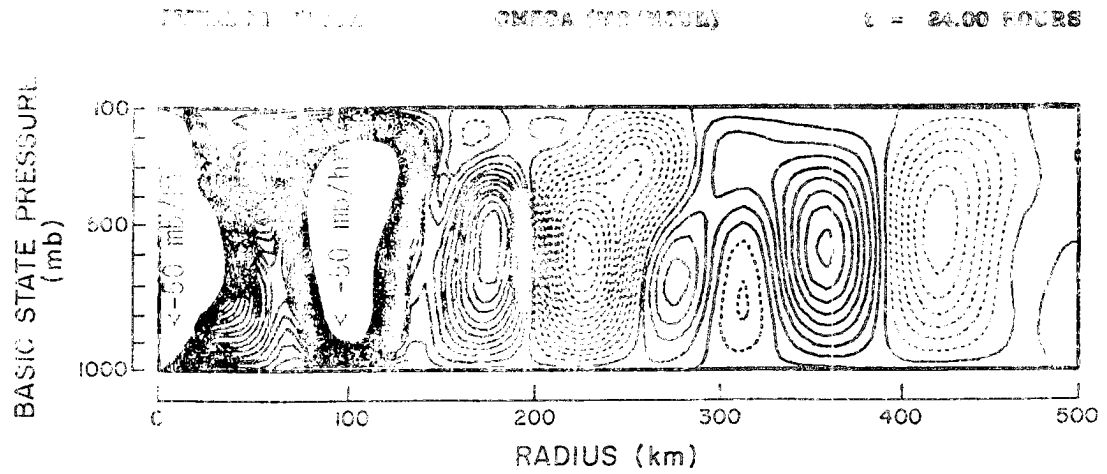
Figure 5.15 The vertical motion field at 24 hours for experiment
AA4. The contour interval is 2.5 mb/hr with sinking
motion denoted by dashed contours.

is that the results first presented by Rosenthal (1978) do not seem to be dependent upon the technique employed to represent the process of latent heat release. By using a fairly crude large-scale condensation process we have been able to simulate the development of a cyclone-scale circulation. Although small scale features are produced at the onset of large-scale condensation (see Fig. 5.15), nonlinear effects appear to be quite capable of controlling their growth. We note that the nonlinear horizontal diffusion process is not necessary in order to effect such control since we have also been able to simulate the growth of a hurricane circulation using only a linear horizontal diffusion coefficient of 10^3 m^2/s.

5.3 Sensitivity of Model Storm Development to the Lateral Boundary Condition

In this section we will show the sensitivity of model storm development to the particular form of the lateral boundary condition. Rosenthal (1971) has numerically examined the sensitivity of an axisymmetric tropical cyclone model to two lateral boundary conditions as functions of computational domain size. These were the conditions of zero divergence (BCIV) and zero radial wind (BCV). In chapter 3, the problem of the proper formulation of the lateral boundary condition is approached from a linear point of view with the goal of minimizing the reflection of gravity-inertia waves. A reflectivity analysis shows that both BCIV and BCV are unit reflectors of gravity-inertia waves, which leads to the derivation of an approximate cylindrical pure gravity wave radiation condition for a stratified atmosphere (BCIII).

Each of the above boundary conditions is of course deficient in some regard, but BCV can be expected to have the largest impact upon

the numerical solution since it mechanically closes the system and consequently restricts the radial circulation to the size of the computational domain. The condition of zero divergence (BCIV) represents an improvement since it allows mass to flow through the lateral boundary of the computational domain. By comparing the numerical results obtained using BCIV and BCV for a computational domain comparable in size to that used in the present study, Rosenthal (1971) found significant differences in the development times and final intensities of the model vortices. The mechanically closed system produced a weaker vortex that took longer to develop than the vortex simulated with the condition of zero divergence at the lateral boundary.

Although BCIV does not suffer from the obvious deficiency associated with BCV, it nevertheless is a perfect reflector of any gravity-inertia wave activity generated in the interior of the computational domain. In chapter 3, the argument is made that such improper reflection of outward propagating gravity-inertia waves can result in a false modulation of latent heat release through nonlinear interactions between vertical motion fields associated with the reflected waves, and the moisture field. For example, if a convergence field (associated with a reflected gravity-inertia wave) acts for a long enough period or a region whose temperature and moisture structure is favorable for convection, a net release of latent heat will likely occur in the column. In the real atmosphere, this period of time is probably on the order of one to several hours, but in a numerical model which incorporates a cumulus parameterization such a period may be on the order of minutes. Thus, in order to avoid this potential problem, BCII is proposed for use in our tropical cyclone model.
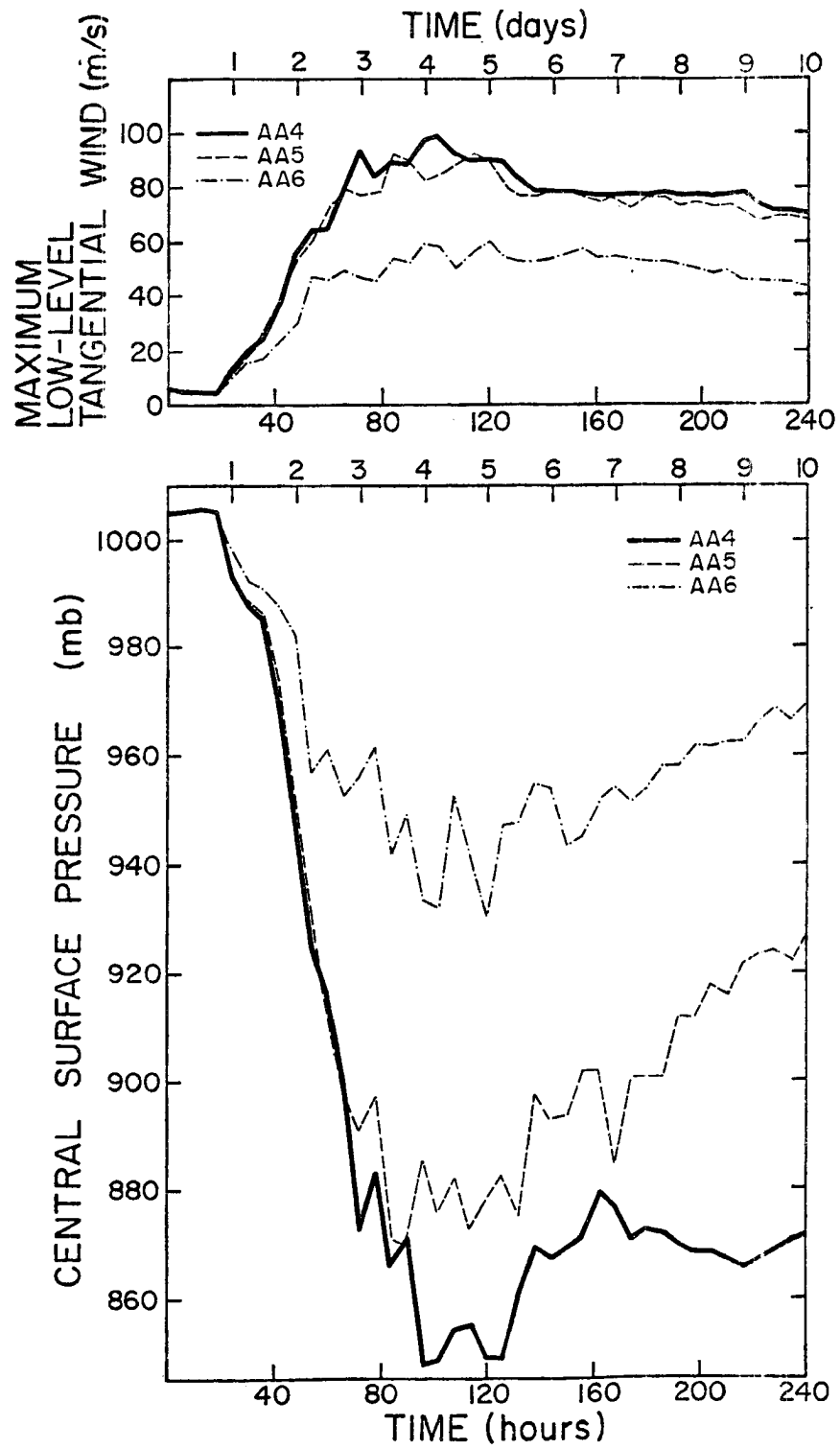
Figure 5.16 Same as Figure 5.1 but for experiment AA4, AA5 and AA6.

Numerical solutions are now presented using the three boundary conditions BCII, BCIV and BCV for experiments incorporating parameterized convection (AB4, AB5, AB6) and those in which convection is explicitly resolved (AA4, AA5, AA6). Figs. 5.16 and 5.17 show the time evolution of the maximum low level tangential wind and central surface pressure for the sets of experiments making use of explicit latent heat release and parameterized heat release, respectively. In each case, the use of BCV (zero radial wind) results in slower development and a weaker mature storm as was suggested by Rosenthal (1971). For the explicit latent heat release experiments, note that intensification of the model vortices begins at essentially the same time, regardless of the boundary condition. Experiment AA6 (BCV) develops more slowly, however, and even at the deepest stage is considerably weaker than either AA4 or AA5. The difference in the ultimate intensities is not as great when the convection is parameterized, but in this case more than six days is required for AB6 to reach an intensifying stage.

Significant differences in the development of the model storm when using BCII and BCIV appear only when cumulus convection is parameterized. In those experiments using only explicit heat release, the development of the model storms is almost identical for the first three days of the numerical integrations (AA4 vs AA5). Thereafter, the solutions diverge with AA4 producing a deeper, slowly varying mature storm. When the cumulus convection is parameterized the use of BCIV results in a storm which takes a longer period of time to develop, although the ultimate intensity is similar to the vortex simulated with BCII (AB4 vs AB5).
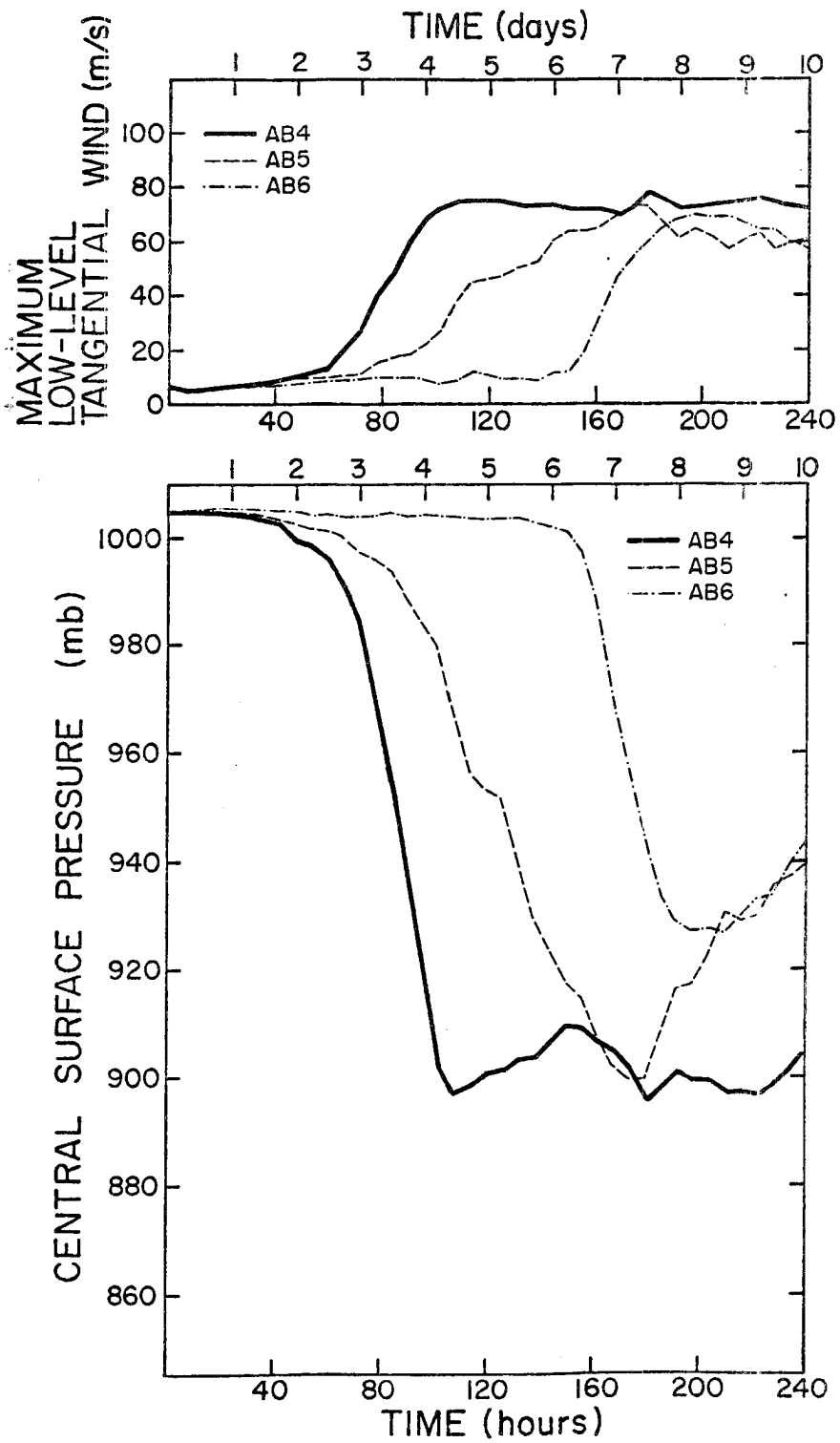
Figure 5.17   Same as Figure 5.1 but for experiments
AB4, AB5 and AB6.
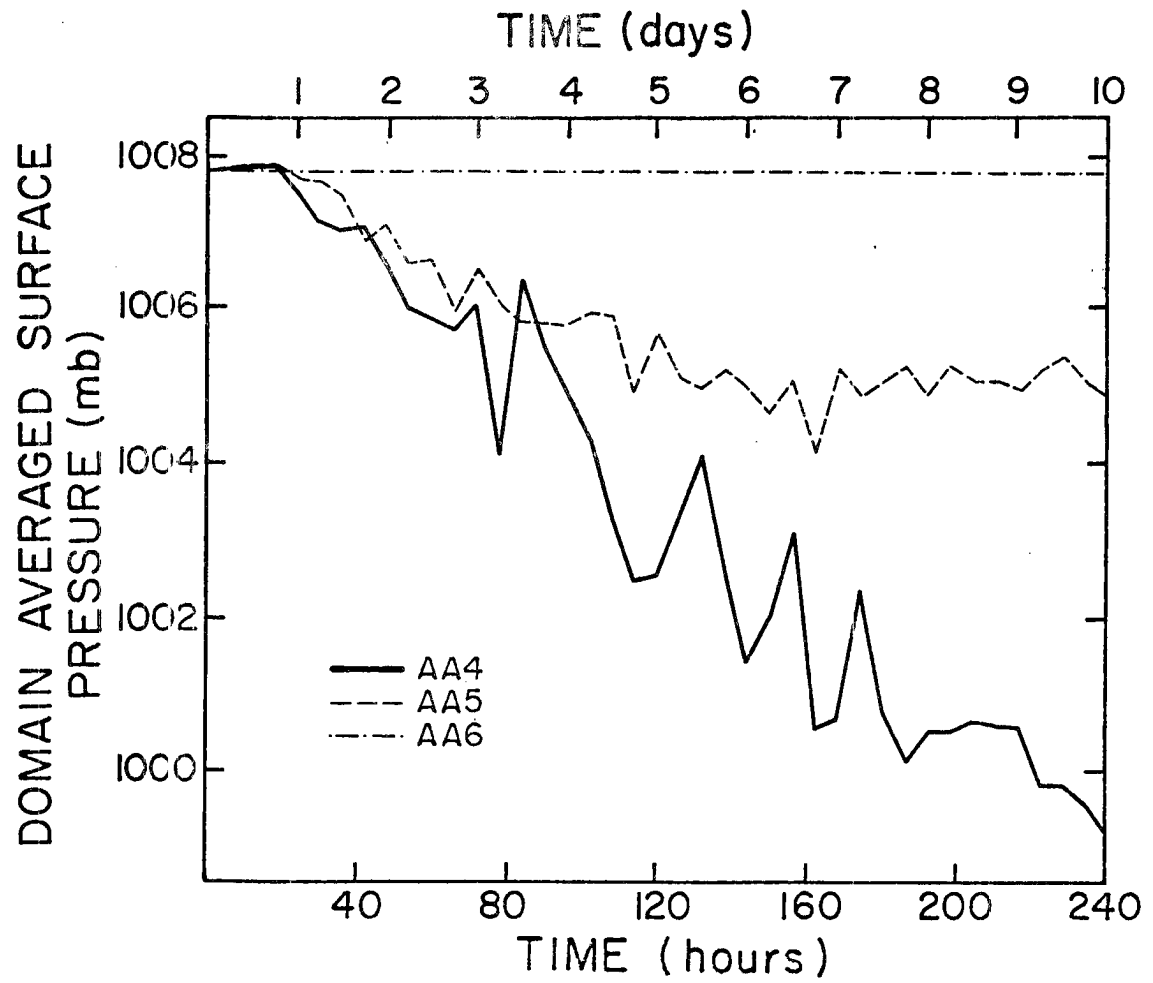
Figure 5.18 Time evolution of the domain averaged surface pressure for experiments AA4, AA5 and AA6.

Figures 5.18 and 5.19 summarize the behavior of the domain aver-
aged surface pressure in time. For the experiments using BCV (AA6,
AB6), the domain averaged surface pressure is invariant as one would
expect. This quantity does change, however, for boundary conditions
BCII (AA4, AB4) and BCIV (AA5, AB5). In both the case of parameter-
ized convection and the case where convection is explicitly resolved,
there is a tendency for the domain averaged surface pressure to be
lower when using BCII. This is generally true at all times when con-
sidering the experiments using explicit heat release, and during the
early and late stages of the simulations with parameterized convection.
During the early stages of the numerical integrations, a significant
fraction of the difference in the domain averaged surface pressure is
likely to be directly attributable to gravity-inertia waves which are
transmitted by BCII but are reflected by BCIV.

In conclusion, we note that the general character of the numeri-
cal integrations does appear to depend on the particular form of the
lateral boundary condition. The condition of zero radial wind (BCV)
clearly contributes to significant departures in the numerical solu-
tions obtained when using BCII and BCIV. The acceptability of such a
lateral boundary condition is highly questionable since it artificially
restricts the horizontal extent of the radial circulation, which has an
obvious impact on the numerical solution. The adequacy of the condi-
tion of zero divergence is much more difficult to determine. During
the developing stages of those experiments in which convection is ex-
plicitly resolved on the scale of the grid, little difference is seen
between the simulations using BCII and BCIV (AA4, AA5). There are,
however, substantial differences in the solutions when cumulus
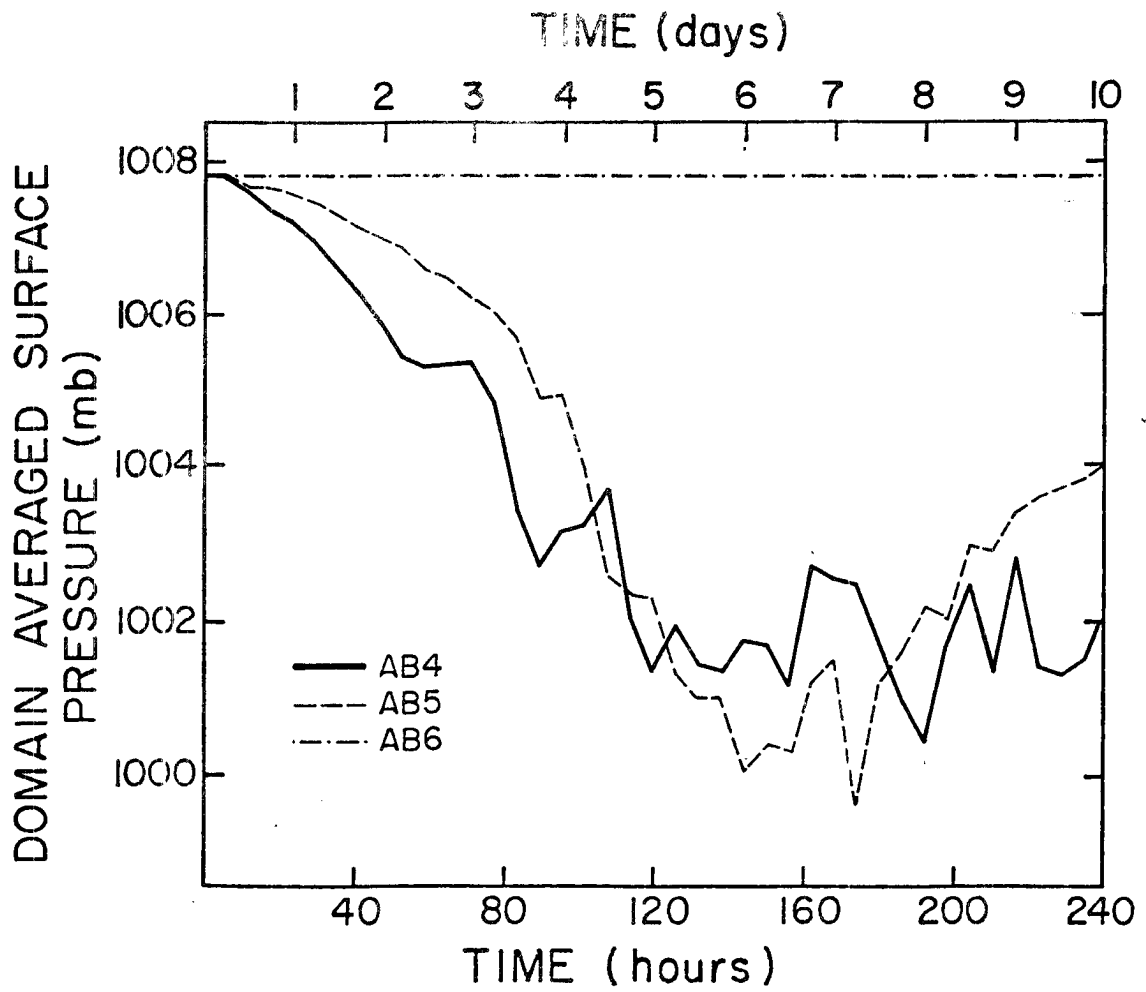
Figure 5.19   Same as Figure 5.18 but for experiments AB4, AB5 and AB6.

convection is parameterized (AB4, AB5). Since the linear analysis
of chapter 3 shows that gravity-inertia waves are reflected from the
boundary of the computational domain when using BCIV, one might specu-
late that in the early stages of the numerical integrations these dif-
ferences are produced by an interaction between reflected gravity-
inertia waves and the cumulus parameterization resulting in a net
release of latent heat away from the interior. Such an event would be
unlikely to occur in the case where convection is explicitly resolved
since the atmosphere would have to be very near saturation, which it
generally is not.

One additional distinction in the integrations which use BCII and
BCIV is the steady state nature of the storms simulated with BCII.
This is probably attributable to some nonlinear aspect of the boundary
condition which is beyond the scope of the analysis presented in
chapter 3.

6.0 EXAMPLES OF THE ROLES OF RADIATION AND CUMULUS MOMENTUM TRANSPORT

In this chapter we consider the effect of a simple radiation parameterization and the effect of 'cumulus friction' on the development of a model storm. These numerical examples make use of the initial moisture distribution given by IC2 and the lateral boundary condition proposed in chapter 3 (BCII). Thus they can be compared directly to experiment AB4 which incorporated the parameterized transports of heat and moisture only (see Table 5.1).

6.1 Incorporation of Radiation

The role of radiative processes in large-scale tropical weather systems is not yet well understood. Albrecht and Cox (1975) have suggested that infrared (or longwave) cooling may be a significant component of the total diabatic source occurring in a tropical wave. More recent diagnostic studies of convection using both spectral and bulk representations of the cloud field have indicated a marked sensitivity to the choice of a radiative heating (e.g. Yanai et al., 1976; Stephens and Wilson, 1980). The fact that the longwave radiative cooling is primarily modulated by upper level cloud has led Gray and Jacobson (1977) to propose that horizontal gradients in the longwave radiative cooling are fundamental to the maintenance of tropical disturbances.

The role of longwave radiation in the development of a tropical cyclone was first addressed by Sundqvist (1970b), who included this process in a ten level axisymmetric balanced model. A net radiative cooling profile was applied only to those regions in which condensation was not taking place. His results showed a noticeable increase in the rate of intensification despite the small magnitude of the radiative

139
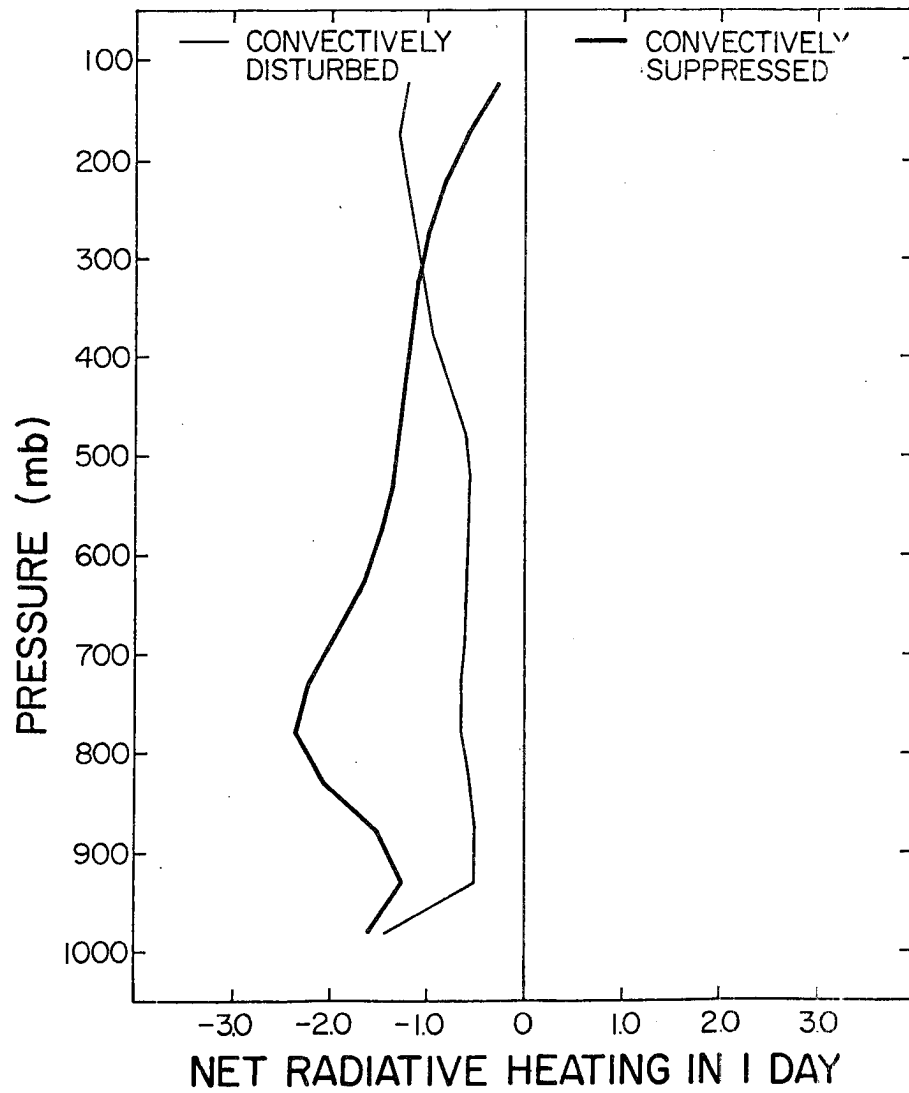
Figure 6.1   The net radiative heating rate used in experiment
AD1 and AF1.
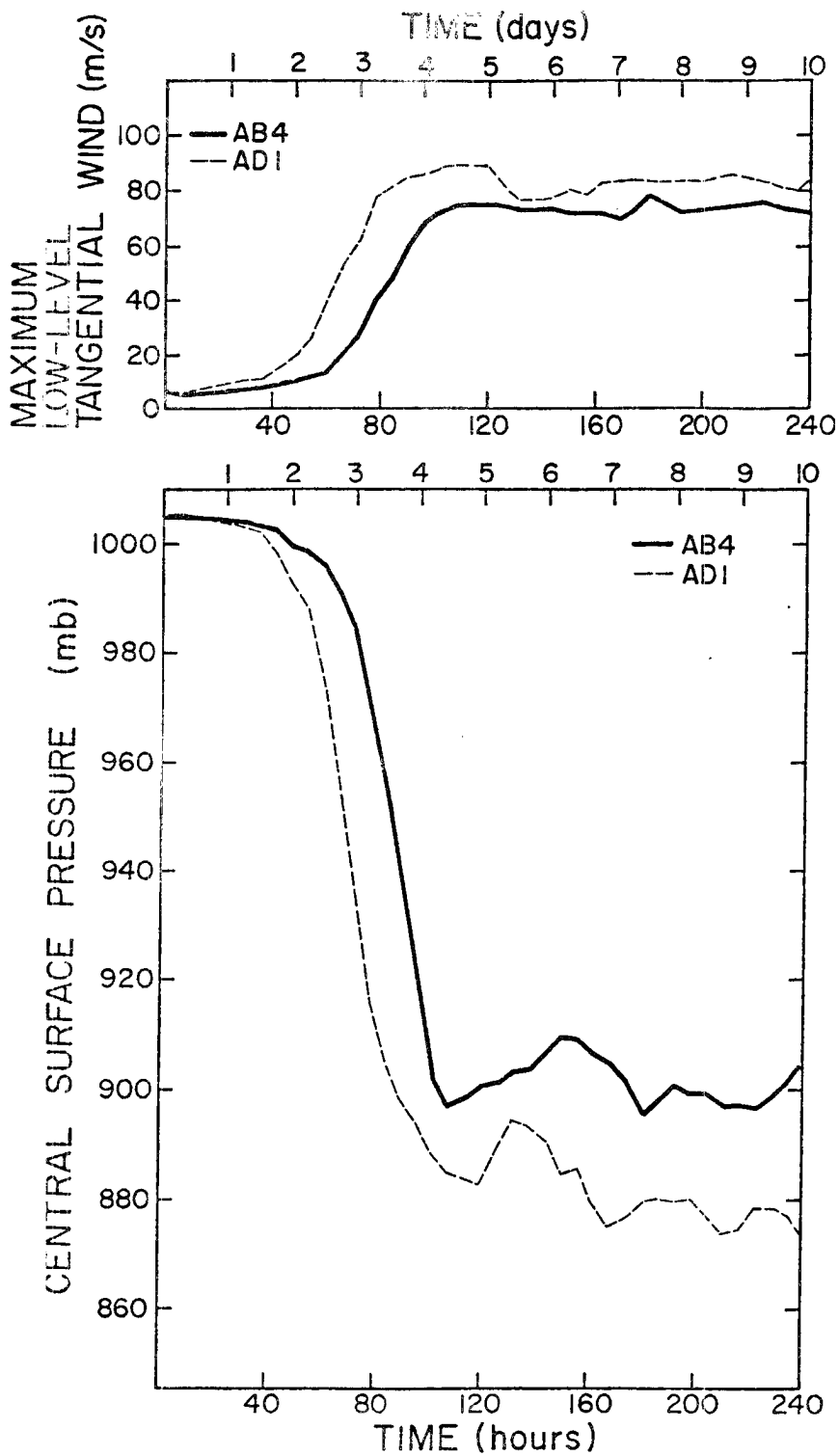
Figure 6.2 The time evolution of the maximum low level (z ∿ 225 m) wind and central surface pressure for experiments AB4 and AD1.
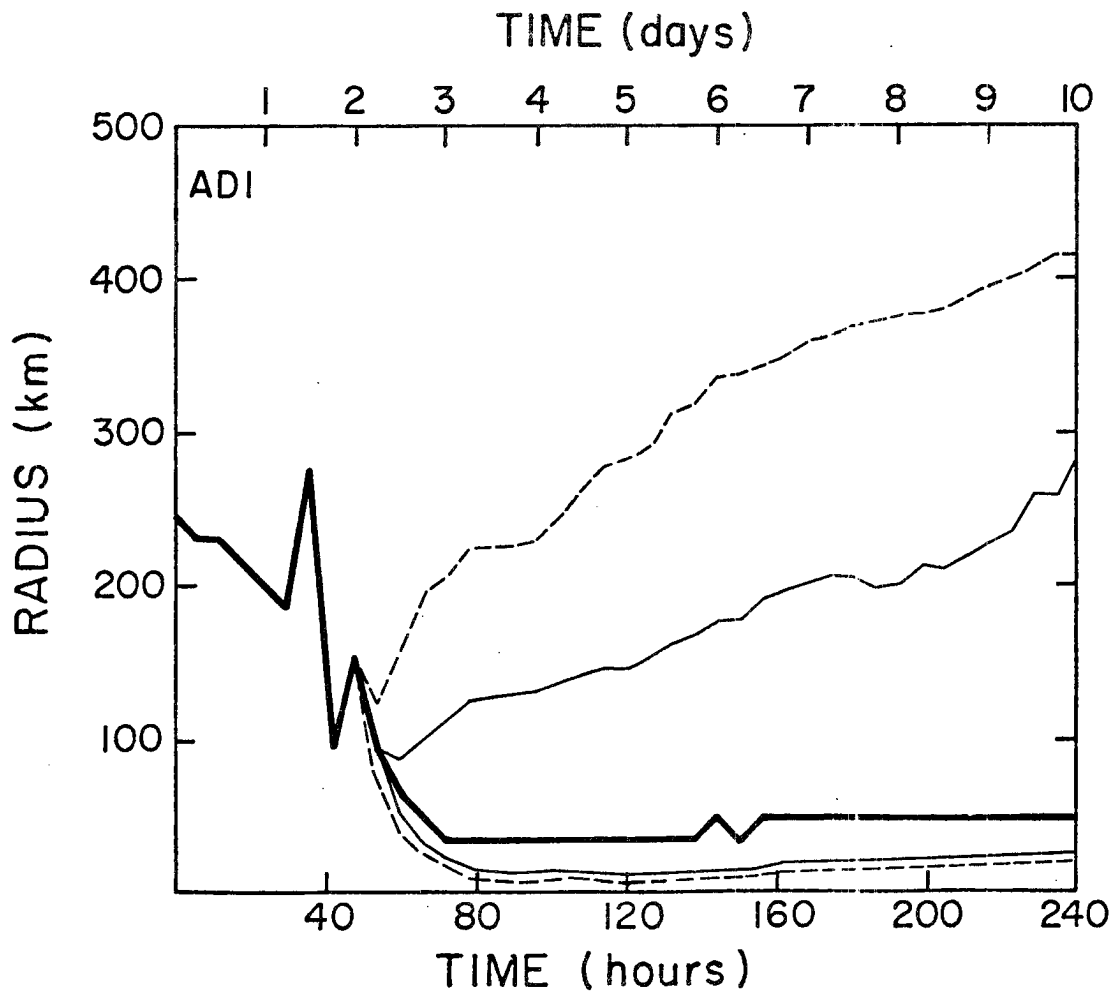
Figure 6.3 The time evolution of the radius of maximum wind
(heavy solid line) and the horizontal extent of
the gale (light dashed line) and hurricane (light
solid line) force winds for experiment AD1.

cooling (maximum values of -2°C/day at 300 mb). Interestingly, the peak intensity of the storm showed no sensitivity to the incorporation of radiation.

In order to determine what, if any, effect net radiational cooling would have on our model storm development, a numerical experiment (AD1) was conducted which incorporated the simple radiation parameterization described in section 2.3.4. We note that the diurnal variation in the shortwave radiative heating was not included, and only the daily averaged net radiative heating rate was considered (see Fig. 6.1). A comparison of the time evolution of the maximum low level ($z \sim 225$ m) tangential wind and central surface pressure for experiments AB4 and AD1 is shown in Fig. 6.2. This diagram clearly indicates that the incorporation of radiation results in significantly earlier intensification as well as a deeper more intense mature storm. The rate at which the model storm deepens, however, appears to be insensitive to the inclusion of the radiation parameterization.

Fig. 6.3, which depicts the gross horizontal structure of the simulated disturbance suggests a tighter more organized circulation than the ore obtained in experiment AB4 (see Fig. 5.3). Comparison of the tangential wind field at 120 hours for AB4 (Fig. 5.9) and AD1 (Fig. 6.4) confirms that experiment AD1 exhibits a more intense tangential circulation confined to a smaller radius. The tangential circulation in the outer regions appears to be more organized as well with large values of v restricted to a smaller interior region. Noticeable differences in the organization of the vertical motion field are also seen. These results appear to suggest that radiative processes may play a role in determining the horizontal scale of a tropical disturbance.

EXPERIMENT AD1   V VELOCITY (M/S)   t = 120.00 HOURS

EXPERIMENT AD1   RELATIVE HUMIDITY   t = 120.00 HOURS

EXPERIMENT AD1   TEMPERATURE PERTURBATION (K)   t = 120.00 HOURS

EXPERIMENT AD1   OMEGA (MB/HOUR)   t = 120.00 HOURS

EXPERIMENT AD1   CLOUD BASE MASS FLUX(KG/M**2/HR)   T = 120.00 HOURS
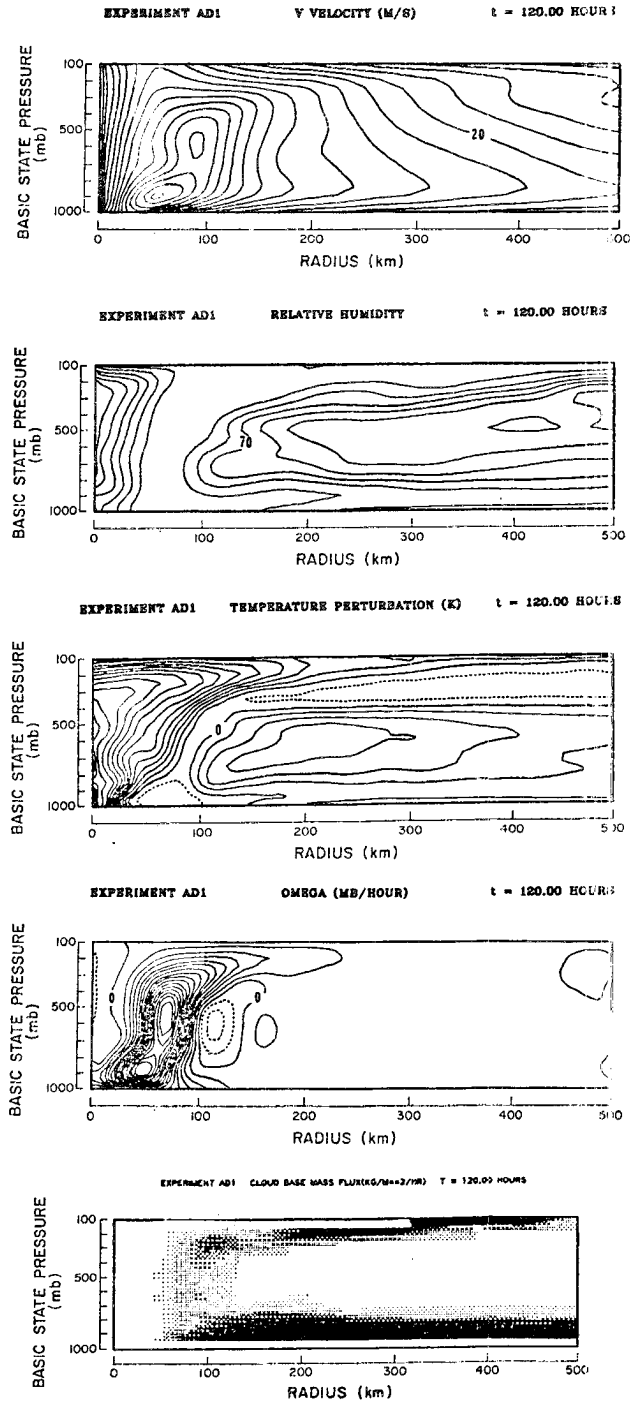
Figure 6.4   The tangential wind (5 m/s), relative humidity (10%), temperature deviation (1°C), vertical motion (25 mb/hr) and cloud base mass flux distribution fields at 120 hours for experiment AD1. The quantities in parentheses denote the respective contour interval.
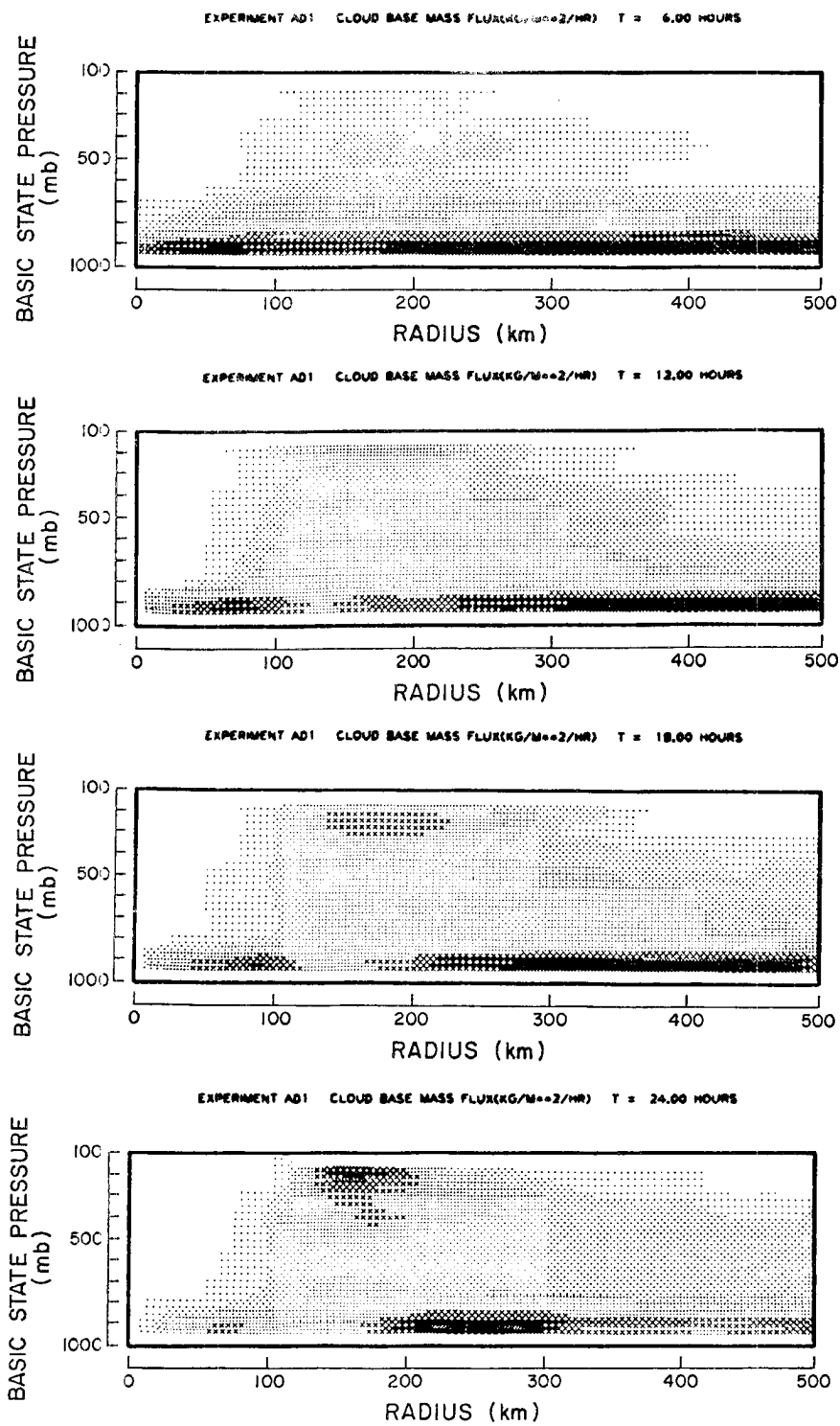
Figure 6.5   Cloud base mass flux distribution for experiment AD1.
The intensity of the shading at any level p is pro-
portional to the cloud base mass flux of the sub-
ensemble detraining at that level.

The relative humidity field at 120 hrs is much more reasonable in experiment AD1, showing a pronounced drying in middle levels at the larger radii (cf. Frank, 1977). This is most likely a consequence of the strongly bimodal character of the parameterized corvection which is occurring in the same region. Fig. 6.5 shows the early time evolution of the cloud base mass flux distribution field for experiment AD1. The incorporation of a radiative cooling appears to contribute to earlier development of strong deep convection in the interior (cf. Fig. 5.5). This pronounced difference in the convective activity is more clearly seen in Figs. 6.6-6.9 which among other things show the convective-scale flux of total water ($LF_{q+\ell}$) and the convective scale heating rate ($g \frac{\partial}{\partial p} F_{s-L\ell} + LR$) for experiments AB4 and AD1 at twelve and twenty-four hours. Note the large horizontal gradients which develop in these convective scale properties by twenty-four hours. A more rapid development of the transverse circulation accompanies the accelerated growth of deep cumulus convection as can be seen from the omega fields presented in Figs. 6.6-6.9. At twelve hours experiment AD1 exhibits a vertical motion field (150-200 km) which is twice as large as the one produced in AB4. By twenty-four hours this difference is even more extreme. The intensity of both low and middle inflow is enhanced when radiation is included which accounts for the discrepancy in the vertical position of the maximum in the omega field.

The numerical results presented here suggest that radiative cooling does play a significant role in the development of a tropical disturbance. Even though the magnitude of this cooling is small when compared to the diabatic heating rates associated with organized
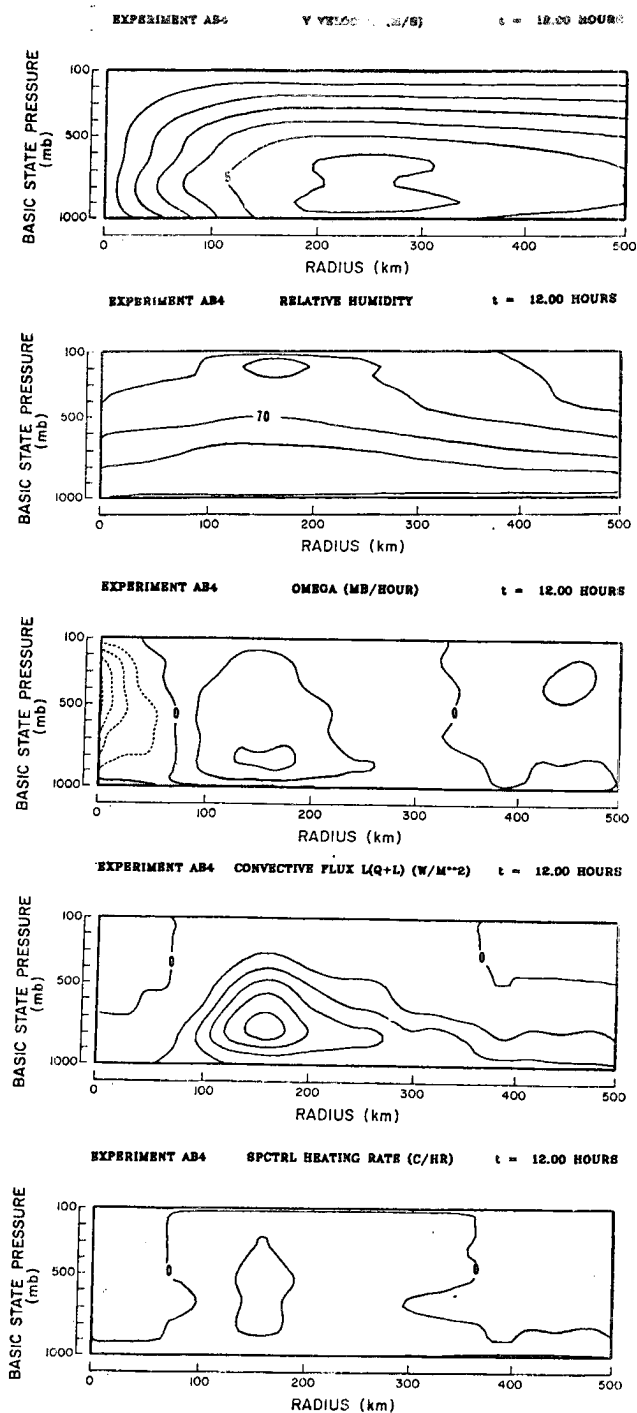
Figure 6.6 The tangential wind (1 m/s), relative humidity (10%), vertical motion (2.5 mb/hr), convective-scale flux of total water (50 w/m²) and convective-scale heating rate (0.25°C/hr) fields for experiment AB4 at 12 hours. The quantities in parentheses denote the respective contour intervals.

EXPERIMENT AB4   V VELOCITY (M/S)   t = 24.00 HOURS

EXPERIMENT AB4   RELATIVE HUMIDITY   t = 24.00 HOURS

EXPERIMENT AB4   OMEGA (MB/HOUR)   t = 24.00 HOURS

EXPERIMENT AB4   CONVECTIVE FLUX L(Q+L) (W/M**2)   t = 24.00 HOURS

EXPERIMENT AB4   SPCTRL HEATING RATE (C/HR)   t = 24.00 HOURS
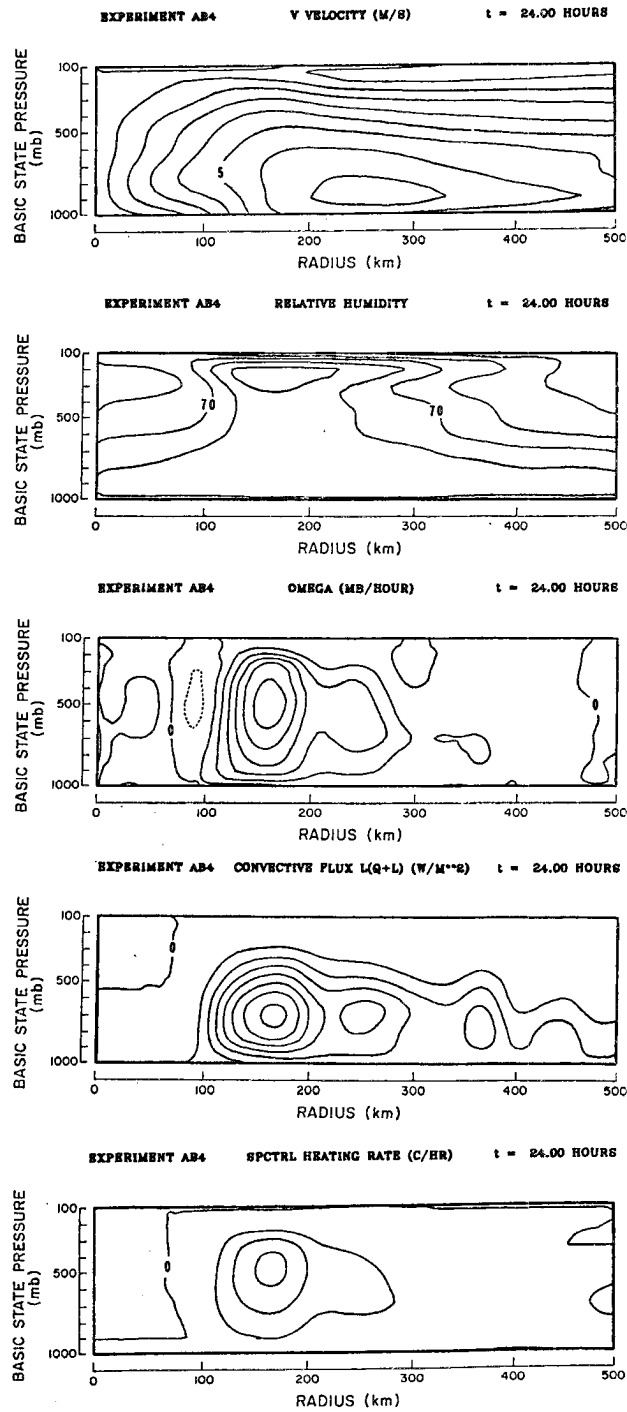
Figure 6.7   Same as Figure 6.6 but at 24 hours.

EXPERIMENT AD1   **V VELOCITY (M/S)**   **t = 12.00 HOURS**

EXPERIMENT AD1   **RELATIVE HUMIDITY**   **t = 12.00 HOURS**

EXPERIMENT AD1   **OMEGA (MB/HOUR)**   **t = 12.00 HOURS**

EXPERIMENT AD1   **CONVECTIVE FLUX L(Q+L) (W/M**2)**   **t = 12.00 HOURS**

EXPERIMENT AD1   **SPCTRL HEATING RATE (C/HR)**   **t = 12.00 HOURS**
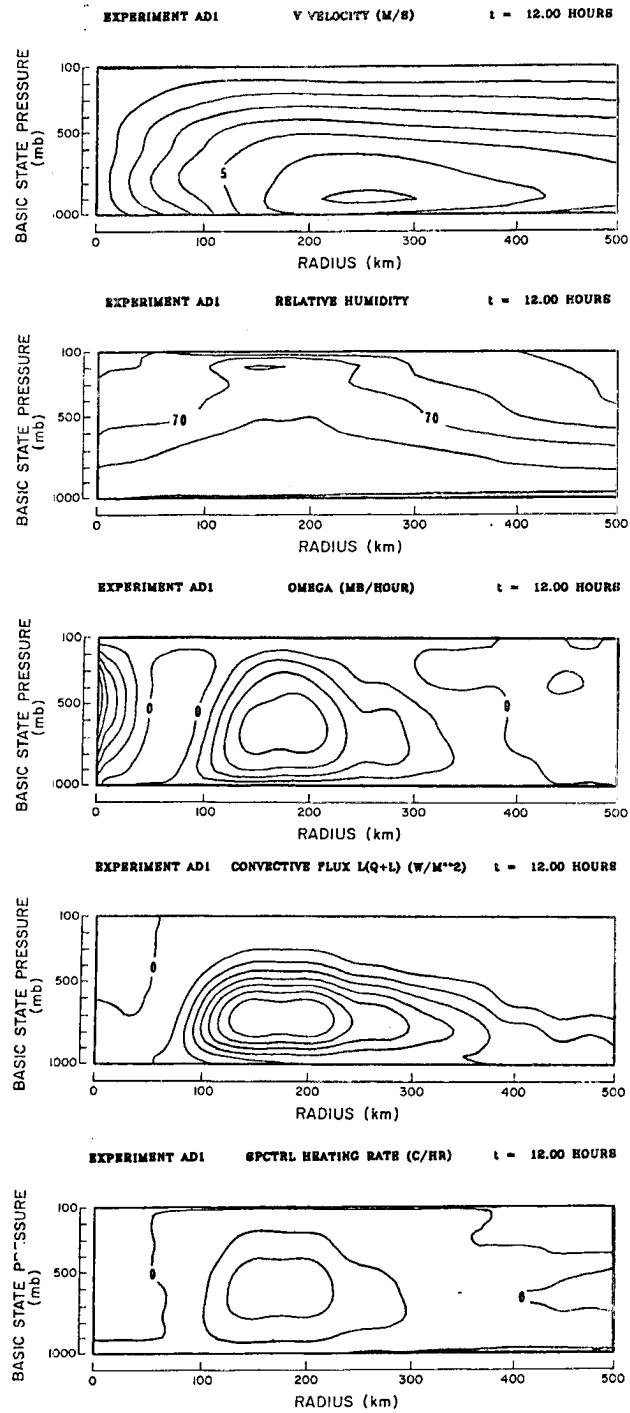
Figure 6.8   Same as Figure 6.6 but for experiment AD1.

EXPERIMENT AD1   V VELOCITY (M/S)   t = 24.00 HOURS

EXPERIMENT AD1   RELATIVE HUMIDITY   t = 24.00 HOURS

EXPERIMENT AD1   OMEGA (MB/HOUR)   t = 24.00 HOURS

EXPERIMENT AD1   CONVECTIVE FLUX L(Q+L) (W/M**2)   t = 24.00 HOURS

EXPERIMENT AD1   SPCTRL HEATING RATE (C/HR)   t = 24.00 HOURS
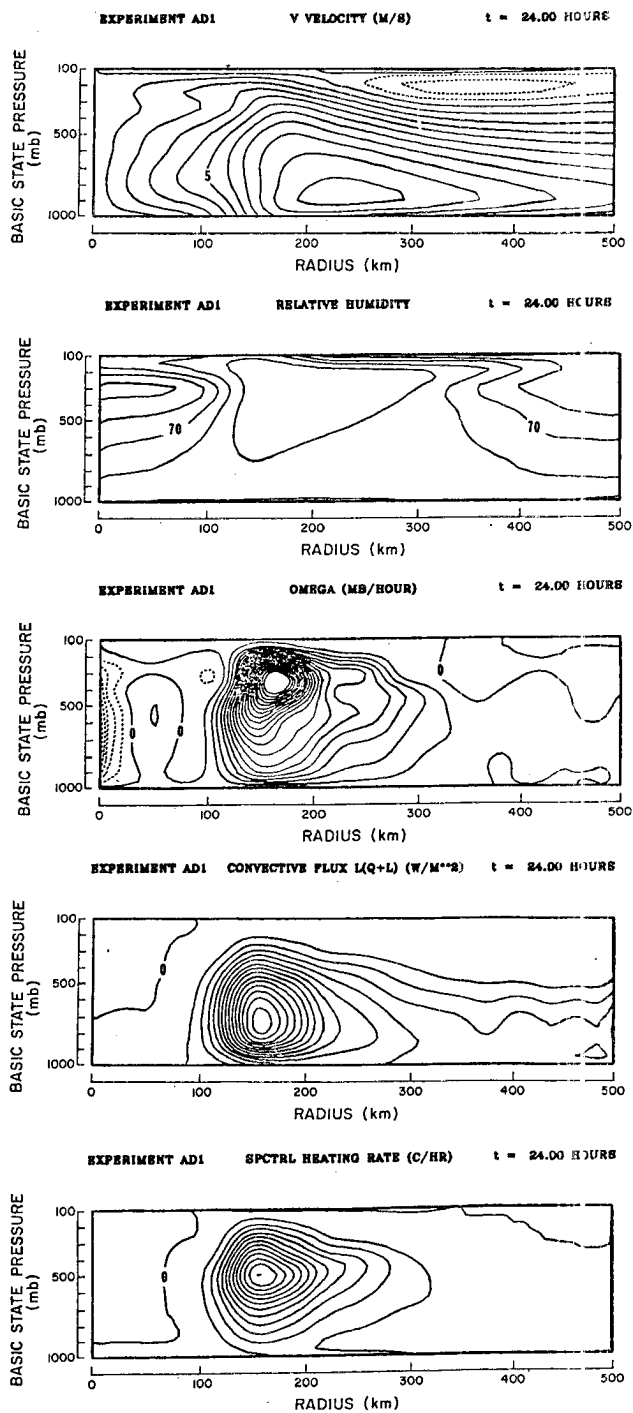
Figure 6.9   Same as Figure 6.6 but for experiment AD1 at
24 hours.

cumulus convection, the horizontal gradients appear to play a role in the organization of the radial circulation, contributing to a determination of both horizontal scale and intensity. We also note a pronounced response of cumulus convection to the incorporation of a radiational cooling as has been suggested by the diagnostic studies of Yanai et al. (1976) and Stephens and Wilson (1980). This is most clearly seen in Fig. 6.4 which shows a strongly bimodal distribution of convection in the outer regions (cf. Fig. 5.9). Consequently, we are led to conclude that radiative processes should not be neglected in numerical investigations of the development of tropical disturbances.

6.2 Incorporation of Cumulus Momentum Transport

The modification of the large-scale momentum fields by parameterized cumulus convection has generally been ignored in numerical modeling efforts even though many observational and theoretical studies have indicated that convective-scale contributions to the large-scale dynamic budgets can be significant (e.g. Gray, 1967; Houze, 1973; Reed and Johnson, 1974; Stevens et al., 1977; Schneider and Lindzen, 1977; Stevens and Lindzen, 1978; Shapiro, 1978; Stevens, 1979; Silva Dias, 1979). Since this process appears to be fundamental to large-scale tropical circulations, we have included a convective-scale momentum transport which essentially involves a redistribution of horizontal momentum by the cumulus ensemble predicted by the Arakawa-Schubert cumulus parameterization. This down gradient approach is frequently referred to as 'cumulus friction' (e.g. Stevens et al., 1977).

Recently, Gray (1979) and McBride (1979) have suggested that cumulus induced momentum accelerations may be important to the genesis of tropical storms by accelerating the tangential wind in the upper
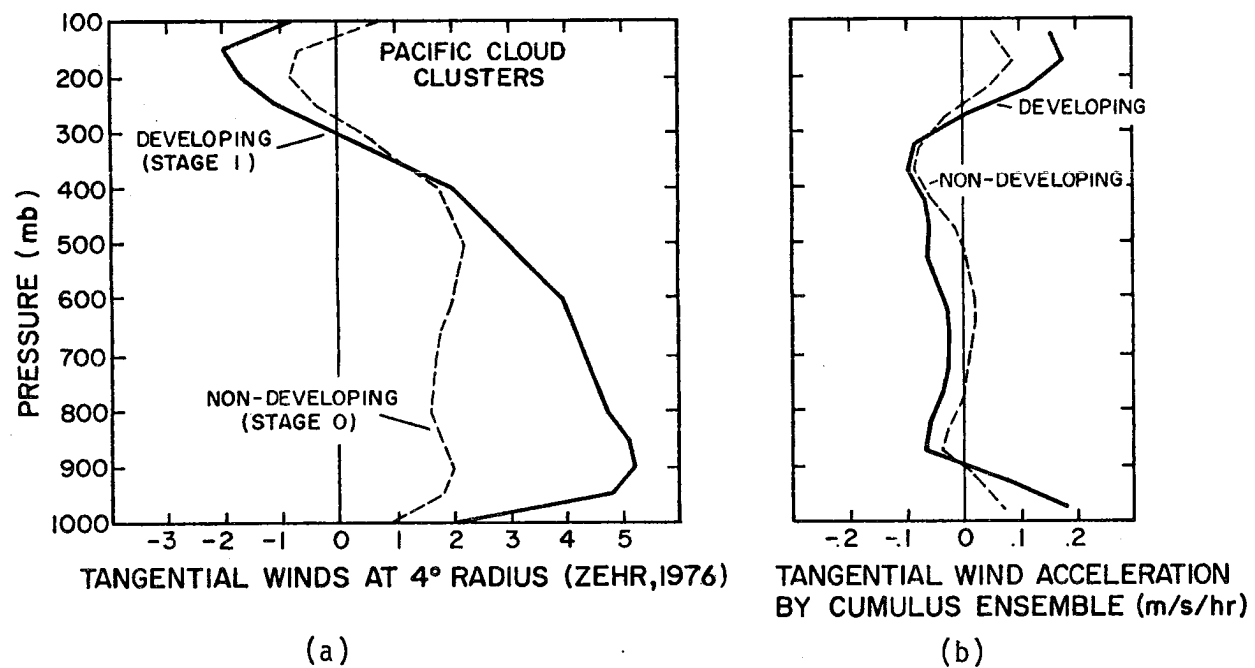
Figure 6.10 (a) Vertical profiles of tangential wind at 4 degrees
radius for a developing and nondeveloping Pacific
cloud cluster (Zehr, 1976).

(b) Cumulus induced accelerations of tangential wind
profiles given in Figure 6.10a (see text).

and lower troposphere. Although a convective-scale momentum source is invoked to produce such accelerations, we shall show that a simple redistribution of horizontal momentum by the cumulus ensemble can be expected to produce similar accelerations of the tangential wind. The vertical profiles of the tangential wind for developing and nondeveloping cloud clusters are quite different with the developing systems generally exhibiting more vertical shear (Zehr, 1976; McBride, 1979). Fig. 6.10a gives an example of the vertical profiles of tangential wind at 4 degrees radius for a developing and nondeveloping Pacific cloud cluster (Zehr, 1976). In order to determine in an approximate sense what effect cumulus friction would have on these profiles, sub-ensemble budgets of v momentum were calculated for each profile using the mean Marshall Islands thermodynamic structure to estimate the entrainment rate for each sub-ensemble (Yanai et al., 1973, 1976). Using the diagnostically obtained cloud base mass flux distribution of Yanai et al. (1976) an acceleration of the tangential wind profiles by cumulus convection was obtained. These are illustrated in Fig. 6.10b. Upper and lower tropospheric accelerations are seen in both cases but with much larger magnitudes for the developing cluster wind profile suggesting that cumulus friction may be a process which helps to differentiate between developing and nondeveloping vortices.

The vertical redistribution of horizontal momentum by cumulus clouds may be more important to the dynamics of an evolving tropical disturbance than one might expect. In section 3.3 it was demonstrated that heating the atmosphere on horizontal scales typical of a tropical cloud cluster is an inefficient means of generating balanced
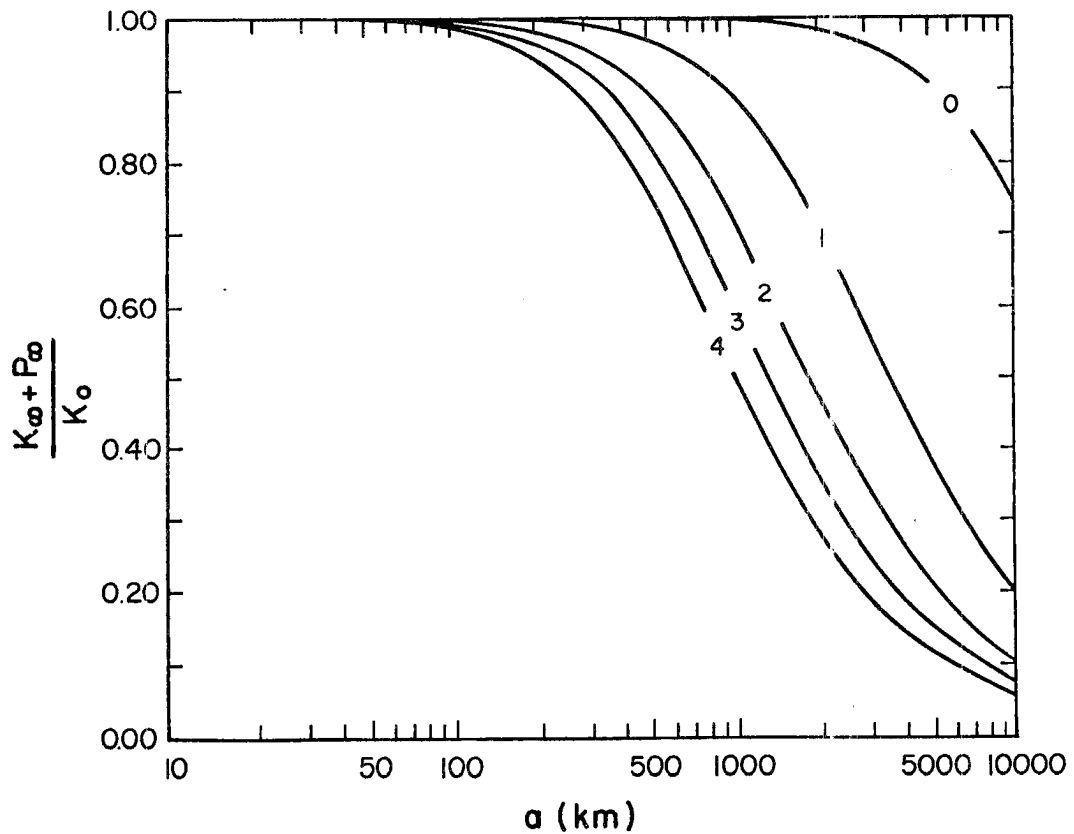
Figure 6.11 The fraction of the initial energy which is
partitioned to geostrophic flow as a function
of the horizontal scale of an initial tangen-
tial wind disturbance. The curves have been
computed using (6.3) for the first five values
of $(gh_n)^{1/2}$ given in the last column of Table 3.1
and with an f corresponding to a latitude of
20°N.

(geostrophic) flow. On the other hand, it can be shown that forcing the rotational part of the wind field (tangential component in this study) on similar horizontal scales can be a very efficient means of generating balanced flow (cf. Schubert et al., 1980; Silva Dias and Schubert, 1979).

In the example discussed in chapter 3 we considered an initial potential vorticity of the form

$$\frac{\partial r\hat{v}(r,0)}{r\partial r} - \frac{f}{gh_n} \hat{\Phi}_n(r,0) = \begin{cases} f & r < a \\ \\ 0 & r \geq a \ , \end{cases} \tag{6.1}$$

for which the initial relative vorticity was assumed to vanish. A second interpretation of this initial condition on the potential vorticity is that there is no initial geopotential perturbation and the initial tangential wind is given by

$$r\hat{v}_n(r,0) = \begin{cases} \dfrac{fr^2}{2} & r < a \\ \\ \text{const.} & r \geq a \ . \end{cases} \tag{6.2}$$

In order to compute the energetics of such an initial condition it is necessary to assume that const. $= 0$, i.e. a discontinuous initial tantential wind. The energy partition $\dfrac{K_\infty + P_\infty}{K_0}$ is then obtained in a similar fashion to the case discussed in section 3.3, and is given by

$$\frac{K_\infty + P_\infty}{K_0} = 4K_2 \left[\frac{f}{(gh_n)^{\frac{1}{2}}} a \right] I_2 \left[\frac{f}{(gh_n)^{\frac{1}{2}}} a \right] \ . \tag{6.3}$$

This energy partition is plotted in Fig. 6.11 as a function of dimensional horizontal scale a, at 20°N, for the first five values of
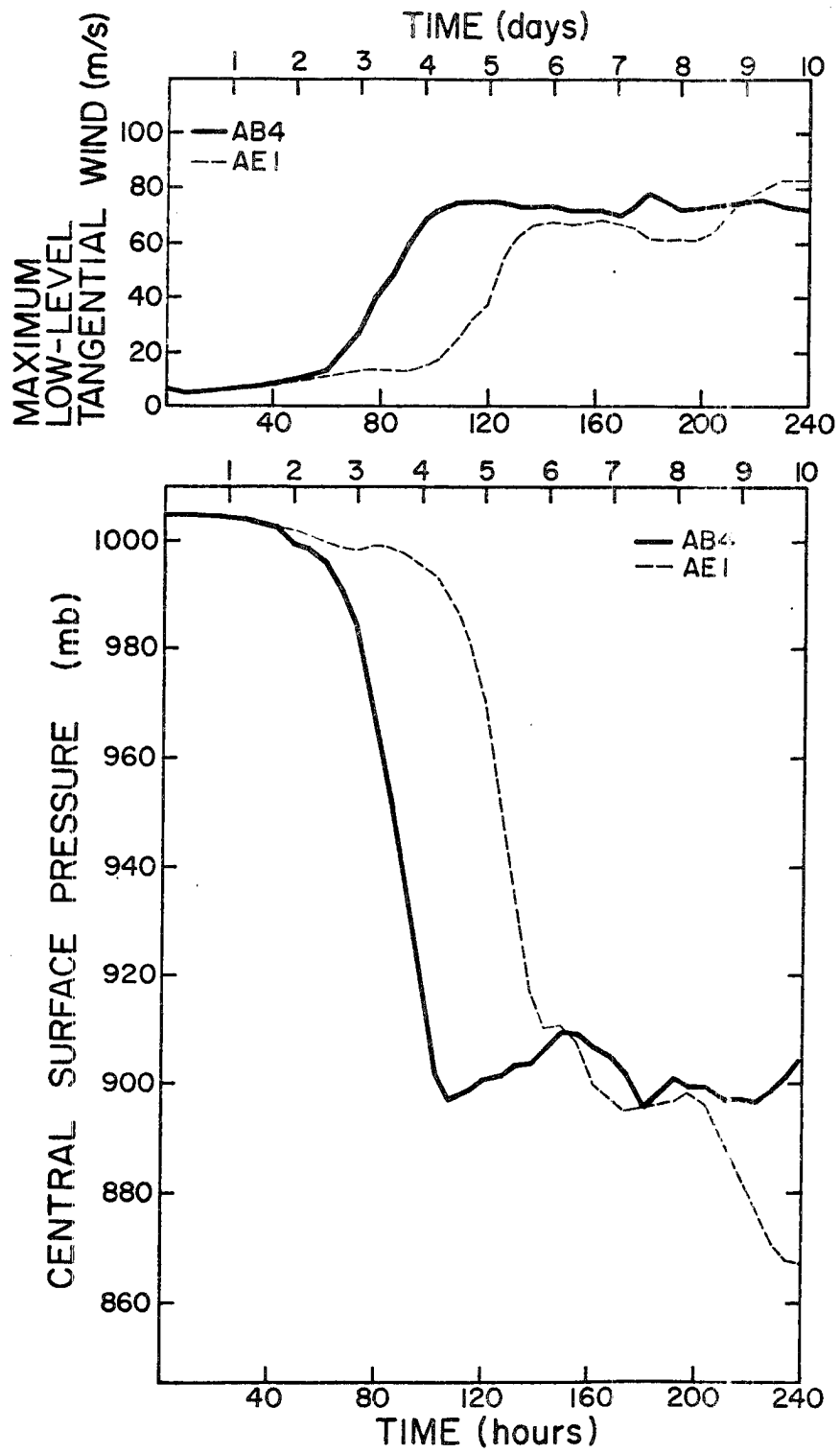
Figure 6.12   Same as Figure 6.2 but for experiments AB4 and AE1.
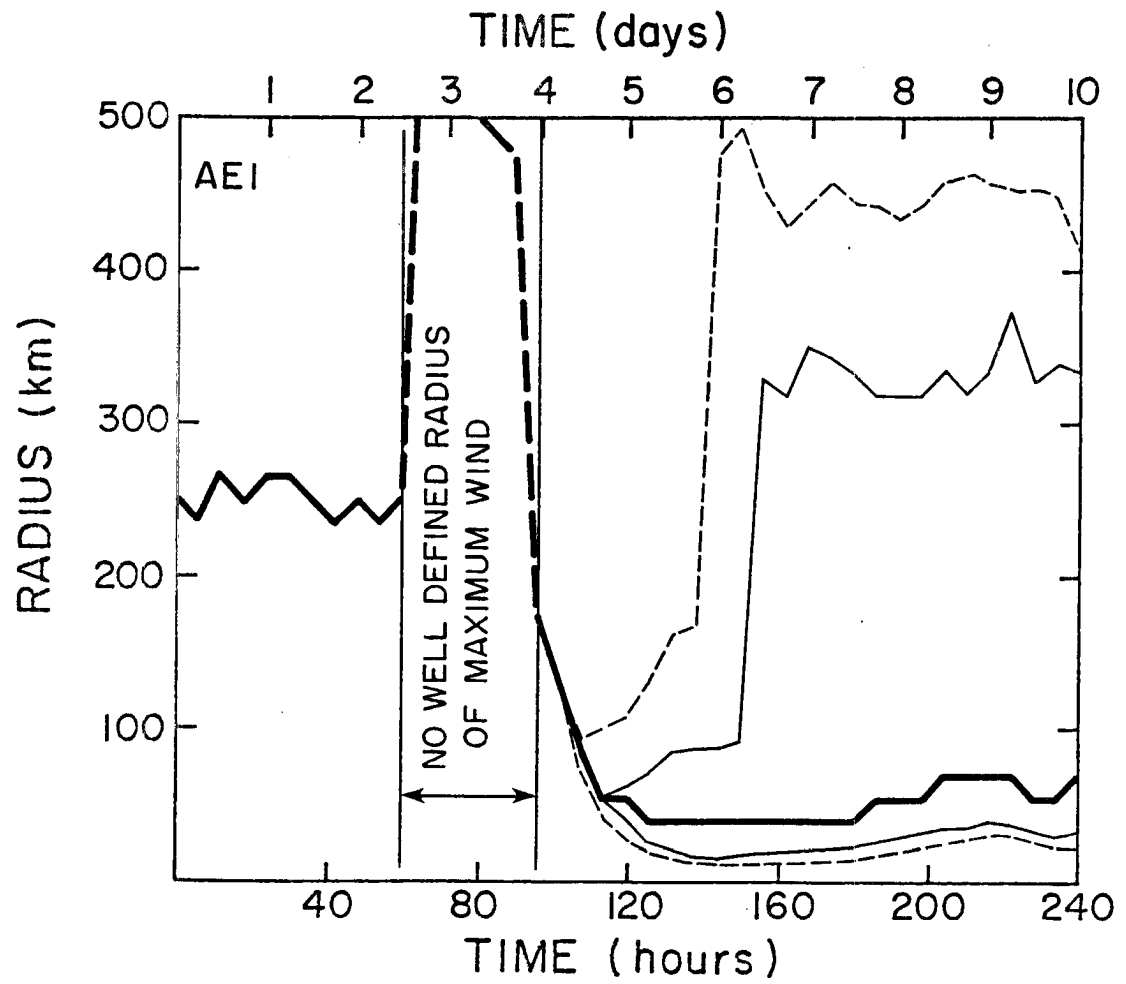
Figure 6.13   Same as Figure 6.3 but for experiment AE1.

$(gh_n)^{1/2}$ given in the last column of Table 3.1. As in Fig. 3.4, for a given horizontal scale a, the difference between $\dfrac{K_\alpha + P_\infty}{K_0}$ and unity represents the fraction of the initial energy partitioned to outward propagating gravity-inertia waves. In sharp contrast to Fig. 3.4 however, we see that for horizontal scales typical of a tropical cloud cluster (e.g. $\leq$ 300 km), the majority of the initial energy is partitioned to balanced flow. Thus, we conclude that the mass field will tend to adjust to changes in the tangential momentum field produced by cumulus convection. Even though convective-scale accelerations of the wind field are likely to be small (see Fig. 6.10b), Fig. 6.11 suggests that they are a highly efficient means of generating balanced flow. It is worthwhile to note that although modifications of the divergent part of the wind field (the radial component in our case) are of little dynamic importance in the linear initial value problem discussed above (since this type of perturbation has zero potential vorticity and is projected entirely onto gravitational modes), such modifications can be of importance in a nonlinear way as we shall see.

Shown in Fig. 6.12 is a comparison of the time evolution of the maximum low level (z $\sim$ 225 m) tangential wind and central surface pressure for experiments AB4 and AE1. The incorporation of cumulus momentum transport in experiment AE1 appears to have a pronounced negative impact on the development of the model storm. Similar results have been obtained by Bliss (1980) who simulated tropical cyclone genesis using the Ooyama (1969a, b) fluid system on an equatorial β-plane. Simulations which included a crude cumulus momentum transport showed a reduction in genesis and development.

EXPERIMENT AE1   V VELOCITY (M/S)   t = 120.00 HOURS

EXPERIMENT AE1   RELATIVE HUMIDITY   t = 120.00 HOURS

EXPERIMENT AE1   TEMPERATURE PERTURBATION (K)   t = 120.00 HOURS

EXPERIMENT AE1   OMEGA (MB/HOUR)   t = 120.00 HOURS

EXPERIMENT AE1   CLOUD BASE MASS FLUX(KG/M**2/HR)   T = 120.00 HOURS
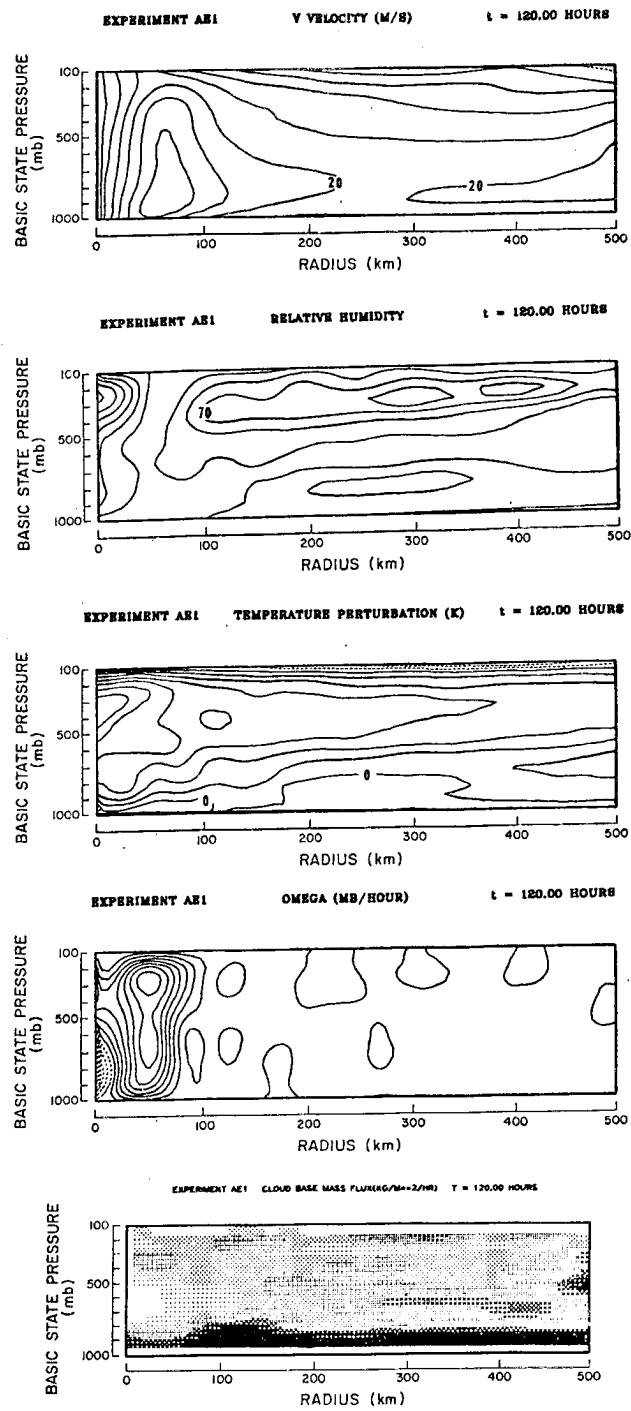
Figure 6.14   Same as Figure 6.4 but for experiment AE1.
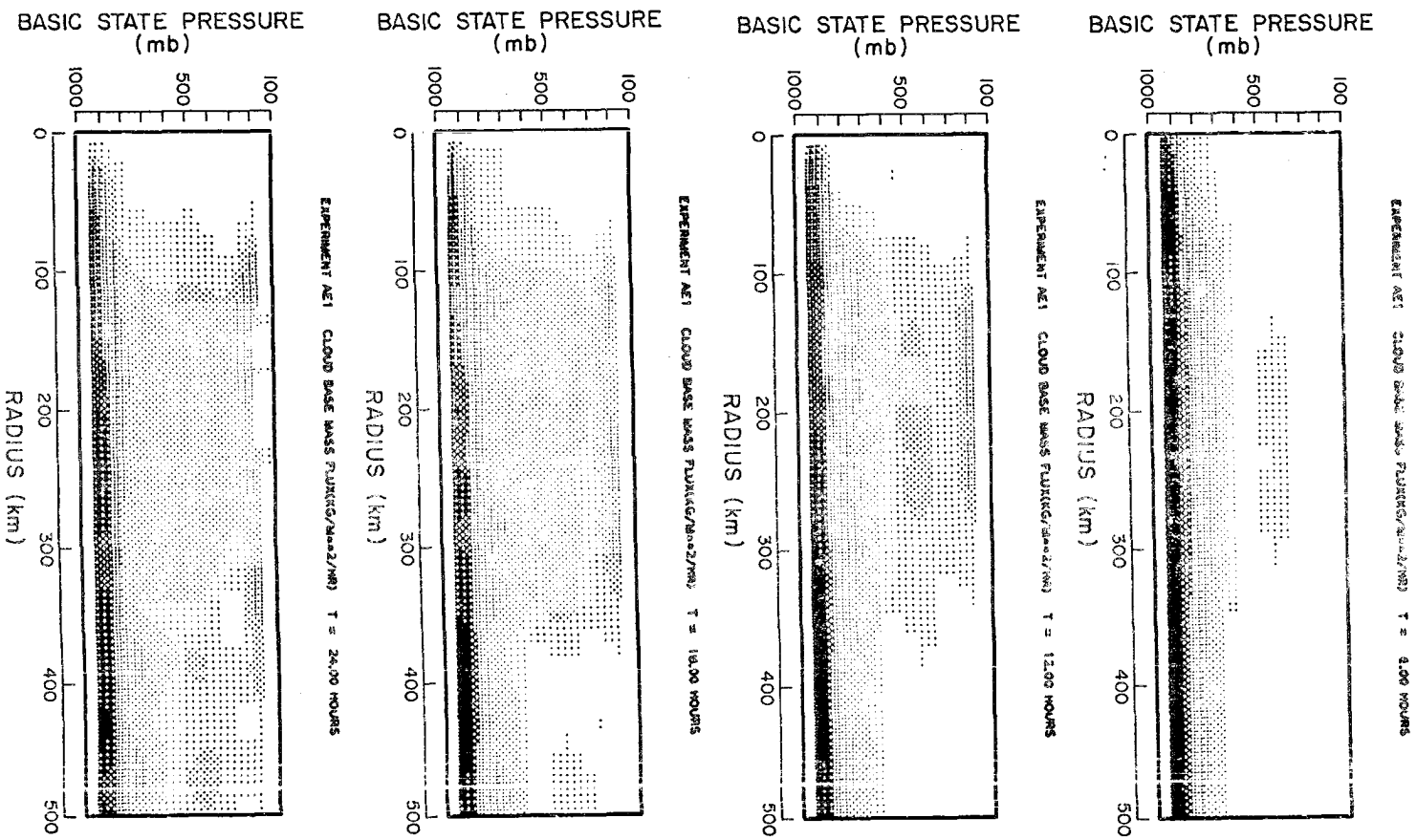
Figure 6.15 Same as Figure 6.5 but for experiment AE1.

EXPERIMENT AE1   V VELOCITY (M/S)   t = 12.00 HOURS

EXPERIMENT AE1   RELATIVE HUMIDITY   t = 12.00 HOURS

EXPERIMENT AE1   OMEGA (MB/HOUR)   t = 12.00 HOURS

EXPERIMENT AE1   CONVECTIVE FLUX L(Q+L) (W/M**2)   t = 12.00 HOURS

EXPERIMENT AE1   SPCTRL HEATING RATE (C/HR)   t = 12.00 HOURS
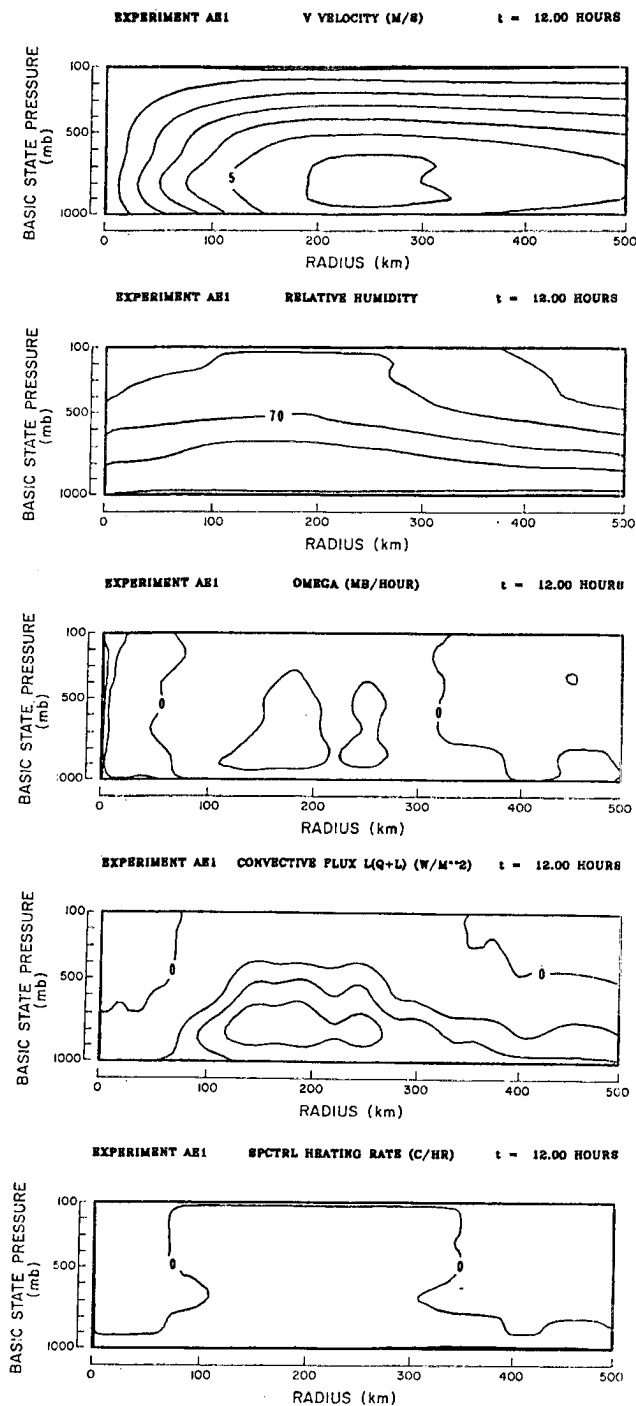
Figure 6.16   Same as Figure 6.5 but for experiment AE1.
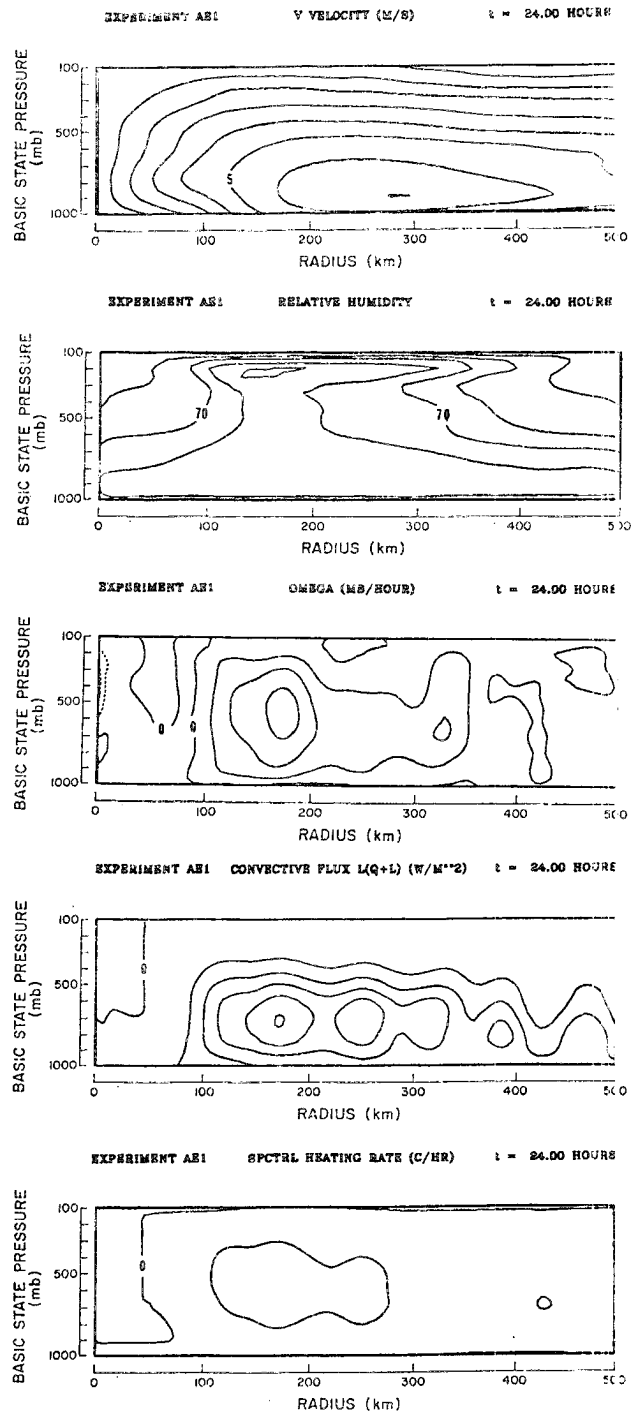
Figure 6.17 Same as Figure 6.6 but for experiment AE1 at 24 hours.

The time evolution of the gross horizontal structure of the model storm is shown in Fig. 6.13. From Figs. 6.12 and 6.13 it can be seen that the model vortex goes through a period of four days with little intensification during which the tangential circulation in the exterior region spins up to give a broad horizontal circulation without a well defined radius of maximum winds. This period is followed by rapid intensification which is similar to that obtained in AB4. The horizontal scale and intensity of the mature storm (before 200 hrs) is quite similar in scale and intensity to AB4 as well (see Fig. 6.13).

The delay in the development of model storm AE1 does not appear to be related to the horizontal distribution of the parameterized convection. The development of the cloud base mass flux distribution field (see Fig. 6.15) in experiment AE1 is similar to AB4 (see Fig. 5.5) although the magnitude is somewhat smaller. This difference in the magnitude of the convective activity is most clearly seen by comparing Figs. 6.16 and 6.17 with Figs. 6.6-6.9. Both the convective-scale transports of total water and the convective-scale heating rates for AE1 are smaller than those in AB4 and considerably smaller than those produced in AD1. Also note the weak, poorly organized character of the vertical motion field in the early stages. This indicates a very slow development of the large-scale transverse circulation which we believe can be explained to be a consequence of the vertical redistribution of horizontal momentum.

Plotted in Fig. 6.18 are vertical profiles of the convective-scale heating rate, and the convective-scale acceleration of the tangential and radial wind at $r = 240.0$ km and $t = 30$ hours (Note that these are fairly typical of the region 100-300 km). The accelerations
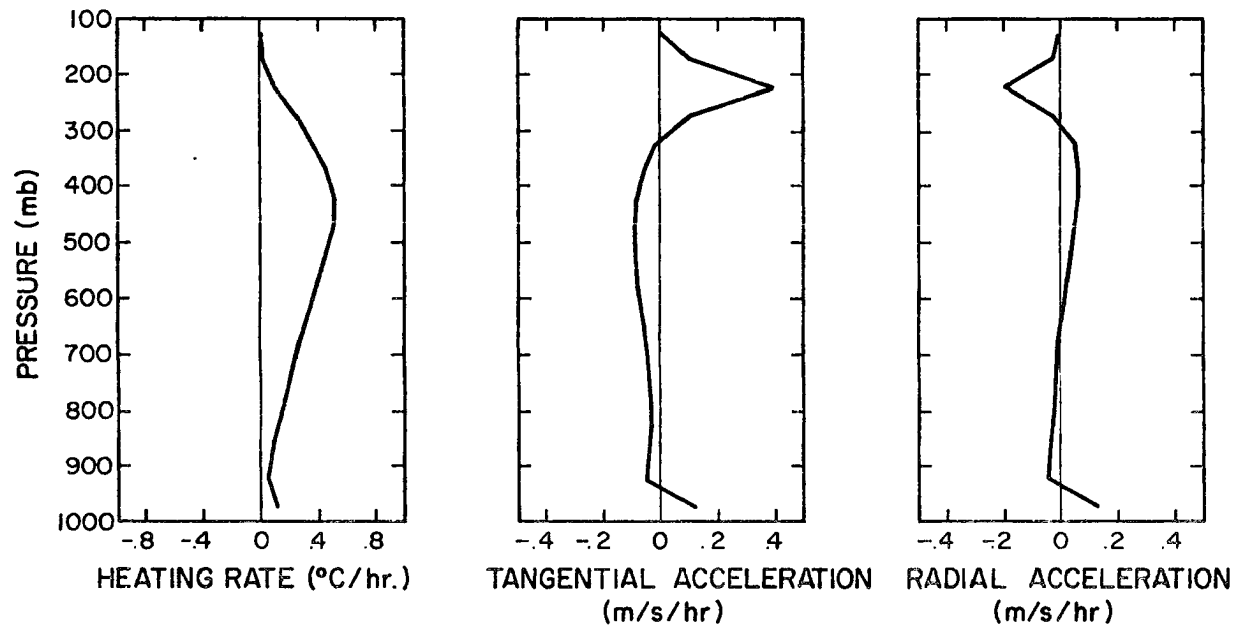
Figure 6.18   Vertical profiles of the convective-scale heating rate, and
the convective-scale accelerations of the tangential and
radial wind components at a radius of 240 km at 30 hours
into the numerical integration.

of the tangential wind component produced by the model are very similar in both vertical structure and magnitude to the diagnostically determined accelerations of Fig. 6.10b. What is of most significance, however, is the acceleration of the radial component of the wind, which shows a strong positive acceleration in the mixed layer and a strong negative acceleration in the upper levels. Thus, the rearrangement of the radial component of momentum by cumulus clouds tends to retard the development of a transverse circulation by slowing both low level inflow and upper level outflow. In this case (AE1) a significant reduction in the horizontal convergence of water vapor accompanies the slowdown in the low level circulation which has the effect of suppressing the cumulus activity in the interior during the early stages of development.

One additional numerical experiment was conducted to address the role of cumulus friction in which the convective-scale rearrangement of radial momentum was neglected (no figures are shown). In this case, there is a slight acceleration of model storm development (2-4 hours) with respect to experiment AB4. The mature storm which is produced is also deeper. This result appears to confirm that it is the vertical redistribution of the radial component of momentum which retards the development of the model storm in experiment AE1.

It is clear from these results that the incorporation of convective-scale transports of horizontal momentum can contribute to significant alterations of the numerical solution. However, we are not yet prepared to conclude that these convective-scale effects will always act one way, i.e. to either accelerate or retard tropical cyclone development. Since the convective-scale accelerations of the
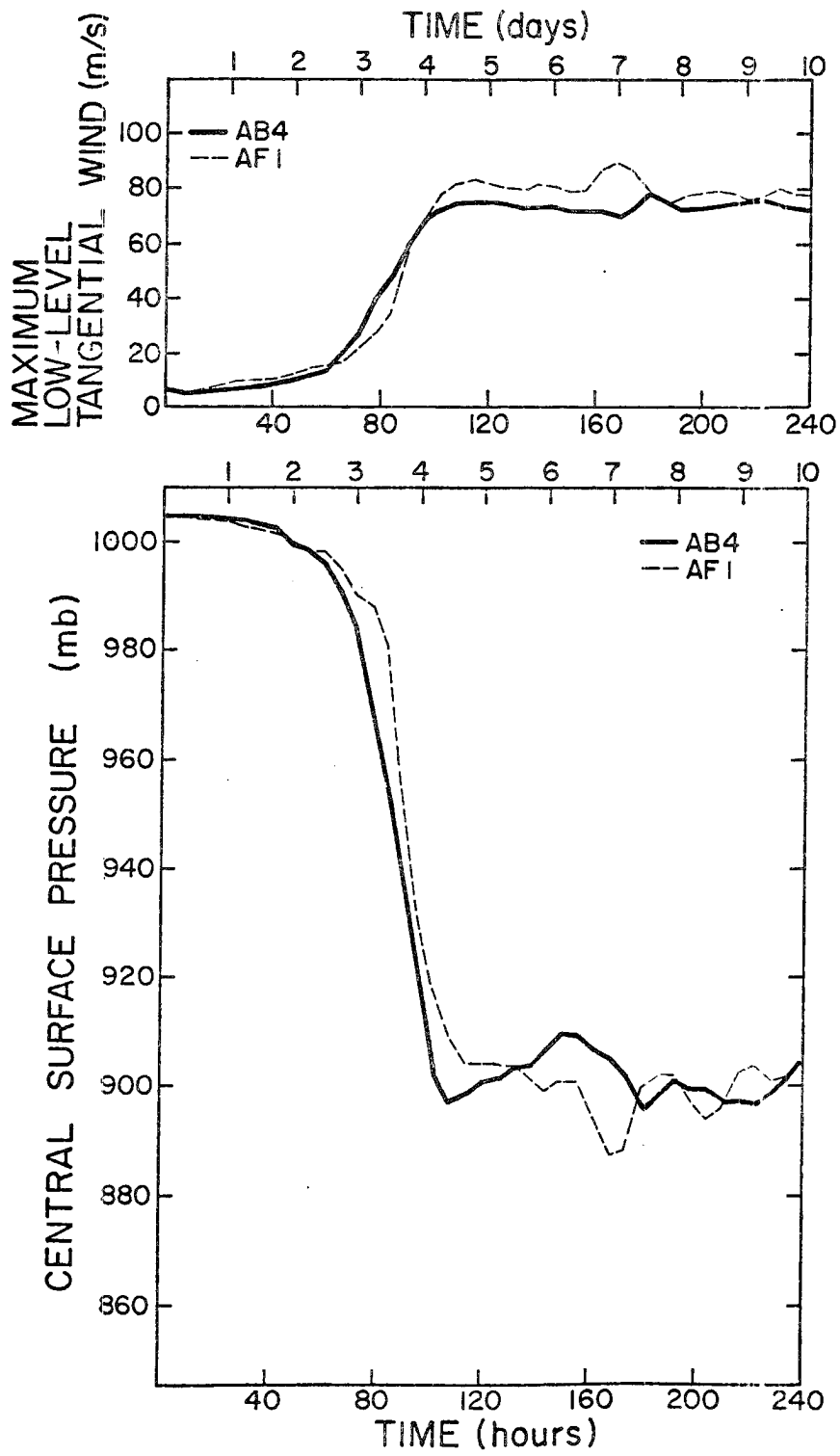
Figure 6.19   Same as Figure 6.2 but for experiments
            AB4 and AF1.
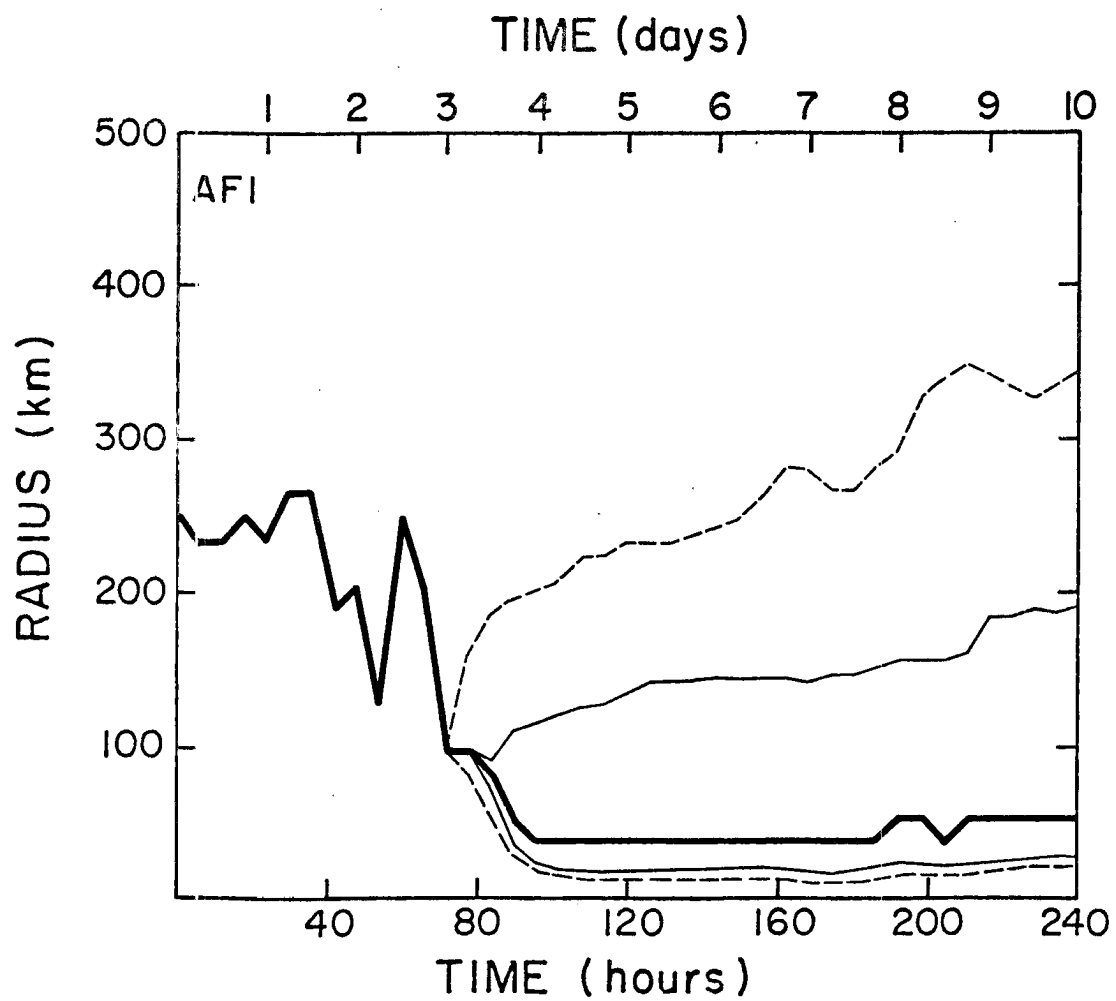
Figure 6.20   Same as Figure 6.3 but for experiment AF1.

large-scale wind are so closely dependent upon the vertical structure of the large-scale wind, and to the intensity of cumulus activity, additional sensitivity studies to the initial condition should be conducted. The sensitivity of the above results to the particular form of the cloud model should also be addressed (such as the incorporation of moist downdrafts). Finally, it is entirely possible that convective-scale redistribution of horizontal momentum may play an important role in the asymmetric structure of a tropical storm. This question goes beyond the present scope of this study, but should be addressed in future asymmetric modeling efforts.

6.3 Incorporation of Both Radiation and Cumulus Momertum Transport

As a final experiment (AF1) we examine the sensitivity of model storm development to the incorporation of both the raciation parameterization used in experiment AD1 and the convective-scale transport of horizontal momentum which was considered in experiment AE1. The results of this numerical experiment are summarized in Figs. 6.19-6.24.

In experiment AD1 we saw that the incorporation of radiation accelerated storm development while experiment AE1 indicated that cumulus transport of momentum retarded development. Thus, it should not be too surprising to see that the development of the model storm including both processes is similar to the development of the model storm which includes neither process. The time evolution of the maximum low level ($z \sim 225$ m) tangential wind and central surface pressure for experiments AF1 and AB4 are compared in Fig. 6.19. The time required to reach the intensification stage is almost identical for each of these simulations, and the final steady state mature storm is also very similar in intensity as determined by central surface pressure. The structure of

EXPERIMENT AF1   V VELOCITY (M/S)   t = 120.00 HOURS

EXPERIMENT AF1   RELATIVE HUMIDITY   t = 120.00 HOURS

EXPERIMENT AF1   TEMPERATURE PERTURBATION (K)   t = 120.00 HOURS

EXPERIMENT AF1   OMEGA (MB/HOUR)   t = 120.00 HOURS

EXPERIMENT AF1   CLOUD BASE MASS FLUX(KG/M**2/HR)   T = 120.00 HOURS
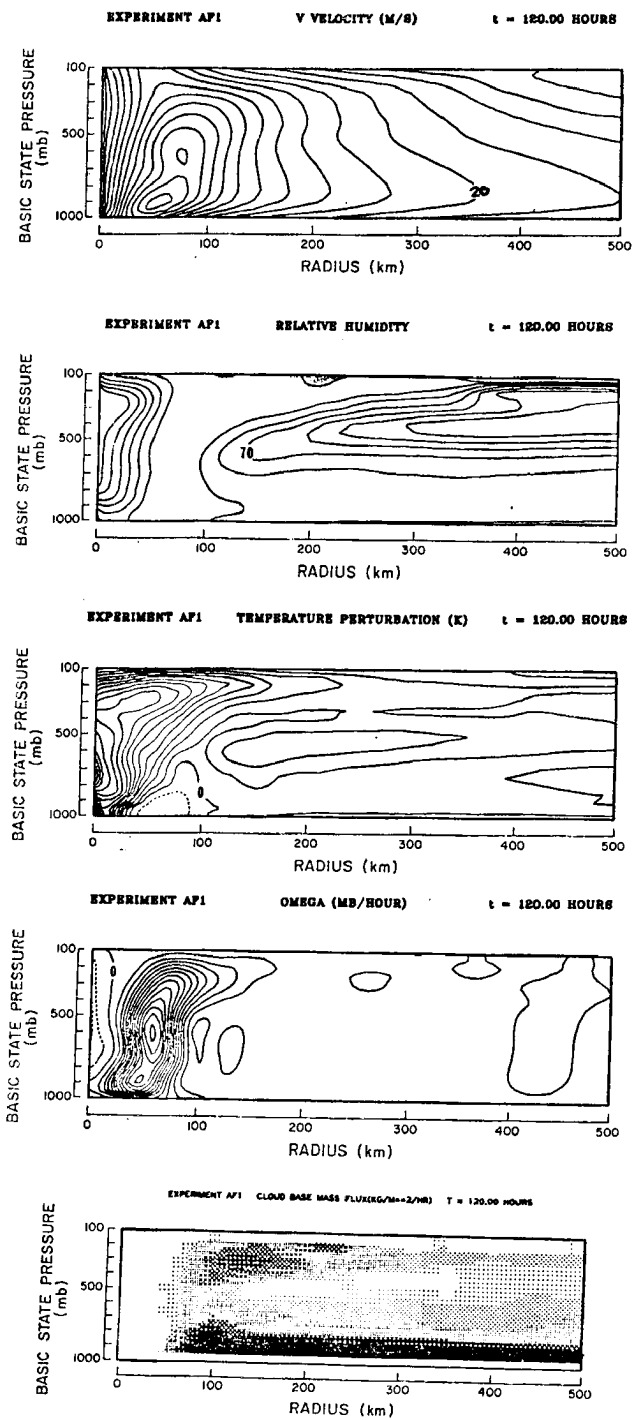
Figure 6.21   Same as Figure 6.4 but for experiment AF1.

EXPERIMENT AF1   CLOUD BASE MASS FLUX(KG/M==2/HR)   T =   6.00 HOURS

EXPERIMENT AF1   CLOUD BASE MASS FLUX(KG/M==2/HR)   T = 12.00 HOURS

EXPERIMENT AF1   CLOUD BASE MASS FLUX(KG/M==2/HR)   T = 18.00 HOURS

EXPERIMENT AF1   CLOUD BASE MASS FLUX(KG/M==2/HR)   T = 24.00 HOURS
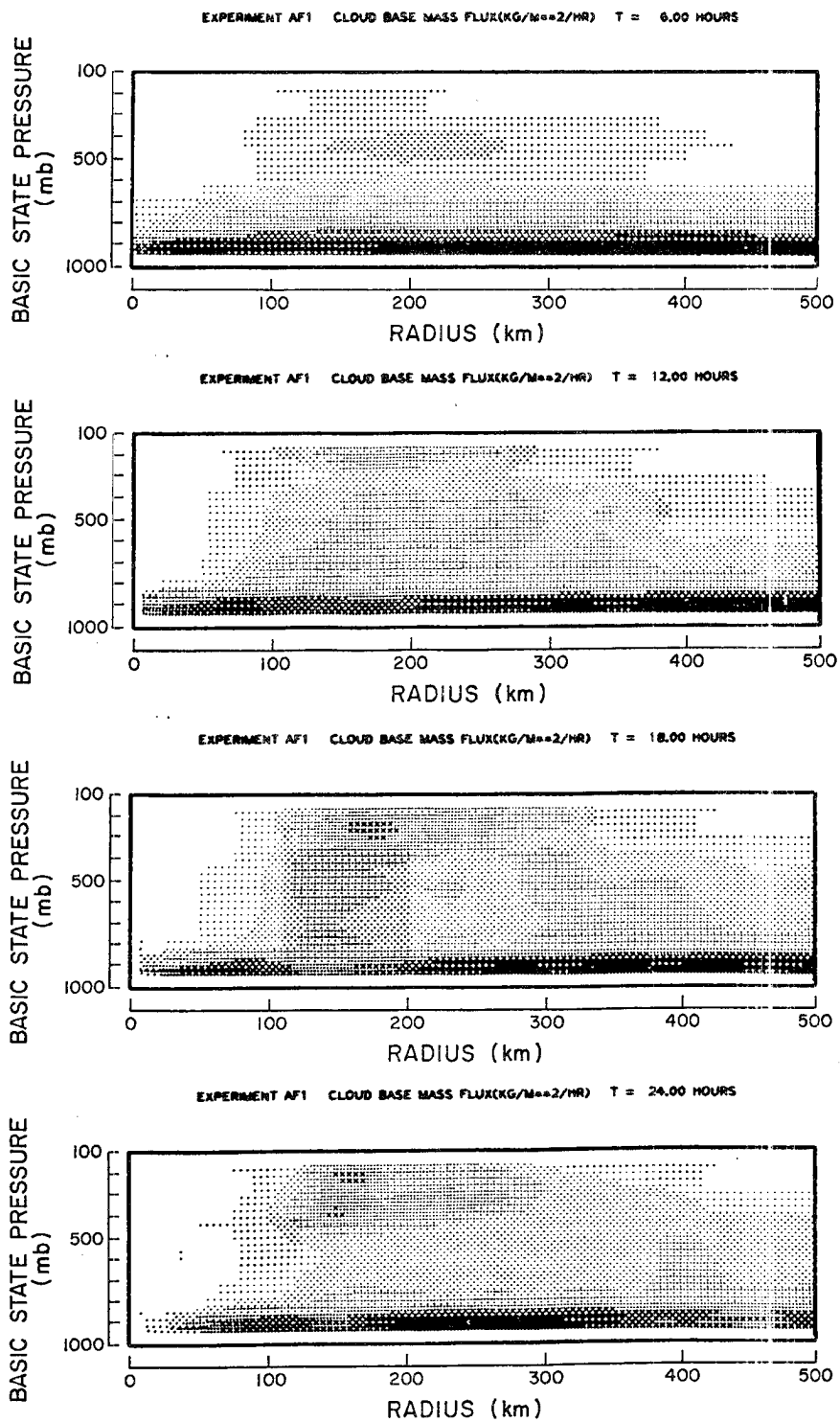
Figure 6.22   Same as Figure 6.5 but for experiment AF1.

the mature storm is quite different, however, as can be seen in Figs. 6.20 and 6.21. The tangential circulation appears to be much more acceptable with regard to the overall organization producing gale and hurricane force winds which are restricted to more reasonable radii. The vertical motion field which is obtained in experiment AF1 appears to be better organized especially in the eyewall region (cf. Figs. 5.9 and 6.4). The relative humidity distribution is also much more reasonable than the one produced in experiment AB4.

The early time evolution of the cloud base mass flux distribution is most like experiment AD1, although not as large in magnitude (see Figs. 6.21 and 6.5). We note that the convective-scale flux of total water most resembles experiment AB4 while the convective-scale heating rate is most like experiment AD1 (Figs. 6.23 and 6.24). The development of the vertical motion field and tangential circulation is obviously more rapid than in experiment AB4 but still somewhat slower than AD1.

These results show that the incorporation of both radiation and cumulus momentum transport leads to reasonable development of a tropical disturbance. The very early development of the transverse circulation is apparently accelerated although the time required to reach a mature stage is somewhat longer. The most significant aspect of the incorporation of both these processes is the marked improvement in the structure of the mature storm.

EXPERIMENT AF1   V VELOCITY (M/S)   t = 12.00 HOURS

EXPERIMENT AF1   RELATIVE HUMIDITY   t = 12.00 HOURS

EXPERIMENT AF1   OMEGA (MB/HOUR)   t = 12.00 HOURS

EXPERIMENT AF1   CONVECTIVE FLUX L(Q+L) (W/M**2)   t = 12.00 HOURS

EXPERIMENT AF1   SPCTRL HEATING RATE (C/HR)   t = 12.00 HOURS
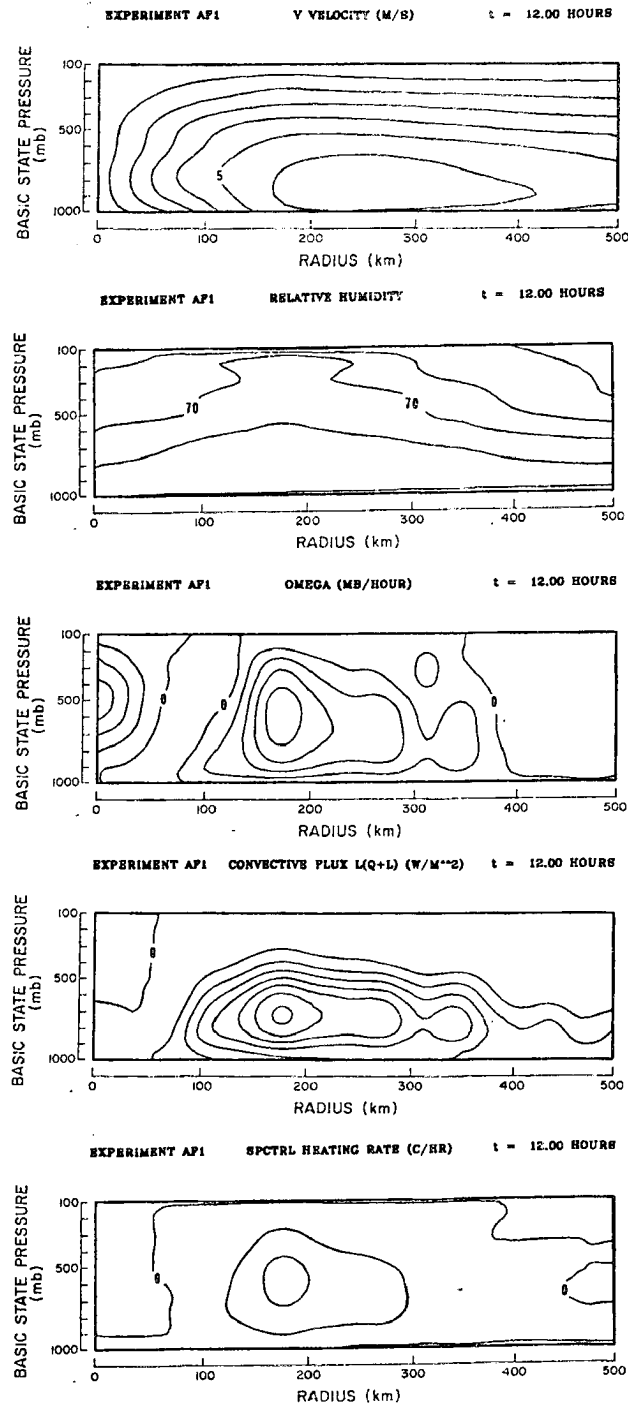
Figure 6.23   Same as Figure 6.6 but for experiment AF1.
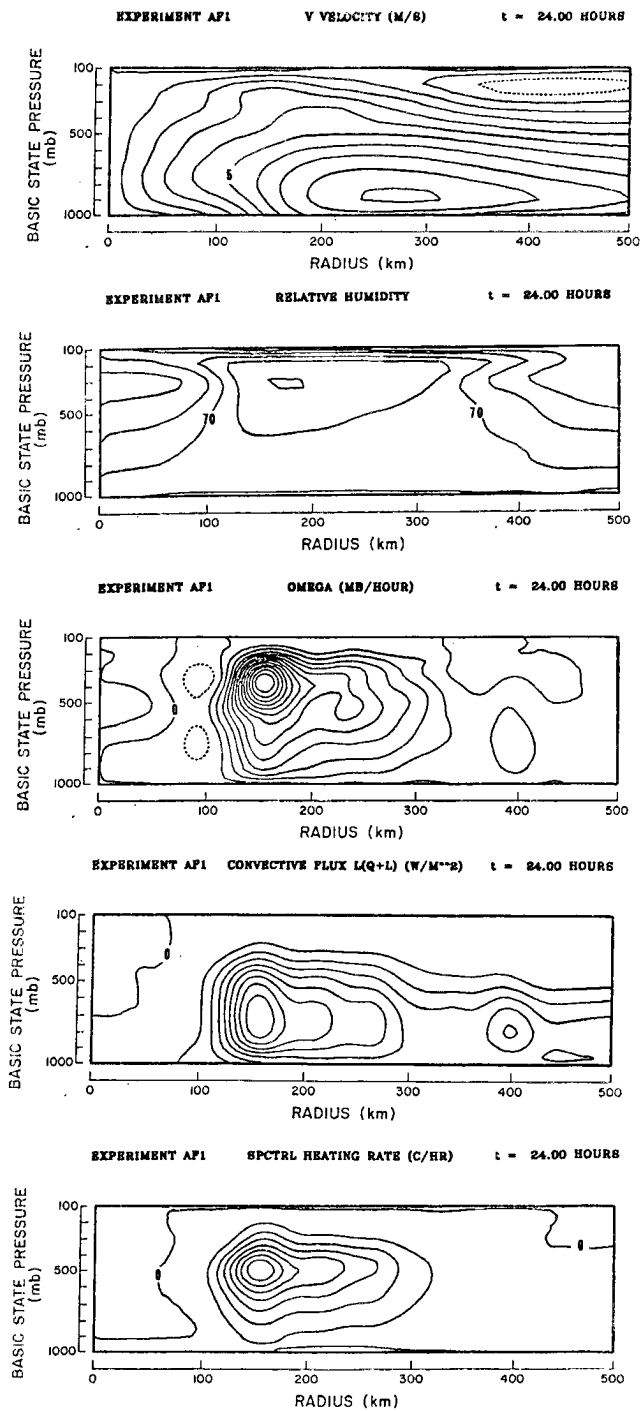
Figure 6.24 Same as Figure 6.6 but for experiment AF1 at 24 hours.

7.0 SUMMARY AND CONCLUSIONS

We have developed an eighteen level, axisymmetric primitive equation tropical cyclone model which uses the Arakawa-Schubert spectral cumulus parameterization and have successfully simulated the development of a weak tropical disturbance into a mature hurricane. The quasi-equilibrium hypothesis, which involves the solution of an integral equation for the cloud base mass flux distribution function, has been formulated as an optimization problem (the optimal adjustment method). The cloud base mass fluxes which are produced using this formulation are quite reasonable bearing great resemblance to the mass flux distributions obtained in diagnostic budget studies (e.g. Yanai et al., 1976).

Rosenthal (1978) has shown that the development of a reasonable hurricane circulation can be achieved without the use of a cumulus parameterization in models with horizontal grid resolutions of a few tens of kilometers. Despite the crude nature of the large-scale condensation process employed in our model, we too have been able to simulate the development of a hurricane with only the explicit release of latent heat. These results appear to verify the conclusion that the early attempts to simulate tropical cyclones along these lines were flawed (e.g. Kasahara, 1961, 1962; Syono, 1962). The initial growth of small-scale features is apparently controlled by nonlinear effects which were probably not well represented in these early models. Although we have been successful in simulating hurricane development with explicit latent heat release, the differences in the development, intensity and structure of the model storms simulated with parameterized convection are significant. It is difficult to draw a general conclusion regarding the

174

desirability of explicitly resolving cumulus convection, but in our opinion such an approach would probably most appropriately be employed in a non-hydrostatic model with a much finer grid resolution (on the order of several hundred meters).

The linear analysis of chapter 3 demonstrates that most of the available potential energy generated by latent heat release, on horizontal scales typical of a tropical cloud cluster, is partitioned to gravity inertia wave motion rather than to the balanced flow. In this way most of the generated energy is radiated away to the far field emphasizing the need for the lateral boundary condition in a primitive equation model to be able to transmit gravity-inertia waves. Since most boundary conditions are deficient in this regard, an approximate cylindrical pure gravity wave radiation condition has been derived for use in axisymmetric primitive equation models. Simple diagnostic numerical integrations show that for the first few vertical modes, gravity inertia waves are, for all practical purposes, transmitted by this boundary condition. Several numerical experiments with the tropical cyclone model have also been conducted to illustrate the sensitivity of the solution to the exact form of the lateral boundary condition. Noticeably earlier development of the model storm occurs with the radiation condition when cumulus convection is parameterized as compared to the two most common boundary conditions in present use, the conditions of zero divergence and zero radial wind.

The Arakawa-Schubert cumulus parameterization demonstrates a strong sensitivity to the initial moisture distribution in the absence of an initial transverse circulation. In an experiment with a moisture distribution which is independent of radius, development of the model

vortex is extremely slow and highly unusual. The incorporation of a horizontal gradient in the initial moisture distribut on results in more rapid and more reasonable growth of the initial circulation.

The sensitivity of model storm development to the processes of radiation and cumulus momentum transport has been examined. A simple net radiational cooling parameterization was included in the model which produced earlier intensification and a deeper mature storm. Additionally, a marked decrease in the horizontal scale of the simulated hurricane was observed suggesting that radiative processes may play an important role in determining the scale of tropical disturbances.

The incorporation of cumulus transports of horizontal momentum had a strong negative effect on the development of our model vortex. Strong accelerations of the upper and lower level radial wind field tended to slow the development of the transverse circulation which in turn slowed the development of the model storm. The accelerations of the low level inflow appear to reduce the low level convergence of water vapor which has a significant impact on the development of cumulus convection in the interior. Although the results of this experiment indicate that cumulus momentum transport does not enhance tropical cylcone development, further study is required. The sensitivity of this process to the initial condition as well as the sensitivity to the particular form of the cloud model employed in the cumulus parameterization should be explored.

The most interesting numerical experiment conducted is the final one which includes both radiation and the convective-scale transport of horizontal momentum. In a gross sense, the development of this model storm is remarkably similar to the development of a model storm

which incorporates neither the process of radiation nor cumulus momentum transport. One very important distinction, however, is the much more reasonable structure of the mature storm indicating that these processes may be fairly important to the organization and scale of tropical cyclones.

There are, of course, several shortcomings of the present model which became evident during the experimental part of this study. In all cases extremely deep storms are produced by the model, much deeper than are generally observed in nature. Previous experience has indicated that the final intensity of the model storm is somewhat sensitive to frictional effects (in particular the choice of a vertical mixing length for the nonlinear vertical diffusion process). We have treated the surface energy exchanges perhaps too simply, choosing a constant value of the drag coefficient c_D which is likely too low for the mature stage of the simulated storm. A more sophisticated treatment of the eddy surface fluxes of heat, moisture and momentum should be included in future versions of the model. This is likely to improve the results so that the intensity and structure of the mature model storm will bear more resemblance to those observed in nature (cf. Frank, 1977).

The treatment of the mixed layer is also a fairly weak aspect of the present model. Since a mixed layer of variable depth is not included, we find it necessary to allow cumulus convection to interact directly with the heat, moisture and momentum budgets of our constant depth 'mixed layer'. This formulation, coupled with the simple cloud model used in the cumulus parameterization, results in direct heating

of the mixed layer by parameterized cumulus convection. The magnitude of this heating can probably be reduced by a more careful selection of the jump in dry static energy across the top of the mixed layer, but this will not completely eliminate the questionable heating in the mixed layer. We feel there are two ways to improve this aspect of the tropical cylone model, the first of which involves a generalization of the cloud model in the cumulus parameterization so as to include moist downdrafts (e.g. Johnson, 1976). Such a modification might help to correct the low level heating produced by the convection as well as give different and perhaps improved results with regard to cumulus transports of horizontal momentum. Secondly, a mixed layer of variable depth should eventually be incorporated into the model. In the present sigma coordinate model, the introduction of such a mixed layer has certain computational disadvantages since the top of the mixed layer is not necessarily a coordinate surface. However, it is possible to design a generalized sigma coordinate system in which both the ground and the top of the mixed layer are coordinate surfaces.

Finally, a liquid water budget equation and a rain water budget equation should probably be included in the system of governing equations (cf. Rosenthal, 1978). Since the present model does not allow storage of liquid water, the large-scale condensation process is required to remove excess condensate immediately. This approach, although probably adequate for a general circulation model, is not realistic for the type of phenomena we are attempting to simulate. We believe that the incorporation of liquid water will help to improve the structure of the inner core of the simulated disturbance (see Shea and Gray, 1973; Gray and Shea, 1973).

REFERENCES

Anthes, R.A., 1971: A numerical model of the slowly varying tropical cyclone in isentropic coordinates. Mon. Wea. Rev., 99, 617-635.

_____, 1972: Development of asymmetries in a three-dimensional numerical model of the tropical cyclone. Mon. Wea. Rev., 100, 461-476.

_____, 1977: Hurricane model experiments with a new cumulus parameterization scheme. Mon. Wea. Rev., 105, 287-300.

_____, S.L. Rosenthal and J.W. Trout, 1971a: Preliminary results from an asymmetric model of the tropical cyclone. Mon. Wea. Rev., 99, 744-758.

_____, J.W. Trout and S.L. Rosenthal, 1971b: Comparisons of tropical cyclone simulations with and without the assumption of circular symmetry. Mon. Wea. Rev., 99, 759-766.

Albrecht, B. and S.K. Cox, 1975: The large-scale response of the tropical atmosphere to cloud-modulated infrared heating. J. Atmos. Sci., 32, 16-24.

Arakawa, A., 1969: Parameterization of cumulus convection. Proc. WMO/IUGG Symp. N.W.P. in Tokyo, November 26-December 4, Tokyo, Japan Meteorological Agency, IV, 1-6.

_____, 1972: Design of the UCLA general circulation model. Numerical simulation of weather and climate, Technical Report 7, Dept. of Meteorology of California, Los Angeles.

_____, Y. Mintz, and collaborators, 1974: The UCLA atmospheric general circulation model. Dept. of Meteorology, UCLA, Los Angeles, California.

_____, and W.H. Schubert, 1974: Interaction of a cumulus cloud ensemble with the large-scale environment, Part I. J. Atmos. Sci., 31, 674-701.

_____, and V.R. Lamb, 1977: Computational design of the basic dynamical processes of the UCLA general circulation model. Methods in Computational Physics, 17, 173-265.

Asselin, R., 1972: Frequency filter for time integrations. Mon. Wea. Rev., 100, 487-490.

Augstein, E., H. Riehl, F. Ostapoff and V. Wagner, 1973: Mass and energy transports in an undisturbed Atlantic trade wind flow. Mon. Wea. Rev., 101, 101-111.

Bennett, J.R., 1976: Open boundary conditions for dispersive waves. J. Atmos. Sci., 33, 176-182.

Betts, A., 1975: Parametric interpretation of trade-wind cumulus budget studies. J. Atmos. Sci., 32, 1934-1945.

Bliss, V.L., 1980: Numerical simulation of tropical cyclone genesis. Ph.D. dissertation, Dept. of Atmos. Sci., University of Washington, 268 pages.

Businger, J. and W. Sequin, 1977: Sea-air surface fluxes of sensible and latent heat and momentum. Report of the U.S. GATE Central Program Workshop held at National Center for Atmospheric Research, Boulder, Colorado, 25 July-12 August 1977, 441-453.

Charney, J.G., and A. Eliassen, 1964: On the growth of the hurricane depression. J. Atmos. Sci., 21, 68-74.

Clark, T.L., 1979: Numerical simulations with a three-dimensional cloud model: lateral boundary condition experiments and multi-cellular severe storm simulations. J. Atmos. Sci., 36, 2191-2215.

Cox, S.K. and K.T. Griffith, 1979: Estimates of radiative divergence during Phase III of the GARP Atlantic Tropical Experiment: Part II: Analysis of Phase III results. J. Atmos. Sci., 36, 586-601.

Daley, R., 1979: The application of non-linear normal mode initialization to an operational forecast model. Atmosphere-Ocean, 17, 97-124.

Dantzig, G.B., 1963: Linear programming and extensions. Princeton University Press, Princeton, 631 pages.

Elvius, T., 1977: Experiments with a primitive equation model for limited area forecasts. Beiträge zur Phys. der Atmosphäre, 50, 367-392.

Erdelyi, A., W. Magnus, F. Oberhettinger, and F.G. Tricomi, 1954: Tables of Integral Transforms, 2 volumes, McGraw-Hill, New York.

Fingerhut, W.A., 1978: A numerical model of a diurnally varying tropical cloud cluster disturbance. Mon. Wea. Rev., 106, 255-264.

Frank, W.M., 1977: The structure and energetics of the tropical cyclone, I: Storm structure. Mon. Wea. Rev., 105, 1119-1135.

Gray, W.M., 1967: The mutual variation of wind shear, and baroclinicity in the cumulus convective atmosphere of the hurricane. Mon. Wea. Rev., 95, 55-74.

_____, 1973: Cumulus convection and larger scale circulations, I: Broadscale and mesoscale considerations. Mon. Wea. Rev., 101, 839-355.

_____, and D.J. Shea, 1973: The hurricanes inner core region, II: Thermal stability and dynamic characteristics. J. Atmos. Sci., 30, 1565-1576.

_____, E. Ruprecht and R. Phelps, 1975: Relative humidity in tropical weather systems. Mon. Wea. Rev., 103, 685-690.

_____, and R. Jacobson, Jr., 1977: Diurnal variation of deep cumulus convection. Mon. Wea. Rev., 105, 1171-1188.

_____, 1979: Hurricanes: their formation, structure and likely role in the tropical circulation. Quart. J. Roy. Meteor. Soc., Supplement to Meteorology Over the Tropical Oceans, 105, 155-218.

Hack, J.J., and W.H. Schubert, 1976: Design of an axisymmetric primitive equation tropical cyclone model. Colorado State University Atmospheric Science Paper No. 263.

Haque, S.M.A., 1952: The initiation of cyclonic circulation in a vertically unstable stagnant air mass. Quart. J. Roy. Meteor. Soc., 78, 394-406.

Harrison, E.J., 1973: Three-dimensional numerical simulations of tropical systems utilizing nested finite grids. J. Atmos. Sci., 30, 1528-1543.

Holland, J.Z. and E.M. Rasmusson, 1973: Measurements of the atmospheric mass, energy and momentum budgets over a 500-kilometer square of tropical ocean. Mon. Wea. Rev., 101, 44-55.

Houze, R.A., Jr., 1973: A climatological study of vertical transports by cumulus-scale convection. J. Atmos. Sci., 30, 1112-1123.

Johnson, R.H., 1976: The role of convective-scale precipitation downdrafts in cumulus and synoptic-scale interactions. J. Atmos. Sci., 33, 1890-1910.

_____, 1977: The effects of cloud detrainment on the diagnosed properties of cumulus populations. J. Atmos. Sci., 34, 359-366.

Jones, R.W., 1977: A nested grid for a three-dimensional model of a tropical cyclone. J. Atmos. Sci., 34, 1528-1553.

Kasahara, A., 1961: A numerical experiment on the development of a tropical cyclone. J. Meteor., 18, 259-282.

_____, 1962: The development of forced convection caused by the release of latent heat of condensation in a hydrostatic atmosphere. Proc. Int. Symp. Numerical Weather Prediction, Tokyo, Sigekata Syôno, Ed., Meteor. Soc. Japan, 387-404.

_____, and K. Puri, 1980: Spectral representation of three-dimensional global data by expansion in normal mode functions. Submitted to Mon. Wea. Rev.

Klemp, J.B., and R.B. Wilhelmson, 1978: The simulation of three-dimensional convective storm dynamics. J. Atmos. Sci., 35, 1070-1096.

Kondo, J., 1975: Air-sea bulk transfer coefficients in diabatic conditions. Bound.-Layer Meteor., 9, 91-112.

Kuo, H.L., 1965: On formation and intensification of tropical cyclones through latent heat release by cumulus convection. J. Atmos. Sci., 22, 40-63.

Kurihara, Y., 1975: Budget analysis of a tropical cyclone simulated in an axisymmetric numerical model. J. Atmos. Sci., 32, 25-59.

_____, and R.E. Tuleya, 1974: Structure of a tropical cyclone developed in a three-dimensional numerical simulation model. J. Atmos. Sci., 31, 893-919.

_____, G.J. Tripoli, and M.A. Bender, 1979: Design of a moveable nested-mesh primitive equation model. Mon. Wea. Rev., 107, 239-249.

Lilly, D.K., 1960: On the theory of disturbances in a conditionally unstable atmosphere. Mon. Wea. Rev., 88, 1-17.

_____, 1980: Proper lateral boundary conditions for convective cloud and storm simulations. To be published.

Lopez, R.E., 1973: A parametric model of cumulus convection. J. Atmos. Sci., 30, 1354-1373.

Lord, S.J., 1978: Development and observational verification of a cumulus cloud parameterization. Ph.D. dissertation, Dept. of Atmos. Sci., UCLA, 359 pages.

Lorenz, E.N., 1960: Energy and numerical weather prediction. Tellus, 12, 364-373.

Luenberger, D.G., 1973: Introduction to linear and nonlinear programming. Addison Wesley Publishers, 364 pp.

Madala, R.V., and S.A. Piacsek, 1975: Numerical simulation of asymmetric hurricanes on a β-plane with vertical shear. Tellus, 27, 453-468.

Mathur, M.B., 1974: A multi-grid primitive equation model to simulate the development of an asymmetric hurricane (Isebell, 1964). J. Atmos. Sci., 31, 371-393.

McBride, J.L., 1979: Observational analysis of tropical cyclone formation. Dept. of Atmos. Sci. Paper No. 308, Colorado State Univ., Fort Collins, CO, 230 pp.

Nitta, T., 1975: Observational determination of cloud mass flux distribution. J. Atmos. Sci., 32, 73-91.

_____, 1977: Response of cumulus updraft and downdraft to GATE A/B-scale motion systems. J. Atmos. Sci., 34, 1163-1186.

_____, 1978: A diagnostic study of the interaction of cumulus updrafts and downdrafts with large-scale motions in GATE. J. Met. Soc. Japan, 56, 232-242.

Obukhov, A.M., 1949: On the question of the geostrophic wind (in Russian), Izv. Akad. Nauk SSSR Ser. Geograf.-Geofiz., 13(4), 281-306. (Engl. transl. available from W. Schubert, Dept. of Atmospheric Science, Colorado State University.)

Ogura, Y., 1964: Frictionally controlled, thermally driven circulation in a circular vortex with application to tropical cyclones. J. Atmos. Sci., 21, 610-621.

_____, and H.R. Cho, 1973: Diagnostic determination of cumulus cloud population from observed large-scale variables. J. Atmos. Sci., 30, 1276-1286.

Ooyama, K., 1964: A dynamical model for the study of tropical cyclone development. Geofis. Int., 4, 187-198.

_____, 1969a: Numerical simulation of the life cycle of tropical cyclones. J. Atmos. Sci., 26, 3-40.

_____, 1969b: Numerical simulation of tropical cyclones with an axisymmetric model. Proceedings of the WMO/IUGG Symposium on Numerical Weather Prediction, Tokyo, 1968. III:81-88.

_____, 1971: A theory on parameterization of cumulus convection. J. Meteor. Soc. Japan, 46, 178-201.

_____, 1973: A preliminary test of the CONTRIBE parameterization of cumulus convection. Paper presented at Study Conference on the Modeling Aspects of GATE, Joint Organizing Committee for GARP, Talahasse, Florida.

Orlanski, I., 1976: A simple boundary condition for unbounded hyperbolic flows. J. Computational Physics, 21, 251-269.

Phillips, N.A., 1957: A coordinate system having some special advantages for numerical forecasting. J. Meteor., 14, 184-185.

Reed, R.J., and R.H. Johnson, 1974: The vorticity budget of synoptic-scale wave disturbances in the tropical western Pacific. J. Atmos. Sci., 31, 1784-1790.

Riehl, H. and J.S. Malkus, 1961: Some Aspects of Hurricane Daisy, 1958. Tellus, 13, 181-213.

Robert, A.J., J. Henderson, and C. Turnbill, 1972: An implicit time integration scheme for baroclinic models of the atmosphere. Mon. Wea. Rev., 100, 329-335.

Rosenthal, S.L., 1970: A circularly symmetric primitive equation model of tropical cyclone development containing an explicit water vapor cycle. Mon. Wea. Rev., 98, 643-663.

_____, 1971: The response of a tropical cyclone model to variations in boundary parameters, initial conditions, lateral boundary conditions, and domain size. Mon. Wea. Rev., 99, 767-777.

_____, 1973: Hurricane modeling experiments with a new parameterization for cumulus convection. NOAA Technical Memorandum, ERL WMPO-4, U.S. Department of Commerce, National Hurricane Research Laboratory, Miami, Florida.

_____, 1978: Numerical simulation of tropical cyclone development with latent heat release by the resolvable scales, I: model description and preliminary results. J. Atmos. Sci., 35, 258-271.

Schneider, E.K. and R.S. Lindzen, 1976: A discussion of the parameterization of momentum exchange by cumulus convection. J. Geophys. Res., 31, 3158-3160.

_____, and _____, 1977: Axially symmetric steady state models of the basic state for instability and climate studies, 1: Linearized calculations. J. Atmos. Sci., 34, 263-279.

Schubert, W.H., 1974: Cumulus parameterization theory in terms of feedback and control. Colorado State University, Atmospheric Science Paper No. 226, Fort Collins, Colorado.

_____, J.J. Hack, P.L. Silva Dias and S.R. Fulton, 1980: Geostrophic adjustment in an axisymmetric vortex. J. Atmos. Sci., 37, 1464-1484.

Shapiro, L.J., 1978: The vorticity budget of a composite African tropical wave disturbance. Mon. Wea. Rev., 106, 806-817.

Shea, D.J. and W.M. Gray, 1973: The hurricanes inner core region, I: Symmetric and asymmetric structure. J. Atmos. Sci., 30, 1544-1564.

Silva Dias, M.F., 1979: Linear spectral model of tropical mesoscale systems. Dept. of Atmos. Sci. Paper No. 311, Colorado State University, Fort Collins, Colorado, 213 pp.

Silva Dias, P.L., and W.H. Schubert, 1977: Experiments with a spectral cumulus parameterization theory. Atmospheric Science Paper No. 275, Dept. of Atmospheric Science, Colorado State University, Fort Collins, Colorado. 132 pages.

_____, and W.H. Schubert, 1979: The dynamics of equatorial mass-flow adjustment. Atmospheric Science Paper No. 312, Department of Atmospheric Science, Colorado State University, Fort Collins, Colorado, 203 pages.

Smagorinsky, J., 1963: General circulation experiments with the primitive equations: I. The basic experiment. Mon. Wea. Rev., 91, 99-164.

Stephens, G.L. and K.J. Wilson, 1980: The response of a deep cumulus convection model to changes in radiative heating. J. Atmos. Sci., 37, 421-434.

Stevens, D.E., R.S. Lindzen, and L.J. Shapiro, 1977: A new model of tropical waves incorporating momentum mixing by cumulus convection. Dyn. Atmos. Oceans, 1, 365-425.

_____, and _____, 1978: Tropical wave-CISK with a moisture budget and cumulus friction. J. Atmos. Sci., 35, 940-961.

_____, 1979: Vorticity, momentum and divergence budgets of synoptic-scale wave disturbances in the tropical eastern Atlantic. Mon. Wea. Rev., 107, 535-550.

Sundqvist, H., 1970a: Numerical simulation of the development of tropical cyclones with a ten-level model, part I. Tellus, 22, 359-390.

_____, 1970b: Numerical simulation of the development of tropical cyclones with a ten-level model, part II. Tellus, 22, 504-510.

Syono, S., 1953: On the formation of tropical cyclones, Tellus, 5, 179-195.

_____, 1962: A numerical experiment of the formation of tropical cyclones. Proc. Int. Symp. Numerical Weather Prediction, Tokyo, Sigekata Syono, Ed., Meteor. Soc. Japan, 405-418.

Temperton, C., and D.L. Williamson, 1979: Normal mode initialization for a multi-level gridpoint model. Tech. Rept. No. 11, European Centre for Medium Range Weather Forecasts, Shinfield Park, Reading, England.

Twomey, S., 1977: Introduction to the mathematics of inversion in remote sensing and indirect measurements. Elsevier Scientific Publishing Co., Amsterdam.

Wada, M., 1979: Numerical experiments of the tropical cyclone by use of the Arakawa-Schubert parameterization. J. Meteor. Soc. Japan, 57, 505-530.

Yamasaki, M., 1968a: Numerical simulation of tropical cyclone development with the use of primitive equations. J. Meteor. Soc. Japan, 46, 178-201.

_____, 1968b: Detailed analysis of a tropical cyclone simulated with a 13-layer model. Papers in Meteorology and Geophysics, 19, 559-585.

_____, 1977: A preliminary experiment of the tropical cyclone without parameterizing the effects of cumulus convection. J. Meteor. Soc. Japan, 55, 11-30.

Yanai, M., 1961a: A detailed analysis of typhoon formation. J. Meteor. Soc. Japan, 39, 187-213.

_____, 1961b: Dynamical aspects of typhoon formation. J. Meteor. Soc. Japan, 39, 283-309.

_____, S. Esbensen, and J.-H. Chu, 1973: Determination of bulk properties of tropical cloud clusters from large-scale heat and moisture budgets. J. Atmos. Sci., 30, 611-627.

_____, J.-H. Chu, T.E. Stark and T. Nitta, 1976: Response of deep and shallow tropical maritime cumuli to large-scale processes. J. Atmos. Sci., 33, 976-991.

Zehr, R., 1976: Tropical disturbance intensification. Colorado State University Atmospheric Science Paper No. 259, Fort Collins, Colorado.

APPENDIX A

Finite Differencing of the Large-Scale Governing Equations

A.1 Space Differencing

For a more complete discussion of the derivations of the finite difference equations the reader is referred to Hack and Schubert (1976).

In the vertical we denote by integer k (1,2,3...K) those levels at which the prognostic variables u, v, T, and q are carried (see Fig. A.1), and by the half integers (1/2, 3/2,...K+1/2) those levels where $\dot{\sigma}$ is carried. The integer level k is representative of a layer of thickness

$$\Delta\sigma_k = \sigma_{k+\frac{1}{2}} - \sigma_{k-\frac{1}{2}} \quad , \tag{A.1}$$

so that

$$\sum_{k=1}^{K} \Delta\sigma_k = 1 \ .$$

We define

$$\sigma_k \equiv \frac{1}{2}(\sigma_{k+\frac{1}{2}} + \sigma_{k-\frac{1}{2}}) \ . \tag{A.2}$$

For the horizontal we will use a distribution of variables as shown in Fig. A.2. The variables u and v are carried at the half integer locations in the horizontal domain while π, T and q are carried at the integer locations. Horizontal momentum fluxes are also defined at the half integer positions. Thus we are led to Fig. A.3 as a 3-dimensional conceptualization of our finite difference mesh.

We will now write the discrete analogues of (2.16)-(2.25). They appear in differential-difference form, leaving the time differencing to a discussion at the end of this appendix.
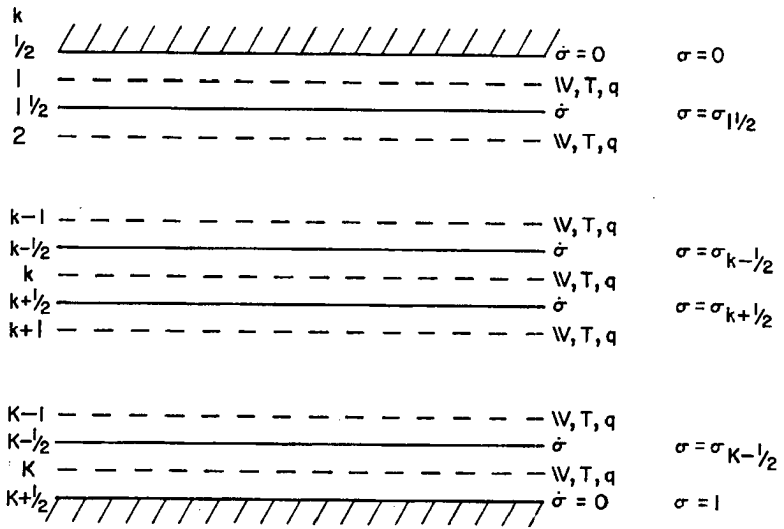
Figure A.1   Vertical finite differencing scheme.
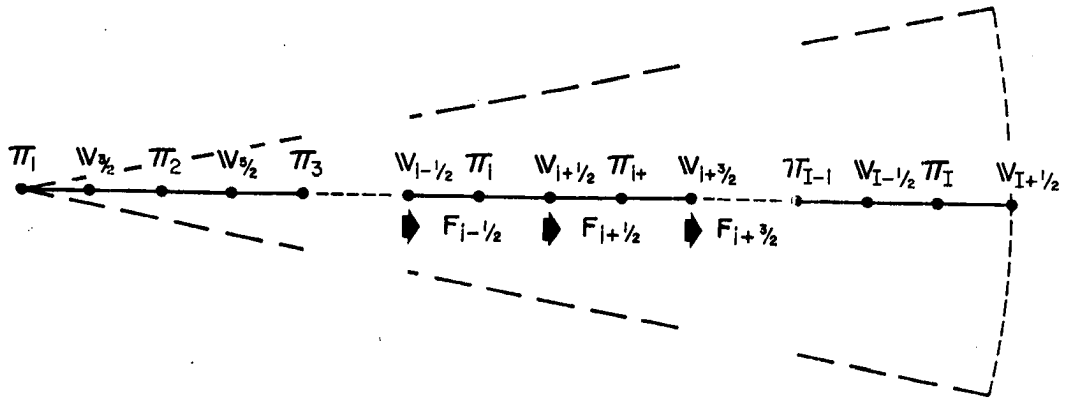
Figure A.2   Horizontal finite differencing scheme.

The mass continuity equation takes the forms

$$\frac{\partial \Pi_i}{\partial t} = - \sum_{k=1}^{K} \left(F_{i+\frac{1}{2},k} - F_{i-\frac{1}{2},k}\right) \Delta\sigma_k \; , \tag{A.3}$$

$$\dot{S}_{i,k+\frac{1}{2}} = \dot{S}_{i,k-\frac{1}{2}} - \left[\frac{\partial \Pi_i}{\partial t} + F_{i+\frac{1}{2},k} - F_{i-\frac{1}{2},k}\right]\Delta\sigma_k \; , \tag{A.4}$$

where we have defined

$$\Pi_i \equiv \pi_i r_i \Delta r \; , \tag{A.5}$$

$$F_{i+\frac{1}{2},k} \equiv \tfrac{1}{2}(\pi_i + \pi_{i+1})(ru)_{i+\frac{1}{2},k} \; , \tag{A.6}$$

$$\dot{S}_{i,k+\frac{1}{2}} \equiv \Pi_i \dot{\sigma}_{i,k+\frac{1}{2}} \; , \tag{A.7}$$

and where

$$p_{i,k} = p_T + \pi_i \sigma_k \; . \tag{A.8}$$

The hydrostatic equation is given by

$$\phi_{i,K} = \sum_{k=1}^{K} \left[\pi_i \sigma_k \frac{R}{p_{i,k}} \Delta\sigma_k - c_p(\sigma_{k-\frac{1}{2}}\alpha_{i,k} + \sigma_{k+\frac{1}{2}}\beta_{i,k})\right] T_{i,k} \; , \tag{A.9}$$

and by

$$\phi_{i,k} - \phi_{i,k+1} = c_p \left[\alpha_{i,k+1}T_{i,k+1} + \beta_{i,k}T_{i,k}\right] \; , \tag{A.9}'$$

where

$$\alpha_{i,k} \equiv \begin{cases} 0 \text{ or any value} & \text{for } k = 1 \\[2mm] \tfrac{1}{2}\left[1 - \left(\dfrac{p_{i,k-1}}{p_{i,k}}\right)^K\right] & \text{for } k \geq 2 \; , \end{cases} \tag{A.10}$$

$$\beta_{i,k} \equiv \begin{cases} \tfrac{1}{2}\left[\left(\dfrac{p_{i,k+1}}{p_{i,k}}\right)^K - 1\right] & \text{for } k \leq K-1 \\[2mm] 0 & \text{for } k = K \; . \end{cases} \tag{A.11}$$

Figure A.3 Three dimensional conceptualization of
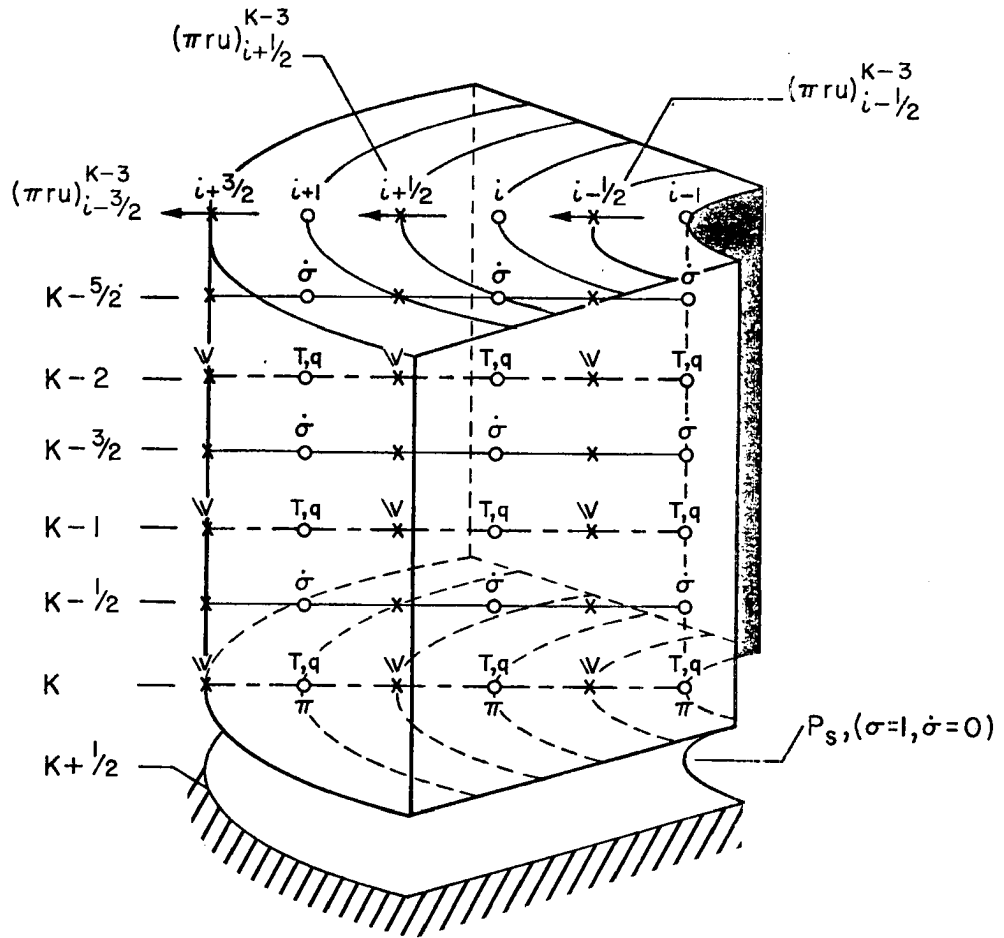vertical and horizontal finite differencing
scheme.

The equation of state is

$$\rho_{i,k}^{-1} = \frac{RT_{i,k}}{p_{i,k}} \quad . \tag{A.12}$$

The radial and tangential momentum equations are given respectively by

$$\frac{\partial}{\partial t} \left(\Pi_{i+\frac{1}{2}} u_{i+\frac{1}{2},k} \right) = -\frac{1}{2} \left[F_{i+1,k}\left(u_{i+\frac{1}{2},k} + u_{i+\frac{3}{2},k}\right) - F_{i,k}\left(u_{i-\frac{1}{2},k} + u_{i+\frac{1}{2},k}\right) \right]$$

$$- \frac{1}{\Delta\sigma_k} \frac{1}{2} \left[\dot{S}_{i+\frac{1}{2},k+\frac{1}{2}}\left(u_{i+\frac{1}{2},k} + u_{i+\frac{1}{2},k+1}\right) - \dot{S}_{i+\frac{1}{2},k-\frac{1}{2}}\left(u_{i+\frac{1}{2},k-1} + u_{i+\frac{1}{2},k}\right) \right]$$

$$+ \frac{1}{4} \left[(\pi_i + \pi_{i+1})(C_{i,k} + C_{i+1,k}) \right] v_{i+\frac{1}{2},k}$$

$$- \frac{r_{i+\frac{1}{2}}}{2} \left[(\pi_i + \pi_{i+1})(\phi_{i+1,k} - \phi_{i,k}) + \left[(\sigma\pi\rho^{-1})_{i,k} + (\sigma\pi\rho^{-1})_{i+1,k} \right] (\pi_{i+1} - \pi_i) \right]$$

$$+ \Pi_{i+\frac{1}{2}} S_{u_{i+\frac{1}{2},k}} \quad , \tag{A.13}$$

and

$$\frac{\partial}{\partial t} \left(\Pi_{i+\frac{1}{2}} v_{i+\frac{1}{2},k} \right) = -\frac{1}{2} \left[F_{i+1,k}\left(v_{i+\frac{1}{2},k} + v_{i+\frac{3}{2},k}\right) - F_{i,k}\left(v_{i-\frac{1}{2},k} + v_{i+\frac{1}{2},k}\right) \right]$$

$$- \frac{1}{\Delta\sigma_k} \frac{1}{2} \left[\dot{S}_{i+\frac{1}{2},k+\frac{1}{2}}\left(v_{i+\frac{1}{2},k} + v_{i+\frac{1}{2},k+1}\right) - \dot{S}_{i+\frac{1}{2},k-\frac{1}{2}}\left(v_{i+\frac{1}{2},k-1} + v_{i+\frac{1}{2},k}\right) \right]$$

$$- \frac{1}{4} \left[(\pi_i + \pi_{i+1})(C_{i,k} + C_{i+1,k}) \right] u_{i+\frac{1}{2},k} + \Pi_{i+\frac{1}{2}} S_{v_{i+\frac{1}{2},k}} \quad , \tag{A.14}$$

where

$$\Pi_{i+\frac{1}{2}} \equiv \frac{1}{2}(\Pi_i + \Pi_{i+1}) \quad , \tag{A.15}$$

$$F_{i,k} \equiv \frac{1}{2}(F_{i-\frac{1}{2},k} + F_{i+\frac{1}{2},k}) \quad , \tag{A.16}$$

$$\dot{S}_{i+\frac{1}{2},k+\frac{1}{2}} \equiv \frac{1}{2}(\dot{S}_{i,k+\frac{1}{2}} + \dot{S}_{i+1,k+\frac{1}{2}}) \quad , \tag{A.17}$$

$$C_{i,k} \equiv fr_i \Delta r + \frac{\Delta r}{2} \left(v_{i+\frac{1}{2},k} + v_{i-\frac{1}{2},k} \right) \, , \tag{A.18}$$

$$\left(\sigma \pi \rho^{-1} \right)_{i,k} \equiv \sigma_k \pi_i \frac{RT_{i,k}}{P_{i,k}} \, . \tag{A.19}$$

The thermodynamic equation is written in its final form as

$$\frac{\partial}{\partial t} \left(\Pi_i T_{i,k} \right) = -\tfrac{1}{2} \left[F_{i+\frac{1}{2},k}(T_{i,k} + T_{i+1,k}) - F_{i-\frac{1}{2},k}(T_{i-1,k} + T_{i,k}) \right]$$

$$- \frac{1}{\Delta\sigma_k} \tfrac{1}{2} \left[\dot{S}_{i,k+\frac{1}{2}}(T_{i,k} + T_{i,k+1} - 2\alpha_{i,k+1} T_{i,k+1}) \right.$$

$$\left. - \dot{S}_{i,k-\frac{1}{2}}(T_{i,k} + T_{i,k-1} + 2\beta_{i,k-1} T_{i,k-1}) \right]$$

$$+ \frac{(\sigma\pi\rho^{-1})_{i,k}}{c_p} \left\{ \frac{\partial \Pi_i}{\partial t} + \tfrac{1}{2} \left[(ru)_{i-\frac{1}{2}}(\pi_i - \pi_{i-1}) + (ru)_{i+\frac{1}{2}}(\pi_{i+1} - \pi_i) \right] \right\}$$

$$+ \frac{\Pi L}{c_p} (C-E) + \Pi_i \, S_{T_{i,k}} \, . \tag{A.20}$$

And finally, the continuity equation for water vapor may be written

$$\frac{\partial}{\partial t} \left(\Pi_i q_{i,k} \right) = - \left[F_{i+\frac{1}{2},k} \left(\frac{q_{i,k} + q_{i+1,k}}{2} \right) - F_{i-\frac{1}{2},k} \left(\frac{q_{i-1,k} + q_{i,k}}{2} \right) \right]$$

$$- \frac{1}{\Delta\sigma_k} \left[\dot{S}_{i,k+\frac{1}{2}} q_{i,k+\frac{1}{2}} - \dot{S}_{i,k-\frac{1}{2}} q_{i,k-\frac{1}{2}} \right] + \Pi_i (-C+E)_{i,k} + \Pi_i \, S_{q_{i,k}} \, .$$

$$\tag{A.21}$$

A.2 Time Differencing

The time differencing for the governing equations is accomplished with a leapfrog scheme coupled with an Asselin (1972) time filter. We illustrate the time differencing procedure by applying it to the equation

$$\frac{d\psi}{dt} = f(\psi) \, . \tag{A.22}$$

The leapfrog scheme can be written

$$\psi^{(n+1)} = \psi^{(n-1)} + 2\Delta t \, f\left[\psi^{(n)}\right] , \qquad (A.23)$$

where the superscripts denote discrete time levels. The Asselin time filter is applied in order to avoid separation of the odd and even time steps (sometimes referred to as time splitting) and can be written

$$\bar{\psi}^{(n)} = \psi^{(n)} + \frac{a}{2}\left[\bar{\psi}^{(n-1)} - 2\psi^{(n)} + \psi^{(n+1)}\right] , \qquad (A.24)$$

where a is the filter parameter.

In order to begin the time stepping procedure, information is needed at two time levels since the leapfrog scheme is a two level scheme. Consequently, a simulated backward time difference (Matsuno, 1966) is used for the first time step such that

$$\psi^{(1)*} = \psi^{(0)} + \Delta t \, f\left[\psi^{(0)}\right] , \qquad (A.25a)$$

$$\psi^{(1)} = \psi^{(0)} + \Delta t \, f\left[\psi^{(1)*}\right] , \qquad (A.25b)$$

where the * denotes a tentative value. The time stepping procedure then proceeds as shown in table A.1. We note that all diffusion (decay) terms are evaluated using a forward time difference, i.e.

$$\psi^{(n+1)} = \psi^{(n-1)} + 2\Delta t \, f\left[\psi^{(n-1)}\right] . \qquad (A.26)$$

The time differencing scheme must maintain the CFL (Courant, Friedrichs, Lewy, 1928) linear stability criterion which can be stated as

$$\nu \, \Delta t \leq 1 , \qquad (A.27)$$

Leapfrog scheme	$\psi^{(2)} = \psi^{(0)} + 2\Delta t\ f\left[\psi^{(1)}\right]$
Asselin filter	$\overline{\psi}^{(1)} = \psi^{(1)} + \dfrac{a}{2}\left[\psi^{(0)} - 2\psi^{(1)} + \psi^{(2)}\right]$
Leapfrog scheme	$\psi^{(3)} = \overline{\psi}^{(1)} + 2\ t\Delta f\left[\psi^{(2)}\right]$
Asselin filter	$\overline{\psi}^{(2)} = \psi^{(2)} + \dfrac{a}{2}\left[\overline{\psi}^{(1)} - 2\psi^{(2)} + \psi^{(3)}\right]$
	.
	.
	.
Leapfrog scheme	$\psi^{(n+1)} = \overline{\psi}^{(n-1)} + 2\Delta t\ f\left[\psi^{(n)}\right]$
Asselin filter	$\overline{\psi}^{(n)} = \psi^{(n)} + \dfrac{a}{2}\left[\overline{\psi}^{(n-1)} - 2\psi^{(n)} + \psi^{(n+1)}\right]$
	.
	.
	.

Table 4.1. Time stepping procedure

where ν is the frequency, and Δt is the time step used in the time differencing procedure described above. An estimate of the maximum time step can be made by considering the dispersion relation for the shortest wave that can be represented in the model ($2\Delta r$) which moves with a phase speed $(gh)^{\frac{1}{2}}$. We have

$$\nu = (f^2 + gh\ k^2)^{\frac{1}{2}} \simeq (f^2 + gh\ \left(\frac{\pi}{\Delta r}\right)^2)^{\frac{1}{2}} . \qquad (A.28)$$

The results of section 3.2 show that the fastest moving wave in the numerical model is associated with the external mode which has a phase speed $(gh)^{\frac{1}{2}} = 288$ m/s. Choosing $\Delta r = 15000$ m and $f = 5 \times 10^{-5} s^{-1}$ we obtain the result[1]

$$\Delta t \leq 16.6 \text{ seconds} . \qquad (A.29)$$

This should only be regarded as an estimate of the maximum time increment since the dispersion relation is distorted by the finite difference grid, especially for short ($2\Delta r$) waves (see Arakawa and Lamb, 1976; Fig. 5). Numerical tests have indicated that for a 15 km grid, a 20 second time step remains computationally stable.

---

[1] For phase speeds typical of the external mode the contribution of the Coriolis parameter f, to the frequency ν is negligable.

APPENDIX B

Vertical Differencing of Parameterized Convection

In this appendix, we present the vertically discrete forms of the equations presented in sections 2.2.2 and 2.2.3. We begin with the finite difference analogue of (2.45) for which we have chosen the form

$$\eta_{k-\frac{1}{2},n} = [1 + \lambda_n (\Delta p)_k] \, \eta_{k+\frac{1}{2},n} \quad , \tag{B.1}$$

where

$$(\Delta p)_p \equiv p_{k+\frac{1}{2}} - p_{k-\frac{1}{2}} \quad , \tag{B.2}$$

and the subscript n identifies a specific cloud type, the discrete analogue of a sub-ensemble (cloud type n implies detrainment at level n). Note that the horizontal index is neglected in the formulation of this finite difference set of equations.

Using (2.45) we can see that (2.46) may also be written

$$\frac{\partial}{\partial p} [\eta(p,\lambda) h_c(p,\lambda)] = \frac{\partial \eta(p,\lambda)}{\partial p} \, \bar{h} \, (p) \quad . \tag{B.3}$$

The corresponding finite difference equation is

$$\eta_{k-\frac{1}{2},n} \, h_{c_{k-\frac{1}{2},n}} - \eta_{k+\frac{1}{2},n} \, h_{c_{k+\frac{1}{2},n}} = \left[\eta_{k-\frac{1}{2},n} - \eta_{k+\frac{1}{2},n} \right] \bar{h}_k \quad , \tag{B.3}$$

which by (B.1) becomes

$$h_{c_{k-\frac{1}{2},n}} = \frac{1}{1 + \lambda_n (\Delta p)_k} \left[h_{c_{k+\frac{1}{2},n}} + \lambda_n (\Delta p)_k \bar{h}_k \right] \quad . \tag{B.4}$$

In a similar manner the discrete form of (2.47) can be written

$$q_{c_{k-\frac{1}{2},n}} + \ell_{k-\frac{1}{2},n} = \frac{1}{1 + \lambda_n (\Delta p)_k} \left\{ \left(q_{c_{k+\frac{1}{2},n}} + \ell_{k+\frac{1}{2},n} \right) + \lambda_n (\Delta p)_k \, \bar{q}_k \right\}$$

$$- c_o \ell_{k-\frac{1}{2},n} (\Delta p)_k \quad . \tag{B.5}$$

196

The discrete form of the saturation relation (2.48) is simply given by

$$q_{c_{k-\frac{1}{2},n}} = \bar{q}^*_{k-\frac{1}{2}} + \frac{\gamma_{k-\frac{1}{2}}}{1+\gamma_{k-\frac{1}{2}}} \frac{1}{L} \left[h_{c_{k-\frac{1}{2},h}} - \bar{h}^*_{k-\frac{1}{2}} \right] . \tag{B.6}$$

In order to determine the above budget quantities, the fractional entrainment rate λ_n must be known. Let us restate (2.49) as

$$\hat{h}^*(p) - h_c(p,\hat{p}) = 0 , \tag{B.7}$$

where

$$h^*(p) \equiv \bar{h}^*(p) - \frac{(1+\gamma(p))L\varepsilon(p)}{(1+\gamma(p)\varepsilon(p)\delta)} \left[\delta(\bar{q}^*(p) - \bar{q}(p)) \right] \tag{B.8}$$

and

$$\varepsilon(p) = c_p \bar{T}(p)/L . \tag{B.9}$$

The entrainment rate λ_n is a root of the discrete form of (B.7) and can be determined iteratively by defining the function

$$G_n \equiv \hat{h}^*_n - h_{c_{n,n}} . \tag{B.10}$$

Although Newton's method can be used in the solution of (B.7), the complicated form of the derivative of G_n makes this approach more costly from a computational point of view than other methods. Consequently, the variable scant method is used to solve for the fractional entrainment rate λ_n . This procedure, which requires two initial guesses, can be written as

$$\lambda_n^{\nu+1} = \lambda_n^\nu - \frac{G_n^\nu [\lambda_n^\nu - \lambda_n^{\nu-1}]}{G_n^\nu - G_n^{\nu-1}} , \tag{B.11}$$

where the superscripts denote iteration level. Convergence to $G_n \leq 1.0$ J/kg can be expected in 4 or 5 iterations.

Finally, the discrete analogue of the cloud work function must be defined. Let us first rewrite (2.52) as

$$A(\hat{p}) = \int_{p_D(\hat{p})}^{p_B} \beta(p)\eta(p,\hat{p}) \, [h_c(p,\hat{p}) - \bar{h}^*(p)] \, \frac{dp}{p}$$

$$+ \, \delta L \int_{p_D(\hat{p})}^{p_B} \epsilon(p)\eta(p,\hat{p}) \, [\bar{q}^*(p) - \bar{q}(p)] \, \frac{dp}{p} \quad , \qquad (B.12)$$

where

$$\beta(p) \equiv \frac{1 + \gamma(p)\epsilon(p)\delta}{1 + \gamma(p)} \quad . \qquad (B.13)$$

The discrete form of (B.12) is then written

$$A(n) = \sum_{k'=n}^{K-1} \beta_{n'} \left\{ \eta_{k'-\frac{1}{2},n} \left[h_{c_{k'-\frac{1}{2},n}} - \bar{h}^*_{k'} \right] (\Delta p)^-_{k'} \right.$$

$$\left. + \, \eta_{k'+\frac{1}{2},n} \left[h_{c_{k'+\frac{1}{2},n}} - \bar{h}^*_{k'} \right] (\Delta p)^+_{k'} \right\}$$

$$+ \, \delta L \sum_{k'=n}^{K-1} \epsilon_{k'} \left\{ \eta_{k'-\frac{1}{2},n} \left[\bar{q}^*_{k'} - \bar{q}_{k'} \right] (\Delta p)^-_{k'} \right.$$

$$\left. + \, \eta_{k'+\frac{1}{2},h} \left[\bar{q}^*_{k'} - \bar{q}_{k'} \right] (\Delta p)^+_{k'} \right\} \quad , \qquad (B.14)$$

where we have defined

$$\left. \begin{aligned} (\Delta p)^-_k &\equiv \frac{2(p_k - p_{k-\frac{1}{2}})}{(p_k + p_{k-\frac{1}{2}})} \\[2ex] (\Delta p)^+_k &\equiv \frac{2(p_{k+\frac{1}{2}} - p_k)}{(p_k + p_{k+\frac{1}{2}})} \end{aligned} \right\} \quad . \qquad (B.15)$$

APPENDIX C

Numerical Procedures for Large-Scale Condensation and Dry Convection

C.1 Large-Scale Condensation

At level k, let the temperature be denoted by T_k and the water vapor mixing ratio by q_k. If q_k is larger than the saturation value q_k^*, a certain mass of water vapor per mass of dry air must be condensed[1]. This condensation, denoted by $C_k \Delta t$, will reduce q_k to q_k' and increase T_k to T_k',

$$q_k' = q_k - C_k \Delta t ,\qquad (C.1)$$

$$T_k' = T_k + \frac{L}{c_p} C_k \Delta t . \qquad (C.2)$$

The new water vapor mixing ratio q_k' is the saturation value at the new temperature T_k',

$$q_k' = q^*(T_k', p_k) . \qquad (C.3)$$

Equations (C.1), (C.2) and (C.3) form a closed system in the unknowns q_k', T_k' and $C_k \Delta t$. q_k' and $C_k \Delta t$ can be eliminated to give

$$q_k - q^*(T_k', p_k) - \frac{c_p}{L} (T_k' - T_k) = 0 . \qquad (C.4)$$

Because of the complicated form of the function q*(T,p) an explicit equation for T_k' cannot be derived from (C.4). However, an iterative scheme can be developed by applying Newton's method to (C.4), (Hack and Schubert, 1976).

---

[1]The vapor is condensed to liquid water. The ice phase is not considered.

C.2 Dry Convection (Dry Convective Adjustment)

At level k, let the temperature before adjustment be denoted by T_k and the temperature after adjustment by T_k'. Then, if the adjustment involves the contiguous layers beginning with k_b and ending with k_e, we can write

$$\sum_{k=k_b}^{k_e} T_k' \Delta\sigma_k = \sum_{k=k_b}^{k_e} T_k \Delta\sigma_k . \qquad (C.5)$$

If θ denotes the potential temperature which results from the adjustment, then

$$T_k' = \left(\frac{P_k}{P_o}\right)^{\kappa} \theta \quad \text{for} \quad k_b \leq k \leq k_e . \qquad (C.6)$$

Substituting (C.6) into (C.5) we obtain

$$\theta = \frac{\displaystyle\sum_{k=k_b}^{k_e} T_k \Delta\sigma_k}{\displaystyle\sum_{k=k_b}^{k_e} \left(\frac{P_k}{P_o}\right)^{\kappa} \Delta\sigma_k} . \qquad (C.7)$$

After computing θ from (C.7) we can easily compute T_k from (C.6). This procedure may result in an unstable potential temperature stratification at intervals which border k_b and k_e, in which case the procedure is repeated with new k_b and k_e. The procedure is complete when there exists no single pair of k and $k+1$ for which $\theta_k < \theta_{k+1}$ for any integer $1 \leq k \leq K-1$, i.e. when a stable temperature stratification in the entire vertical column is reached.

Finite Difference Form of the Divergent Barotropic System of Equations

The nonlinear divergent barotropic system of equations can be written in flux form as

$$\frac{\partial}{\partial t}(\phi r u) + \frac{\partial}{\partial r}(\phi r u u) - \left(f + \frac{v}{r}\right)\phi r v + \phi r \frac{\partial \phi}{\partial r} = 0 , \qquad (D.1)$$

$$\frac{\partial}{\partial t}(\phi r v) + \frac{\partial}{\partial r}(\phi r u v) + \left(f + \frac{v}{r}\right)\phi r u = 0 , \qquad (D.2)$$

$$\frac{\partial \phi r}{\partial t} + \frac{\partial \phi r u}{\partial r} = 0 . \qquad (D.3)$$

In differential difference form they become

$$\frac{\partial \Phi_i}{\partial t} = -\left(F_{i+\frac{1}{2}} - F_{i-\frac{1}{2}}\right) , \qquad (D.4)$$

$$\frac{\partial}{\partial t}\left(\Phi_{i+\frac{1}{2}} u_{i+\frac{1}{2}}\right) = -\frac{1}{2}\left\{F_{i+1}\left(u_{i+\frac{1}{2}} + u_{i+\frac{3}{2}}\right) - F_i\left(u_{i-\frac{1}{2}} + u_{i+\frac{1}{2}}\right)\right\}$$

$$+ \frac{1}{4}\left\{(\phi_i + \phi_{i+1})(c_i + c_{i+1})\right\} v_{i+\frac{1}{2}} - \frac{r_{i+\frac{1}{2}}}{2}(\phi_i + \phi_{i+1})(\phi_{i+1} - \phi_i) , \quad (D.5)$$

$$\frac{\partial}{\partial t}\left(\Phi_{i+\frac{1}{2}} v_{i+\frac{1}{2}}\right) = -\frac{1}{2}\left\{F_{i+1}\left(v_{i+\frac{1}{2}} + v_{i+\frac{3}{2}}\right) - F_i\left(u_{i-\frac{1}{2}} + u_{i+\frac{1}{2}}\right)\right\}$$

$$- \frac{1}{4}\left\{(\phi_i + \phi_{i+1})(c_i + c_{i+1})\right\} u_{i+\frac{1}{2}} , \qquad (D.6)$$

where

$$\left.\begin{array}{l}
\Phi_i \equiv \phi_i r_i \Delta r \\[6pt]
F_{i+\frac{1}{2}} \equiv \frac{1}{2}(\phi_i + \phi_{i+1}) \, r_{i+\frac{1}{2}} \, u_{i+\frac{1}{2}} \\[6pt]
\Phi_{i+\frac{1}{2}} \equiv \frac{1}{2}(\Phi_i + \Phi_{i+1}) \\[6pt]
F_i \equiv \frac{1}{2}(F_{i-\frac{1}{2}} + F_{i+\frac{1}{2}}) \\[6pt]
c_i \equiv fr_i \, \Delta r + \frac{1}{2}(v_{i-\frac{1}{2}} + v_{i+\frac{1}{2}}) \, \Delta r
\end{array}\right\} \qquad . \qquad (D.7)$$

Equations (D.4)-(D.7) have been used to produce the numerical examples in section (3.5.1).

Solution of the Discrete Vertical Structure Problem For
Implementation of the Lateral Boundary Condition

The vertically discrete flux forms of (2.2)-(2.7) can be linearized
about a resting basic state and written as

$$\frac{\partial u_k}{\partial t} - fv_k + \frac{\partial}{\partial r}\left[\phi_k + \frac{\sigma_k \bar{\pi}}{\bar{p}_k}(\pi/\bar{\pi})\right] = 0 \quad, \tag{E.1}$$

$$\frac{\partial v_k}{\partial t} + fu_k = 0 \quad, \tag{E.2}$$

$$\frac{\partial}{\partial t}\left(\frac{\pi}{\bar{\pi}}\right) = -\sum_{k=1}^{K}\frac{\partial ru_k}{r\partial r}(\Delta\sigma)_k \quad, \tag{E.3}$$

$$\dot{\sigma}_{k+\frac{1}{2}} = -\left[\sigma_{k+\frac{1}{2}}\frac{\partial}{\partial t}\left(\frac{\pi}{\bar{\pi}}\right) + \sum_{k=1}^{K}\frac{\partial ru_k}{r\partial r}(\Delta\sigma)_k\right] \quad, \tag{E.4}$$

$$\frac{\partial T_k}{\partial t} + \left(\bar{T}_k - \frac{\bar{\pi}\,\sigma_k}{\bar{p}_k c_p}\right)\frac{\partial}{\partial t}\left(\frac{\pi}{\bar{\pi}}\right) + \bar{T}_k\frac{\partial ru_k}{r\partial r}$$

$$+ \left(\frac{\bar{p}_k}{p_0}\right)^\kappa \frac{1}{(\Delta\sigma)_k}\left[\dot{\sigma}_{k+\frac{1}{2}}\bar{\theta}_{k+\frac{1}{2}} - \dot{\sigma}_{k-\frac{1}{2}}\bar{\theta}_{k-\frac{1}{2}}\right] = 0 \quad. \tag{E.5}$$

The geopotential ϕ_k is determined from the linearized discrete hydro-
static equation

$$\phi_k = \pi\left\{\sum_{k=1}^{K}\left\{\sigma_k(\Delta\sigma)_k\,\bar{\pi}\,\frac{R\bar{T}_k}{\bar{p}_k}\left[\frac{1}{\bar{\pi}} - \frac{\sigma_k}{\bar{p}_k}\right]\right.\right.$$

$$\left.- c_p\left[\sigma_{k+\frac{1}{2}}\beta_k' + \sigma_{k-\frac{1}{2}}\alpha_k'\right]\bar{T}_k\right\} + \sum_{k'=k}^{K} c_p\left(\alpha_{k'+1}'\,\bar{T}_{k'+1} + \beta_{k'}'\,\bar{T}_{k'}\right)\right\}$$

$$+ \sum_{k=1}^{K}\left\{\left[\sigma_k(\Delta\sigma)_k\,\bar{\pi}\,\frac{R}{\bar{p}_k} - c_p(\sigma_{k+\frac{1}{2}}\bar{\beta}_k + \sigma_{k-\frac{1}{2}}\bar{\alpha}_k)\right]T_k\right\}$$

$$+ \sum_{k'=k}^{K-1} c_p(\bar{\alpha}_{k'+1}\,T_{k'+1} + \bar{\beta}_{k'}\,T_{k'}) \quad, \tag{E.6}$$

where

$$
\alpha_k' \equiv
\begin{cases}
0 & \text{for } k = 1 \\[2ex]
\dfrac{\kappa}{2}\left(\dfrac{\overline{p}_{k-1}}{\overline{p}_k}\right)^{\kappa}\left[\dfrac{\sigma_k}{\overline{p}_k} - \dfrac{\sigma_{k-1}}{\overline{p}_{k-1}}\right] & \text{for } k > 1
\end{cases} \quad,
$$

$$
\beta_k' \equiv
\begin{cases}
\dfrac{\kappa}{2}\left(\dfrac{\overline{p}_{k+1}}{\overline{p}_k}\right)^{\kappa}\left[\dfrac{\sigma_{k+1}}{\overline{p}_{k+1}} - \dfrac{\sigma_k}{\overline{p}_k}\right] & \text{for } k = 1,2,\ldots,K-1 \\[2ex]
0 & \text{for } k = K
\end{cases} \quad,
$$

$$
\overline{\alpha}_k \equiv
\begin{cases}
0 & \text{for } k = 1 \\[2ex]
\tfrac{1}{2}\left[1 - \left(\dfrac{\overline{p}_{k-1}}{\overline{p}_k}\right)^{\kappa}\right] & \text{for } k > 1
\end{cases} \quad,
$$

$$
\overline{\beta}_k \equiv
\begin{cases}
\tfrac{1}{2}\left[\left(\dfrac{\overline{p}_{k+1}}{\overline{p}_k}\right)^{\kappa} - 1\right] & \text{for } k = 1,2,\ldots,K-1 \\[2ex]
0 & \text{for } k = K
\end{cases} \qquad (E.7)
$$

Equations (E.4) and (E.5) can be combined with the use of (E.3) to give

$$
\frac{\partial T_k}{\partial t} + \left(\frac{\overline{\pi}\,\sigma_k}{\rho_k c_p} - \overline{T}_k\right) \sum_{k=1}^{K} \frac{\partial r u_k}{r\partial r}(\Delta\sigma)_k + \overline{T}_k \frac{\partial r u_k}{r\partial r}
$$

$$
+ \left(\frac{\overline{p}_k}{p_o}\right)^{\kappa} \frac{1}{(\Delta\sigma)_k} \left\{ \overline{\theta}_{k+\frac{1}{2}}\left[(\sigma_{k+\frac{1}{2}}-1)\sum_{k=1}^{K}\frac{\partial r u_k}{r\partial r}(\Delta\sigma)_k + \sum_{k'=k+1}^{K}\frac{\partial r u_{k'}}{r\partial r}(\Delta\sigma)_{k'}\right] \right.
$$

$$
\left. - \overline{\theta}_{k-\frac{1}{2}}\left[(\sigma_{k-\frac{1}{2}}-1)\sum_{k=1}^{K}\frac{\partial r u_k}{r\partial r}(\Delta\sigma)_k + \sum_{k'=k}^{K}\frac{\partial r u_{k'}}{r\partial r}(\Delta\sigma)_{k'}\right] \right\} \ . \quad (E.8)
$$

We assume (as in the vertically continuous case) that

$$u_k = U_k H_1^{(1)} (nr) \, e^{i\nu t} ,$$

$$v_k = V_k H_1^{(1)} (nr) \, e^{i\nu t} ,$$

$$T_k = \mathcal{T}_k H_0^{(1)} (nr) \, e^{i\nu t} ,$$

$$\pi = \Pi H_0^{(1)} (nr) \, e^{i\nu t} , \qquad\qquad\qquad \text{(E.9)}$$

where

$$n^2 \equiv \frac{\nu^2 - f^2}{c^2} . \qquad\qquad\qquad \text{(E.10)}$$

Since by definition

$$\frac{dH_0^{(1)}(nr)}{dr} = -n \, H_1^{(1)}(nr)$$

and

$$\frac{dr H_1^{(1)}(nr)}{r dr} = n \, H_0^{(1)}(nr) ,$$

equations (E.3), (E.1), (E.2) and (E.8) can be written

$$i\nu \, \frac{\Pi}{\overline{\pi}} = - \sum_{k=1}^{K} n \, U_k (\Delta\sigma)_k , \qquad\qquad \text{(E.11)}$$

$$i\nu \, U_k - f V_k - n \left\{ \Phi_k + \frac{\sigma_k \Pi}{\overline{\rho}_k} \right\} = 0 , \qquad\qquad \text{(E.12)}$$

$$i\nu \, V_k + f U_k = 0 , \qquad\qquad \text{(E.13)}$$

$$i\nu \, \mathcal{T}_k + n \left\{ \left(\frac{\overline{\pi} \, \sigma_k}{\overline{\rho}_k c_p} - \overline{T}_k + \left(\frac{\overline{p}_k}{p_0} \right)^{\kappa} \frac{1}{(\Delta\sigma)_k} \left[\overline{\theta}_{k+\frac{1}{2}}(\sigma_{k+\frac{1}{2}} - 1) \right. \right. \right.$$

$$\left. - \overline{\theta}_{k-\frac{1}{2}}(\sigma_{k-\frac{1}{2}} - 1) \right] \bigg) \sum_{k=1}^{K} U_k (\Delta\sigma)_k + \left(\frac{\overline{p}_k}{p_0} \right)^{\kappa} \frac{1}{(\Delta\sigma)_k} (\overline{\theta}_{k+\frac{1}{2}} - \overline{\theta}_{k-\frac{1}{2}}) \sum_{k'=k+1}^{K} U_{k'} (\Delta\sigma)_{k'}$$

$$\left. + \left[\overline{T}_k - \left(\frac{\overline{p}_k}{p_0} \right)^{\kappa} \overline{\theta}_{k-\frac{1}{2}} \right] U_k \right\} = 0 . \qquad\qquad \text{(E.14)}$$

Thus, for specified wave number n, (E.11)-(E.14) and (E.6) constitute

an eigenvalue problem where $i\nu$ is the eigenvalue and the quantities

Π, U, V and T comprise the eigenfunctions (or vertical structure

functions). Since in the vertically continuous problem we consider

the case for large n only, equation (E.13) can be neglected as can

the term fV_k in (E.12). This approximation eliminates the stationary

geostrophic modes from the problem and allows the eigenvalue to become

$\frac{i\nu}{n}$, the pure gravity wave phase velocity for the corresponding ver-

tical structure functions. For a model with K levels, the eigenvalue

problem can be solved numerically to yield 2K+1 eigenvalues and

eigenfunctions. The eigenvalues correspond to K inward propagating

modes, K outward propagating modes, and a stationary computational

mode which arises due to the Lorenz (1960) type vertical differencing

employed in the model (i.e. non-staggered temperature).

4. Title and Subtitle			5. Report Date December, 1980
THE ROLE OF CONVECTIVE-SCALE PROCESSES IN TROPICAL CYCLONE DEVELOPMENT			6.

7. Author(s) James J. Hack and Wayne H. Schubert	8. Performing Organization Rept. No. CSU-ATSP-330

9. Performing Organization Name and Address Department of Atmospheric Science Colorado State University Foothills Campus Fort Collins, CO 80523	10. Project/Task/Work Unit No.
	11. Contract/Grant No. ATM-7808125 N00014-79-C-0793

12. Sponsoring Organization Name and Address National Science Foundation Office of Naval Research	13. Type of Report & Period Covered
	14.

15. Supplementary Notes

16. Abstracts

An eighteen level axisymmetric primitive equation tropical cyclone model which incorporates the Arakawa-Schubert (1974) spectral cumulus parameterization is presented. The quasi-equilibrium hypothesis, which involves the solution of an integral equation for the cloud base mass flux distribution, is successfully formulated as an optimization problem to guarantee a nonnegative solution. A linear analysis suggests that in the tropics a large fraction of the available potential energy generated by the release of latent heat is partitioned to gravity-inertia wave motion and hence is radiated away to the far field. Therefore, an approximate pure gravity wave radiation boundary condition is derived which minimizes the reflection of gravity-inertia waves by the lateral boundary of the model.

The sensitivity of axisymmetric model storm development to the exact form of the lateral boundary condition, initial moisture distribution, and latent heat release mechanism is tested. It is demonstrated that the development of a hurricane-like

17. Key Words and Document Analysis. 17a. Descriptors

Tropical cyclones
Hurricanes
Typhoons
Primitive-equation conditions

Lateral boundary conditions
Convective-scale transports
Radiative processes
Cumulus parameterization

17b. Identifiers/Open-Ended Terms

16. Abstract continued.
circulation can be simulated without parameterized convection as suggested by Rosenthal (1978). Several other sensitivity experiments are conducted to address the roles of radiation and cumulus momentum transport in tropical cyclone development. The numerical results lead to the conclusion that neither of these processes should be neglected in attempts to numerically simulate the life cycle of the tropical cyclone since they appear to contribute significantly to the organization and scale of tropical disturbances.

18. Availability Statement	19. Security Class (This Report) UNCLASSIFIED	21. No. of Pages 206
	20. Security Class (This Page) UNCLASSIFIED	22. Price